Deformation Mechanisms in Magnesium Alloy Elektron™ 675

David Randman

Department of Engineering Materials

The University of Sheffield

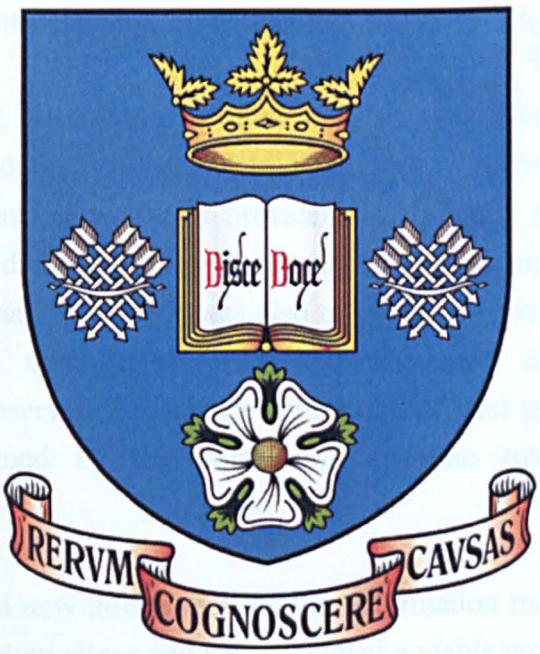

Thesis submitted for the degree of Doctor of Philosophy

June 2010

Summary

Magnesium is a very lightweight and strong material and thus is of particular interest to industries such as aerospace and automotive. Elektron™ 675 is a new alloy developed by Magnesium Elektron Ltd. and based on the magnesium-gadolinium-yttrium system. This gives particularly high strength and high temperature stability but currently proves more difficult to process than conventional magnesium alloys. The objectives in the current work were to study the deformation behaviour with particular emphasis on the flow behaviour during rolling and the deformation mechanisms that are operating.

To study the deformation behaviour over a wide range of conditions, plane strain compression (PSC) tests were carried out in a matrix between 380°C and 520°C and $1s^{-1}$ and $10s^{-1}$ strain rates, similar conditions to those experienced in industrial rolling. The tests showed similar behaviour at all conditions with a rise to a peak stress followed by continuous softening and constitutive equations of flow stress were developed. Further PSC tests were used to study behaviour such as static recrystallisation during annealing and the effect of non-isothermal rolling with cold rolls.

Following deformation, the microstructures were studied using various microscopy techniques, the most common being electron backscatter diffraction (EBSD). It was found that $\{10\bar{1}2\}$ twinning was very prevalent in the early stages of deformation, particularly in the tests deformed at low temperatures or high strain rates. Slip occurred predominantly on the basal plane but was also observed on prismatic planes and there was strong evidence that <c+a> pyramidal slip was also active. Dynamic recrystallisation was observed in necklace formations around grain boundaries and is thought to have formed by the continuous dynamic rotation recrystallisation mechanism.

This study has provided new information on the deformation mechanisms that operate in high strength magnesium alloys and has calculated a viable process window in which Elektron 675 can be rolled.

Contents

Acknowledgements

My greatest thanks go my supervisors, Prof. Mark Rainforth and Dr Brad Wynne, for all of the encouragement, assistance and direction they've given me during the course of my PhD in Sheffield.

I would like to thank the EPSRC (Engineering and Physical Sciences Research Council) and Magnesium Elektron Ltd. for the financial assistance necessary for this research project. I also wish to thank Magnesium Elektron, and especially Dr Bruce Davis, for providing us with the opportunity to work on a new, exciting alloy and for supplying all of the material, information and support needed through the project.

It has been a pleasure to work in the IMMPETUS research group for the last 3½ years; I've learnt a lot and made some great friends. Thanks go especially to all those who I've worked alongside in D1 for creating a great atmosphere to work in and providing endless distractions from my actual work.

Special thanks must go to Dr Krzysztof Muszka, who I have collaborated with on the finite element modelling, and to Jake Corteen and Andy Winder who collaborated on various aspects of the work as part of their Masters Degrees. Their help was incredibly useful and allowed me to look at areas I would not otherwise have studied.

Many members of technical staff within IMMPETUS, the Sorby Electron Microscopy Centre, and the Department of Engineering Materials in general, have helped during this project. I am grateful for all of their assistance.

Final thanks must go to my friends and family for all the encouragement and for attempting to look interested whenever I started talking about magnesium, and especially to my parents for providing endless support through this PhD.

1. Introduction

1.1 Background

Magnesium alloys are known to be exceptionally light and strong and thus have applications wherever weight savings are required. Therefore, there are many possible uses, particularly in the wrought form for areas such as car body panels or internal structures of aircraft. The current work is concerned with a new magnesium alloy known as Elektron™ 675. This has been developed by Magnesium Elektron Ltd. as a particularly strong alloy that can be used at higher temperatures than many other magnesium alloys. It achieves this high strength and temperature range through the addition of the rare earth elements yttrium and gadolinium.

A major disadvantage of magnesium has always been the difficulty of wrought processing due to the lack of ductility, particularly at low temperatures. Magnesium is rolled in much the same way as other materials, reducing a large cast billet to plate or sheet material through a number of different rolling passes. Rolling causes plane strain conditions in the material, with no extension in the transverse direction. The speed and temperature at which the rolling process is carried out has a very strong influence on the ductility of the material and also on the final properties due to changes in microstructure and texture. Deformation occurs through slip and twinning and further changes occur from recovery and recrystallisation. It is generally found that magnesium, along with many other metals having a hexagonal crystal structure, forms a basal texture during compression that is not normally desirable in rolled sheet.

1.2 Main Techniques Used

The basis of this project was the laboratory simulation of industrial rolling using the plane strain compression (PSC) technique. This allows small scale experiments in which the material can be subjected to a similar stress state to that experienced in rolling, giving the opportunity to carry out a greater number of tests at a greater precision than would be possible through rolling trials. The thermomechanical compression machine used was developed for The University of Sheffield and can carry out plane strain compression tests with a very high degree of accuracy in temperature, load and displacement measurements.

Over the past few years, the speed and ease with which automated Electron Backscatter Diffraction (EBSD) can be performed has increased greatly to the point at which it is a conventional tool for many applications. EBSD obtains data on both the microstructure and texture simultaneously and thus is very useful to analyse the changes taking place during thermomechanical processing. Therefore, EBSD was the most important analysis technique in the current work to study the deformed samples.

1.3 Objectives

The overall aim of this work was to gain a greater understanding of the deformation behaviour of Elektron 675 and magnesium alloys in general. To do this, the objectives were to:

- Perform a matrix of PSC tests over a range of conditions
- Use the flow data from PSC tests to calculate constitutive equations of flow stress
- Perform further PSC tests to study other behaviour, such as rolling with cold tools and annealing between rolling passes
- Study the deformed microstructure to identify all the microstructural changes occurring during deformation
- Examine the dynamic recrystallisation behaviour in detail to determine which mechanism is operating
- Identify which slip and twinning modes are active
- Study the age hardening response of the material

2. Literature Survey

2.1 Introduction to Magnesium

The major reason that magnesium is of interest to industry is that it has the lowest density of any structural metal, approximately two thirds that of aluminium and one fifth that of steel[1-4]. In combination with a reasonably high strength this means that many magnesium alloys can have better specific strength than comparable aluminium alloys. This makes it particularly attractive to those industries where weight saving is an issue, namely aerospace, automotive and transportable equipment. With the emphasis on fuel economy getting ever stronger in the modern world, the light metals, and magnesium in particular, are being used and researched to a greater extent.

The advantages of magnesium are not only in the strength to weight ratio, with high machinability and damping capacity often promoted[1-4]. Magnesium can be machined approximately 10 times as fast as steel and twice as fast as aluminium. Historically, magnesium has not been considered for many applications due to concerns over flammability, corrosion resistance and workability. The flammability issue is simply incorrect because it has been proven many times that bulk pieces of magnesium are very difficult to ignite, generally needing to reach the melting point before ignition will occur. Although it is now accepted that bulk magnesium does not cause a fire hazard, the chips and swarf created from machining do pose a certain risk and suitable precautions must be taken[1, 3]. Magnesium is a very chemically reactive metal and the corrosion properties are rather poor when compared to aluminium[1-4]. However, in standard atmospheres, magnesium actually has better corrosion resistance than mild steel and protective coatings have been developed to allow the use of magnesium in most industrial applications. Workability is still an issue, and will be discussed further in this work, although more precise modern thermomechanical processing techniques and newer alloys can generally overcome most problems.

Magnesium is the 8th most common element in the earth's crust and is also very prevalent in sea water, making up about 0.13%[1, 4]. The most common solid ores of magnesium are dolomite and magnesite, both carbonates of magnesium. For many years the main production method of magnesium was electrolytic extraction from sea water but this has recently been overtaken by the Pidgeon process. The Pidgeon process is a direct thermal reduction batch method using ferrosilicon to reduce dolomite[4].

The most recent figures available for the worldwide production of magnesium come from the US geological survey in Jan 2010[5]. This report does not include the production within the United States but recently this has been negligible when compared to other countries. The total worldwide production of magnesium in 2008 was 671,000 tonnes and the estimated value for 2009 was 570,000 tonnes. The drop from 2008 to 2009 was explained by the recent economic downturn and is expected to recover with the general economy. Historically, a majority of magnesium was used as an alloying component for aluminium and, while this proportion is decreasing as more is used for magnesium components, approximately half of the worldwide production was still being used in the aluminium industry in 2004[4].

2.1.1 History of Magnesium Use

Magnesium was first recognised as a new element and isolated by Humphry Davy in 1808[1-4]. Various methods of production were discovered in the first half of the 19th century and by the middle of the century, commercial production had started in Paris. However, the quantity produced remained very low and by about 1890 had only increased to roughly 10 tonnes per year. The advent of aviation caused a substantial change in the use of magnesium due to the strong emphasis on specific strength. By the end of the 1st World War, production had risen to about 3000 tonnes per year and then by the end of the 2nd World War to about 300,000 tonnes per year. Following the end of the 2nd World War, however, the level of production dropped dramatically and only returned to the same levels again in the 1970s. Figure 1[4] compares the differing production levels of magnesium with other metals, and also plastics, over approximately the last 100 years.

Most early magnesium alloys were based on the magnesium-aluminium system because it gave reasonable properties and could be heat treated to increase the strength. Later, zirconium was added to many alloys as it greatly improved the properties of the alloy through grain refinement. More recently, rare earth metals have been used to further improve the properties, particularly at higher temperatures, and these alloys will be discussed in more detail in section 2.2.

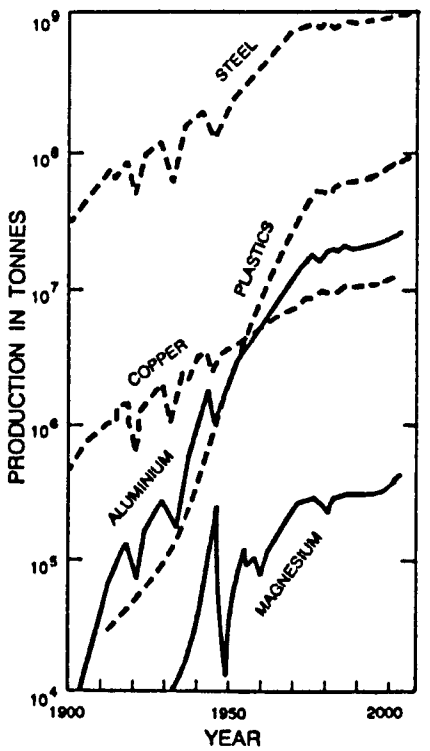

Figure 1 – World production figures for various metals and plastics[4]

2.1.2 Alloy Classifications

There is no international standard for naming magnesium alloys, although the nomenclature developed by the American Society for Testing Materials has been widely accepted and will be used in this work. This system names the alloy with two letters followed by two numbers. The two letters refer to the two largest alloying additions, with greatest addition first, by the following scheme:

A – Aluminium	B – Bismuth
C – Copper	D – Cadmium
E – Rare earths	F – Iron
H – Thorium	K – Zirconium
L – Lithium	M – Manganese
N – Nickel	P – Lead
Q – Silver	R – Chromium
S – Silicon	T – Tin
W – Yttrium	Y – Antimony
Z – Zinc	

The two numbers give the nominal weight percent of each of the two alloying additions, rounded to the nearest percent. For example, AZ31 refers to the alloy with nominal composition Mg-3Al-1Zn. Often a further letter is added to the end of the name to refer to a specific variation on the composition.

2.1.3 Standard Alloy Additions

Many elements have been used in magnesium alloys over the years and those commonly added in commercial alloys, or impurities that must be removed from the alloy, are given in Table 1[6]. Rare earth elements are only covered briefly in this table, but will be discussed in more detail in section 2.2 due to the importance for the current work.

Table 1 – General effects of elements used in magnesium alloys[6]

Alloying element	Melting and casting behaviour	Mechanical and technological properties	Corrosion behaviour
Ag		Improves elevated temperature tensile and creep properties in the presence of rare earths	Detrimental influence on corrosion behaviour
Al	Improves castability, tendency to microporosity	Solid solution hardener, precipitation hardener at low temperatures (<120°C)	Minor influence
Be	Significantly reduces oxidation of melt surface at very low concentrations (<30ppm), leads to coarse grains		
Ca	Effective grain refining effect, slight suppression of oxidation of the molten metal	Improves creep resistance	Detrimental influence on corrosion behaviour

Alloying element	Melting and casting behaviour	Mechanical and technological properties	Corrosion behaviour
Cu	System with easily forming metallic glasses, improves castability		Detrimental influence on corrosion behaviour, limitation necessary
Fe	Magnesium hardly reacts with mild steel crucibles		Detrimental influence on corrosion behaviour, limitation necessary
Li	Increases evaporation and burning behaviour, melting only in protected and sealed furnaces	Solid solution hardener at ambient temperatures, reduces density, enhances ductility	Decreases corrosion properties strongly, coating to protect from humidity is necessary
Mn	Control of Fe content by precipitating Fe-Mn compound, refinement of precipitates	Increases creep resistance	Improves corrosion behaviour due to iron control effect
Ni	System with easily forming metallic glasses		Detrimental influence on corrosion behaviour, limitation necessary
Rare Earths	Improve castability, reduce microporosity	Solid solution and precipitation hardening at ambient and elevated temperatures; improve elevated temperature tensile and creep properties	Improve corrosion behaviour
Si	Decreases castability, forms stable silicide compounds with many other alloying elements, compatible with Al, Zn, and Ag, weak grain refiner	Improves creep properties	Detrimental influence

Alloying element	Melting and casting behaviour	Mechanical and technological properties	Corrosion behaviour
Th	Suppresses microporosity	Improves elevated temperature tensile and creep properties, improves ductility, most efficient alloying element	
Y	Grain refining effect	Improves elevated temperature tensile and creep properties	Improves corrosion behaviour
Zn	Increases fluidity of the melt, weak grain refiner	Precipitation hardening, improves strength at ambient temperatures, tendency to brittleness and hot shortness unless Zr refined	Minor influence, sufficient Zn content compensates for detrimental effect of Cu
Zr	Most effective grain refiner, incompatible with Si, Al and Mn, removes Fe, Al, and Si from the melt	Improves ambient temperature tensile properties slightly	

The nominal compositions of the common alloys studied in the literature and widely used commercially are listed below[4]:

- AZ31: Mg-3Al-1Zn
  Widely used alloy for wrought applications due to reasonable ductility, room temperature strength, cost and weldability.

- WE43: Mg-4Y-3RE
  Alloy developed for high strength at high temperature. WE43 is more isotropic than other alloys.

- WE54: Mg-5Y-4RE
  Alloy developed for high strength at high temperature – used at temperatures above that of WE43. This alloy is also more isotropic than other alloys.

- ZK60: Mg-6Zn-0.4Zr
  The best combination of strength and ductility at room temperature of any wrought magnesium alloy.

2.2 Magnesium-Rare Earth Alloys

As was shown in the previous section, rare earths have long been known as useful additions to magnesium as they can improve strength and corrosion resistance. The rare earth metals consist of elements in group 3 of the periodic table, including scandium, yttrium and the lanthanide series; therefore, they all have similar properties[7]. Rare earth ores are often found together and, following extraction, the resultant combination of metals, predominantly cerium, is known as mischmetal. Initial uses of rare earths in magnesium alloys generally used mischmetal rather than any specific rare earth and it was only later that more in depth studies were carried out. A full investigation of all rare earth additions[7] has shown that the rare earths can be divided into 2 groups, the cerium group and the yttrium group. The cerium group consists of the elements between lanthanum and europium and produces rapid solid solution hardening but no useful age hardening and the yttrium group consists of yttrium and those elements between gadolinium and lutetium and produces a very useful age hardening response[8]. The precipitates are particularly advantageous because they are stable at high temperatures. This is due to the high melting point of the rare earth elements and the slow diffusion of atoms. The precipitate structures also contain a large number of magnesium atoms, and thus the volume fraction is very high[9].

The current study is concerned with the behaviour of Elektron 675. The major constituents of this alloy are gadolinium and yttrium; therefore, there will be an emphasis on those particular systems for the remainder of this section.

2.2.1 High Temperature Alloy Development

To obtain high temperature (~250-350°C), creep resistant magnesium alloys, the dislocation motion must be inhibited. Therefore, the same methods of dislocation inhibition used in any high temperature alloy system are required, namely forming stable precipitates or slowing diffusion within the material[10].

Early developments to increase creep properties attempted to make minor adjustments to existing Mg-Al series alloys by adding elements such as silicon, zinc, manganese, calcium or small amounts of rare earths. This produced improvements to the high temperature properties but the alloys were only stable up to approximately 200°C[3].

Initially rare earth metals were rarely used and, if at all, it was in the form of mishmetal, a mixture of rare earths with cerium as the predominant component[7]. In the 1940s and 50s, important work was carried out to improve the understanding of the properties of rare earth magnesium alloys. Leontis[11, 12] found significant differences between various rare earth metals when used as alloying additions, and the previous assumption that all rare earths had very similar properties was broken. This led to production of neodymium containing alloys that were stronger than the previous mishmetal alloys. In the early 1950s, thorium was considered as a suitable alloying component and was studied in some depth[4]. This was a very useful element as it significantly increased the creep properties at high temperatures due to the production of the thermally stable precipitate $Mg_{23}Th_6$. Commercial alloys such as ZH62 (Mg-6Zn-2Th) and HZ32 (Mg-3Th-2Zn) found use in the industry but have now been phased out due to the radioactive nature of thorium.

In the 1960s, various rare earth metals were investigated as individual additions to magnesium and there were promising results from both yttrium and scandium that led to thorough investigations of the entire rare earth series[7]. The magnesium-yttrium alloys have been particularly commercially successful with WE54 and WE43 in large scale production today, giving a useful upper limit of 300°C. Yttrium, discussed further in section 2.2.3, will form stable precipitates in the alloy and is also a very effective solid solution hardener[8]. The magnesium-scandium alloys can take the upper limit even further, almost to 350°C with reasonable creep properties, due to a very stable Mg_2Sc phase giving good precipitation hardening.

2.2.2 Gadolinium

Magnesium-gadolinium systems have been studied and found to be useful as far back as 1974[13]. It can be seen from the Mg-Gd phase diagram, shown in figure 2, that gadolinium has a relatively high solubility at high temperatures, 23.49 wt% at 548°C, but then decreases dramatically with temperature down to 3.82 wt% at 200°C[13, 14], making it a very useful precipitation-hardening alloy system. It has been found that due to this strong and thermally stable precipitation, the creep resistance of heat treated binary Mg-Gd alloys can be up to 10 times better than WE43, one of the best commercially available creep resistant magnesium alloys[8]. Gadolinium has also been shown to decrease the grain size in certain alloys, thus further increasing the strength of the material[15].

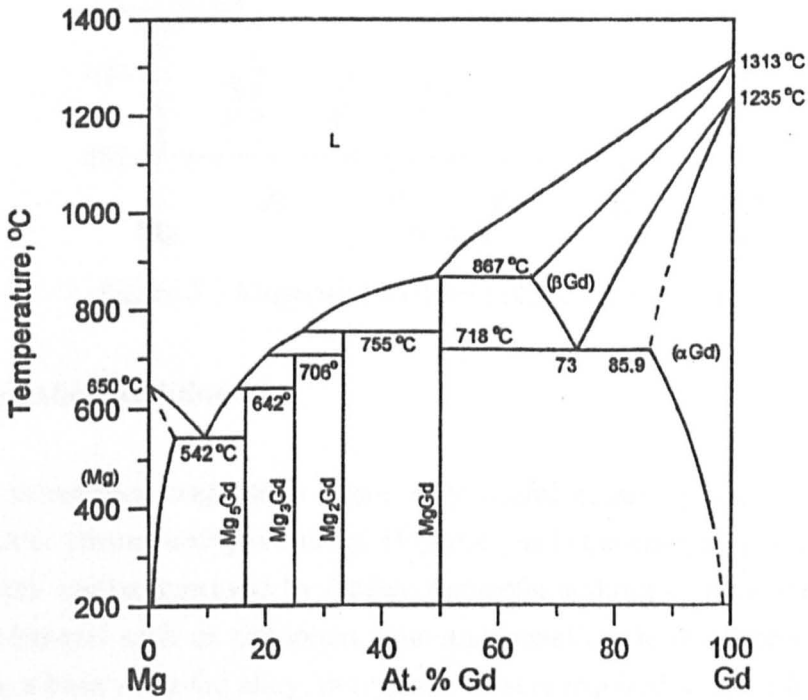

Figure 2 – Magnesium-gadolinium phase diagram[7]

2.2.3 Yttrium

The magnesium-yttrium system is very similar to the magnesium-gadolinium system, as shown by the phase diagram in figure 3. The solubility of Y in Mg at 550°C is 11.5wt%, decreasing to 2.2wt% at 200°C[7], which again leads to a strong precipitation behaviour. Yttrium also provides a useful solid solution strengthening effect along with an increase in ductility. This is due to the increase in friction of dislocation motion on the basal plane giving a higher chance of cross-slip onto other glide planes[16, 17].

Yttrium also distributes along grain boundaries during solidification, decreasing the rate of grain growth[18].

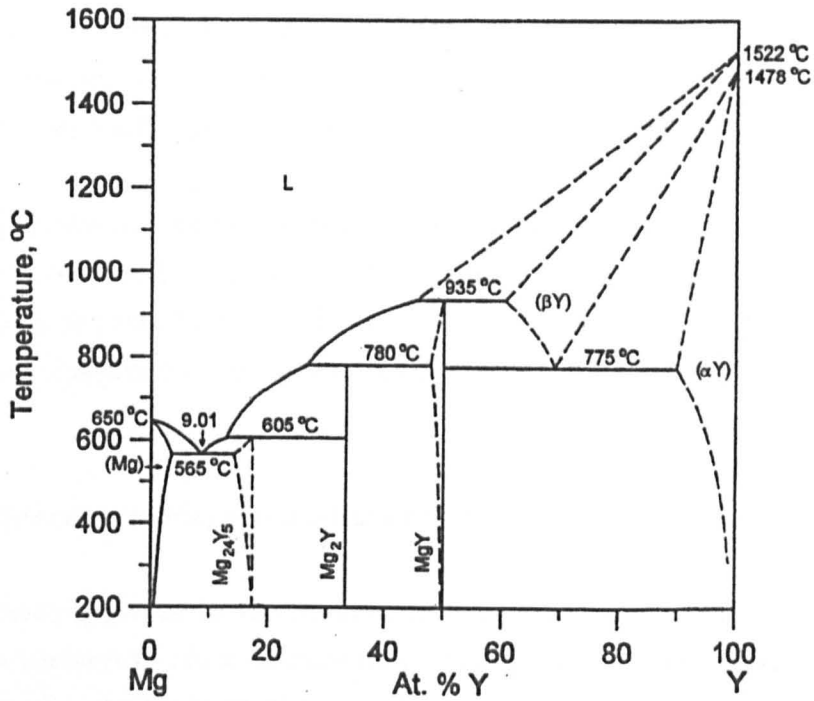

Figure 3 – Magnesium-yttrium phase diagram[7]

2.2.4 Other Alloy Additions

It has been shown that magnesium forms very useful binary systems with rare earth elements such as yttrium and gadolinium. However, as is the case in most alloy systems, the binary form can be improved by further elemental additions. In the case of Mg-Gd and Mg-Y, elements such as zirconium, zinc and scandium have all been found to be useful[14]. In a binary Mg-Gd alloy, over 10wt% Gd is required to provide a reasonable age hardening response[19]. Therefore, other additions are useful to reduce the quantity of Gd needed and thus the overall cost of the material.

Two very common alloying elements in magnesium alloys are zinc and aluminium, both of which have been investigated as additional components in magnesium-rare earth systems. Aluminium has actually been found to decrease the strength of some magnesium-rare earth alloys and have negligible effect in others; however, small strength increases have been reported in magnesium-yttrium alloys[7]. Zinc is very useful in Mg-Gd systems and can increase hardness by up to 20VH, UTS by 80MPa at 25°C and 60MPa at 175°C, and creep resistance by a significant amount[14]. This has

been partly attributed to the formation of basal precipitate plates which can increase resistance to dislocation motion, particularly non-basal slip and cross-slip[14]. Zirconium has often been used in commercial magnesium alloys because it has a strong grain refining effect and also improves castability. While zirconium is incompatible with some elements, such as aluminium, manganese and silicon, there are no adverse reactions with rare earth materials, and it has been used successfully in the past[7].

Ternary magnesium-rare earth systems have been studied and have varying properties. Neodymium is commonly used in conjunction with yttrium in the WE alloys to great effect and has also been shown to increase hardness in Mg-Gd[20]. The understanding of the ternary systems has led to the development of Elektron 675 by Magnesium Elektron.

2.2.5 Precipitation in Magnesium-Rare Earth Alloys

The precipitation sequence in Mg-Gd systems has been well studied[13, 18, 20-26] and has strong similarities to other magnesium-rare earth systems, including Mg-Y. Almost all of the work on the aging of alloys in the Mg-Gd system involved further alloying elements and thus there were slight disparities between each system. However, these differences were generally only kinetic or volume changes and the same sequence of decomposition was followed in all cases where Gd is the major alloying component.

The first precipitate to form from the supersaturated solid solution is metastable β" which has the composition Mg_3Gd[21]. This has a DO_{19} hexagonal ordered crystal structure[13, 21-23] and forms with the same crystallographic orientation as the parent matrix[22]. Many studies[21, 22] show that these precipitates are small, spherical or nearly spherical particles less than 15nm in size, however Apps *et al.*[25] found rod or plate shaped particles of β". This may have been due to the difference in alloy compositions as their alloy contained neodymium, which is in the Ce group of rare earths so may modify the precipitation behaviour.

After a certain period of time, often very soon after β" has started to form[21], the next intermediate precipitate (β') begins to develop. This is an intermetallic, with a formula of approximately $Mg_{3\text{-}5}Gd$, and grows as convex lens shaped discs[22] that are often slightly elongated in the $[0001]_\alpha$ direction[26]. Some studies[24, 25] have shown β' forming as globular particles but this, again, was probably due to other alloying elements modifying the behaviour. The plates form on $\{1\bar{1}20\}_\alpha$ prismatic planes in the

matrix and have the same frequency on each of the different orientations of this type of plane[19]. They have a c-base-centred-orthorhombic (cbco) crystal structure and take up a crystallographic orientation with the matrix such that $[001]_{\beta'}$ is parallel with $[0001]_{\alpha}$ and $(100)_{\beta'}$ is parallel with $\{2\bar{1}\,\bar{1}0\}_{\alpha}$ [13]. The lattice parameters of the β' crystal structure are shown below:

$$a_{\beta'} = 2 \times a_{Mg}, \quad b_{\beta'} = 8 \times d_{(10\bar{1}0)_{Mg}}, \quad c_{\beta'} = c_{Mg} \text{ [22]}$$

Therefore, the plates are coherent with the matrix in the $\{11\bar{2}0\}_{\alpha}$ plane but lose coherency at the edges[13]. At peak aging, generally around 8-16 hours at 250°C[21, 22], β' precipitates dominate the microstructure and have a maximum size of approximately 150nm diameter and 10nm thickness[21, 26]. By examining material in this condition in the transmission electron microscope the precipitates could be clearly seen. When looking down the $[0001]_{\alpha}$ direction there are 3 sets of precipitates lying parallel to the beam on the $\{11\bar{2}0\}_{\alpha}$ planes and projecting a bamboo leaf shape, see figure 4[22]. The aging time for precipitation is reduced if the material has undergone deformation prior to heat treatment. This is because the increased dislocation density provides more nucleation sites for precipitation and also allows more pipe diffusion though the bulk[13]. β' precipitates are extremely beneficial at inhibiting dislocation motion through the magnesium matrix because they lie on the prismatic planes. As the majority of slip in magnesium is on the basal plane, precipitates on the prismatic planes provide a barrier to dislocations over the largest possible cross-sectional area. If the same quantity and size of β' plates were on basal planes rather than prismatic planes, they would only raise the strength by half as much[23]. However, prismatic precipitates are not as good at stopping non-basal slip or cross-slip and thus are partly responsible for the drop in strength at roughly 250°C, when these other deformation modes become more active[26].

When the material is aged past the peak hardness, the β' precipitates continue to grow and eventually form an interlaced network throughout the magnesium matrix[22]. Coarsening has also been observed to act preferentially on one orientation of β' at the expense of the other two in certain situations[19]. While this network is forming, the next intermediate precipitate in the sequence (β_1) starts to develop, partly by an in situ transformation from decomposing sections of β'[22]. The structure and formation of β_1 were first examined by Nie and Muddle[24] in WE54 but it has been shown elsewhere that it is identical in Mg-Gd systems[22]. The precipitate forms as coarse parallelopiped

shaped plates with one pair of facets parallel to $\{1\bar{1}00\}_\alpha$ planes and another pair of facets attached to β' particles[22]. β_1 particles have a face centred cubic structure with lattice parameter 0.74nm and a similar composition to β' of $Mg_{3\text{-}5}Gd$. They form with a crystallographic orientation relative to the matrix where $[110]_{\beta_1}$ is parallel to $[0001]_\alpha$ and $(\bar{1}12)_{\beta_1}$ is parallel to $(1\bar{1}00)_\alpha$ [22].

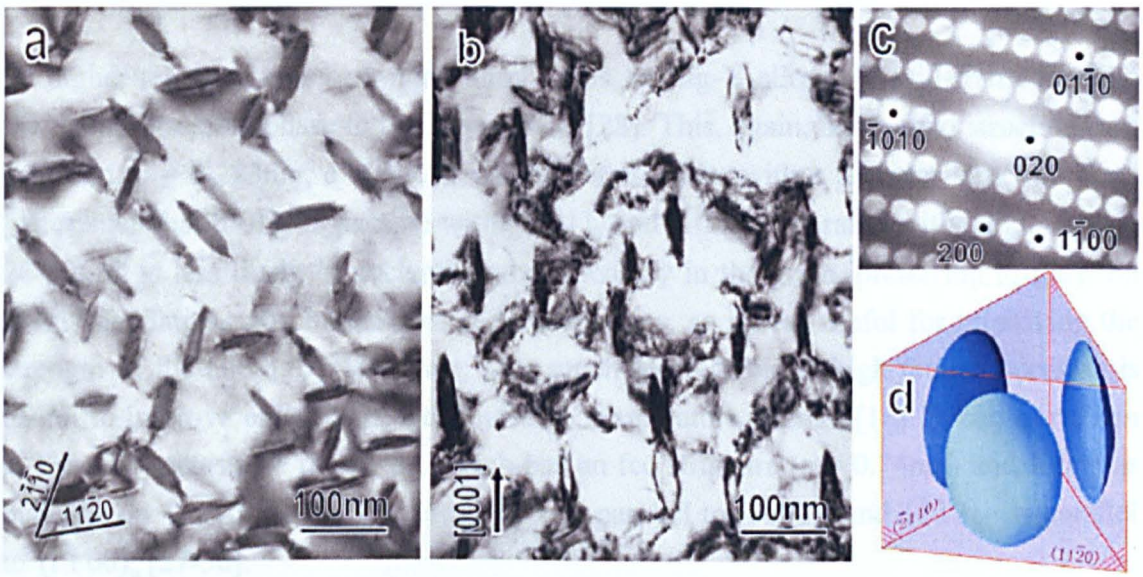

Figure 4 - Transmission electron micrographs recorded from a peak-aged (16 h) Mg-10wt%Gd-3wt%Y-0.4wt%Zr sample: (a) and (b) bright-field images taken along $[0001]$ and $[10\bar{1}0]$ zone axes, respectively; (c) $[0001]$ zone axis microdiffraction pattern recorded from a β' precipitate; (d) schematic representation of the β' precipitate morphology and their arrangement on $\{11\bar{2}0\}$ of α-Mg matrix[22]

When the alloy is over-aged by a significant amount, the equilibrium phase (β), with a composition of Mg_5Gd, starts to precipitate out at the expense of β' and β_1 [21, 23]. This has a face centred cubic structure[13, 21-23] with lattice parameter 2.22nm[22] and is completely incoherent with the matrix[13]. It generally forms as large, coarse plates on the $\{1\bar{1}00\}_\alpha$ planes in the matrix with a crystallographic orientation relative to the matrix where $[110]_\beta$ is parallel to $[0001]_\alpha$ and $(\bar{1}12)_\beta$ is parallel to $(1\bar{1}00)_\alpha$ [22]. β has also been observed as cuboidal shaped precipitates that form during solution treatment and remain during all further heat treatment[26]. These particles are generally large (0.3-3μm[20, 26]) and randomly oriented in the matrix. Due to their size and the relatively low volume fraction they provide very little strengthening to the material.

The precipitation sequence described above for Mg-Gd is almost identical for the Mg-Y system[7, 24, 27]. As before, the first phase to form is the β'' phase[28] and this has a

$D0_{19}$ hexagonal ordered crystal structure with a double hexagonal cell (a = 0.642nm, c = 0.521nm)[17, 28, 29]. This is a metastable phase with composition Mg_3Y that forms as fully coherent platelet precipitates on $(1\bar{1}00)$ and $(11\bar{2}0)$ planes in the parent matrix[28]. β" precipitates nucleate homogeneously throughout the grain interior which gives them good hardening properties, although they are unstable at high temperatures so cannot be used to strengthen alloys for high temperature use[16].

At higher temperatures, or longer aging times, in Mg-Y alloys, β" will transform into the next metastable phase in the sequence, β'[28]. This, again, has a cbco structure (a = 0.640nm, b = 2.223nm, c = 0.521nm) and forms either with a globular structure or as plates such that $[001]_{\beta'}$ is parallel with $[0001]_\alpha$ and $(100)_{\beta'}$ is parallel with $\{2\bar{1}\bar{1}0\}_\alpha$ [17, 28-30]. β' is less likely to nucleate homogeneously in the grain, preferring to grow on grain boundaries, twin boundaries and dislocations, so is less useful for improving the strength of the alloy[16]. However, β' is much more stable at high temperatures so is useful to improve creep resistance and high temperature strength[16]. β' can transform to the next metastable phase, β_1, which has an fcc structure (a = 0.74nm) and forms as platelets on $\{1\bar{1}00\}_\alpha$ planes where $[110]_{\beta_1}$ is parallel to $[0001]_\alpha$ and $(\bar{1}12)_{\beta_1}$ is parallel to $(1\bar{1}00)_\alpha$ [27-30].

The equilibrium phase, β, that forms in Mg-Y alloys is slightly different to that in Mg-Gd as it has a body-centred-cubic structure instead of face-centred-cubic[31, 32]. The composition is $Mg_{24}Y_5$[16, 31, 32] and there are contradicting reports of the lattice parameter; either 1.126nm[32] or 2.2158nm[31]. It forms as platelets, incoherent with the matrix, and generally on matrix planes of either $\{10\bar{1}0\}$ or $\{31\bar{4}0\}$ with an orientation such that $[011]_\beta$ is parallel to $[0001]_\alpha$ and $(1\bar{1}1)_\beta$ is parallel to $(\bar{1}2\bar{1}0)_\alpha$ [32]. These precipitates are perpendicular to the basal slip plane so give the largest possible cross-section to the most common slip system and thus provide the best possible strengthening effect[32].

2.3 Crystallography and Deformation Modes

2.3.1 Magnesium Crystal Structure

Magnesium has a hexagonal close packed (hcp) crystal structure[1], as shown in figure 5. The lattice parameters are given below:

a = 0.32092nm [3]
c = 0.52105nm [3]

These lattice parameters give a c/a ratio of 1.6236 which is very close to the ideal close packing ratio of 1.633, and thus magnesium can be thought of as perfectly close-packed[3].

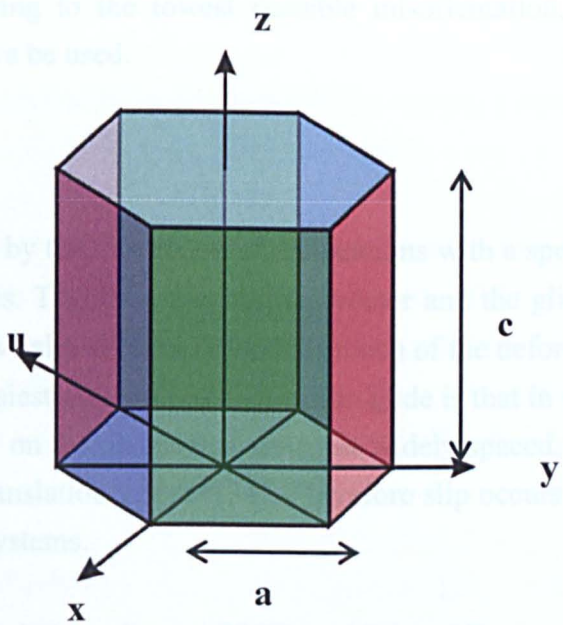

Figure 5 – Diagram of the magnesium unit cell showing the lattice parameters a and c

2.3.2 4-Figure Crystallographic Indexing

The crystallography of cubic materials can be described using the simple 3 figure Miller indices. However, if this is used in the hexagonal structure then crystallographically similar planes are given quite different indices. To avoid confusion, the Miller-Bravais indices are used instead. A third axis, designated as u, is chosen such that x, y and u all

lie in the basal plane and are rotated 120° from each other. The third index is essentially redundant and is always written as the negative of the sum of the x and y indices. In this way, crystallographically similar planes and directions have similar indices and families of planes and directions can be easily understood[33].

2.3.3 Boundary Disorientation

There is a small amount of confusion over the definitions of misorientation and disorientation. Both terms refer to the difference in orientation between two crystals or between two areas of one crystal. This is expressed as an angle by which the first orientation must be rotated to obtain the second orientation. However, due to the symmetric nature of many crystal systems, there are various different rotations that can bring them into alignment; these different angles are the various misorientations, the lowest of which is termed the disorientation. The boundary disorientations studied in the current work are referring to the lowest possible misorientation, and thus the term disorientation will always be used.

2.3.4 Slip Systems

Slip deformation occurs by the movement of dislocations with a specific Burgers vector along defined slip planes. Together, the Burgers vector and the glide plane make up a slip system, and the active slip systems determine much of the deformation behaviour of the material[34]. The easiest direction of dislocation glide is that in which the density of atoms is the highest, i.e. on the planes that are most widely spaced, and in the direction of 'the shortest lattice translation vectors'[34]. Therefore slip occurs predominantly on a limited number of slip systems.

2.3.4.1 Critical Resolved Shear Stress (CRSS) and Schmid Factor

When a stress is applied to a material, there is a driving force for the movement of dislocations. The stress experienced by the dislocations is that of the applied stress resolved onto the active slip system. The various directions and angles between the principal stresses and slip plane directions are shown in figure 6 for plane strain conditions. In simple uniaxial tension or compression, only σ_1 is applicable and the resolved shear stress (τ) on the slip system is given by equation 1:

$$\tau = \sigma \cos\alpha_a \cos\beta_a \qquad (1)$$

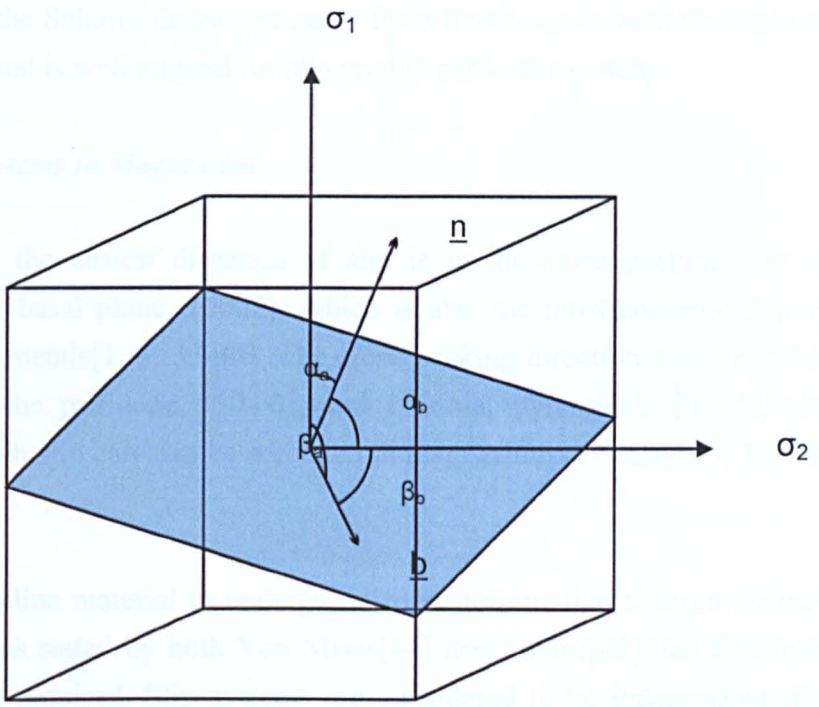

Figure 6 – Diagram showing the angles between the applied stresses and slip system directions in plane strain

The critical resolved shear stress (CRSS) is the value of τ that is required to move dislocations on a specific slip system. Therefore, the conditions required to activate a particular slip system in a crystal rely on both the magnitude of the applied stress as well as the orientation of that stress with respect to the crystal axes. The Schmid factor of a crystal is a measure of the ease of slip, given a specific direction of applied stress, as given in equation 2:

$$Schmid\ factor = \cos\alpha_a \cos\beta_a \tag{2}$$

The Schmid factor for uniaxial stress ranges from 0 to 0.5, where a grain perfectly aligned for slip has a Schmid factor of 0.5.

Plane strain conditions have a much more complex stress state so a simplification is used such that plane stress is also assumed. Therefore, the Schmid factor for plane strain conditions is given in equation 3:

$$Schmid\ factor = \cos\alpha_a \cos\beta_a + \cos\alpha_b \cos\beta_b \tag{3}$$

In plane strain, the Schmid factor can range from 0 to 1, again with the higher numbers indicating a crystal is well aligned for slip on this particular system.

2.3.4.2 Slip Systems in Magnesium

For magnesium the easiest direction of slip is in the close packing <a> direction, $\langle \bar{1}2\bar{1}0 \rangle$, on the basal plane, {0002}, which is also the most common slip system in many other hcp metals[1, 3, 35-40]. The close packing direction also lies within other planes, namely the prismatic, $\{10\bar{1}0\}$, and 1st order pyramidal, $\{10\bar{1}1\}$, planes, see figure 7, on which slip can also be activated in magnesium crystals[1, 3, 36, 38, 39, 41-43].

For a polycrystalline material to undergo uniform deformation without failure at grain boundaries, it was stated by both Von Mises[44] and Taylor[45] that five independent slip systems are required. Slip systems are considered to be independent if they can bring about a unique crystal shape change that is not possible through any combination of other slip systems[46]. Groves and Kelly[46] showed that the basal and non-basal <a> type slip systems in an hcp metal allow only four independent slip systems. The basal slip systems contain three possible directions and one plane; only two of these systems are independent as the strain produced by the third can already be produced by a simple addition of the previous two. The prismatic slip systems also contain only two further independent slip systems due to containing only the three basal directions. When the pyramidal <a> slip systems are considered, it can be seen that these do not provide any further independent shape changes above those already introduced via the basal and prismatic planes. Therefore, it has been stated by various authors[39, 46, 47] that the number of possible independent slip systems with the shortest lattice vector in hcp metals, $\langle \bar{1}2\bar{1}0 \rangle$, is less than that required for full ductility. Twinning can provide a further mode of strain accommodation but, due to the polar nature, cannot be thought of as a full independent deformation mechanism[48]. Kocks and Westlake[48] have argued that, although five independent slip systems are required for full ductility, it is still possible for a material to exhibit limited ductility with a lower number of independent systems.

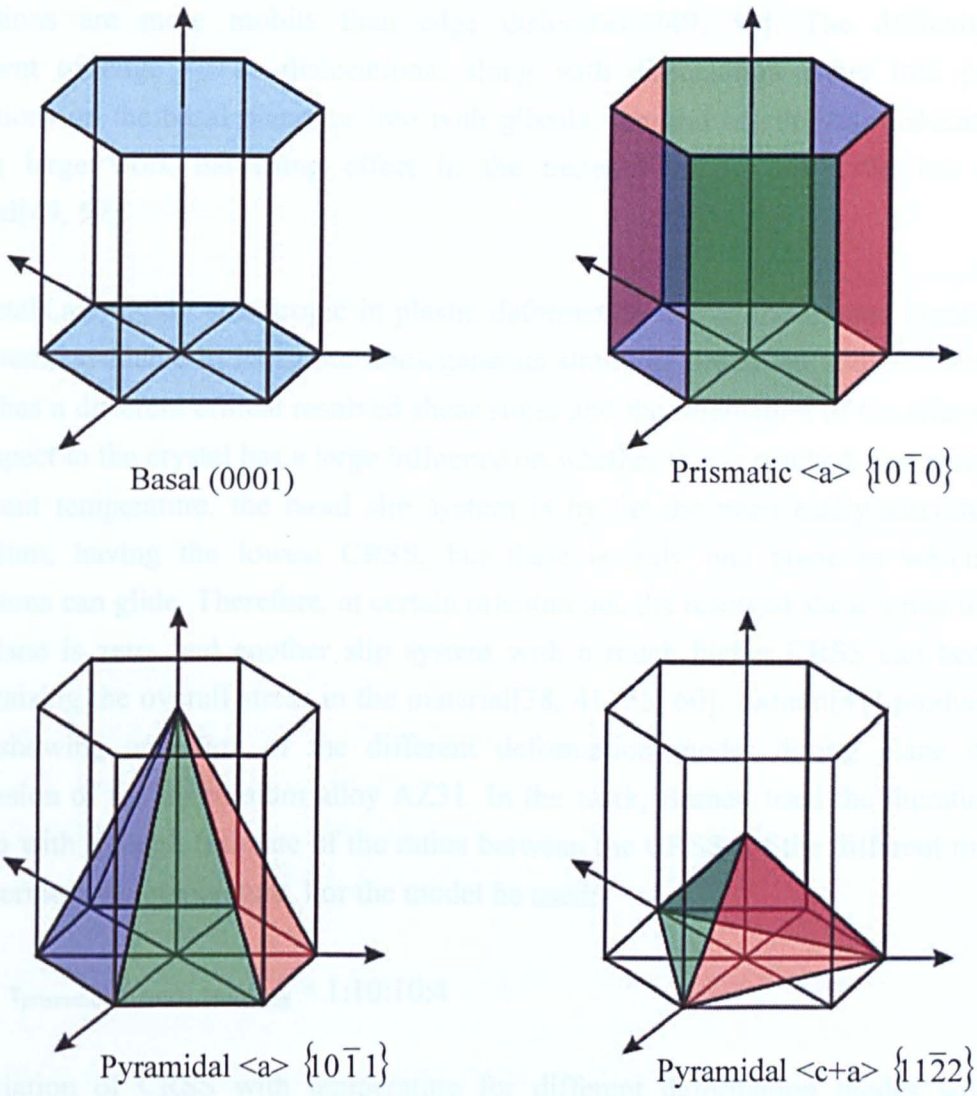

Figure 7 – Diagrams showing the possible slip planes in magnesium

It has been observed in a small number of studies[38, 49-51], and deduced in others[41, 52-56], that a further slip system can be activated in hcp metals to provide the missing independent slip system. This is the <c+a> slip system, so called because it has a Burgers vector containing both the c and a directions of the crystal. The dislocations have a Burgers vector of $\frac{1}{3}\langle\bar{1}\,\bar{1}23\rangle$ and glide on the $\{11\bar{2}2\}$ second order pyramidal plane. As the <c+a> dislocations have a c-component, this mode can accommodate strain in the c-axis direction. However, the <c+a> dislocations have a much larger slip vector than <a> dislocations and thus require a much larger shear stress to be activated[57]. The movement of <c+a> dislocations through the lattice is more

complicated than most of the other slip systems and it is generally found that screw dislocations are more mobile than edge dislocations[49, 58]. The difficulty of movement of edge <c+a> dislocations, along with dissociation either into partial dislocations on the basal plane, or into both glissile <a> and sessile <c> dislocations, gives a large work hardening effect in the material once <c+a> slip has been activated[49, 59].

Hcp metals are highly anisotropic in plastic deformation due to the limited number of slip systems available to carry out homogeneous strain, as described above. Each slip system has a different critical resolved shear stress and the orientation of the stress axis with respect to the crystal has a large influence on whether this is reached. For example, at ambient temperature, the basal slip system is by far the most easily activated in magnesium, having the lowest CRSS, but there is only one plane in which the dislocations can glide. Therefore, at certain orientations, the resolved shear stress on the basal plane is zero, and another slip system with a much higher CRSS can become active, raising the overall stress in the material[38, 41, 55, 60]. Barnett[41] produced a model showing operation of the different deformation modes during plane strain compression of the magnesium alloy AZ31. In the work, Barnett used the literature to come up with a rough estimate of the ratios between the CRSSs of the different modes at an intermediate temperature. For the model he used:

$$\tau_{basal}: \tau_{prismatic}: \tau_{<c+a>}: \tau_{twinning} = 1:10:10:4$$

The variation of CRSS with temperature for different deformation modes will be discussed in more detail in section 2.3.8.1 but it can be seen from other literature[52, 53] that this is a reasonable approximation at intermediate temperature. The model showed how much strain was being accommodated by each deformation mechanism at any orientation of the crystal. This is displayed in an orientation distribution function (ODF) representation in figure 8a with a key showing the deformation conditions in figure 8b. The twinning mechanism included here is $\{10\bar{1}2\}$ twinning, the most common in magnesium, as described in section 2.3.5.

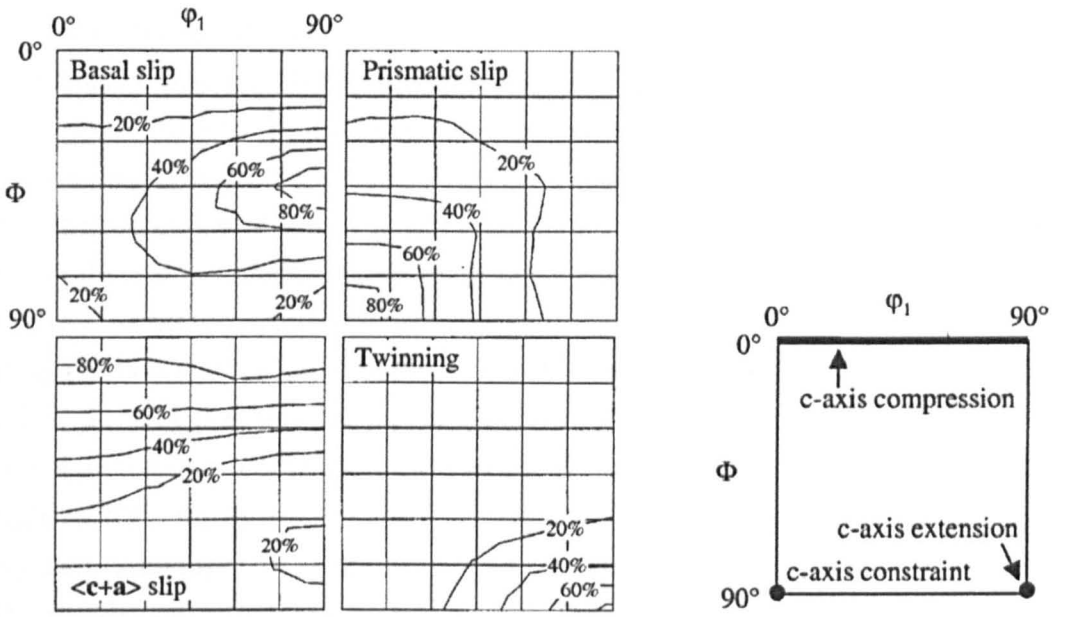

Figure 8 – (a) The influence of orientation on the fraction of the total shears born by the different deformation systems, calculated using a full constraint Taylor model and setting τ_{basal}: $\tau_{prismatic}$: $\tau_{<c+a>}$: $\tau_{twinning}$ = 1:10:10:4. (b) The relationship between deformation and the c-axis in plane-strain deformation shown using ODF representation (Bunge convention). This holds true for all values of φ_2 [41]

It can be seen from this model that different slip and twinning mechanisms are dominant at different orientations and even the basal slip system, the most easily activated, appears to be dominant over only a small range of deformation conditions. The paper states that the model actually underestimates the importance of basal slip and that the range of orientations where basal slip is significant in a real sample would be wider. Indeed, Kelley and Hosford[39] stated that a magnesium crystal would experience a significant amount of basal slip if the basal plane was even slightly misoriented from the compression axis. Despite this small issue with the Barnett model, the orientations at which the deformation mechanisms are easiest to activate and the general shape of the ODFs are valid. The most important information to take from this study is that basal slip dominates at Φ=45, φ_1=90, prismatic slip dominates at Φ=90, φ_1=0, <c+a> slip dominates at Φ=0 φ_1=0-90 and twinning dominates at Φ=90, φ_1=90. Other studies have also shown the same dependencies of deformation mechanisms on crystal orientation, for example references [38, 39, 55, 61].

For a single crystal, the resolved shear stresses can be easily calculated from the external applied stresses. When this approach is applied to polycrystalline materials, only an approximation of the average stresses can be calculated; individual grains will experience widely different stresses from each other due to differences in orientation and the strain accommodated by neighbours. Even within individual grains, the regions closest to the grain boundaries can often have higher stresses than those in the grain interior due to the compatibility stresses resulting from the shape change needed to avoid grain boundary separation[62]. It has been seen previously in magnesium alloys[35, 51, 55] that this high stress level near grain boundaries can activate slip systems with a higher CRSS than the average shear stress in the grain. In magnesium, the higher CRSS slip systems are the non-basal <a> systems and the pyramidal <c+a> slip system. Although there are significant differences between the deformation of single crystals and polycrystals, Kelley and Hosford[39, 63] have shown that, for magnesium at least, a textured polycrystal behaves very similarly to a single crystal, and thus the information gained in single crystal studies can be applied to polycrystals.

2.3.5 Twinning Systems

The definition of a twin is very simple and it is stated in Hall[64] that a twin is present when there is a relationship such that 'the twinned and untwinned parts of a crystal are mirror reflections of each other in a certain plane of the crystal'. There are three types of twin that can be formed in metals[65]: growth twins formed during solidification, thermal and transformation twins, and mechanical twins formed through shear. The current work is concerned with mechanical twins, so the remainder of the section will focus on them in more detail. In these twins, an external shear stress on the crystal causes deformation to occur through shearing on every lattice plane within the twin, giving a reorientation of the atomic lattice. This generally allows only a relatively small amount of strain to be accommodated but can occur much faster than standard slip.

A useful way to visualise the twinning mechanism is to consider a sphere of material, twinned across the centre, as shown in figure 9[64]. Due to the twinning shear, the top half of the sphere has been skewed to the right. Twins are generally defined by the two undistorted planes, K_1 and K_2, and the two directions coming from the intersection of these planes and the plane of shear, η_1, and η_2. The descriptors for each of the twin systems common in magnesium are given in table 2. While it is necessary to define either K_1 and η_2 or K_2 and η_1 to identify a specific twin, it can be seen from the table that when only the twins possible in magnesium are considered, the twins can be

identified by the composition plane (K_1) alone. This is the standard method used to name twins in the literature and will be used through the remainder of this work.

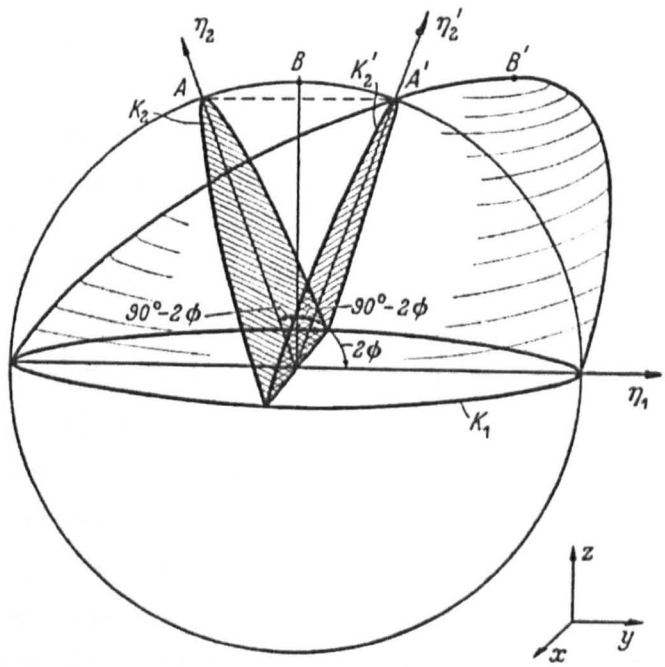

Figure 9 – Relation of sphere and twinned ellipsoid[64]

The formation of twins is very rapid, with the strain being accommodated much faster than would be possible from slip[66]. Speeds close to the speed of sound[67] and times of formation of the order of 10μs[65] have been reported. However, the high velocity of twinning is only present in the shear direction, and the other boundaries travel out at a much slower rate. It is this behaviour that gives twins their characteristic lenticular shape[51, 65, 67]. It has also been found that twins with a lower shear form more lenticular, i.e. wider and less parallel sided, structures[65, 67, 68]. Due to the high speed nature of twinning, it is generally more prevalent than slip in samples deformed at higher strain rates[36, 69]. The relative activation of slip and twinning systems with respect to processing conditions will be discussed further in section 2.3.8.1.

As discussed in section 2.3.4, the von Mises criterion requiring 5 independent slip systems for full plasticity in a polycrystalline material is not easily fulfilled in magnesium or hcp metals in general. At low homologous temperatures, the only mechanism that allows a strain in the c-axis direction of an hcp crystal is twinning, and therefore twinning is much more common in hcp than face-centred-cubic or body-centred-cubic materials[33, 58, 67]. The dominant mechanism that allows strain in the

c-axis direction is $\{10\bar{1}2\}$ twinning[55, 65, 66] and numerous studies have shown this to be true in magnesium, for example references [35, 36, 42, 51, 70, 71]. The $\{10\bar{1}2\}$ twin is a polar twin and, dependent on the c/a ratio, can be either a 'tension twin' or a 'compression twin'. If the c/a ratio is less than $\sqrt{3}$, as it is in magnesium, then the twin will cause an extension in the c-axis direction and thus only c-axis extension, not c-axis compression, strain can be accommodated by this mechanism. This gives a strong asymmetry when textured materials are deformed in tension or compression[55, 72]. Lower yield stresses are experienced when the material can undergo $\{10\bar{1}2\}$ twinning, i.e. when the imposed strain will cause extension along the c-axis direction. This is shown in figure 10, from Gharghouri *et al.*[73], where textured samples of pure magnesium and Mg-7.7at% Al were deformed such that the majority of the grains were oriented well for $\{10\bar{1}2\}$ twinning in compression and oriented poorly in tension. It can be seen that this caused a difference in stress of over 50 MPa. Although many studies have stated that twinning cannot occur if the c-axis of the grains are constrained or compressed, it has still been observed in some samples where this is the case[71, 74]. Both of these studies claim that the majority of the twins formed during unloading due to stresses induced by the constraints of surrounding grains. Therefore, these studies do not contradict the requirement of c-axis extension for $\{10\bar{1}2\}$ twinning to occur.

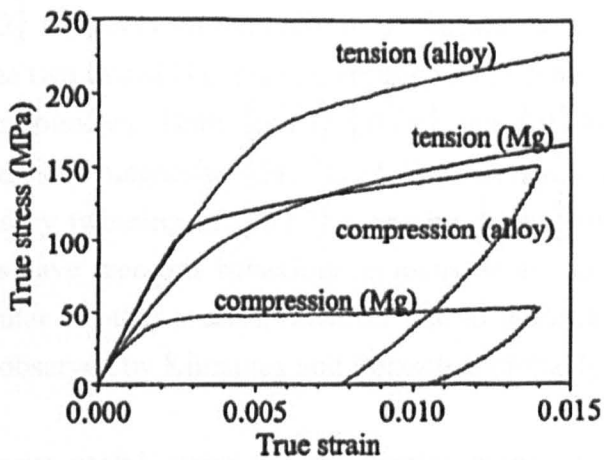

Figure 10 – Stress-strain curves for tension and compression of textured samples of pure magnesium and Mg-7.7at% Al[73]

Along with $\{10\bar{1}2\}$ twinning, both $\{10\bar{1}1\}$ and $\{10\bar{1}3\}$ systems have been shown to be active to a lesser extent in magnesium[35, 36, 38, 74-76]. $\{10\bar{1}1\}$ twinning provides a mechanism for compression along the c-axis direction; however, it requires higher stresses to activate than $\{10\bar{1}2\}$ twinning so is generally only present in areas of high

stress concentration[35, 48]. Reed-Hill and Robertson[77] stated that they had also observed $\{30\bar{3}4\}$ twins in magnesium but it has since been shown by Christian and Mahajan[66] that this is more likely to be due to double twinning, first on the $\{10\bar{1}1\}$ system then followed by the $\{10\bar{1}2\}$ system. Double twinning will be explained in more detail below. Therefore, the only twins that can be expected in magnesium and magnesium alloys are those listed in table 2.

Table 2 – Full descriptors of the common twinning modes in magnesium[33, 66]

K_1	K_2	η_1	η_2
$\{10\bar{1}1\}$	$\{10\bar{1}3\}$	$\langle 10\bar{1}\bar{2}\rangle$	$\langle 30\bar{3}2\rangle$
$\{10\bar{1}2\}$	$\{\bar{1}012\}$	$\langle 10\bar{1}\,\bar{1}\rangle$	$\langle \bar{1}01\bar{1}\rangle$
$\{10\bar{1}3\}$	$\{10\bar{1}1\}$	$\langle 30\bar{3}2\rangle$	$\langle 10\bar{1}2\rangle$

Although both $\{10\bar{1}1\}$ and $\{10\bar{1}3\}$ twins have been seen as single twins, they are more commonly seen as a precursor to $\{10\bar{1}2\}$ twinning through the mechanism of double twinning[66]. Double twinning occurs when either a $\{10\bar{1}1\}$ or $\{10\bar{1}3\}$ twin forms in the material and leaves the twinned material in an orientation ideal for $\{10\bar{1}2\}$ twinning. Therefore, the $\{10\bar{1}2\}$ twin acts on the entirety of the old twin, only rarely leaving a boundary between the two twins[71], and can appear as a different type of twin entirely when examining the boundary. Both $\{10\bar{1}1\}$-$\{10\bar{1}2\}$ and $\{10\bar{1}3\}$-$\{10\bar{1}2\}$ twins have been observed in studies on magnesium[51, 71, 74, 76]. Klimanek and Potzsch[70] have also observed secondary twinning of $\{10\bar{1}2\}$ twins by $\{10\bar{1}1\}$ twins. It is not known why no other studies have seen this behaviour as many of the processing and material parameters were similar to other studies, however due to the lack of further evidence, the double twinning observed by Klimanek and Potzsch is probably an anomaly.

EBSD provides a very useful technique to identify twins as it can calculate the disorientation angle and axis across the twin boundaries. Each specific twin has a different disorientation with the matrix, which have all been collated by Nave and Barnett[76] and are shown in table 3. It has also been shown that it is common for more than one twin variant to be active in individual grains[76, 78], and thus, in magnesium, there are three common disorientations corresponding to the $\{10\bar{1}2\}$ twin-twin boundaries. These disorientations are given in table 4.

Table 3 – Disorientations between the matrix and primary or secondary twins commonly observed in Mg[76]

Type of boundary	Disorientation Angle (°)	Disorientation Axis
$\{10\bar{1}1\}$	56	$\langle 1\bar{2}10\rangle$
$\{10\bar{1}2\}$	86	$\langle 1\bar{2}10\rangle$
$\{10\bar{1}3\}$	64	$\langle 1\bar{2}10\rangle$
$\{10\bar{1}1\}-\{10\bar{1}2\}$	38	$\langle 1\bar{2}10\rangle$
$\{10\bar{1}3\}-\{10\bar{1}2\}$	22	$\langle 1\bar{2}10\rangle$

Table 4 - Disorientations generated between different $\{10\bar{1}2\}$ twin variants[76]

Type of boundary	Disorientation Angle (°)	Disorientation Axis
$(10\bar{1}2)-(\bar{1}012)$	7.4	$\langle 1\bar{2}10\rangle$
$(10\bar{1}2)-(01\bar{1}2)$	60.0	$\langle 10\bar{1}0\rangle$ [a]
$(10\bar{1}2)-(0\bar{1}12)$	60.4	$\langle 8\bar{1}\bar{7}0\rangle$ [b]

[a] Actual axis is 3.7° off $\langle 10\bar{1}0\rangle$

[b] Actual axis is 0.2° off $\langle 8\bar{1}\bar{7}0\rangle$

Critical resolved shear stresses (CRSSs) for twinning have been mentioned and used by various authors, for example references [41, 52-55]. These have often been used to model the active deformation modes within a material and in most cases give a good fit with experimentally observed flow behaviour and texture changes. However, there has been dispute from other sources as to the validity of using any CRSS for twinning due to the large scatter in the reported values in the literature[65-67]. Gharghouri *et al.*[73] have studied this in one particular material, Mg-7.7at% Al, and found that a CRSS for $\{10\bar{1}2\}$ twinning is reasonable and does not have a large amount of scatter in the data. Their tests were all carried out under approximately the same conditions with very similar material. Therefore, it is probably correct to say that a critical stress is valid for twinning, but that it is strongly dependent on the initial microstructure and the applied stress state.

One of the most significant changes that twinning brings about is the crystallographic rotation of the grains. This can make it easier or harder for certain slip systems to operate and can often change the behaviour of the material more than the strain that twinning itself induces. These effects are discussed in more detail in section 2.5.3.

2.3.6 Grain Boundary Sliding

Due to the lack of enough independent slip systems for full ductility in magnesium alloys, other deformation mechanisms can come into effect to accommodate strain, particularly in the c-axis direction. One mechanism that has been observed in magnesium alloys is grain boundary sliding (GBS)[35, 79-82]. GBS can occur in any direction within the sample and therefore can increase ductility by allowing compression in the c-axis direction[35, 55]. A small grain size, generally less than 10μm, and a reasonably high temperature are required for GBS to operate[35, 38, 79, 83]. Hauser *et al.*[84] observed a similar mechanism of strong shearing in the grain boundary region at lower temperature. It was unresolved whether this was truly shearing or sliding but it led to fracture at the boundaries so does not increase ductility.

2.3.7 Shear Bands

Shear bands are narrow regions within a material where strain is localised. The bands can be formed over a wide range of length scales, from small single grain bands, to macroscopic bands that cross an entire sample[85]. The width of the shear band is generally related to the length, with macroscopic bands up to 500μm wide and grain scale shear bands of approximately 1μm typical in fcc metals[86]. The orientation of shear bands is related to the stress axis and they are normally found approximately 35-45° to the principal stress direction[51, 86]. In cases of plane strain compression or rolling, the bands are normally found on planes perpendicular to the transverse plane[87]. Shear bands are generally formed when standard slip and twinning mechanisms are unable to accommodate the applied strain[42]. They form in an orientation such that slip is easier within the band and, therefore, further deformation is concentrated in this area. In magnesium, the bands form with the basal plane parallel to the plane of the shear band[71, 87]. Features similar to shear bands, and that can be confused with them, are microbands. These are on a finer scale than shear bands, often only 0.1μm in width, and consist of two parallel low angle boundaries surrounding a narrow sheet on a specific glide plane[86]. Microbands are not commonly seen in magnesium studies so will not be considered further.

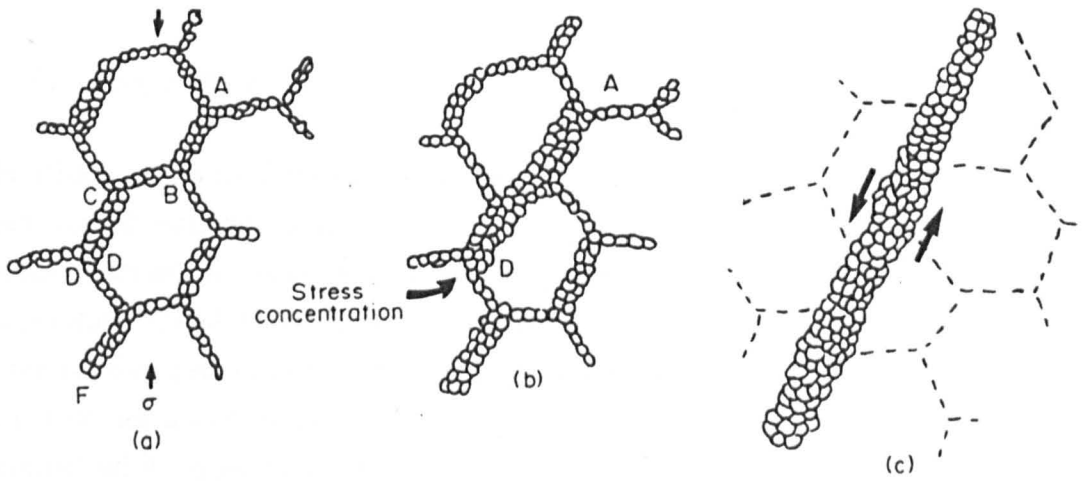

Figure 11 – Schematic diagram illustrating the formation of a shear zone from the bands of recrystallised grains[51]

Shear bands have often been observed in magnesium and magnesium alloys[39, 42, 51, 71, 87-89] but the mechanism of formation has caused some debate. Early works concluded that the shear bands formed through a double twinning mechanism of $\{10\bar{1}1\}$ twinning followed by $\{10\bar{1}2\}$ twinning[87]. Barnett *et al.*[71] stated that, although the twinning mechanism is important in shear band formation, it only nucleates the band, rather than forming it entirely. Ion *et al.*[51] observed similar features to shear bands, termed shear zones, that form through a dynamic recrystallisation mechanism. Shear zones form at approximately the same angle to the stress axis as shear bands and can vary in size from microscopic to macroscopic. However, they form mostly along pre-existing grain boundaries and can be less straight than shear bands. The formation of shear zones, shown in figure 11[51], starts with the formation of necklace recrystallisation at the grain boundaries. Those grain boundaries that are aligned with the principal shear direction will undergo higher levels of deformation and thus the dynamic recrystallisation will be more active in those areas. This creates a thicker necklace and these regions can link with others from surrounding grains and form a continuous band of recrystallised grains. As these zones are more favourable for slip, the strain will be localised there and stresses will concentrate at the zone tips, allowing the zones to grow. This mechanism was also observed by del Valle *et al.*[88].

2.3.8 Factors Changing the Active Mode

2.3.8.1 Temperature

The CRSS values for different slip systems in magnesium and other hcp materials have been studied numerous times in the literature[41, 53-55, 90]. There are a wide range of values reported for each slip system because of the differences in material and temperatures tested. However, the salient points to carry through to the current work are in the relative ease of slip on each system and the general variation with temperature, facts that are qualitatively, if not quantitatively, agreed on by most authors. This is summarized in figure 12 from Barnett's work[41] and it can be seen that the basal slip system always has the lowest CRSS, followed by the prismatic slip system and finally the <c+a> slip system with the highest CRSS. The $\{10\bar{1}2\}$ twinning system is indicated by a temperature independent line, discussed further below, that is crossed by the prismatic and <c+a> lines at higher temperatures. The pyramidal <a> slip system is often disregarded as it is much less commonly activated, but when included it is generally found to have a CRSS approximately between that of prismatic and <c+a> slip. It can be seen that the CRSSs of all slip systems decrease with increasing temperature, and those with the highest critical stresses decrease the furthest. The same differences in ease of activation of slip systems and variation with temperature are also seen in other studies[39, 42, 52-55, 90]. It should be noted that the slip systems are also affected by the strain rate, and that, rather than a simple variation of CRSS with temperature, a combined factor can be used instead. This is the Zener-Hollomon parameter (Z)[91], given in equation 4:

$$Z = \dot{\varepsilon} e^{\frac{Q}{RT}} \tag{4}$$

where $\dot{\varepsilon}$ is the strain rate, Q is the activation energy of deformation, R is the universal gas constant and T is the temperature.

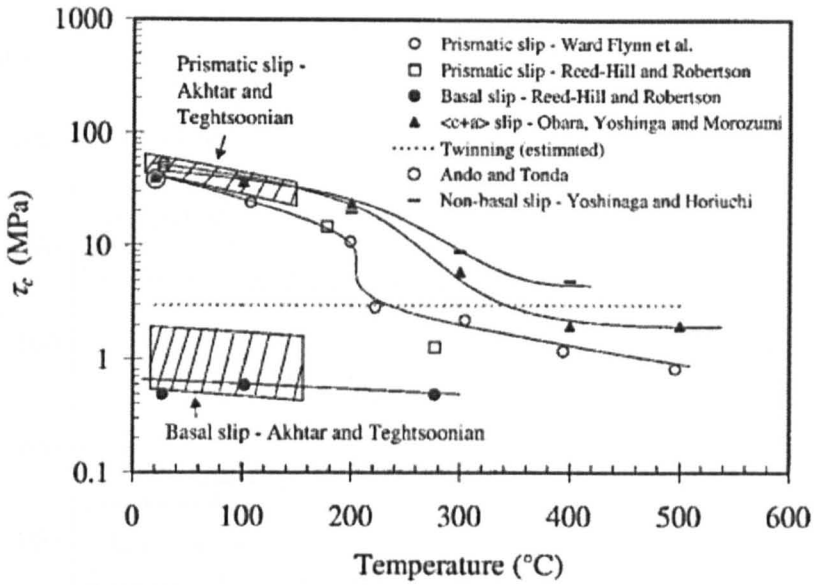

Figure 12 – Influence of deformation temperature on the critical resolved shear stress[41]. Includes data from references [40, 43, 49, 92-95]

At ambient temperature the main modes of deformation in magnesium are basal slip and $\{10\bar{1}2\}$ twinning[1, 3, 36-38, 55, 57, 84, 96]. As has been shown in section 2.3.4, given the correct orientation, the different slip systems can be activated at any temperature. However, the difference in CRSSs is greater at lower temperature, see figure 12, and thus the tendency to slip on the basal plane is enhanced[35, 41]. As the temperature is increased, the CRSSs of all slip systems are lowered and the variance between them becomes much less. Therefore, it is comparatively easier to activate the other slip systems during higher temperature deformation[36, 51, 55, 92, 96, 97]. The non-basal <a> and <c+a> type slip systems generally become more active above approximately 225°C[1].

Large variations in twinning are seen at different temperatures, with generally lower levels of twinning at higher temperatures[65-67, 69, 98]; therefore, it might be expected that the stresses required to activate twinning also change with temperature. However, it has been generally accepted that this is false and that the difference in amounts of twinning is due to the relative necessity of twinning to accommodate strain that cannot come about through slip[65, 69, 99]. Therefore, when further slip systems are activated, the twinning systems are no longer necessary to allow certain shape changes. Meyers *et al.*[99] carried out a review of the literature for twinning stresses in various materials,

shown in figure 13, which showed that the critical stresses for twinning are independent of temperature.

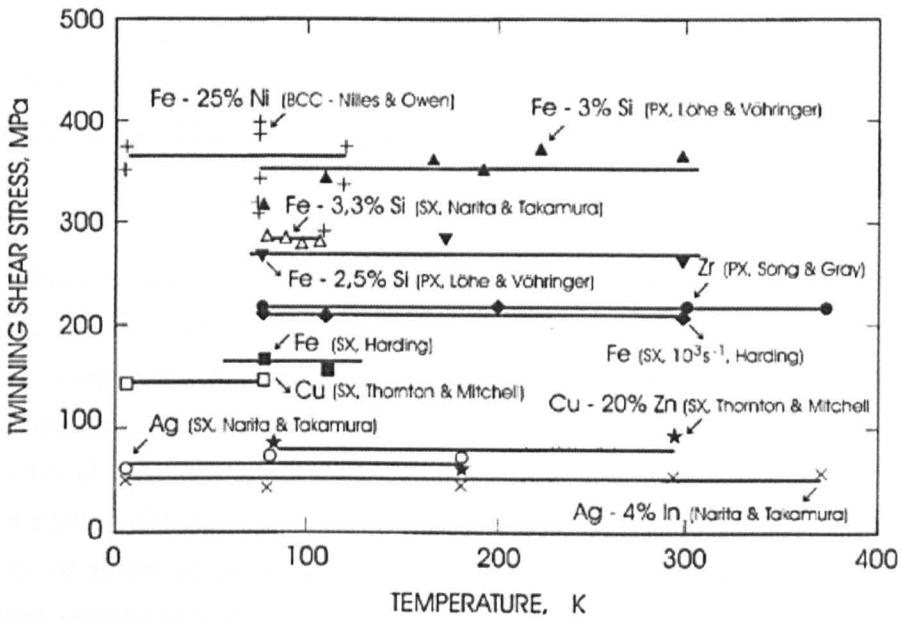

Figure 13 – Twinning stress as a function of temperature for a number of metals (both mono and polycrystals)[99]. Includes data from references [100-106]

2.3.8.2 Grain Size

Along with the well known Hall-Petch effect of grain size on the strength of a material, the grain size can also affect the tendency for different deformation mechanisms to operate. It has been shown in many studies that grain refinement will suppress the formation of twins and enhance deformation through slip[38, 72, 107, 108]. According to Meyers *et al.*[99] the critical stress required for twinning is raised by the presence of more grain boundaries, although the reason for this is unknown. Grain boundary sliding is also enhanced by a refinement of grain size in magnesium alloys[79].

2.3.8.3 Alloy Composition

The presence of common alloying elements in magnesium generally increases the activation of non-basal slip. Both zinc and aluminium have been seen to lower the CRSS for non-basal slip systems and, in some cases, raise that for basal slip[40, 43, 109]. This causes more slip to occur on the non-basal planes and thus the ductility of the material is increased. Rare earth additions, such as yttrium or gadolinium, generally

increase the difficulty to move all types of dislocation, due to increased friction or solute atmospheres[16, 110]. Therefore, the propensity for cross-slip is increased and dislocations are more likely to move on non-basal planes. It has also been found that additions of lithium can increase the amount of <c+a> slip occurring[35, 39, 52, 111]. The activation of twinning is not directly affected by the alloy composition but the relative activation of different slip systems causes the level of twinning to change[65, 67].

Alloying additions also have an effect on the shear banding behaviour of the material. More shear bands were observed by Gehrmann *et al.*[42] in AZ31 than pure magnesium, suggesting that the alloy additions have increased the propensity for shear banding. However, Barnett *et al.*[71] did not find any difference in the volume of banded material between pure magnesium, AZ31 and Mg-0.2Ce. Despite this, the addition of cerium did cause a higher ductility and it was concluded that cerium restricts the severity of strain accommodated by individual shear bands, instead distributing it more widely across many shear bands.

2.4 Restoration Mechanisms

2.4.1 Introduction

When a material is deformed, the number of defects, such as dislocations, within the crystal structure increases, steadily increasing the stored energy of the system. There is a driving force to lower this free energy and thus certain processes are activated to remove the defects. These are known as restoration mechanisms and can generally be divided into 3 categories: recovery, recrystallisation and grain growth. When the restoration processes occur concurrently with deformation they are termed dynamic and when they occur during a later annealing step they are termed static[112]. The reason that these processes are of interest in the current work is because they cause a significant change in the deformation behaviour of a material, generally giving a softening effect. If dynamic processes are active then this softening manifests in the flow curves, as discussed in section 2.6.3. The current work has studied dynamic processes in much more detail than static and thus dynamic behaviour will be looked at more closely here.

During recovery, the stored energy of the system is reduced through the annihilation and rearrangement of dislocations into low energy configurations[112]. The rearrangements

generally form cell or subgrain walls and the entire process will be discussed in more detail in section 2.4.2. Recrystallisation causes the formation of entirely new grains, surrounded by high angle boundaries and containing a low defect density[112]. There are various mechanisms of recrystallisation put forward and these will be discussed in sections 2.4.3 and 2.4.4. Grain boundaries can also be thought of as defects as they raise the stored energy of the material and thus there is also a driving force for a reduction in the number of grain boundaries, achieved through grain growth producing a larger average grain size. Grain growth is generally only a significant restoration mechanism once recrystallisation is complete and, therefore, is less important during dynamic restoration so will only be discussed briefly in the following sections[112].

Most materials undergo some form of restoration mechanism, although the tendency to either undergo recovery or recrystallisation is often dependent on the stacking fault energy (SFE). In general, it is found that materials of high SFE, for example aluminium or ferritic steels, contain dislocations that can climb and cross-slip very easily, and thus undergo extensive recovery. In some cases this can remove enough stored energy to stop any recrystallisation from occurring. Materials of low SFE, for example copper or nickel, hinder dislocation climb or cross-slip and thus recovery is much less extensive and it is common to observe high levels of recrystallisation[112, 113]. The literature does not agree on a single value for the SFE of magnesium, with the most common values quoted being 78 and 125 mJ/m^2 [114, 115]. These values would place the metal in the low SFE and medium to high SFE regions respectively and, therefore, there is not any indication as to whether magnesium should undergo recrystallisation or recovery. Somekawa *et al.*[116] also showed that the effect of adding solute to a magnesium alloy can dramatically change the stacking fault energy, from the quoted 78 mJ/m^2 [114] for pure magnesium down to 5.8 mJ/m^2 for Mg-9wt.%Al. Given that the majority of magnesium studies are carried out in significantly alloyed materials, and the effects of other solutes are unknown, it is unreasonable to predict any behaviour from the stacking fault energies.

It should also be noted that the mechanisms of recovery and recrystallisation are generally not mutually exclusive and combine many of the same activities. As will be seen in section 2.4.3.2, the mechanism of continuous dynamic recrystallisation can be thought of as an entirely recovery based process, but is included with recrystallisation as fully new grains are formed. In other ways recovery can also assist recrystallisation because, although it reduces the stored energy, it produces viable nuclei for recrystallisation; recovery reduces the growth rate but increases nucleation[117].

2.4.2 Recovery

Recovery occurs whenever the concentration of dislocations and the temperature are sufficiently high. Koike *et al.*[38] have shown that dynamic recovery is possible during room temperature deformation of AZ31 alloys; however, it is more usual to see these processes during higher temperature deformation. Recovery and subgrain formation has been observed during and after deformation in many magnesium studies, for example references [51, 96, 118-120].

During deformation, the density of dislocations builds up within the grains, increasing the stored energy. As mentioned above, recovery acts to reduce this stored energy by rearranging dislocations into low energy structures and also causing dislocations to annihilate. The dislocation motion in recovery can be through glide, climb or cross-slip; the particular mechanism is dependent on the material and temperature, as well as the stress conditions when dynamic recovery is considered. Each dislocation is subject to stresses from surrounding dislocations and, in dynamic recovery, from the applied stress. Therefore, they will move through the structure and when dislocations of opposite sign meet, they will annihilate each other. In this way, the total density is reduced and a small number of types of dislocation will dominate. The remaining dislocations, predominantly of a small number of Burgers vectors, will continue to move through the material and find the lowest energy configurations possible. In very simple cases, this would be tilt boundaries, but in more complex polycrystalline samples, the dislocations will form cells and subgrain boundaries. Cell walls are loose 3 dimensional tangles of dislocations and, through further recovery and reduction in dislocations within the cells, can transform into more well defined subgrain boundaries consisting of regular arrays of dislocations[80, 112, 121, 122].

The formation of subgrains at the grain boundaries can lead to the grain boundaries acquiring a serrated shape in the final microstructure. However, it was also noted by Mote and Dorn[123] that, in a Mg-3wt.%Nd alloy, serrations in grain boundaries could also be caused by slip on regularly spaced basal planes. Therefore, the occurrence of serrated grain boundaries cannot be used as a clear indicator of recovery induced subgrain formation.

2.4.3 Dynamic Recrystallisation

Dynamic recrystallisation (DRX) is the formation of new grains with much lower internal dislocation densities. These are formed from the pre-existing deformed microstructure during further deformation. There are two major classes of dynamic recrystallisation: discontinuous dynamic recrystallisation (DDRX) and continuous dynamic recrystallisation (CDRX). Both mechanisms give a similar final microstructure but the method by which that is reached is quite different. DDRX was recognised first and is the most common mechanism in many materials so is often referred to as conventional dynamic recrystallisation. It is also very similar to the process operating during standard static recrystallisation. DDRX progresses by a standard nucleation and growth mechanism, whereas CDRX has a very close relation to recovery and does not have any defined start and end points[112]. The two mechanisms will be discussed in more detail in sections 2.4.3.1 and 2.4.3.2.

Despite the differences in formation mechanism, there are many general points that are common to both. The softening effect that dynamic recrystallisation has on the flow behaviour is clearly shown in stress-strain curves. The initial delay, before the stored energy has reached a critical value, allows work hardening of the material. Once DRX has begun, the hardening slows and a peak stress is reached, followed by softening. This peak stress and the relation to the onset of DRX is discussed in more detail in section 2.6.3. DRX generally gives a similar microstructure, with new recrystallised grains forming first in the vicinity of grain and twin boundaries and giving a necklace type formation, as seen in various magnesium studies, for example references [124-127]. This is due to the preferential nucleation of DRX at these boundaries, generally because of the higher stresses experienced and further slip systems activated to accommodate deformation around the boundaries[65, 126, 128]. In certain alloy systems there are particles present during deformation that also experience higher stresses and thus are suitable sites for nucleation of DRX. This is referred to as particle stimulated nucleation (PSN) and can significantly affect the recrystallised grain size, as discussed in section 2.4.3.4[127, 129].

Dynamic recrystallisation has been studied in many different materials and the type of DRX has been ascertained. For example, discontinuous dynamic recrystallisation has been observed in copper[130], austenitic stainless steel[131] and nickel[112], while continuous dynamic recrystallisation has been seen in quartz[132], copper[133, 134] and aluminium[135]. Both discontinuous dynamic recrystallisation and continuous

dynamic recrystallisation have been observed in magnesium. Generally DDRX occurs at the higher temperatures or lower strain rates, for example references [36, 96, 136, 137], whereas CDRX occurs at lower temperatures or higher strain rates, for example references [96, 120, 138, 139]. These changes with deformation conditions will be discussed further in section 2.4.3.3. It is likely that at many conditions, both DDRX and CDRX are occurring simultaneously, but with one at a much greater rate[140].

2.4.3.1 Discontinuous Dynamic Recrystallisation (DDRX)

DDRX progresses through a standard nucleation and growth mechanism. New grains nucleate at original grain boundaries or twin boundaries within the material through bulging of these high angle boundaries. The recrystallised grains grow into the parent grain until the increasing dislocation density within the new grains lowers the driving force for further growth to a point at which it will cease. This process creates a necklace structure around the original grain boundaries until all nucleation sites are full, at which point new grains will then nucleate on the newly created high angle boundaries by the same process[96, 112]. As discussed above, DDRX has been shown to be active in many different magnesium studies[36, 96, 136, 137].

2.4.3.2 Continuous Dynamic Recrystallisation (CDRX)

Continuous dynamic recrystallisation is classed as a recrystallisation mechanism because it forms entirely new grains. However, the process by which it occurs is generally closer to that of recovery than conventional recrystallisation because the major operation is the rearrangement of dislocations[112, 137]. The trigger for more in-depth study of CDRX was the development of automated electron backscatter diffraction analysis, when the subgrain boundaries could be studied in more detail[141]. Therefore, there has been an increase in the number of studies carried out in recent years. There have been various mechanisms put forward under the CDRX umbrella that have been observed in different materials.

The feature common to most CDRX mechanisms is the rearrangement of dislocations into cells, subgrains and recrystallised grains. The rearrangement of dislocations into low energy structures was discussed in section 2.4.2. Initially the dislocations form into cells, with tangled arrays of dislocations forming a relatively wide structure. As the dislocation movement continues, and more dislocations reach the cell walls, further recovery processes occur and the cell walls become more defined. Through continuous

addition of dislocations and some amalgamation of cell walls, well defined, but low angle, subgrain boundaries are formed. The addition of further dislocations slowly increases the disorientation across these boundaries and thus they become high angle grain boundaries. The process of dislocation motion causes most dislocations to migrate from the interior of the newly formed grains into the boundaries and thus the dynamically recrystallised grains have a low dislocation density[85, 112].

The conventional mechanism of CDRX consists of the processes described above rearranging the dislocations that are produced through relatively homogeneous strain within the material. As was shown in section 2.3.4, slip in magnesium is generally restricted by the crystallography and causes heterogeneous strain. The compatibility stresses caused by grain boundaries, along with twinning and the pile up of basal dislocations, often create a disparity between the deformation behaviour near the grain boundaries and in the grain interior.

During low temperature deformation, twinning plays a major role in strain accommodation, see section 2.3.5, and consequently influences the DRX behaviour as well. A mechanism similar to standard CDRX operates from the dislocation build up in the highly stressed regions, primarily the twinned areas. Subgrain boundaries form in these regions around the twins and twin intersections and, through the absorption of further dislocations, both the subgrain and twin boundaries convert to random high angle grain boundaries[96, 142].

At higher temperatures, more slip is active and twinning becomes less significant as a site of recrystallisation. There is still a concentration of stress surrounding the grain boundaries, and it is in this region that non-basal slip becomes active. A mechanism that is initiated by this stress concentration was described by Ion *et al.*[51] in magnesium and is based on 'rotation recrystallisation' seen previously in geological materials[132, 143]. In the current work this will be termed 'Continuous Dynamic Rotation Recrystallisation' (CDRRX). The polycrystal can be thought of as a series of non-deforming grain cores with a plastic 'mantle' around the grain boundaries. Thus, on a macroscopic scale, the deformation will be carried out by a shear parallel to the grain boundary. This grain boundary plane is unlikely to be an easily activated slip plane and thus there will be lattice rotations in this region, as shown in figure 14. The lattice rotations create bent planes and thus a large number of geometrically necessary dislocations are formed. These dislocations act as described previously and will form into the low energy configurations of cell and subgrain walls. Further strain causes more

rotation and consequently more dislocations, which will add to the disorientation of the subgrain boundaries, eventually creating new grains in a necklace around the pre-existing grain boundaries. This mechanism was put forward by Ion *et al.*[51] but has since been confirmed in magnesium alloys by other studies[88, 96, 138].

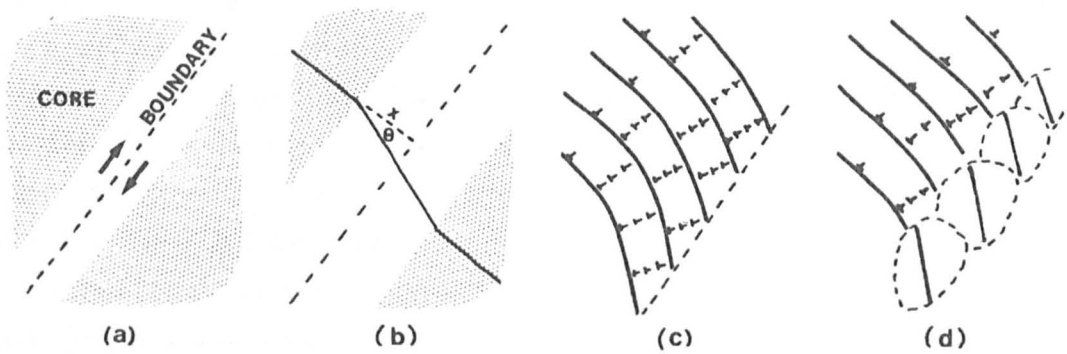

Figure 14 - Deformation in the mantle leading to recrystallisation[144]

Following the initial formation of recrystallised grains, further straining can cause changes. Grain coarsening can occur but has been shown to be slower in CDRX than DDRX[141] and, therefore, is not expected to play a significant role while deformation is still occurring. It was shown by both Ion *et al.*[51] and Spigarelli *et al.*[125] that strain often concentrates in DRX regions because slip is easier due to the changes in texture. This can result in strain localisation in these regions and repeated recrystallisation, as well as the formation of shear zones, as described in section 2.3.7. He *et al.*[119] argued that grain boundary sliding in the shear zones, due to the reduced grain size, actually halts DRX because it stops the production of further dislocations. Therefore, the occurrence of repeated DRX in localised areas is connected to the grain size formed.

2.4.3.3 Influence of Deformation Conditions

As with most aspects of dynamic material behaviour, the conditions under which a sample is deformed have a large influence on how a material dynamically recrystallises. Both Galiyev *et al.*[96] and Sitdikov and Kaibyshev[142] studied the differences in DRX behaviour over a range of conditions in ZK60 and pure magnesium respectively. They found that the mechanism of DRX was different at different temperatures, with both DDRX and CDRX active, as well as variations within those mechanisms. At low temperatures, twinning is a major deformation mechanism and, therefore, CDRX

temperatures, twinning is a major deformation mechanism and, therefore, CDRX nucleating at twins and twin intersections takes place, as described above. At intermediate temperatures, a greater level of dislocation slip is active and therefore a build up of dislocations is more likely to occur at grain boundaries. Both Galiyev *et al.* and Sitdikov and Kaibyshev found that this allowed standard CDRX to occur, as there were sufficient dislocations of the non-basal type to form a 3 dimensional array of low angle boundaries; in their studies CDRRX is not seen. At even higher temperatures, the mobility of grain boundaries becomes sufficiently high to allow DDRX to occur. Therefore, this is the dominant mechanism at the highest temperatures. Although the mechanisms described above were dominant in the domains given, Sitdikov and Kaibyshev stated that there was a reasonable amount of overlap between the various mechanisms and thus it is expected that at all conditions the other mechanisms are also active, just at a slower rate. It should also be remembered that there is generally an equivalence between the temperature and the strain rate through the Zener-Hollomon parameter. Therefore, the mechanisms that require a higher temperature can also be activated by reducing the strain rate.

These findings from Galiyev *et al.*[96] and Sitdikov and Kaibyshev[142] are, in general, confirmed by other studies in magnesium, such as references [36, 120, 136-138]. However, there are certain studies that have observed CDRX at high temperatures. Some of these can be explained by a high strain rate but others, such as Tan and Tan[80] and Yang *et al.*[145], do not conform to the expected rules, exhibiting CDRX even though they were deformed at a high Zener-Hollomon parameter. The reason for these results is currently unknown.

2.4.3.4 Recrystallised Grain Size

In both continuous and discontinuous dynamic recrystallisation, the final recrystallised grain size is strongly dependent on the temperature and strain rate of deformation. In CDRX the grains form at a certain size that stays constant at all levels of strain[51]; whereas, in DDRX, the grains grow throughout deformation from very small nuclei. However, a steady state grain size is reached in DDRX, due to the constant nucleation and re-recrystallisation once a certain strain has passed, and it is this size that is influenced by the deformation conditions.

In general, if a material is deformed under conditions in which DRX will occur, the lower the Zener-Hollomon parameter (Z) (i.e. the higher the temperature or lower the

strain rate) the larger the resultant grains[51, 96, 127, 137, 142]. It is often stated that the relationship between Z and the DRX grain size follows equation 5[127, 140, 146]:

$$Z = kd^{-N} \tag{5}$$

where Z is the Zener-Hollomon parameter, d is the recrystallised grain size and k and N are constants.

This relationship is sometimes given with peak stress instead of Zener-Hollomon parameter[130, 131, 134]. As stress is normally a function of Z, this does not dramatically change the dependence of grain size on deformation conditions, although the shape of the curve and the constants would be different. Hakamada *et al.*[127] looked at various studies in Mg-Al-Zn alloys and found that most followed the relationship given in equation 5, see figure 15. The alloy that they studied in their own work was a Mg-Al-Ca-RE alloy and did not show any dependence of grain size on deformation conditions. The presence of precipitates in the material during deformation meant that DRX occurred by particle stimulated nucleation and the recrystallised grain size was dictated by the particle distribution. This has also been noted in magnesium alloys containing Zr rich particles, usually added for grain refining purposes in casting[147, 148]. This effect is expected in any material containing a significant level of precipitates.

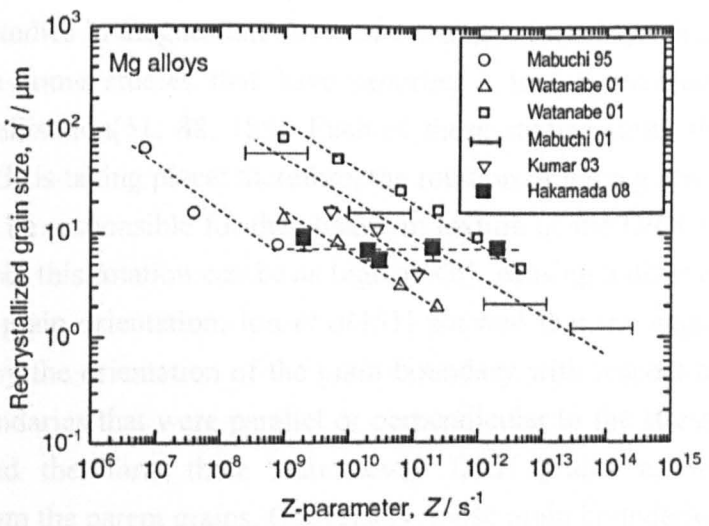

Figure 15 – Variation in dynamically recrystallised grain size as a function of Z-parameter for Mg alloys[127]. Includes data from references [83, 146, 149, 150]

As well as the deformation conditions, some studies state that the size of the recrystallised grains can also be affected by the initial grain size. Watanabe *et al.*[146] and Barnett[151] both come to the conclusion that the initial grain size affected the final DRX grain size produced. The reason for this is linked to the greater number of grain boundaries giving more nucleation sites. However, Barnett carried out a more in depth study of this effect a year after the previous work, and disagreed with his initial conclusion[140]. In the initial work, the samples with different starting grain sizes were actually deformed using different methods; therefore, the final grain size was probably affected more by these differences than the initial grain size. A similar effect is present in the work from Watanabe *et al.* as well.

2.4.3.5 Texture Changes during Dynamic Recrystallisation

The recrystallisation textures in hexagonal metals have been much less studied than those in cubic materials[112]. In general it is found in hexagonal materials, and specifically in magnesium alloys, that recrystallised materials retain much of the pre-existing deformation texture[118, 138, 152-154]. However, the extent to which DRX retains or weakens the texture is a matter of debate. Due to the mechanism of grain boundary bulging and migration in DDRX the texture of the DRX grains cannot deviate far from the parent grain orientation and thus texture is normally retained well in materials undergoing DDRX. It would appear, from consideration of the mechanism, that CDRX would also retain a very similar texture to that of the parent grains. Although most studies in magnesium alloys show that texture is retained through DRX, there have been some studies that have reported a texture weakening effect from dynamic recrystallisation[51, 88, 155]. Each of these studies states that a mechanism similar to CDRRX is taking place; therefore, the rotation of the regions near to the grain boundaries must be responsible for the change in texture of the DRX grains. Del Valle *et al.*[88] state that this rotation can be as high as 40°, causing a difference of up to 40° from the parent grain orientation. Ion *et al.*[51] showed that the angle of the rotation was influenced by the orientation of the grain boundary with respect to the stress axis. Those grain boundaries that were parallel or perpendicular to the stress axis underwent less rotation and therefore, there were fewer DRX grains as well as a lower disorientation from the parent grains. Conversely, those grain boundaries oriented 45° to the stress axis underwent much more recrystallisation and had higher rotations from the parent grains.

2.4.4 Annealing

Following deformation in a material, there is often a large amount of stored energy that has built up due to increased defect and dislocation densities. Although dynamic recovery and recrystallisation may have significantly reduced this during deformation, there will generally be a certain amount remaining. If the temperature is kept high enough following deformation, annealing processes can act to reduce the energy of the system. These are static recovery, grain growth and recrystallisation[112].

Static recovery was described in section 2.4.2 and produces the same cell and subgrain structures as in dynamic recovery. Grain growth is a process that occurs in most materials given the correct temperature and is driven by the reduction in energy stored by the grain boundaries. The grain boundaries migrate through the material, increasing the size of some grains and decreasing the size of others until they disappear. This will normally only happen after recrystallisation because, when the dislocation density is high, the driving force for recrystallisation is greater. Therefore, grain growth is likely to occur in materials that have fully recrystallised either dynamically or statically. Static recrystallisation is the formation of new grains from the deformed microstructure and as with dynamic recrystallisation, this can be continuous or discontinuous. These mechanisms occur in the same way as described for dynamic recrystallisation in section 2.4.3, although the stored energy is not being replaced so an end point is reached when the stored energy drops to a critical level. In a previously deformed material there can often be pre-formed nuclei from dynamic recovery and recrystallisation that can later grow in static recrystallisation, a process known as metadynamic recrystallisation[112].

Studies into the annealing of hot worked magnesium alloys have observed that static restoration mechanisms are often very active. Recovery, grain growth and recrystallisation have all been reported and, depending on the deformation and annealing conditions, the different mechanisms of static recrystallisation have all been seen[156-161], although there is little direct evidence of metadynamic recrystallisation in magnesium.

2.5 Texture

2.5.1 Measurement of Texture

The fundamentals of texture analysis have been covered in great detail by Randle and Engler[162] and the parts of their book that are relevant to the current work will be discussed here. Texture analysis is the study of the specific orientations and distributions of orientations of grains found in a polycrystalline material. It is of interest because different orientations can dramatically change the properties of many polycrystalline materials. The macrotexture of a material is an overall view of the distribution of orientations over a large number of different grains. Microtexture is the study of both the macrotexture of a material and the spatial distribution of the different orientations; the word comes from a contraction of microstructure and texture. Historically, only macrotexture was possible, using X-ray and neutron diffraction techniques, but more recently the development of fully automated Electron Backscatter Diffraction (EBSD) in the scanning electron microscope, has allowed routine acquisition of microtexture. The texture measurements in the current work have all come from EBSD analysis and therefore, can be classed as microtexture, but will simply be referred to as texture measurements.

2.5.2 Representation of Texture

Textures are commonly displayed using either pole figures or orientation distribution functions (ODFs). Pole figures generally use the stereographic projection method to display the 3 dimensional orientation of a specific pole in the crystal on a 2 dimensional circle, see figure 16. In EBSD analysis each pixel is treated as a separate crystal and the pole of each orientation is plotted on the pole figure. When the densities of these poles are calculated for each area of the pole figure, a contour map is produced and the overall texture can be seen.

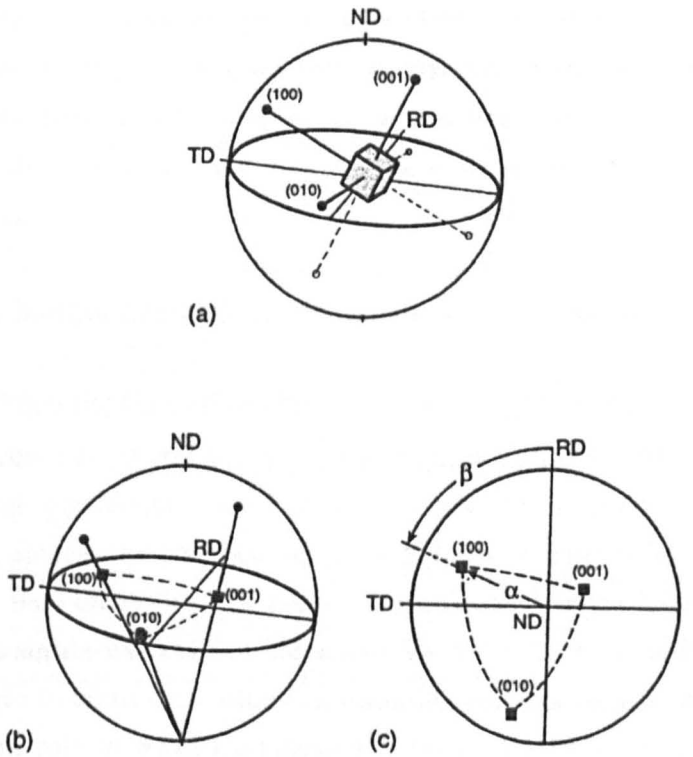

Figure 16 – Presentation of the {100} poles of a cubic crystal in the stereographic projection. (a) crystal in the unit sphere; (b) projection of the {100} poles onto the equatorial plane;
(c) {100} pole figure[162]

ODFs are a representation of Euler space, which has a coordinate system made up of the 3 Euler angles determining the orientation. The Euler angles are a sequence of three rotations that transform the specimen coordinate system into the crystal coordinate system[162]. Randle and Engler[162] stated that the most commonly used convention is the Bunge notation and defined the rotations as:

1. φ_1 about the normal direction ND, transforming the transverse direction TD into TD' and the rolling direction RD into RD';
2. Φ about the axis RD' (in its new orientation);
3. φ_2 about ND" (in its new orientation)

Therefore, ODFs are 3 dimensional spaces with axes φ_1, Φ and φ_2. In order to display an ODF on the printed page it is generally necessary to take sections through the 3 dimensional space and display a sequence of ODF sections at certain intervals.

A single pole figure is almost always an incomplete description of the texture because rotations about the specific pole used are not distinguished. An ODF contains a full description of the texture but requires many sections to display it on the page. Therefore, a decision must be made as to which is the most suitable method to use in any particular work.

2.5.3 Texture Changes during Thermomechanical Processing

It can be assumed that the starting product for thermomechanical processing, before any processes have been carried out, has an equiaxed grain structure with a random texture. Thermomechanical processing can change the texture in many materials, which, depending on the final properties, can be desirable or not. This section will look at the textural changes that occur in hcp metals, specifically magnesium and magnesium alloys. Due to the similarity between the active deformation mechanisms in various hcp metals, the changes in texture are often very similar. As will be shown below, twinning plays an important role in texture changes and thus only those materials with similar twinning behaviour can be considered analogous, which rules out those metals with c/a greater than $\sqrt{3}$. For the commonly studied metals this means that titanium and zirconium should show similar behaviour to magnesium whilst zinc and cadmium will not.

Many authors have observed a 'basal texture' from compression of magnesium and other similar metals, for example references [37, 57, 87, 163-165]. Basal texture means that the <0001> direction is aligned with the compression axis, and is a fibre texture as the other poles of the crystal are oriented relatively randomly. The fact that magnesium has a c/a ratio that is very close to that for perfect close packing should mean that the basal texture formed is also almost perfect[166]. Despite this, many observed textures, particularly in hot rolling, show a split in the basal pole towards the rolling direction of approximately 10-20°. According to Kocks *et al.*[166], this type of texture should theoretically only form in hcp metals with c/a>1.633. However, they also point out that strain rate, temperature and chemical composition can all affect texture development and, from the observed textures in rolled magnesium, it can be concluded that these factors play a large role.

The strong basal texture is generally considered to be a disadvantage in magnesium sheet because of the tension-compression asymmetry that arises in textured magnesium, see section 2.3.5. Therefore, a sheet or plate in bending or buckling will deform more

easily on one side than the other, creating problems for design[4]. Unfortunately, the thermomechanical processes that create the basal texture are almost entirely unavoidable in sheet production.

It is generally accepted that both basal slip and $\{10\bar{1}2\}$ twinning cause the pure basal texture in magnesium[37, 51, 52, 70, 163]. Slip causes a gradual reorientation of the crystal over a large strain, whereas twinning causes a dramatic reorientation of the crystal with a specific relation to the starting texture[78, 166]. In conditions where $\{10\bar{1}2\}$ twinning is highly active, this can cause the majority of the reorientation with a relatively small strain. Kelley and Hosford[39] showed that in a single crystal of magnesium ideally oriented for $\{10\bar{1}2\}$ twinning, the entire crystal was reoriented by a strain of 6%. Yang *et al.*[163] showed a similar effect in a heavily pre-textured polycrystal, again with the grains almost perfectly oriented for twinning, where almost all grains had rotated by a strain of 8%. Although the texture change from twinning is very rapid in grains perfectly oriented for twinning, it is only grains that are more than 68° from the basal texture that will undergo twinning[37]. Therefore, any grains with orientations closer to the basal texture will not twin, and only slip can cause a texture reorientation.

Although most authors are agreed on the formation of the pure basal texture, there is some difference of opinion in the literature over the origin of the split towards the rolling direction. Prismatic slip does not cause a reorientation of the c-axis[52, 78] and it has already been shown that basal slip and $\{10\bar{1}2\}$ twinning rotate the crystals into a pure basal texture. Therefore, the only common deformation mechanisms remaining that could cause the split in texture are compression twinning and <c+a> slip. Philippe *et al.*[53] and Wonsiewicz and Backofen[74] both stated that the rotation of the basal poles towards the rolling direction could be due to compression twinning or secondary twinning of $\{10\bar{1}2\}$ twins within $\{10\bar{1}1\}$ twins. This is a feasible mechanism that would theoretically rotate the crystals in the correct direction but later studies have generally argued against it. Philippe *et al.* did also suggest that <c+a> slip could be the responsible mechanism, and other authors have shown that this is more significant than compression twinning[52, 78]. Agnew *et al.*[52] carried out a simulation using a 'viscoplastic self-consistent model' and showed that changing the activity of <c+a> slip altered the strength of the split in texture.

Dynamic and static recrystallisation processes can also alter the texture of the material and are discussed further in sections 2.4.3 and 2.4.4.

2.6 Flow Behaviour in Magnesium Alloys

There have been many studies that have looked at the flow behaviour of various magnesium alloys[70, 142, 167-170]. The studies that are of most interest to the current work are those in which compression was carried out, either uniaxial[140, 171-173] or plane strain compression[42, 76]. As with work on most features in magnesium, the most common alloys studied are the AZ series, particularly AZ31[72, 140, 167, 169, 174]. In many cases the flow behaviour of these, and other, alloys show a similar shape with a rise to a peak stress, followed by softening and finally reaching a steady state stress, caused by a balance between the hardening and softening mechanisms[36, 169, 175-177]. A very good example of this behaviour is shown in figure 17 from Prasad and Rao[169], and gives the flow curves of samples of AZ31 deformed in uniaxial compression at 350°C and a range of strain rates.

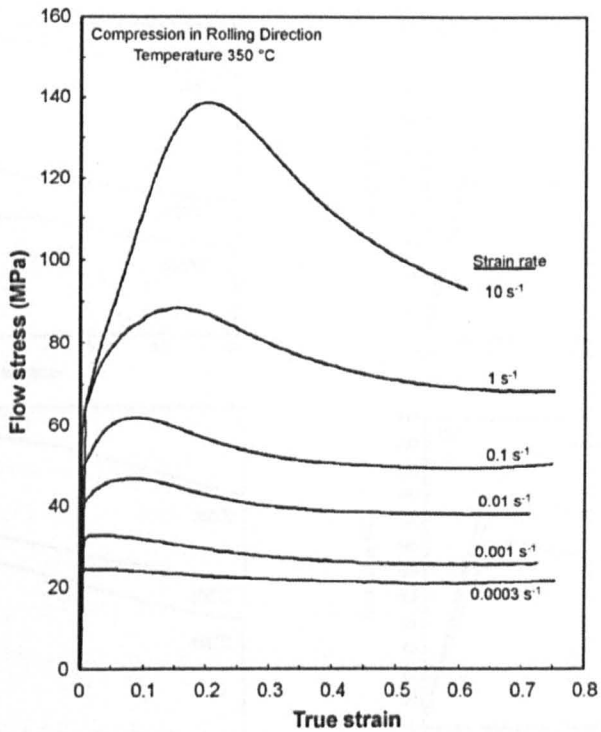

Figure 17 – True stress-true strain curves obtained at different true strain rates on cylindrical specimens of AZ31 compressed parallel to the rolling direction at 350°C[169]

Figure 17 also shows that the shape of the stress-strain curve can change significantly due to changes in strain rate. At the higher strain rates, the peak in the stress is more pronounced and steady state is reached later. At lower strain rates, the material does not

undergo and significant hardening and steady state is reached almost immediately. Prasad and Rao also showed that variation in temperature has a similar effect, with an increase in temperature causing a lower peak strain as well as steady state at a lower strain. Therefore, the Zener-Hollomon parameter can be used again to combine the effects of temperature and strain rate. Many studies confirm that the shape of flow curves seen by Prasad and Rao are common in magnesium alloys[36, 175-177].

Although a steady state stress is observed in many studies, this is not true of all magnesium alloys under all conditions. It appears that by raising the alloy content of the material, the strain at which steady state is reached can be increased. This is true in some alloy systems, particularly in rare earth alloys, but not necessarily for smaller increases in aluminium[126, 178, 179]. This means that, in many cases, the steady state stress is not reached by the end of standard compression testing.

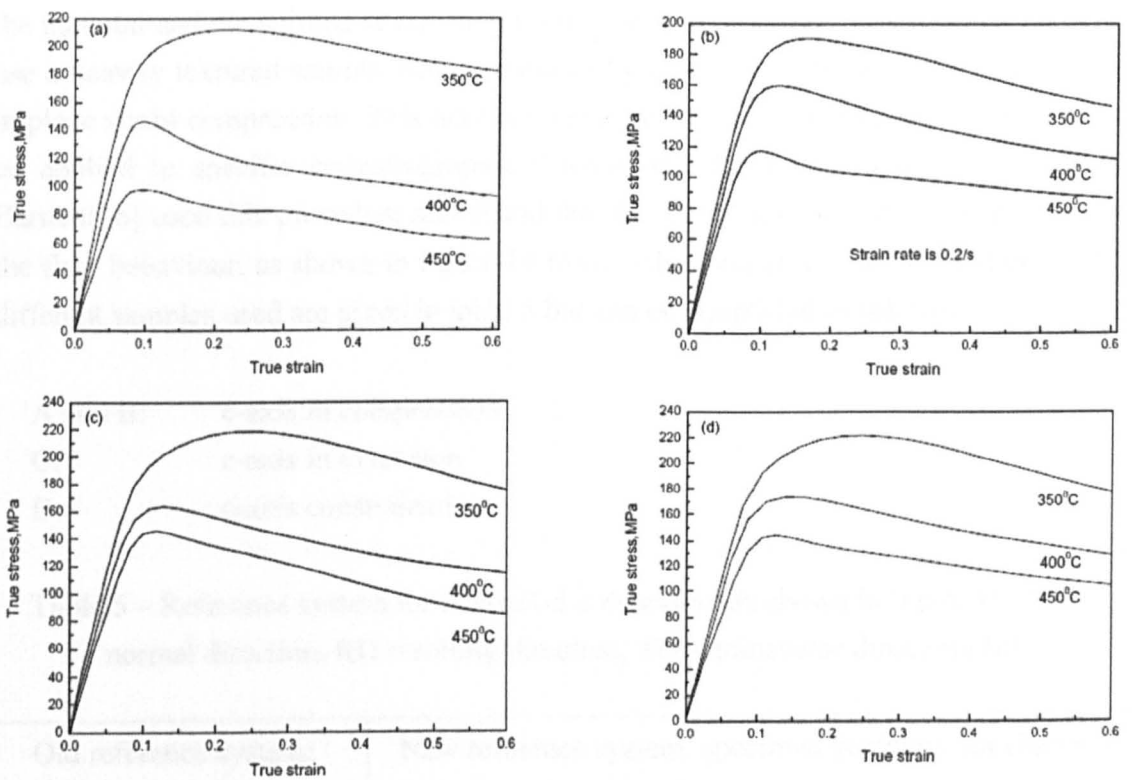

Figure 18 – True stress-strain curves for an Mg-12Gd-3Y alloy in uniaxial compression at (a) $0.1s^{-1}$, (b) $0.2s^{-1}$, (c) $0.3s^{-1}$, (d) $0.4s^{-1}$ and various temperatures[170]

Zhang and Wang[170] carried out compression testing to a strain of 0.6 on an Mg-12Gd-3Y alloy at various conditions and found that no true steady state stress was

reached. It can be seen in figure 18, from Zhang and Wang's work, that at higher temperatures and lower strain rates, there is a more defined peak, followed by a softening rate that decreases with strain. This is similar behaviour to that seen above, where steady state stresses are reached; therefore, it is likely that steady state could have been reached in these tests at strains only slightly larger than 0.6. However, in the tests carried out at higher values of Z, there is no decrease in the softening rate, and thus it does not appear that steady state would be reached shortly after a strain of 0.6. Therefore, the deformation conditions, as well as the alloy content, can change the flow behaviour, an observation also made in various other studies[96, 142, 177, 180-182]. Despite this, some studies have seen continuous softening in alloys and conditions where it would not be expected[174]. Therefore, the dependence on alloy content and processing conditions is rather weak.

The shape of the flow curve is also affected by the relationship between the texture of the material and the applied stress conditions. The most common way to study this is to use a heavily textured sample, often produced by rolling or extrusion, and to deform it in plane strain compression. This allows a very precise set of deformation conditions to be applied to specific crystallographic orientations. Both Gehrmann *et al.*[42] and Barnett[36] used this procedure and found that the initial texture had a strong effect on the flow behaviour, as shown in figure 19 from Gehrmann *et al.* The orientations of the different samples used are given in table 5 but can be simplified as follows:

A and B: c-axis in compression
C: c-axis in extension
D: c-axis constrained

Table 5 – Reference system for channel-die experiments shown in figure 19. ND = normal direction, RD = rolling direction, TD = transverse direction[42]

Old reference system: rolling geometry	New reference system: specimen geometry for channel-die experiment			
	A	B	C	D
ND	ND	ND	RD	TD
RD	RD	TD	TD	ND
TD	TD	RD	ND	RD

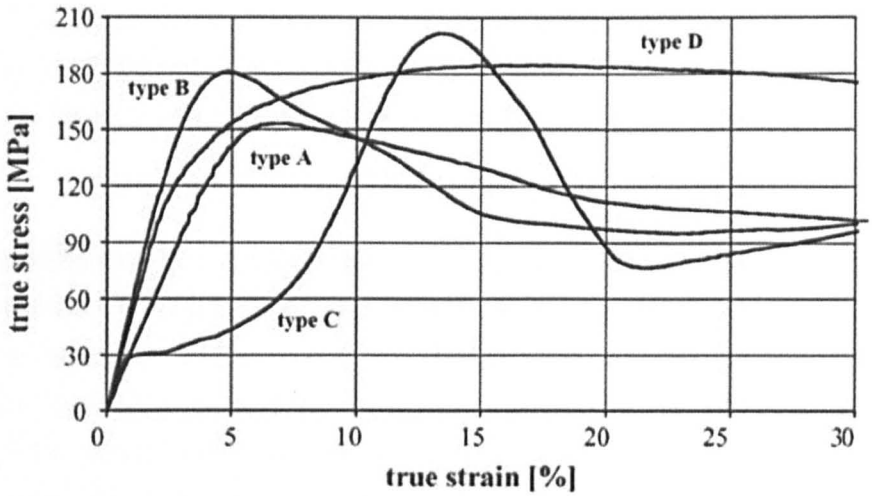

Figure 19 – Flow curves of different specimens of pure Mg at 100°C. Different types refer to the sample orientations given in [42]

The variations in flow behaviour caused by different starting textures are due to the active deformation mechanisms[36, 42]. The orientation of the samples determines whether basal slip, prismatic slip, pyramidal slip or twinning are the most significant mechanisms. Samples A and B in figure 19 are oriented such that basal and prismatic slip, as well as $\{10\bar{1}2\}$ twinning, are hard to operate and, therefore, there is rapid hardening to a peak. Following this, different mechanisms can operate to cause softening, such as dynamic recrystallisation or shear band formation. Sample C is oriented such that $\{10\bar{1}2\}$ twinning is very easily activated, and it is this mechanism that is thought to be responsible for the concave shape of the curve. Sample D hinders both basal slip and $\{10\bar{1}2\}$ twinning but is ideally oriented for prismatic slip. This does not significantly alter the texture and thus there is not such a pronounced peak. The changes in work hardening rate will be discussed further in section 2.6.2 and the differences in flow softening will be examined in section 2.6.3.

2.6.1 Activation Energy of Deformation (Q_{def})

The activation energy of deformation (Q_{def}) is a measure of the ease with which a material will deform. There have been many studies on magnesium and magnesium alloys that have calculated activation energies of both creep (Q_c) and deformation (Q_{def}). Q_c was calculated from tests carried out at strain rates below approximately 0.01 and often has very similar results to Q_{def}; in these cases it is expected that the deformation mechanisms are similar over a range of strain rates. Other studies have found that there

can be quite a significant change in activation energy between the creep and hot working regimes. Therefore, the values for Q_c from the literature often give a reasonable indication of Q_{def} but cannot be compared directly with those obtained at higher strain rates.

The self diffusion energy of magnesium is 134 kJ mol^{-1} [2] and it has been reported that both Q_{def} and Q_c for magnesium are generally in a range similar to this[36, 125, 174, 183-186]. However, it is often noted that composition, temperature and strain rate can dramatically affect the activation energies quoted. Guo *et al.*[174] and Liu and Ding[126] both stated that increased concentrations of aluminium in AZ series alloys caused Q_{def} and Q_c to also increase. However, Somekawa *et al.*[116] also studied the effect of aluminium concentration on magnesium alloys and found that Q_c was not changed. Anyanwu *et al.*[187] looked at Q_c from various magnesium-gadolinium-yttrium alloys and observed quite a large variation with different ratios of Gd and Y, between 160 and 240 kJ mol^{-1}. They found that the higher Y:Gd ratio alloys had higher activation energies. Despite this, there have also been reports of Mg-Gd-Y alloys having fairly low values of Q_c, in the range 119 to 131 kJ mol^{-1} [170, 186]. Therefore, it can be concluded that alloy composition has an effect on the activation energy of the material but that it is also influenced by other factors.

The processing conditions have also been shown to have a strong effect on the activation energies for both deformation and creep. It is often reported that the temperature has a large influence on the activation energy[9, 96, 178, 183, 185, 188, 189]. There is often a change in creep behaviour at around three quarters of the melting point of magnesium (approximately 450°C) that raises the value of Q_c dramatically to around 220-230 kJ mol^{-1}. In certain studies it was also seen that the low temperature creep behaviour gave lower values of Q_c than self diffusion[96, 116, 179]. These differences are attributed to different mechanisms operating at different temperatures, often stating that the activation of cross-slip at higher temperatures raises Q_c [185, 188, 189]. There has been much less study of Q_{def} than Q_c but it is reasonable to assume that there will be similar differences in Q_{def} with the operation of different mechanisms due to changes in temperature, strain rate and composition.

2.6.2 Work Hardening

Work hardening is the increase in stress required to deform a material, generally in the early stages of deformation. Normally this is due to the increasing dislocation density,

and the consequent interaction between the dislocations. This makes it much harder for the dislocations to move and thus the stress in the material is raised[34]. In most cases, this work hardening produces a convex stress-strain curve during hot deformation of polycrystalline metals; however, a concave curve has been observed in magnesium and some other metals, under specific conditions, for example references [38, 39, 63, 171, 190]. These show a low work hardening rate following yield that increases as strain progresses. After a short period of time a point of inflection is reached and the work hardening rate decreases, often rather sharply, to a peak stress. Generally, this behaviour is only seen in samples that are deformed at particularly low temperatures or high levels of strain. Kelley and Hosford[39] studied the flow behaviour of single crystal magnesium, magnesium-lithium and magnesium-thorium. They showed that the tendency for concave shapes in flow curves is entirely dependent on the orientation of the crystal. By carrying out plane strain compression tests on three different samples oriented such that the c-axis of the crystal was either being extended, constrained or compressed, they found three different flow curves produced. Both the c-axis compression and c-axis constraint samples showed convex curves, while the c-axis extension sample showed a very clear concave curve. A subsequent study by Kelley and Hosford[63] showed that the same effect is present, although to a slightly lower extent, in textured polycrystalline materials where the majority of grains have the c-axis in the extension direction, an observation also made in other studies[42, 76, 171].

Section 2.3 has already described the various deformation modes that are available to magnesium alloys. It can be seen that a sample in which the c-axis is aligned with the extension direction has a very low resolved shear stress for basal slip, but is ideally oriented for $\{10\bar{1}2\}$ twinning. Therefore, in the absence of any non-basal slip systems, the material will initially deform almost exclusively by $\{10\bar{1}2\}$ twinning and it has been concluded by various authors[36, 39, 42, 51, 55, 63, 72, 76, 171] that this mode of twinning is primarily responsible for the concave nature of the flow curves. The increase in strain hardening due to twinning is thought to come from the increase in boundaries[36, 52, 99, 171], effectively decreasing the grain size, the 86° reorientation of the crystals[36, 55, 171], making slip even more difficult, and the gradual exhaustion of twinning[42], forcing the higher levels of stress required for slip to be reached. Although some specific dislocations can pass through twin boundaries with little problem[67], it has been shown that twin boundaries have a repulsive force on many dislocations, or can cause a transformation leaving sessile dislocations at the boundary, and therefore provide as effective a barrier to slip as grain boundaries[58, 72]. Different studies have come to the conclusion that different mechanisms are primarily responsible

for the increase in hardening rate. For example, both Barnett[36] and Jiang *et al.*[171] agree that both grain reorientation and twin boundaries play a role, but Barnett argues that the reorientation mechanism is dominant, while Jiang states that the increased level of boundaries is more important. It is possible that the different conditions used for deformation are responsible for the difference between the hardening mechanisms, but it is more likely that many mechanisms are active at all times and play a role in increasing the work hardening rate.

2.6.3 Flow Softening

The peak stress in the flow curves is caused by the initiation of a softening mechanism that counteracts the previous work hardening. In tests carried out at lower values of the Zener-Hollomon parameter, the peak can be much less obvious because work hardening is occurring at a much lower rate, and softening at a much higher rate; consequently, the peak is reached very early on and the softening to steady state is negligible. Therefore, the curve appears as a very slight increase in stress followed by a horizontal steady state plateau[96, 169, 191, 192]. In curves that show a more prominent peak, the effect of softening can be seen and studied more clearly.

Often, the peak strain itself is used to measure the onset of softening but it is more accurate to measure the start of flow softening from a point of inflection in a $d\sigma/d\varepsilon - \sigma$ plot, that occurs prior to the peak strain[96]. Both the stress and strain at which the peak occurs are strongly affected by the conditions under which the deformation is taking place. Deformation conditions with a higher Z value give a higher peak stress at a higher strain[167, 174, 191]. This indicates that the softening mechanism is strongly affected by both temperature and strain rate. The most common cause of softening given in the literature is dynamic recrystallisation[51, 181, 182, 193], which agrees well with the dependence on temperature and strain rate and is often seen in magnesium alloys during deformation.

Other theories have, however, been put forward for the softening effect in magnesium alloys. Gehrmann *et al.*[42] studied both pure magnesium and AZ31 at relatively low temperatures and did not observe any recrystallisation. They attributed the softening behaviour to inhomogeneous deformation and the subsequent formation of shear bands and shear cracks. Yang *et al.*[145] observed dynamic recrystallisation but stated that this was not responsible for the softening effect and instead linked the softening to the texture evolution. Their work looked at the compression of extruded AZ31 bar where

the starting texture for compression had the c-axes perpendicular to the stress axis. According to the authors this meant that, in order for the texture to finish as standard basal, the c-axes must rotate 90° and thus pass through angles where basal slip is easier. Although this would cause some softening effect if the rotation was continuous, it is thought that twinning would be more likely to operate and thus the rotation would be instant. Therefore, the grains would not pass through any soft orientations and Yang *et al.*'s theory can be discounted. Beladi and Barnett[194] studied the deformation behaviour of a peak aged WE54 alloy and found that the precipitates retarded any dynamic recrystallisation. However, they still observed softening to a small degree and were not confident of the mechanism; texture softening or a reduction in solute strengthening due to dynamic precipitation were both put forward. They suggested that the steady state behaviour was due to dynamic recovery.

2.6.4 Process Window

The process window of a material describes the range of conditions under which it can be successfully processed, avoiding the operation of any failure mechanisms. There has been very little published[195] on the process windows of magnesium alloys, probably because it is often more relevant industrially than academically. A more complex version of the process window is the process map, which has been looked at by a number of authors, for example references [169, 176, 178, 196]. This provides information on the various mechanisms that are active at different conditions and shows which regions are most suitable to provide the best microstructure. These various studies show that the process window is very dependent on the specific forming process used, whether it is rolling, extrusion or simple compression, and that both temperature and strain rate influence the limit behaviour.

2.7 Constitutive Equation Development

Constitutive equations of flow behaviour allow the flow stress of a material to be predicted under different conditions of temperature and strain rate, enabling the modelling of forming processes[197]. Davenport *et al.*[197] set out a reliable method to develop equations for a microalloyed steel that work equally well with many other materials exhibiting dynamic recrystallisation. This method gives two sets of equations; the first stage equations allow stress to be calculated at specific values of strain and the second stage equations use the first to give a continuous flow curve.

1st stage constitutive equations correlate the stress at certain points on the flow curve to the processing conditions, given by the Zener-Hollomon parameter. Different functions have been used in the literature for the relationship between the stress and the Zener-Hollomon parameter: exponential, power law or hyperbolic sine (sinh) equations, as shown below.

Exponential:	$Z = Ae^{\beta\sigma}$	(6)
Power Law:	$Z = A\sigma^{n}$	(7)
Sinh:	$Z = A(\sinh \alpha\sigma)^{n}$	(8)

McQueen and Ryan[198] have stated that the power law was traditionally used for studies of creep, but becomes unreliable at high stresses, and the exponential law was used for hot working, but breaks down at low stresses. Therefore, the hyperbolic sine law was introduced in the 1960s as it can be used across the full range of conditions[199, 200]. Different studies have successfully used the exponential relationship[174, 201], the power law relationship[96, 109, 174, 183] and the sinh relationship[41, 176, 184, 185] to model magnesium alloys under a range of deformation conditions.

While equations have been developed numerous times to calculate the stress at specific points of strain, very little work has been carried out to produce full simulated curves in any magnesium alloys[202, 203]. Li *et al.*[202] developed 1st stage equations for a sequence of strain intervals in an AZ31 alloy but did not calculate 2nd stage equations using the Davenport *et al.* method. Instead, a finite element model used the 1st stage equations to model the full flow curve for an extrusion test, which gave a good correlation with the experimental results. Bhattacharya *et al.*[203] also modelled the behaviour of AZ31 but used the Davenport *et al.* method to calculate full constitutive equations. Although this was a simpler method, they also found a good fit with the experimental data.

3. Experimental Methodology

This chapter introduces the methods used in the experimental aspects of the work. The research was based around the simulation of industrial rolling through Plane Strain Compression (PSC) testing and thus this will be discussed in detail. The main techniques used to study the deformed material were Electron Backscatter Diffraction (EBSD) and Transmission Electron Microscopy (TEM). In addition to these, a small amount of XRD was used, and the procedure of all techniques will be discussed here.

3.1 Material

Elektron™ 675 is a developmental alloy from Magnesium Elektron Ltd which is based on the magnesium-yttrium-gadolinium system. It has been designed as a wrought alloy that has particularly high strength and that can be used at higher temperatures than many other current magnesium alloys. The material was sand-cast by Magnesium Elektron in rectangular billets of 50x200x200mm. These slabs were then heat treated at 525°C for 16 hours to fully homogenise the microstructure, before machining to size for test specimens (see section 3.2.2).

3.2 Plane Strain Compression (PSC)

When studying the hot deformation of metals there are various techniques available, for example, tensile, torsion, extrusion, axisymmetric compression and plane strain compression testing. All of these techniques have their own benefits and provide useful information about the way in which materials deform under different conditions. This research required a technique that could simulate as closely as possible the stresses experienced during rolling under a range of conditions, and therefore plane strain compression (PSC) was chosen. PSC produces a very similar stress distribution to that found in rolling and thus the microstructural changes experienced here will be mirrored in large scale rolling. By using PSC on small samples it is possible to investigate a much wider range of conditions than would be feasible even by carrying out small, laboratory scale rolling experiments.

3.2.1 History and Equipment

Plane strain compression testing was developed over 50 years ago to provide a method of measuring stress and strain curves for samples under plane strain conditions[204, 205]. The test was designed to give similar deformation conditions to rolling and has been improved over the years to include very precise control systems. A Good Practice Guide[206] was published in 2006 to provide an overview of the technique and the best practices when carrying it out. The Department of Engineering Materials at The University of Sheffield has over 30 years of experience in plane strain compression testing with 2 different machines. The current machine was delivered in 2002 from Servotest Ltd. using specifications based on this long experience. The machine can be used for both plane strain compression and axisymmetric compression and details are given in table 6[205]. The geometry of the specimen and the tools are shown in figure 20 and the entire machine is pictured in figure 21.

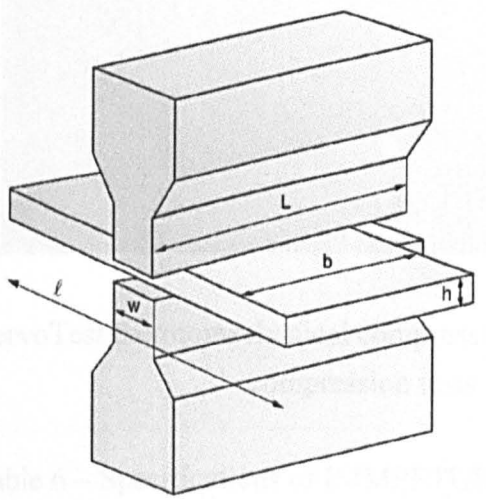

L > 60mm
w = 15mm
l = 60mm
b = 50mm
h = 10mm

Figure 20 – Geometry of standard plane strain compression tests[206]

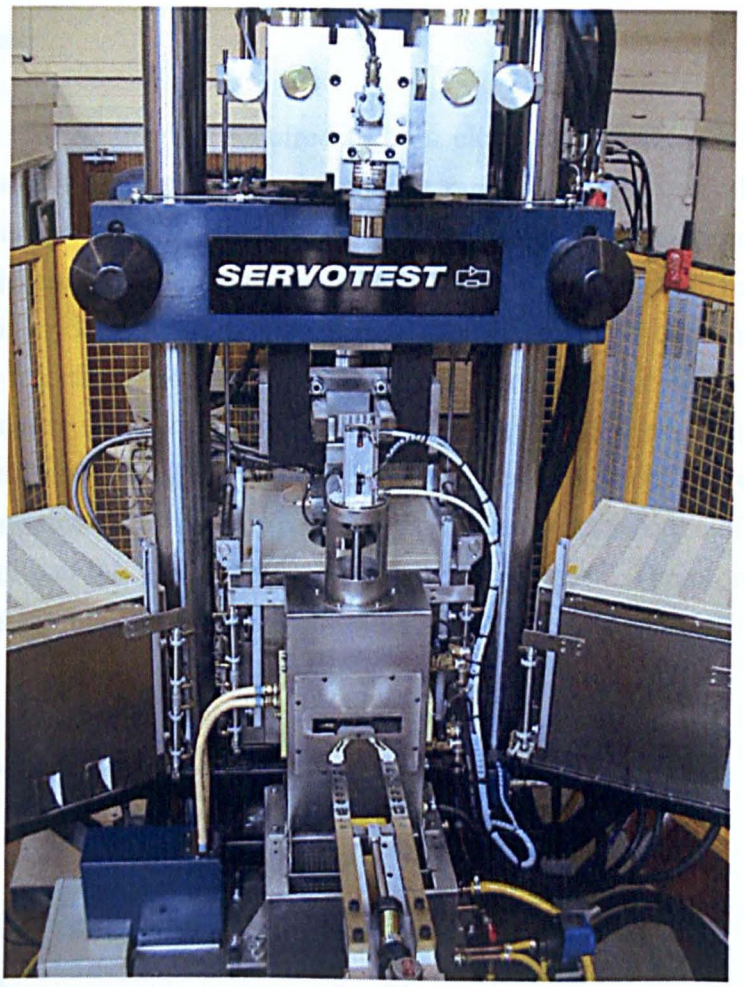

Figure 21 – ServoTest thermomechanical compression machine used for plane strain compression tests

Table 6 – Specifications of IMMPETUS TMC machine[205]

	Machine Characteristics
Actuators	Servo-hydraulic
Max strain	~ 2
Max strain rate	150 – 200 s^{-1}
Max temperature	1200°C
Max load	500kN
Quench	Either air/water cooled/quenched
Controllable variables	Load, displacement
Atmosphere control	None (air)
Temperature measurement	Up to 3 thermocouples in specimen

3.2.2 Specimen

Specimens for PSC testing are required to be a close fit with the robot arms and the deformation tools, whilst providing the correct ratio of length, breadth and height to give the best approximation of plane strain conditions. The maximum load of the machine must be considered when selecting the breadth of the sample to ensure that the machine is able to deform the sample across the full range of conditions and strains expected[206]; therefore, 50mm was chosen for this material. Loveday *et al.* also state in the Good Practice Guide for PSC Testing[206] that a ratio of at least 1.5 is required between the width and height of the deformation zone to 'avoid extremely localised deformation conditions'. However, by increasing this ratio further, the effects of friction between the tool and the specimen become more pronounced. Therefore it is common practice to use a sample 10mm thick with tools 15mm wide.

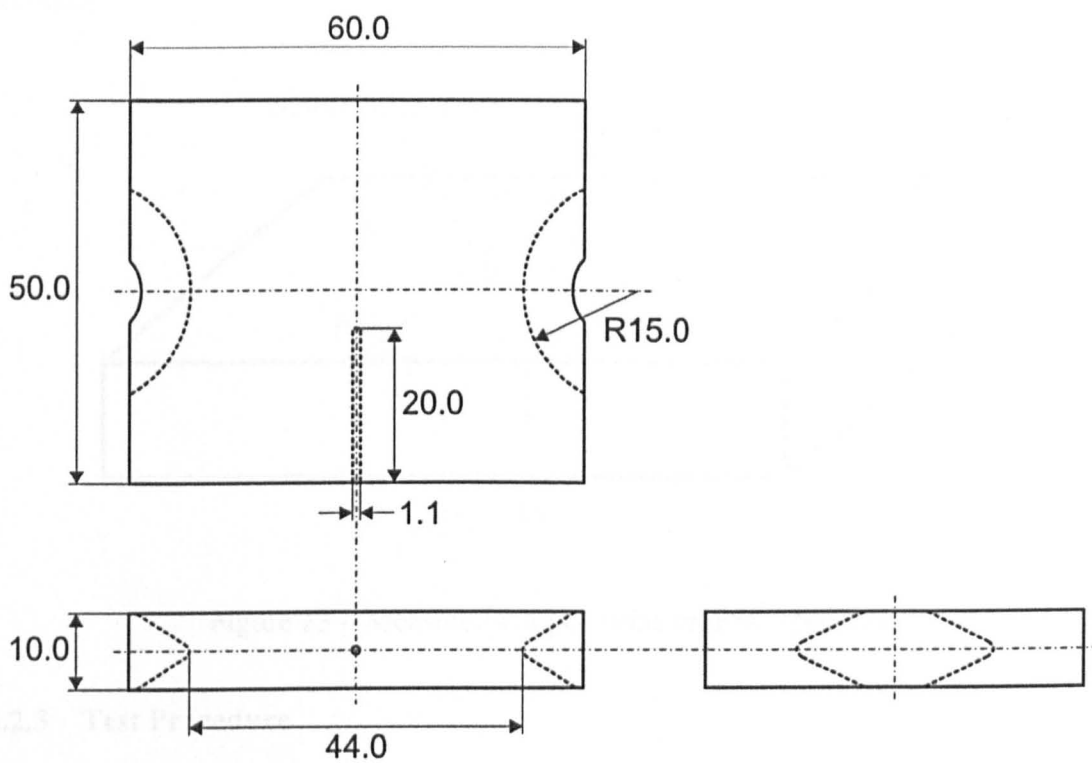

Figure 22 – Plane strain compression sample specifications (all dimensions in mm)

The specimens were received from Magnesium Elektron at the correct size but required further machining to provide grips for the robot arms and a hole for the thermocouple to be fitted. This machining was carried out at Ashmark Engineering to the specifications shown in figure 22. It is possible to use up to 3 thermocouples to study the temperature

variations across the sample during deformation, however in this study it was felt that the only temperature required was that directly in the deformation zone and thus any more than one thermocouple was superfluous. It was decided that the thermocouple should be inserted 20mm into the sample to provide the temperature as close to the centre of the deformation zone as possible, whilst allowing a representative microstructure to be analysed from the centre line.

Both before and after testing it is necessary to measure the height and breadth of the sample. This is carried out in 5 positions for the height and 3 for the breadth, as shown in figure 23, and averages are calculated. On the final measurements of the sample the average breadth is calculated from $(2b_1 + b_2 + b_3)/4$, to account for the curved nature of the deformed specimen (see section 3.2.5 for further details). These measurements are required for calculations of spread and strain, and also to allow the machine to run correctly.

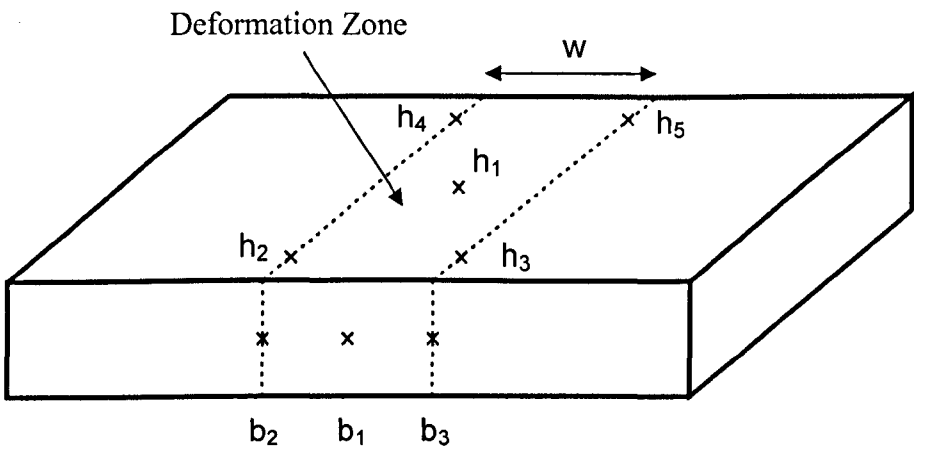

Figure 23 – Measurement positions on PSC specimen

3.2.3 Test Procedure

For the majority of the test procedure, the Good Practice Guide[206] was followed to give a high level of accuracy and repeatability. This section will outline the method used, and give details of any differences from the standard procedure. Most practices are common to all tests so will be covered in section 3.2.3.1, before any variations are mentioned in the following sections.

3.2.3.1 Single Hit Tests

The sample for testing is measured as outlined in section 3.2.2 and the thermocouple is fully inserted. It is placed into the robot arms and coated with a graphite based lubricant to lower any effects of friction and create the best plane strain conditions possible. At the temperatures used here, graphite is the most effective lubricant and the friction coefficient has been experimentally determined as described in section 3.2.3.4. The lubricant is applied to the whole specimen to ensure good coverage over the entire deformation area and also to keep even rates of temperature loss from all surfaces of the sample. The machine is zeroed before every test to guarantee that the displacement reading from the machine is correct.

Once these initial steps have been completed, the specimen and machine are ready for testing. The entire testing procedure is automated and the parameters are programmed into the software before starting, according to the profile shown in figure 24. The first stage of the test is to heat the specimen to the required testing temperature in the Fast Thermal Treatment Unit (FTTU), an induction furnace. The specimen is heated at 2°C/s, about as fast as can be comfortably handled by the FTTU. The sample is held for 5 minutes at the final temperature to allow the temperature to equalize across the material and then it can be taken by the robot arms through to the testing furnace.

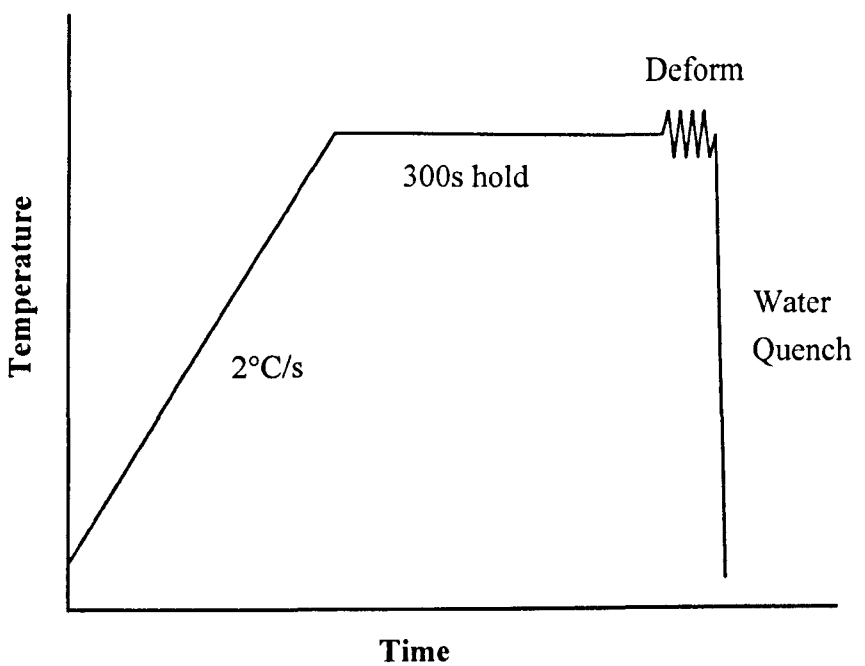

Figure 24 – Plane strain compression testing profile

The testing furnace is held at the same temperature as the material to ensure isothermal tests, and the deformation begins immediately once the specimen is between the platens. The machine is run in displacement control at a constant strain rate and, in the majority of tests, the deformation is stopped when a total equivalent strain of 0.7 is reached.

Immediately following deformation, the robot withdraws the sample from the test furnace and it is quenched down to room temperature in the FTTU to preserve the microstructure for later analysis.

3.2.3.2 Double Hit Tests

A small number of double hit tests were carried out in order to study the behaviour of the material between deformations, the equivalent of the inter-pass hold time in industrial rolling. These tests follow a very similar procedure to that of the single hit tests with the only difference being during the deformation step. For short hold times, generally less than 20-30s, it is possible to leave the sample in the testing furnace and the temperature will not change significantly. For longer holds it is necessary to remove the sample to the FTTU and keep heating to retain the temperature, before taking back to the testing furnace for the second deformation as before. At each temperature tested, a double hit test was carried out with nominally zero hold time. In reality this hold time is approximately 0.2-0.3s due to the time required for the machine to release and then reapply the load. In order to study the microstructure evolution during the hold time, certain tests have also been carried out where the material is held at temperature for the inter-pass time but then quenched to retain this new evolved microstructure.

3.2.3.3 Cold Tools Tests

In order to simulate the feeding of material into cold rolls in an industrial rolling process, two tests were carried out using cold tools. These tests were identical to standard single hit tests except the testing furnace and tools were held at 70°C. This temperature was chosen because it is approximately that reached by the rolls in industry under normal rolling conditions. Both tests were carried out with material heated to 470°C and then deformed at either $0.5s^{-1}$ or $5s^{-1}$ strain rates to allow different amounts of heat loss.

3.2.3.4 Friction Calculation Tests

Three further tests were carried out to assess the friction coefficient. The method used here is similar to that in Alexander[207] and relies on specimens of different thicknesses being tested to the same strains. These tests were carried out at 460°C and $1s^{-1}$ as a representative condition for the entire range. Due to the nature of the friction correction carried out on the raw data (see section 3.2.5), the stress-strain curves from these tests will not be equal unless the friction coefficient used is correct. Therefore, a manual trial and error method is used to find the best fit between the curves and thus the correct coefficient of friction for the conditions studied. This is discussed further in section 4.3.1.4.

3.2.4 Summary of PSC tests carried out

Table 7 – Single hit tests to 0.7 equivalent strain

	$1s^{-1}$	$5s^{-1}$	$10s^{-1}$
380°C	✓	✓	
400°C	✓	✓	✓
420°C	✓	✓	✓
440°C	✓	✓	✓
460°C	✓	✓	✓
480°C	✓	✓	✓
500°C	✓	✓	✓
520°C	✓	✓	✓

Table 8 – Double hit tests

Temperature (°C)	Strain Rate (s^{-1})	Hold time (s)	
		Full double hit	No 2nd hit
420	1	0	0
		300	300
		600	600
500	1	0	0
		5	
		100	100
		300	300

Table 9 – Tests to different strains

Temperature (°C)	Strain Rate (s^{-1})	Strain
460	5	0.1
460	5	0.2
460	5	0.3
460	5	0.5
420	1	1
460	5	1
500	1	1

Table 10 – Other tests

	Temperature (°C)	Strain Rate (s^{-1})	
Cold tools	470	0.5	Test furnace and tools at 70°C. Single hit to total strain of 0.7
	470	5	
Friction Determination Tests	460	1	Height of 5mm
	460	1	Height of 7.5mm
	460	1	Height of 10mm

3.2.5 Processing of Raw Data

During the test a large amount of data is logged at set intervals. For the tests carried out in this work, the vital information is load, displacement, temperature and time, and the frequency of data logging is between 1000 and 10,000 s^{-1}, dependent on strain rate. In order to process the raw data correctly, there are other values that need to be found. These are the initial and final measurements of the sample thickness and breadth (see section 3.2.2), the friction coefficient (see sections 3.2.3.4 and 4.3.1.4), the thermal expansion coefficient and the spread exponent. Two spreadsheets have been developed within IMMPETUS to carry out the processing of this data, and the actions included are summarised in the flowchart in figure 25. The remainder of this section will explain each step in turn.

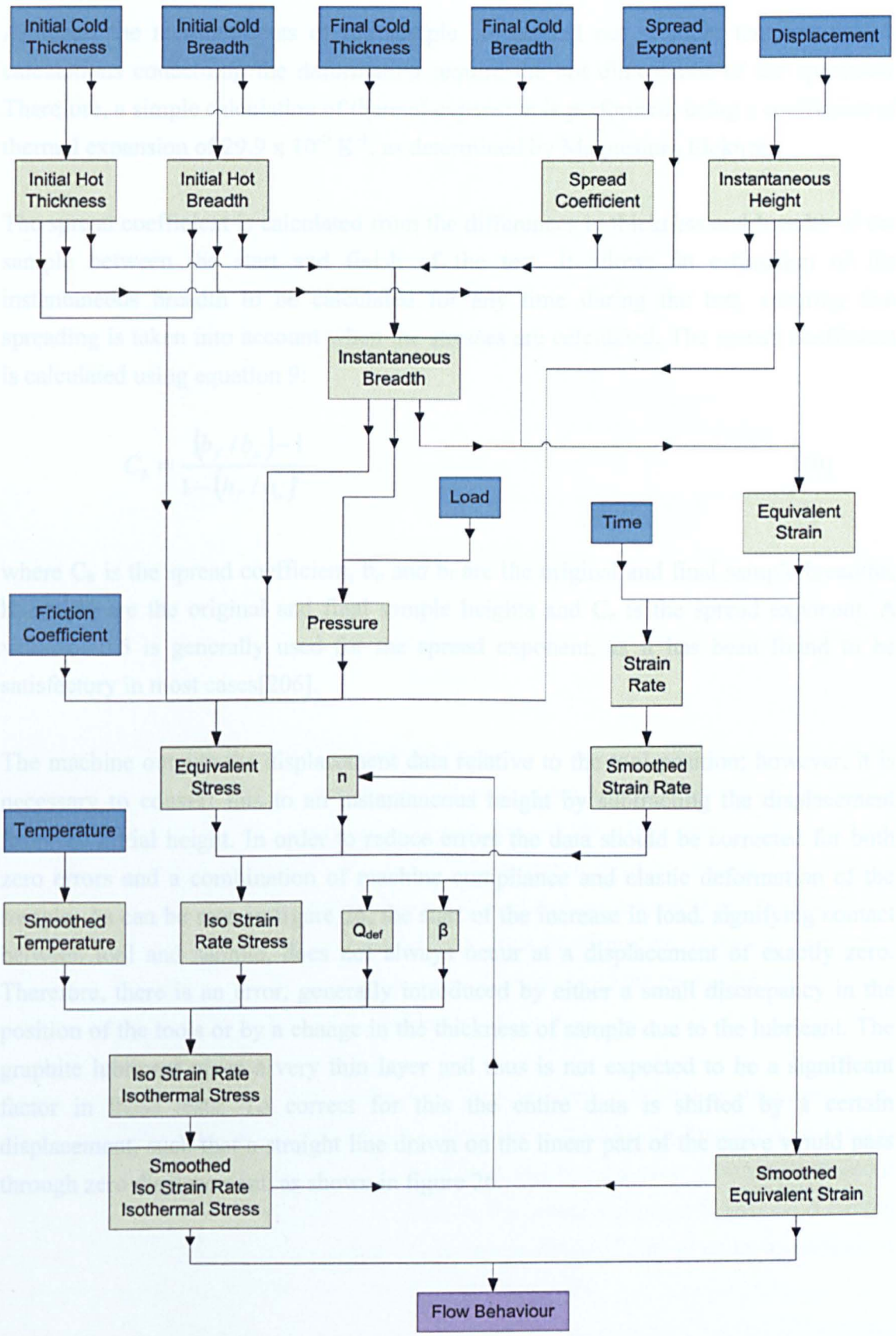

Figure 25 – Flowchart showing how raw data from the TMC machine is processed to give accurate flow behaviour

Although the measurements of the sample are carried out at room temperature, all calculations concerning the deformation require the hot dimensions of the specimen. Therefore, a simple calculation of thermal expansion is performed, using a coefficient of thermal expansion of 29.9 x 10^{-6} K^{-1}, as determined by Magnesium Elektron.

The spread coefficient is calculated from the differences in thickness and breadth of the sample between the start and finish of the test. It allows an estimation of the instantaneous breadth to be calculated for any time during the test, ensuring that spreading is taken into account when the stresses are calculated. The spread coefficient is calculated using equation 9:

$$C_b = \frac{(b_f / b_o) - 1}{1 - (h_f / h_o)^{C_e}} \tag{9}$$

where C_b is the spread coefficient, b_o and b_f are the original and final sample breadths, h_o and h_f are the original and final sample heights and C_e is the spread exponent. A value of 0.5 is generally used for the spread exponent, as it has been found to be satisfactory in most cases[206].

The machine outputs the displacement data relative to the tool position; however, it is necessary to convert this to an instantaneous height by subtracting the displacement from the initial height. In order to reduce errors the data should be corrected for both zero errors and a combination of machine compliance and elastic deformation of the sample. As can be seen in figure 26, the start of the increase in load, signifying contact between tool and sample, does not always occur at a displacement of exactly zero. Therefore, there is an error, generally introduced by either a small discrepancy in the position of the tools or by a change in the thickness of sample due to the lubricant. The graphite lubricant gives a very thin layer and thus is not expected to be a significant factor in these tests. To correct for this the entire data is shifted by a certain displacement, such that a straight line drawn on the linear part of the curve would pass through zero displacement, as shown in figure 26.

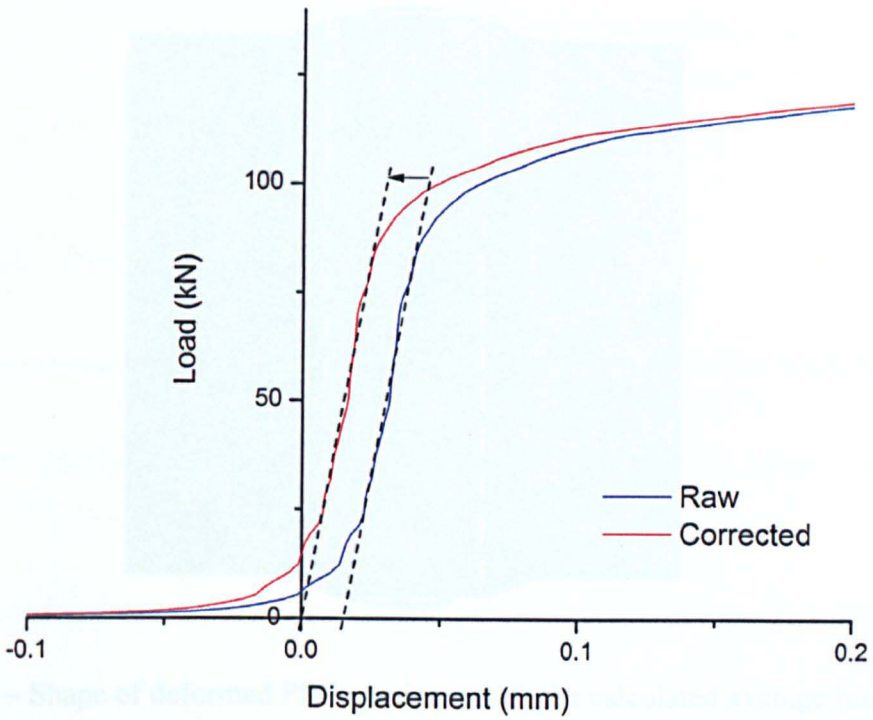

Figure 26 – An example of a load-displacement curve showing the zero correction required

It can also be seen in figure 26 that the early stages of the load-displacement curve are approximately linear and this is due mostly to the compliance of the machine, with a small contribution from elastic deformation in the sample. Only plastic deformation is of interest in these tests and, therefore, this linear region must be removed. To achieve this, the gradient of the compliance region is found and subtracted from the data in this region. The further, plastic, deformation is shifted in displacement by the difference between the final height measurements and maximum machine measured displacement so that the yield point occurs at zero displacement.

As stated previously, the instantaneous breadth is required to allow a correct calculation of pressure and thus stress from the load data. The instantaneous breadth is calculated using the spread coefficient and spread exponent and is a function of the instantaneous height, as given in equation 10. The shape of the actual sample will include a curved section where the spread has occurred. As shown in figure 27, the average breadth gives a rectangle of the same area as the curved physical sample.

Figure 27 – Shape of deformed PSC specimen with the calculated average breadth shown in yellow

$$b = b_o\left[1 + C_b - C_b\left(\frac{h}{h_o}\right)^{C_e}\right] \tag{10}$$

where b is the instantaneous breadth and h is the instantaneous height.

The full details and derivations of equivalent tensile strain are given in the Good Practice Guide and for the plane strain conditions used in this work, whilst still accounting for lateral spread, the calculation used is given in equation 11:

$$\varepsilon = \frac{2}{\sqrt{3}}\left(\varepsilon'^2_2 + \varepsilon'_2\,\varepsilon'_3 + \varepsilon'^2_3\right)^{\frac{1}{2}} \tag{11}$$

where ε is equivalent strain, ε'_2 is given by $\ln(b/b_o)$ and ε'_3 is given by $\ln(h/h_o)$.

The first calculation to be carried out on the load data is to convert the force to a pressure. By using the instantaneous breadth and the width of the platens, an area of contact is found and thus the pressure on the sample can be calculated. Following this, the pressure can be corrected for friction effects and converted to equivalent stress. There are different methods to correct for friction depending on whether the sample is experiencing sticking friction, sliding friction or a combination of the two. This is

detailed in the Good Practice Guide but it has been found that, for the tests carried out in the current work, only sliding friction is ever encountered. Therefore, the shear flow stress (k) can be found from equation 12:

$$\frac{p}{2k} = \frac{1}{bw}\left[\frac{2h^2}{\mu^2} + \frac{(b-w)h}{\mu}\right]\left[e^{\frac{\mu w}{h}} - 1\right] - \frac{2h}{\mu b} \qquad (12)$$

where p is the pressure, w is the width of the platens and μ is the friction coefficient.

The equivalent tensile stress (σ) is calculated from the shear stress as given in equation 13:

$$\sigma = \frac{2k}{f} \qquad (13)$$

where f is a factor found from equation 14:

$$f = \frac{-\varepsilon}{\varepsilon'_3} \qquad (14)$$

The equivalent tensile stress that is calculated here is strongly influenced by changes in both strain rate and temperature during the test. It is preferable to have stress-strain data that is at constant values of strain rate and temperature and thus corrections are required.

To correct for strain rate it is first necessary to calculate accurate values of strain rate through the entirety of the test. This is done with a curve fitting approach, developed by Silk and van der Winden[208], to find the slope of the strain-time graph at all points. A second order polynomial is fitted using the Gauss method to a range stretching 5 data points either side of the point of interest. The derivative of this polynomial gives the strain rate at that point in time. This is a more accurate method than using the raw velocity data that is output from the machine.

It can be seen from figure 28 that there is a large amount of noise in the calculated strain rate. This is due to discrepancies in the displacement measurements being amplified in the calculation process and is not a true material effect. Therefore, it is necessary to use a smoothing function to give a more reliable value of strain rate and the methods described by Tukey[209] have been used here. This method has also been used for noise reduction of the strain and stress values.

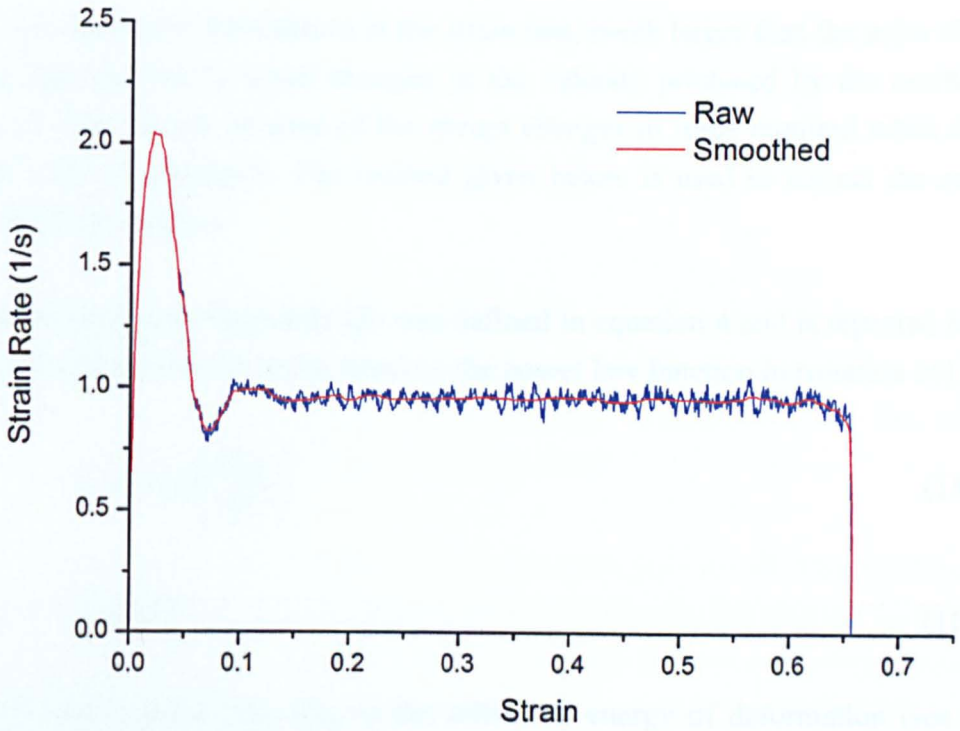

Figure 28 – Plot showing the noise present in strain rate data and the smoothing function used to remove it

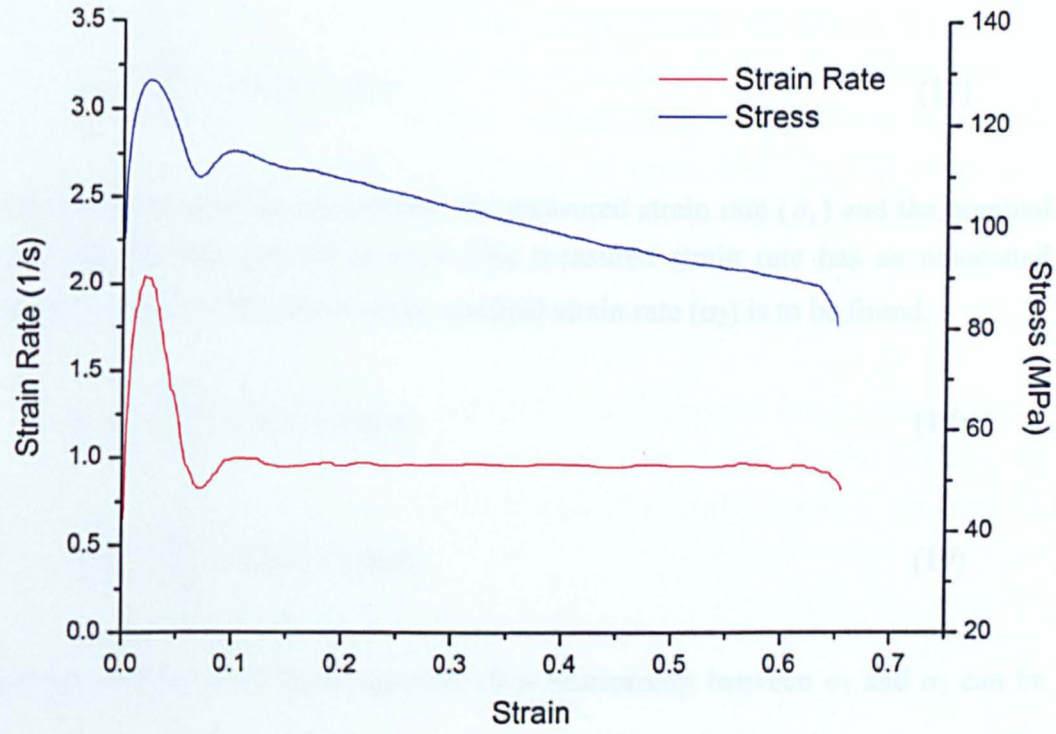

Figure 29 – Plane strain compression flow curve showing the effects of strain rate on the measured stress

There are often other fluctuations in the strain rate, much larger than the noise discussed earlier, that are due to actual changes in the velocity produced by the machine, see figure 29. This occurs because of the abrupt changes in force required when the tools contact with the specimen. The method given below is used to correct the measured stress for these changes.

The Zener Hollomon Parameter (Z) was defined in equation 4 and is repeated below. It can also be approximated to the stress by the power law function in equation 16[197]:

$$Z = \dot{\varepsilon} \exp\left(\frac{Q_{def}}{RT}\right) \tag{15}$$

$$Z = K\sigma^n \tag{16}$$

where $\dot{\varepsilon}$ is the strain rate, Q_{def} is the activation energy of deformation (see section 4.3.1.1 for calculation), R is the universal gas constant, T is the temperature, σ is the stress and K and n are constants that can be found from a plot of ln(Z) against ln(σ) for uncorrected data. By combining equations 15 and 16 and taking natural logarithms, equation 17 is obtained.

$$\ln \dot{\varepsilon} + \frac{Q_{def}}{RT} = \ln K + n \ln \sigma \tag{17}$$

Two values of strain rate are considered, the measured strain rate ($\dot{\varepsilon}_1$) and the nominal strain rate that the test was set at ($\dot{\varepsilon}_2$). The measured strain rate has an associated measured stress (σ_1) and the stress at the nominal strain rate (σ_2) is to be found.

$$\ln \dot{\varepsilon}_1 + \frac{Q_{def}}{RT} = \ln K + n \ln \sigma_1 \tag{18}$$

$$\ln \dot{\varepsilon}_2 + \frac{Q_{def}}{RT} = \ln K + n \ln \sigma_2 \tag{19}$$

By subtracting equation 18 from equation 19 a relationship between σ_1 and σ_2 can be found.

$$\ln \dot{\varepsilon}_2 - \ln \dot{\varepsilon}_1 = n \ln \sigma_2 - n \ln \sigma_1 \tag{20}$$

$$\left(\frac{\dot{\varepsilon}_2}{\dot{\varepsilon}_1}\right)^{\frac{1}{n}} = \frac{\sigma_2}{\sigma_1} \tag{21}$$

$$\sigma_2 = \sigma_1\left(\frac{\dot{\varepsilon}_2}{\dot{\varepsilon}_1}\right)^{\frac{1}{n}} \tag{22}$$

Equation 22 defines the predicted stress at the nominal strain rate in terms of the measured stress, measured and nominal strain rates and the constant 'n'. n is found from the gradient of a ln Z vs ln σ plot and this is calculated in section 4.3.1.2. This strain rate correction is carried out on all stress data for each test.

Another large influence on the final stress is the change in temperature during the test. This is mostly due to deformation heating within the sample, but also can be affected by factors such as cooling through the furnace door and differences between sample and tool temperature. A thermocouple is inserted into the centre of the deformation zone at a distance of 20mm from the front edge of the sample. Therefore, in most tests, the reading from the thermocouple gives a very accurate measure of the temperature of within the deformation zone. In some cases the thermocouple is not in direct contact with the material and there is a delay in the response to the temperature rise. Once a small amount of deformation has occurred, the compression of the sample ensures that the thermocouple is in full contact with the material and thus the temperature is recorded correctly. In order to calculate isothermal flow behaviour, a smooth temperature profile is required over the full range of strain, including that at the very start when the thermocouple may not be in contact with the sample. To estimate the temperature rise over this region, a polynomial is fitted to the latter part of the temperature curve and extrapolated back to the known temperature at the start.

To correct for changes in temperature and obtain an isothermal stress strain curve, a similar technique[197] to that used for strain rate is employed. In this instance an exponential approximation of the Zener-Hollomon Parameter provides the best fit, shown in equation 23.

$$Z = C\exp(\beta\sigma) \tag{23}$$

where C is an empirical constant and σ is the stress. β is a constant that can be found from the gradient of a plot of ln(Z) against σ. Each value of β is only valid at a specific

strain and therefore a function describing how β varies with strain must also be found, see section 4.3.1.3.

By combining equations 15 and 23 and taking natural logarithms, equation 24 is obtained.

$$\ln\dot{\varepsilon} + \frac{Q_{def}}{RT} = \ln C + \beta\sigma \tag{24}$$

Again, two cases are considered, the measured temperature and stress (T_1 and σ_1) and the nominal temperature and stress which is to be found (T_2 and σ_2).

$$\ln\dot{\varepsilon} + \frac{Q_{def}}{RT_1} = \ln C + \beta\sigma_1 \tag{25}$$

$$\ln\dot{\varepsilon} + \frac{Q_{def}}{RT_2} = \ln C + \beta\sigma_2 \tag{26}$$

By subtracting equation 25 from equation 26, a relationship between σ_1 and σ_2 can be found. Equation 27 defines the predicted stress at the intended temperature.

$$\sigma_2 = \sigma_1 + \frac{Q_{def}}{\beta R}\left(\frac{1}{T_2} - \frac{1}{T_1}\right) \tag{27}$$

Following all calculations and corrections a final minor smoothing operation is carried out to remove any noise remaining in the data, and then truly isothermal, iso strain rate, equivalent tensile flow behaviour is produced.

3.3 Finite Element Modelling

Finite element (FE) modelling allows variables to be examined that are often impossible or impractical to study using experimental techniques. For example, it is often useful to know the precise strain and temperature experienced by many different positions within a sample undergoing a complex deformation. These parameters could be studied experimentally, using techniques such as microgrid analysis and multiple thermocouples. However, the required alterations to the samples will always affect the results obtained and the spatial resolution of the distributions is limited by the

techniques themselves. Nowadays, FE modelling has become an accepted and trusted technique to study these types of variations, provided that the data input to the model is reliable.

The stress-strain data used in the FE model was that of the constitutive equations, see section 4.3.3, which were derived from the single hit PSC testing. As explained in section 5.1.3, a slight variation on the standard constitutive equations must be used to ensure that no negative stresses are calculated; therefore, for FE modelling a power law relationship for the 1st stage equations is used. The modelling itself was carried out in collaboration with Dr Krzysztof Muszka, using Abaqus FE modelling software. A 2D cross-section of the PSC test was modelled using explicit coupled temperature-displacement mode, with a deformable meshed testpiece and a rigid analytical tool, as shown in figure 30. The symmetry of the PSC test was used to reduce the area studied by modelling a quarter of the cross-section and applying symmetrical boundary conditions at the bottom and left hand edges. The mesh was made up of rectangular components and adaptive meshing was required to cope with the large shape changes experienced in the testpiece at the corner of the tool. Models were carried out at a variety of temperatures and strain rates to gain an understanding of the variations in strain and temperature across the range of PSC tests carried out.

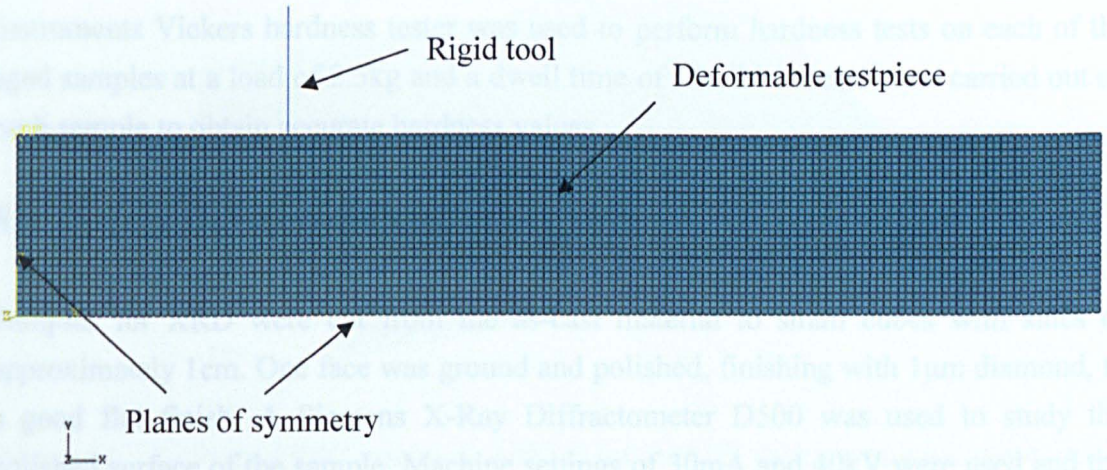

Figure 30 – Diagram showing the model assembly for a PSC test

3.4 Age Hardening

The age hardening studies were carried out in collaboration with Mr Andrew Winder as part of his Masters Degree dissertation[210]. The starting material for age hardening came from PSC tests carried out at 500°C and $1s^{-1}$ to a strain of 0.25 and held for 5 minutes at 500°C before water quenching. This gave almost fully recrystallised material with a homogeneous microstructure over a large area of the samples. The samples were sectioned approximately down the centre line, on the rolling plane, opening up 2 large surfaces that had undergone the same deformation and on which the hardness tests could be carried out. These sections were cut into smaller pieces to allow different heat treatments on each. The samples were heat treated in a muffle furnace at either 250°C or 275°C for a range of ageing times between 1 and 170 hours. No protective atmosphere was used and the temperature was calibrated with an independent thermocouple. Following ageing, the samples were allowed to air cool.

3.4.1 Hardness Testing

Following heat treatment, the faces of the samples to be tested were ground with 1200 grade SiC paper and polished with 6μm diamond paste to ensure any oxide layer had been removed and that the surface was suitably flat for hardness testing. A CV Instruments Vickers hardness tester was used to perform hardness tests on each of the aged samples at a load of 2.5kg and a dwell time of 15s. 20 indents were carried out on each sample to obtain accurate hardness values.

3.5 X-Ray Diffraction (XRD)

Samples for XRD were cut from the as-cast material to small cubes with sides of approximately 1cm. One face was ground and polished, finishing with 1μm diamond, to a good flat finish. A Siemens X-Ray Diffractometer D500 was used to study the polished surface of the sample. Machine settings of 30mA and 40kV were used and the detector was set to read from 5° to 80° at 2°/min with a 0.02° step size. Once XRD has been carried out, the Bragg law, given in equation 28, can be used to calculate the lattice spacings.

$$\lambda = 2d\sin\theta \tag{28}$$

where λ is the wavelength of the x-rays, d is the lattice spacing and θ is the angle of reflection.

3.6 Sample Preparation for Microscopy

3.6.1 Sectioning and Grinding

Initial cuts were made on the samples with a manually operated Buehler Abrasimet abrasive saw. This was used to remove the shoulders of the sample but could not be used for cuts near to the area needed for microscopy as the Abrasimet was too aggressive and more precision was required. For the cuts within the deformation zone a Struers Accutom, an automatic precision abrasive saw, was used. In general, samples were cut to a size of 30 x 10 x 5mm for use in EBSD and were cut such that the transverse plane in the deformation zone could be studied, see figure 31 and figure 32. A small number of studies were also carried out on the rolling plane.

Once cut to size, the samples were ground to a flat surface using standard grinding wheels and silicon carbide paper, finishing on 1200 grade paper.

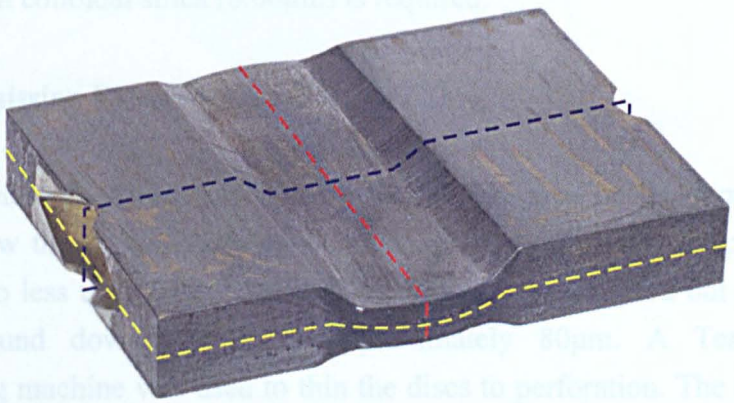

Figure 31 – Deformed PSC specimen with planes marked: yellow = normal plane, red = rolling plane and blue = transverse plane

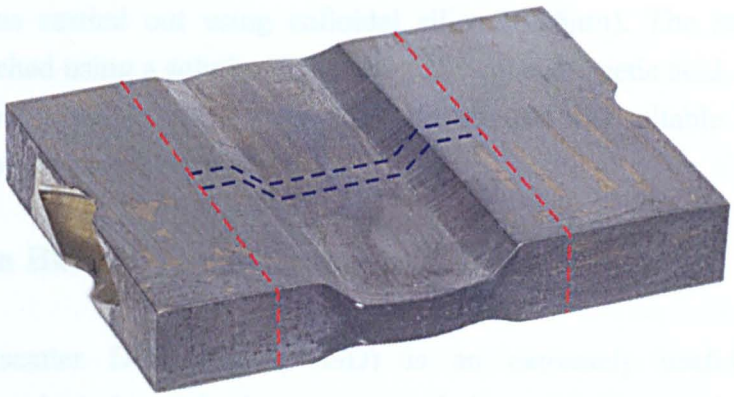

Figure 32 – Deformed PSC specimen showing locations of initial (red) and precision (blue) cuts for most microscopy samples

3.6.2 Electron Backscatter Diffraction (EBSD)

For EBSD to be successful and accurate, the surface finish of the sample must be very flat and smooth. To achieve this it is necessary to take the ground samples and polish at 6μm diamond and then 1μm diamond. This was carried out manually on standard polishing wheels, using a water based lubricant. Following the diamond polishing, a final polish with colloidal silica (0.06μm) is required.

3.6.3 Transmission Electron Microscopy (TEM)

Transmission electron microscopy (TEM) requires an area on the sample that is thin enough to allow the transmission of electrons. A section of the sample is taken and ground down to less than 1 mm. 3mm diameter discs are punched out of the strip and these are ground down further to approximately 80μm. A Tenupol twin jet electropolishing machine was used to thin the discs to perforation. The electrolyte used was a 185ml methanol, 35ml butoxyethanol, 1.94g Lithium Chloride and 4.09g Magnesium Perchlorate solution, based on that from He *et al.*[22], and was cooled to -45°C with liquid nitrogen. A current of 30mA gave good quality polishing with a reasonably large thin area for investigation.

3.6.4 Optical Microscopy

Samples for optical microscopy were polished with 6μm and then 1μm diamond paste to provide a flat, clean surface. Before etching, to reveal the underlying microstructure, a

final polish was carried out using colloidal silica (0.06μm). The sample was then immediately etched using a solution containing 20% glacial acetic acid, 20% picric acid and 60% ethanol. Etching was stopped when the sample was suitable for microscopy, normally after approximately 10-15s.

3.7 Electron Backscatter Diffraction (EBSD)

Electron Backscatter Diffraction (EBSD) is an extremely useful technique to characterise the orientation and microstructure of a material. By carrying out an EBSD map, information is gained on the overall texture, the orientation and changes in orientation across individual grains, and disorientation across grain boundaries. The maps also give the overall microstructure and thus the orientation data can be related to this.

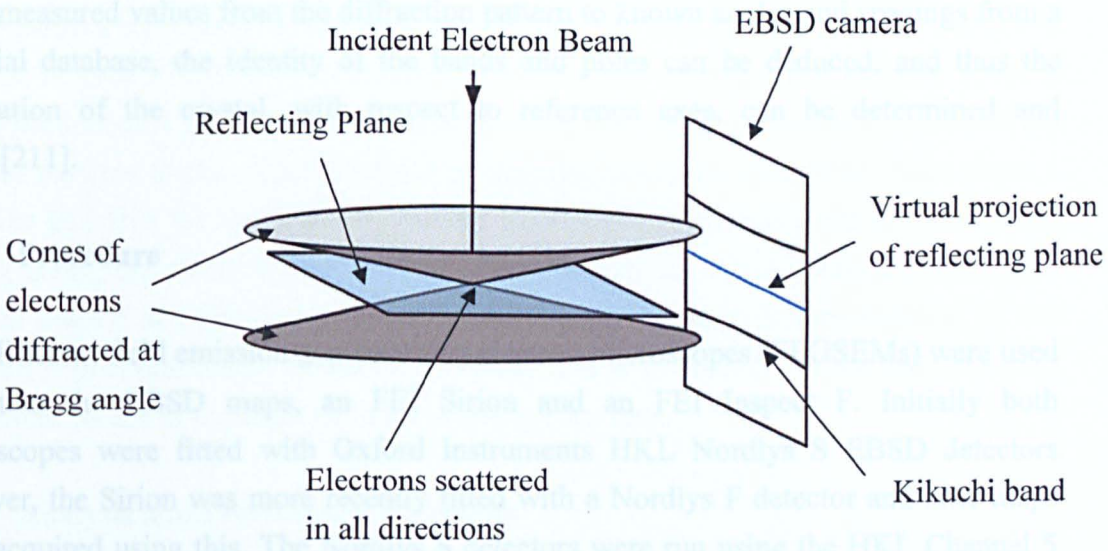

Figure 33 – Diagram showing the production of Kikuchi bands

EBSD works by focussing an electron beam in a Scanning Electron Microscope (SEM) onto a specific point on a sample. At the point at which the electron beam interacts with the sample, the electrons are scattered in all directions. Therefore, there will be electrons travelling in such a direction that they are at the Bragg angle for every set of lattice planes in the structure and will be diffracted accordingly[211]. This produces a higher intensity of electrons in these directions, which form the surfaces of two symmetrical cones radiating out from the point of interaction. The part of the cones that are diffracted back out of the material and fall on the camera used for EBSD are recorded

and form a Kikuchi pattern unique to the specific orientation of the material, see figure 33. Due to the wavelength of the electrons used and the lattice spacings in most crystals, the Bragg angle is very low (of the order of 0.5°) and thus the cones of diffracted electrons produced are close together and, at the point at which they fall on the camera, can be considered as parallel lines[211].

Once the camera has recorded the Kikuchi pattern, the software can automatically index it to give the orientation of that particular point. The first step in the indexing process is for the software to find the Kikuchi bands in the pattern. This is achieved by using the Hough transform to integrate the intensity of all possible lines in the image into single points of data, in which peaks can be correlated back to the position of Kikuchi bands in the pattern[211]. From this is it possible to measure the distance between the parallel lines, a parameter dependent on the lattice spacing, and the angles between the Kikuchi bands, which is directly related to the interplanar angles in the crystal. By comparing these measured values from the diffraction pattern to known angles and spacings from a material database, the identity of the bands and poles can be deduced, and thus the orientation of the crystal, with respect to reference axes, can be determined and stored[211].

3.7.1 Procedure

Two different field emission gun scanning electron microscopes (FEGSEMs) were used to obtain the EBSD maps, an FEI Sirion and an FEI Inspect F. Initially both microscopes were fitted with Oxford Instruments HKL Nordlys S EBSD detectors however, the Sirion was more recently fitted with a Nordlys F detector and later maps were acquired using this. The Nordlys S detectors were run using the HKL Channel 5 Flamenco software, while data from the Nordlys F was acquired with HKL Fast Acquisition software.

All three systems that have been used have given good, accurate and reliable results. As can be seen in table 11, the major advantage of the Sirion with the Nordlys F is the speed of acquisition. Therefore, more data can be obtained in a shorter time, and consequently more samples can be studied. One advantage of the Inspect F has been a wider field of view as this gives the possibility of a larger map without having to carry out a matrix of jobs by moving the stage between each one.

Table 11 – Parameters used with different equipment

	Sirion		Inspect F
	Nordlys S	Nordlys F	Nordlys S
Magnification	200x	200x	200x
Beam Voltage	20	20	15
Spot Size	4	4	5
Camera Binning	8x8	4x4	4x4
No. averaged frames	3-7	-	3-7
Rate of acquisition	~ 3-12 s^{-1}	~ 10-50 s^{-1}	~ 3-12 s^{-1}

To carry out an EBSD run, the polished sample is put into the SEM and all alignments are carried out on the microscope. The sample is then tilted to 70° relative to the electron beam to ensure the highest possible signal reaches the EBSD camera. When the EBSD camera has been inserted into the chamber, the exposure time on the camera is adjusted to give a high level of contrast without being saturated and Kikuchi patterns can be produced. A calibration is required to allow the acquisition software to match the Kikuchi patterns to the stored database of material constants. Following these steps, a step size and area for the map are decided upon and an automatic run can be started. During a run, the electron beam rasters across the surface of the sample producing a Kikuchi pattern at every point on the defined grid, which is in turn indexed by the software to give orientation data for each point. This is downloaded at the end of the run and further pieces of software are used to analyse the data.

3.7.2 Analysis and Presentation of Results

Electron Backscatter Diffraction provides certain information on each point that is studied within the scan. This includes information such as phase, band contrast and band slope, although the information that is useful in this work is the orientation data, given by the three Euler angles: phi 1 (φ_1), Phi (Φ) and phi 2 (φ_2). The different ways to display this data are explained below. Oxford Instruments HKL Channel 5 software was used for standard analysis and proprietary software has been developed to carry out more complex analysis.

3.7.2.1 Standard EBSD Mapping

The standard EBSD maps are the usual place to start when analysing EBSD data. These maps show the overall microstructure and use different colours to distinguish between different orientations. Abrupt changes in orientation, caused by grain boundaries, can be found and emphasised by the use of further colours and lines, see figure 34 showing a typical EBSD map.

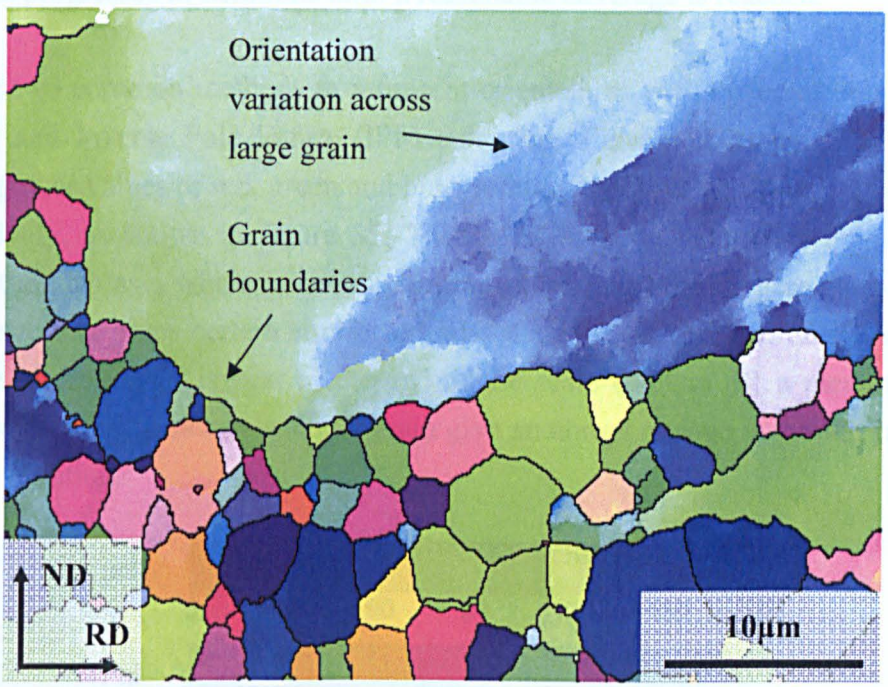

Figure 34 – Typical EBSD map using Inverse Pole Figure (IPF) colouring

Before using any of the data further it is necessary to clean out any misindexed points and to interpolate to fill in any gaps that were not indexed during the run. These mis- and non-indexed points occur due to small inconsistencies on the surface of the sample from either contamination or roughness. These inconsistencies create a lower quality Kikuchi pattern and thus the software often struggles to carry out the indexing procedure as described in section 3.7. Generally misindexed points occur when there is a poor pattern, on which it is harder to exactly define the positions of the Kikuchi bands, and thus the orientation that is fitted to the pattern is incorrect. Non-indexed points often occur when it is impossible to find enough clearly defined bands within the pattern to allow indexing.

To clean these inconsistencies in the maps it is necessary to carry out a number of standard steps in the Channel 5 Tango software. Initially, the map is analysed for all pixels where the orientation is significantly different from all surrounding pixels. These are known as 'wild spikes' and are simply removed from the map. Following this, a manual search of the map is carried out and any further, larger areas of misindexing are identified and removed. Then an interpolation technique can be used to complete any small regions of non-indexed points by using an average of those points surrounding them. This progresses in iterations until a reasonable coverage is reached.

There are two common methods to represent orientations with different colours: Euler colouring and Inverse Pole Figure (IPF) colouring. Euler colouring is calculated by adding together values of red, green and blue, relating to the values of phi 1, Phi and phi 2 respectively, as shown in figure 35. This gives every orientation a unique colour, although the map as a whole is not as intuitive as other systems. There is also a wrap-around issue that gives certain similar orientations very different colours. This occurs when one of the angles is near to the end of the scale and can often mean that small orientation differences across a single grain give an abrupt change in colour, rather than a gradual variation.

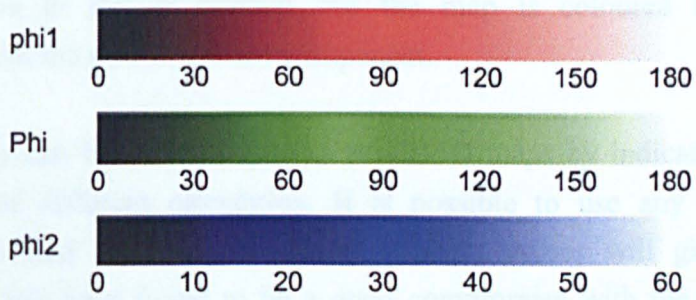

Figure 35 – Scheme used for Euler colouring in hexagonal materials

Inverse pole figure colouring relates the orientation of the material to a single sample direction. In this work the normal direction has been used as the reference direction and, by referring to figure 36, it can be seen that the map will be coloured red if the [0001] direction is parallel to the normal direction or blue if the $[01\bar{1}0]$ direction is parallel to the normal direction. This is a much more intuitive way of displaying the data; however, as only one sample direction is used, the colouring system does not contain the full orientation information. For example, a pixel coloured red will have the c-axis of the crystal aligned with the normal direction, but any rotation around this axis will have exactly the same colouring. Despite these shortcomings, IPF colouring has been used

for the majority of this work as it is often simply the orientation of the c-axis that is the orientation of interest.

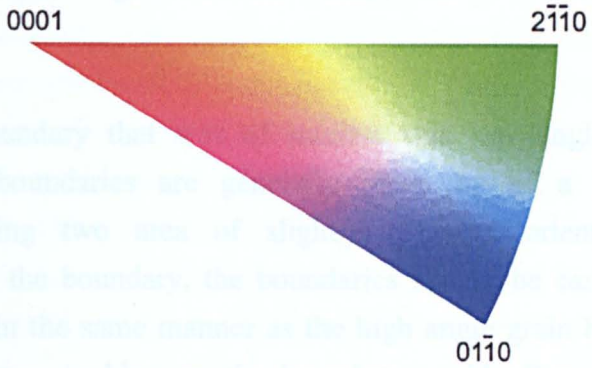

Figure 36 – Scheme used for inverse pole figure colouring in hexagonal materials

Another colour scheme that has been used for a smaller number of maps is texture component mapping. Often a particular texture is prevalent in a sample and it can be useful to display which areas of the microstructure have that texture, and how closely they are aligned to it. To plot this, the texture is defined in terms of a specific crystallographic direction being parallel to a specific sample direction. A maximum angular deviation to this is defined and the map is coloured according to the disorientation from the perfect texture component.

Grain boundaries can be easily displayed on EBSD maps by indicating the boundary between areas of different orientation. It is possible to use any value of critical disorientation to find the boundaries and different values will give more or less boundaries. 10° has been found to be a good compromise with the current materials studied to select a very high fraction of the correct boundaries and a very low fraction of incorrect boundaries.

In the same way that grain boundaries can be identified and plotted by the Channel 5 software, twin boundaries can also be analysed. As stated in section 2.3.5, the twin systems commonly found in magnesium alloys are $\{10\bar{1}2\}$ twins but there can also be $\{10\bar{1}1\}$ and $\{10\bar{1}3\}$ twins present. It has been shown by Nave and Barnett[76] that as well as twin-matrix boundaries, there can also be various twin-twin boundaries present in the material. To identify these various types of twin boundary, the defining features of disorientation axis and angle are used, as listed in table 3 and table 4. Channel 5 is able to calculate the axis and angle of disorientation for each boundary and thus each

type of twin can be identified and marked on the map with a specific colour. Not all twins correspond exactly to the perfect disorientation axis and angle listed in table 3 and table 4 and therefore, a range of 5° difference is used when identifying the twin boundaries.

Another type of boundary that was of interest was low angle cell and subgrain boundaries. These boundaries are generally made up of a tangled network of dislocations separating two area of slightly different orientation. Due to the disorientation across the boundary, the boundaries should be easily identified by the Channel 5 software in the same manner as the high angle grain boundaries; however, the dislocation structure making up the boundary could often cause the change in disorientation to occur over a wider band than the step size of the maps, and consequently give a sequence of small changes in disorientation between neighbouring pixels rather than the abrupt, definite line that would be easier to understand. Due to variations in the width and disorientation of subgrain boundaries, a specific value of disorientation could not be defined to distinguish between a subgrain boundary and other partially recovered substructure. Therefore, a selection of disorientation angles were used to produce a number of maps, and an attempt was made to estimate the true substructure. This procedure is described in more detail in section 4.4.4.1.

3.7.2.2 Pole Figures and ODFs

The texture of a material is commonly displayed using either pole figures or orientation distribution functions (ODFs). More than one pole figure is generally required to truly display all the information about the texture of a material, whereas a single ODF can contain all of the information required; however, the ODF is a three dimensional depiction and thus can only be displayed as a sequence of sections. The great advantage of using pole figures is that they are more directly related to the orientation of the actual crystals and thus are easier to understand. Textures in magnesium, and many other hcp materials, are often purely related to the orientation of the c-axis of the crystals, with a mostly random distribution for the directions of the other principal axes; therefore, a single pole figure, depicting the 0002 pole, generally contains all of the information required to evaluate the texture of magnesium. In the remainder of this work pole figures have been used to display the textures obtained from EBSD analysis.

Figure 16[162] shows the construction of a pole figure and how it displays the orientation of a specific crystal direction with relation to the sample axes. Pole figures

were produced by the Channel 5 Mambo software from EBSD maps and contoured using a half width of 10° and data clustering of 3°. For most texture analysis, an EBSD map of over 3x3mm area was used to ensure a large number of grains were captured and that the resulting texture was statistically valid. Unfortunately this was not possible in all cases, and has been discussed in more detail in the relevant sections. For material tested in PSC, pole figures have the normal direction in the centre of the figure and the rolling and transverse directions on the vertical and horizontal axes respectively. In most cases the 0002, $10\bar{1}0$ and $11\bar{2}0$ pole figures are displayed to give the full information about the texture of the material, although in certain cases a simple comparison between 0002 pole figures has been used, as this contained all of the useful information.

3.7.2.3 Further EBSD Data Analysis

With standard EBSD software, in this case Oxford Instruments HKL Channel 5, certain microstructural features cannot be studied fully in hcp materials. The current work required a deeper study of recrystallisation behaviour and the variation in Schmid factors across the microstructure, as well as the relationship between the two. A method of carrying out slip trace analysis was also required. For these analyses it was necessary to develop new software to allow the required calculations to be carried out. This new program was developed out of some proprietary software, already developed within the IMMPETUS research group for studies on titanium, retaining much of the original code[212]. Descriptions of the calculations will be given in the following sections.

3.7.2.3.1 Grain Determination

The first step for most of the subsequent calculations is to determine which pixels belong to which grains, as well as the position of the grain boundaries in the microstructure. Each grain is given a unique number that is stored and can be referred to in later calculations.

Initially a disorientation map is calculated by measuring the disorientation between neighbouring pixels. It is only necessary to calculate the disorientation with the pixel to the right and the pixel below for each point in the map and these angles are stored for each pixel. A critical disorientation is chosen for the grain boundaries (in this work, generally 10° is used) and any pixels with a disorientation greater than this for the

neighbour either to the right or below can be given a defining colour to visually show the grain boundaries.

To define which pixels are part of which grains, a set of simple iterations is used. The top left pixel is studied first and if it is a correctly indexed point it is assigned the grain number of 1. Then the pixels neighbouring the point are examined and if the disorientation between them and the starting point are less than the critical value they are assigned the same grain number. This process continues on each newly assigned point within the grain, slowly expanding the grain until it impinges on grain boundaries in all directions. Following this, a new point in the map is found, that has not yet been assigned a grain number, and the iterations start again, marking everything as grain number 2. This continues until all points in the map have been assigned a grain number and the grain file is complete for use in further calculations.

3.7.2.3.2 Recrystallisation Analysis

The method for identifying recrystallised grains in this analysis is relatively crude but has been used for speed of calculation. The disorientation within a grain is used to categorise those that have undergone recrystallisation from those that have not. To calculate this, the average orientation over the entire grain is found and the disorientation between this and each pixel within the grain is calculated. To calculate the average orientation of each grain, a quaternion method is used as described by Davies[212], to give the most accurate values. When any point gives a disorientation greater than a critical value, the grain is marked as a non-recrystallised grain and the software moves on to the next grain. If all points are found to have a lower disorientation than the critical value then the grain is marked as a recrystallised grain. Uncertainty is introduced in the case of dynamic recrystallisation, where the dynamically recrystallised grains have the opportunity to undergo further deformation and disorientations will subsequently arise. There is also noise inherent in the orientation data that will create false disorientations across a grain. Therefore, a cut-off value of disorientation must be found that takes these factors into account and in the current work, 3° has been used as it provides the most accurate results. Following the automatic grain selections, a manual method can be used to alter any grains where the shape or size makes it clear that the software is incorrect.

Once the recrystallised grains have been identified, the data can be analysed to find the fraction of recrystallised material and the grain sizes for the recrystallised grains. The

fraction of recrystallisation is simply found from the number of pixels in recrystallised grains divided by the total number of correctly indexed pixels. Grain areas can be found by counting the number of pixels making up the grain and multiplying by the area of each pixel. The diameter is estimated by assuming the cross section of the grain is a perfect circle containing the area found from the number of pixels. Thus the diameter is given by equation 29:

$$Diameter = 2 \times \sqrt{\frac{Area}{\pi}} \tag{29}$$

Both the distribution and average diameter are calculated and output from the program for further analysis.

Further analysis of the data can be carried out in an attempt to correlate the quantity of recrystallised grains with the type of boundaries on which they form. Two different methods have been used to quantify the amount of recrystallisation that has occurred, although both start with the same principles. In order to distinguish which boundaries originally existed, and have subsequently undergone recrystallisation, the original grain structure must be reconstructed. To do this simply and efficiently, the non-recrystallised grains are expanded in turn by one pixel at a time until they impinge upon each other, and thus the boundaries that now exist are taken to be the original ones, and the disorientation across it is calculated as the defining feature.

The first method of quantifying the amount of recrystallisation is to use the fraction of the boundary that has undergone recrystallisation. The program has been developed to group boundaries by disorientation and plot the frequency of recrystallisation along the total length of these boundaries. The second method gives an area of recrystallised material per unit length of each class of grain boundary. For each pixel within a recrystallised grain, the program finds the closest reconstructed boundary and counts that pixel as having recrystallised from there. The length of the grain boundaries in each class are measured by counting the number of pixels that make them up. There is an error introduced in the length measurements because the EBSD maps are carried out on a square grid. As shown in figure 37, the difference in the measured length of horizontal or vertical lines compared to diagonal lines can be significant. If it is assumed that there is an even distribution in the angles of grain boundaries then the error inherent in this method can be found by considering a circle. As shown in figure 38, the perimeter of a circle, when measured using horizontal and vertical lines, is 8r (where r is the radius of

the circle). The true circumference of a circle is $2\pi r$, and therefore the error caused by this method is $8/2\pi$, which is equal to 127%. Taking this into account within the program allows the correct length of line to be more accurately calculated. The amount of recrystallisation per unit length of boundary is therefore the area counted previously divided by the length of the boundaries.

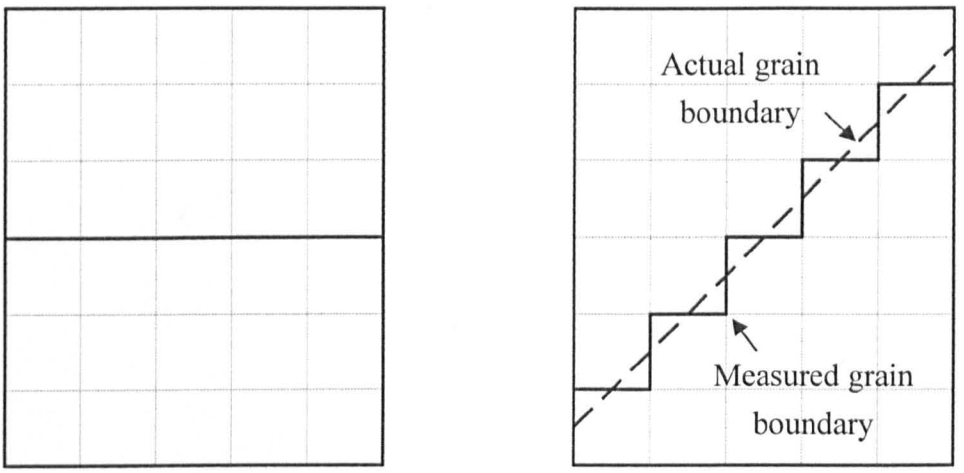

Horizontal Grain Boundary
Actual length of boundary = 5px
Measured length of boundary = 5px

Diagonal Grain Boundary
Actual length of boundary = 7.1px
Measured length of boundary = 9px

Figure 37 – Example of errors introduced by measurement of diagonal grain boundaries

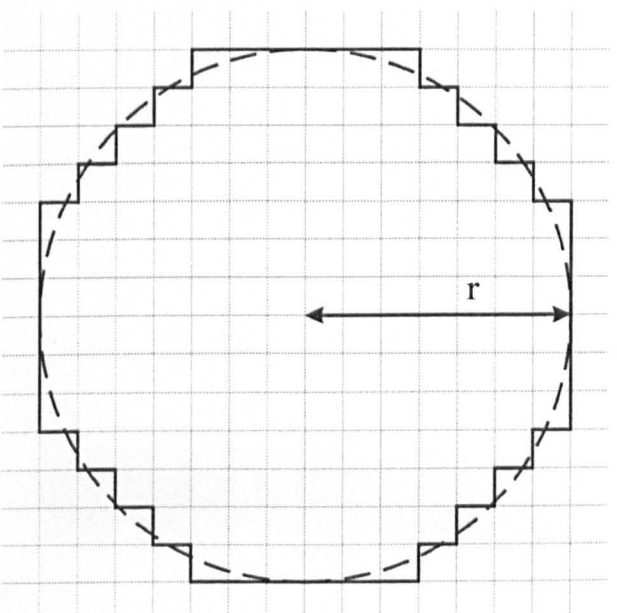

Figure 38 – Diagram showing the different circumference obtained when measuring a circle using horizontal and vertical lines

3.7.2.3.3 Schmid Factor Analysis

The Schmid factor of a particular grain gives a very useful indication of the ease with which it will deform under specific loading conditions, see section 2.3.4.1. Therefore, when an EBSD map of a partly deformed sample is coloured according to the Schmid factor, it will give a good indication as to which grains are currently undergoing the largest strains and which are less conducive to deformation. Then it is possible to see if there is any correlation with other microstructural features, such as areas of recrystallisation.

As discussed in section 2.3.4.1, to easily calculate the Schmid Factor for plane strain compression it is necessary to assume conditions of plane stress along the same axes as strain, as shown in figure 6. Therefore, the calculation required is a modified version of the standard Schmid Factor and is given in equation 30:

$$Schmid\ Factor = \cos\alpha_1 \cos\beta_1 + \cos\alpha_2 \cos\beta_2 \qquad (30)$$

Each half of the equation can have a maximum value of 0.5 and thus the total range of Schmid Factors in plane strain compression is from 0 to 1.

The program can give an average Schmid factor for the entire map, the recrystallised grains or the non-recrystallised grains, simply calculated as the average of every pixel in the required set. To find any correlation between the Schmid factor and the level of recrystallisation, a method similar to that used in the boundary disorientation and recrystallisation analysis is used. This calculates the frequency of each grain boundary that has recrystallised and plots the results with respect to the Schmid factor of that grain.

The Schmid factor colouring of EBSD maps is carried out according to the key in figure 39.

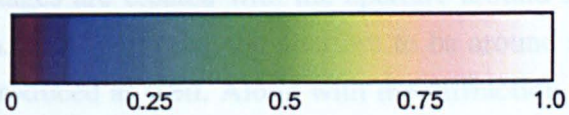

Figure 39 – Colour scheme used for Schmid factor EBSD maps

3.7.2.3.4 Slip Trace Analysis

If slip traces are visible in an EBSD map, as straight lines across a grain, then it is possible to deduce the plane on which they are formed, and thus the active slip systems within a particular grain. The code used to carry out the slip trace analysis was entirely developed by Davies[212]. A point on a slip band is selected and the program is used to calculate the traces that a particular family of planes make with the sample surface at this orientation. These are then drawn onto the EBSD map and the process is repeated for each common family of slip planes, for example in the case of hcp magnesium, $\{0001\}$, $\{10\bar{1}0\}$, $\{10\bar{1}1\}$ and $\{11\bar{2}2\}$. After all possible traces have been plotted and compared with the slip line, the closest fitting trace is taken to be the plane on which slip has occurred.

3.8 Transmission Electron Microscopy

Transmission Electron Microscopy (TEM) is useful because it allows the examination of features within the microstructure at an even smaller scale than is possible in the SEM. Similarly to EBSD it also allows orientation data to be found and related to the microstructure. Relatively little TEM was used in the current work because EBSD was found to give much of the same useful information but with a faster and simpler method. Therefore, TEM was only used for a small number of studies on features that it was impossible to study with EBSD.

3.8.1 Procedure

An FEI Tecnai 20 was used, as detailed in table 12. The initial steps in TEM are to find an area of suitably thin material that can be studied. If the sample preparation is carried out correctly then there should be a reasonably large area around the perforation in the centre of the sample. Once this area has been obtained and the microscope has been correctly aligned then the process of obtaining images and diffraction patterns can begin. Bright field images are created with the aperture around the transmitted spot in the diffraction pattern, and by moving the aperture to be around a diffracted spot, dark field images can be produced as well. Along with the diffraction patterns, this provides a large scope to study a variety of different features.

Table 12 – Details of the FEI Tecnai 20

Filament	LaB_6 for early work Tungsten for later work
Operating Voltage	200kV
TEM Point Resolution	0.24nm
Magnification Range	25 to 1,030,000
Camera Length	30 to 4500 mm
Maximum Tilt Angle	40°

3.9 Optical microscopy

Optical microscopy was carried out on a MET Polyvar microscope and images were taken at various magnifications to study the microstructure and grain size. The manual linear intercept method was used to analyse the grain size, using 12 lines of 1286μm on each micrograph.

4. Results

4.1 Initial Material Characteristics

4.1.1 Microstructure

Figure 40 shows the microstructure of the as-received material before any deformation was carried out. It can be seen that the grains are approximately equiaxed and the average grain size was calculated as approximately 108 ± 10μm. There were no grains that showed any significant levels of substructure or rotation across the grain and therefore, the dislocation density was relatively low. It can be assumed that the microstructure at the start of deformation in all tests was the same as that shown here.

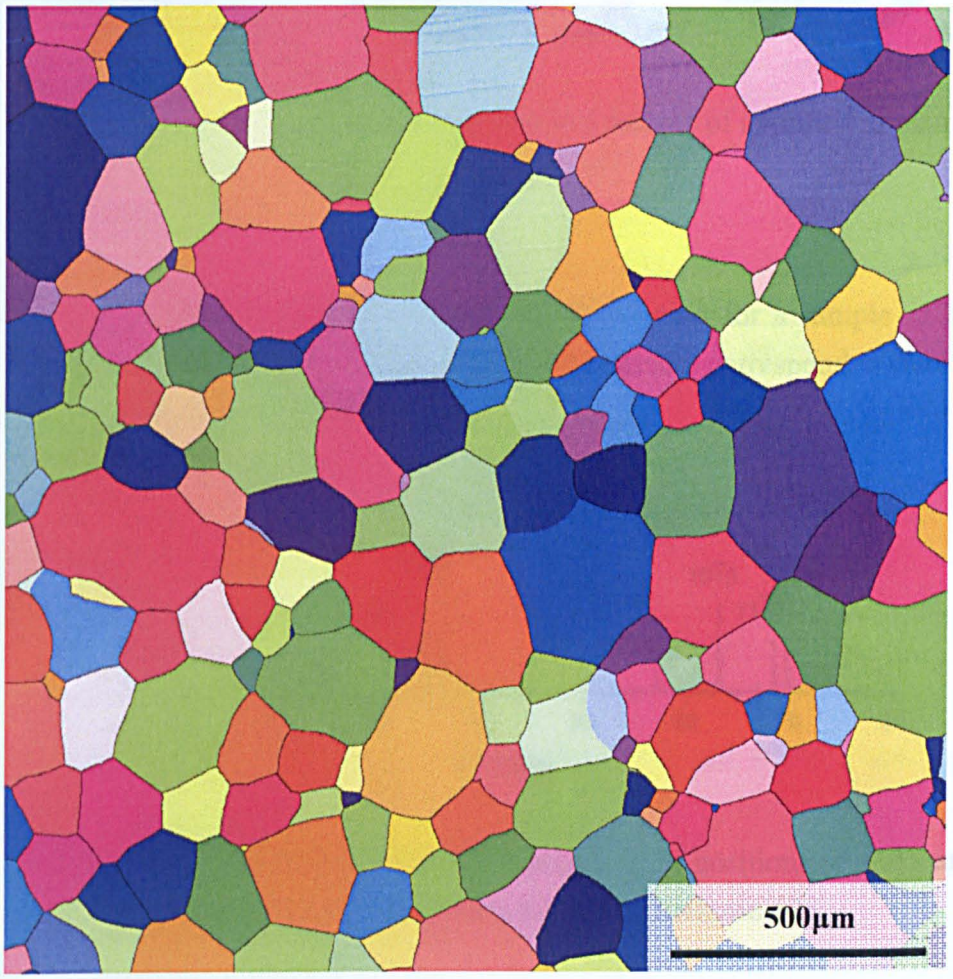

Figure 40 – EBSD map (IPF colouring) showing the as-received material

4.1.2 Texture

Figure 41 shows the texture in the as-received material. The peaks seen in these pole figures are due to the large individual grains and ideally a larger sample area would be used to reduce this effect. Nevertheless, it can be seen that the initial texture of the material was random.

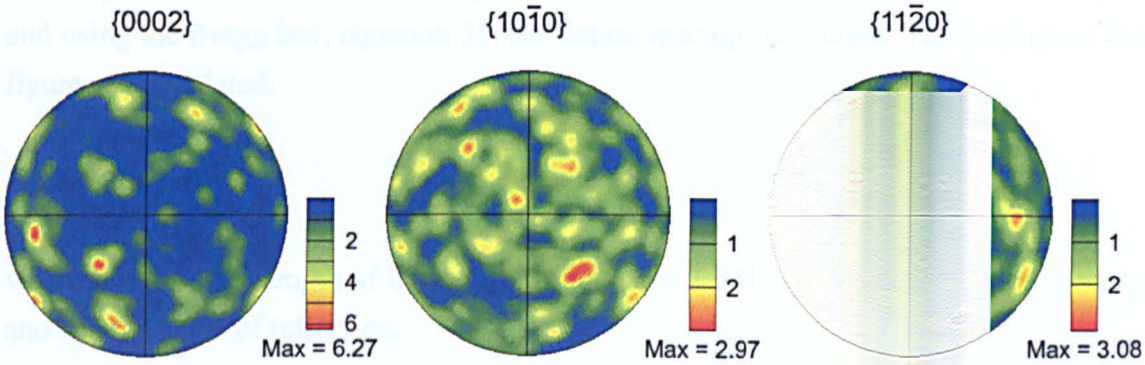

Figure 41 – Pole figures showing the texture in a sample of as-received material

4.1.3 X-Ray Diffraction

Figure 42 shows the X-ray diffraction intensity distribution for a sample of Elektron 675. It was found that the vast majority of peaks in intensity corresponded directly with the theoretical peaks for magnesium.

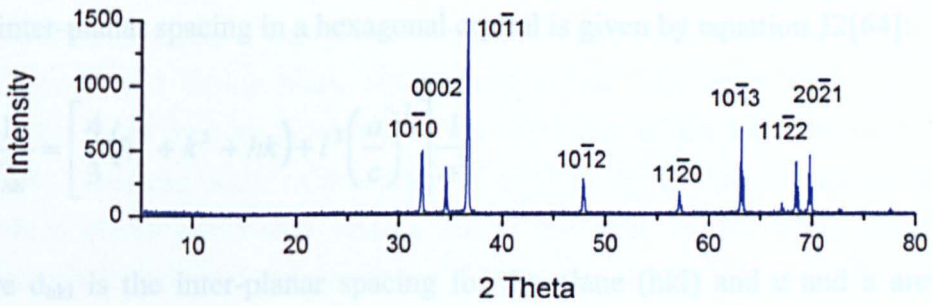

Figure 42 – Intensity plot from XRD analysis showing the positions of peaks and the corresponding planes from a sample of Elektron 675

4.1.3.1 Lattice Parameter Calculation

X-ray diffraction was used to calculate the crystal lattice parameters and 3 samples were studied to obtain a reasonable level of accuracy. It is shown in Cullity[213] that calculations of lattice spacings have a lower error when they are derived from peaks at higher angles. Therefore, in this work the peaks corresponding to the $\{1\bar{1}22\}$ and $\{20\bar{2}1\}$ sets of planes were used. The average values of 2θ were calculated from the 3 samples and using the Bragg law, equation 31, the lattice spacing was found. Table 13 gives the figures as calculated.

$$\lambda = 2d\sin\theta \tag{31}$$

where λ is the wavelength of the x-rays (in this case 1.54178 Å), d is the lattice spacing and θ is the angle of reflection.

Table 13 – Results of XRD experiments showing the values of 2θ and calculated lattice spacings for 2 sets of planes

	2 Theta				
Plane	Sample 1	Sample 2	Sample 3	Average	d (Å)
$\{1\bar{1}22\}$	68.44	68.50	68.42	68.45	1.371
$\{20\bar{2}1\}$	69.68	69.78	69.76	69.74	1.348

The inter-planar spacing in a hexagonal crystal is given by equation 32[64]:

$$\frac{1}{d_{hkl}^2} = \left[\frac{4}{3}\left(h^2 + k^2 + hk\right) + l^2\left(\frac{a}{c}\right)^2\right]\frac{1}{a^2} \tag{32}$$

where d_{hkl} is the inter-planar spacing for the plane (hkl) and c and a are the lattice constants.

Therefore, the inter-planar spacings for the planes $(1\bar{1}22)$ and $(20\bar{2}1)$, in 3 figure indexing (112) and (201) respectively, are given by equations 33 and 34:

$$\frac{1}{d_{112}^2} = \frac{4}{a^2} + \frac{4}{c^2} \tag{33}$$

$$\frac{1}{d_{201}^2} = \frac{16}{3a^2} + \frac{1}{c^2} \tag{34}$$

By combining equations 33 and 34, equations for a and c were found:

$$a = \sqrt{\frac{52}{3\left(\frac{4}{d_{201}^2} - \frac{1}{d_{112}^2}\right)}} \tag{35}$$

$$c = \sqrt{\frac{13}{3\left(\frac{4}{3d_{112}^2} - \frac{1}{d_{201}^2}\right)}} \tag{36}$$

Therefore, the lattice parameters and c/a ratio for Elektron 675 were calculated to be:

a = 3.224Å
c = 5.207Å

c/a ratio = 1.615

4.2 Process Window

A wide range of temperatures and strain rates have been tested during this investigation and from these results it was possible to identify the upper and lower limits of ductility for Elektron 675 during plane strain compression. The lower limit of ductility was shown by shear fracture occurring at the shoulders of the test specimens, as seen in figure 43. This can occur over a range of severity, from total fracture of the specimen into three pieces down to a small crack in one area. In this work, significant shear fracture was considered to have begun if there was at least one area of cracking visible to the naked eye at the shoulder of the sample.

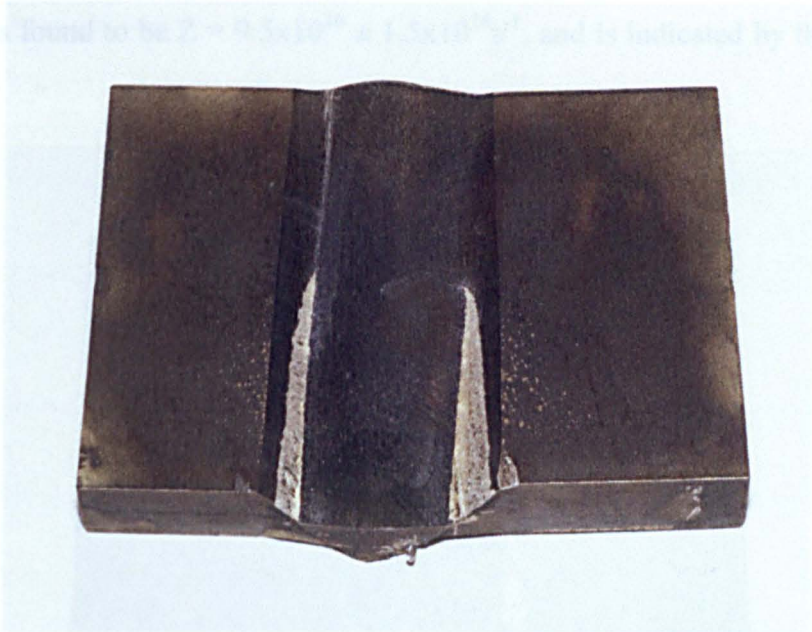

Figure 43 – PSC sample deformed at 400°C and $10s^{-1}$ strain rate showing shear fracture at the corners of the tools

As the material was deformed, there was a significant amount of deformation heating within the specimen due to energy released from plastic deformation. This raised the temperature within the sample, particularly in the areas of greatest strain, and by the end of deformation could be as much as 80°C higher than the starting temperature. A single test from the matrix of single hit tests showed incipient melting, under the starting conditions of 520°C and $10s^{-1}$ strain rate, see figure 44. This occurred around the thermocouple due to the stress concentration introduced there. The thermocouple measurements indicated that the centre of this sample reached 550°C by the end of the test. It is not possible to say at what specific temperature the melting occurred but as it did not happen in the test at $5s^{-1}$, which reached approximately 545°C, the incipient melting must have occurred above 545°C. Due to the safety concerns in dealing with molten magnesium, this upper limit of ductility was not studied further.

The conditions at which shear fracture occurred was defined by both the temperature and strain rate of the deformation, and thus the Zener-Hollomon parameter, Z, as described in section 2.3.8.1, could be used. Figure 45 shows all of the tests carried out and marks which showed fracture or incipient melting. By using axes of inverse temperature and ln (strain rate), values of Z are represented by straight lines and thus a single value of Z can divide the areas of ductility and shear fracture. The lower limit of

ductility was found to be $Z = 9.5x10^{16} \pm 1.5x10^{16} s^{-1}$, and is indicated by the dotted line in figure 45.

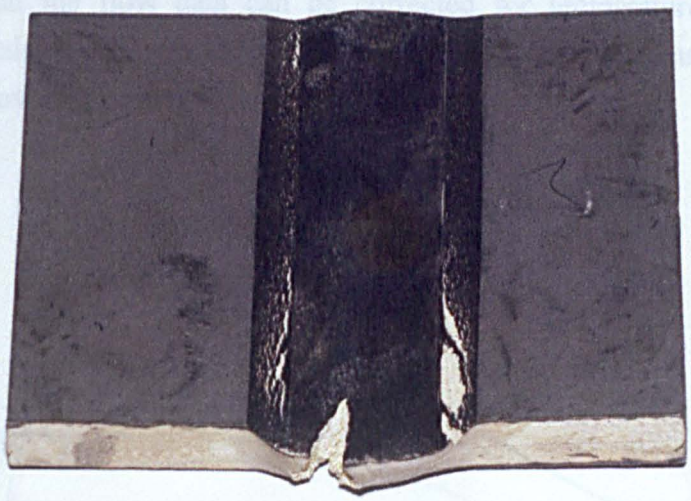

Figure 44 – PSC sample deformed at 520°C and $10s^{-1}$ strain rate showing incipient melting

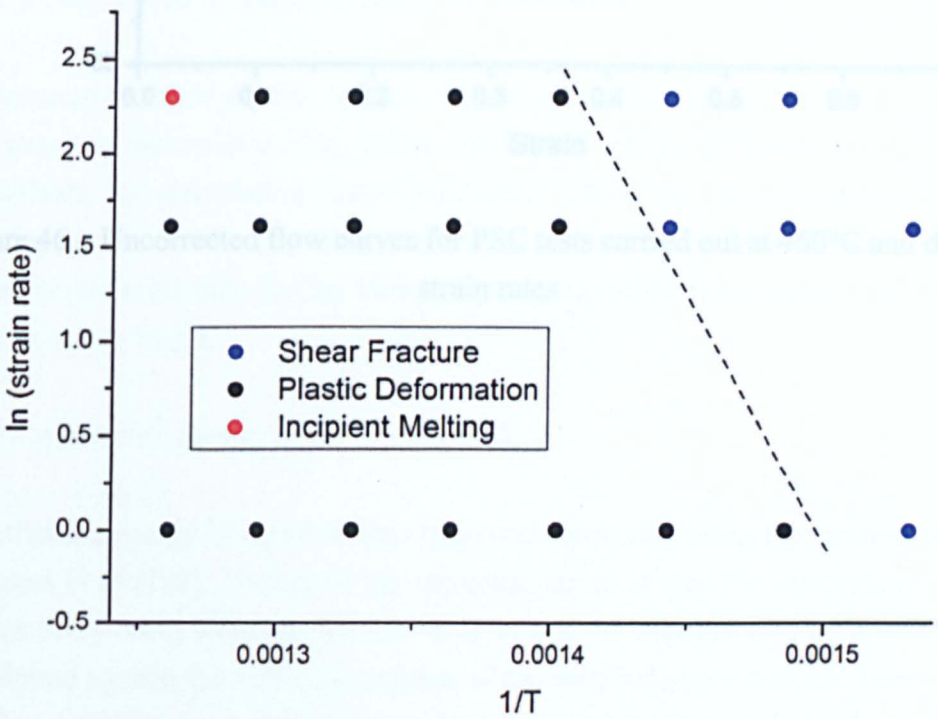

Figure 45 – Plot showing the conditions of plane strain compression testing under which shear fracture, plastic deformation and incipient melting occur

4.3 Flow Behaviour

The raw, uncorrected flow curves from a selection of PSC tests are shown in figure 46 and figure 47. From this raw data, the material constant and correction factors are calculated so that the flow data can be corrected for temperature and strain rate variations. The calculations will be presented in the following sections, followed by the fully corrected flow curves in section 4.3.2.

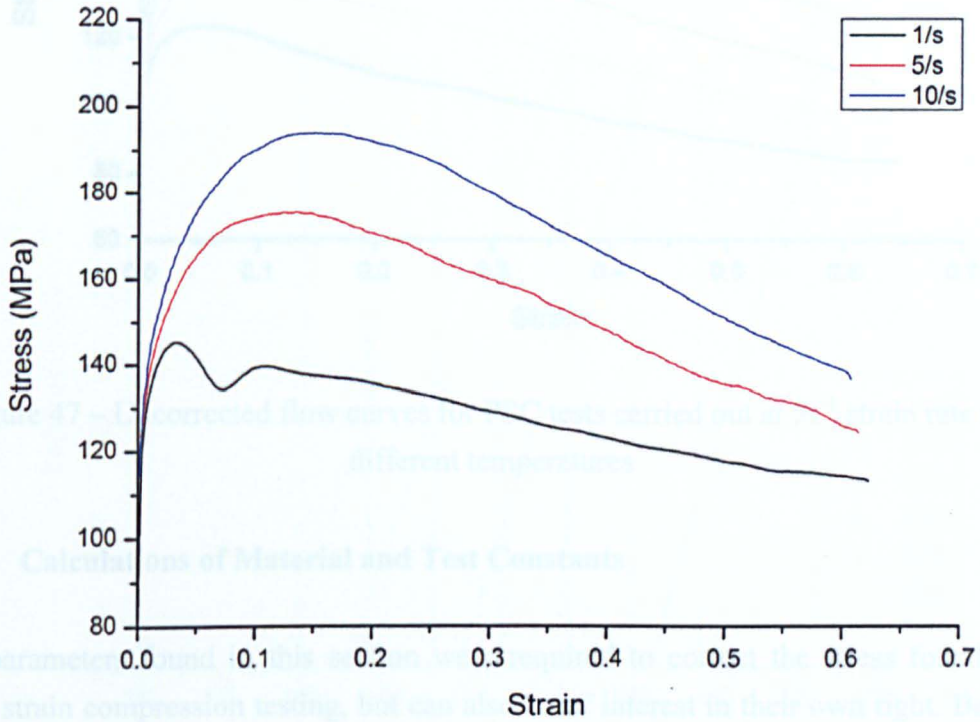

Figure 46 – Uncorrected flow curves for PSC tests carried out at 460°C and different strain rates

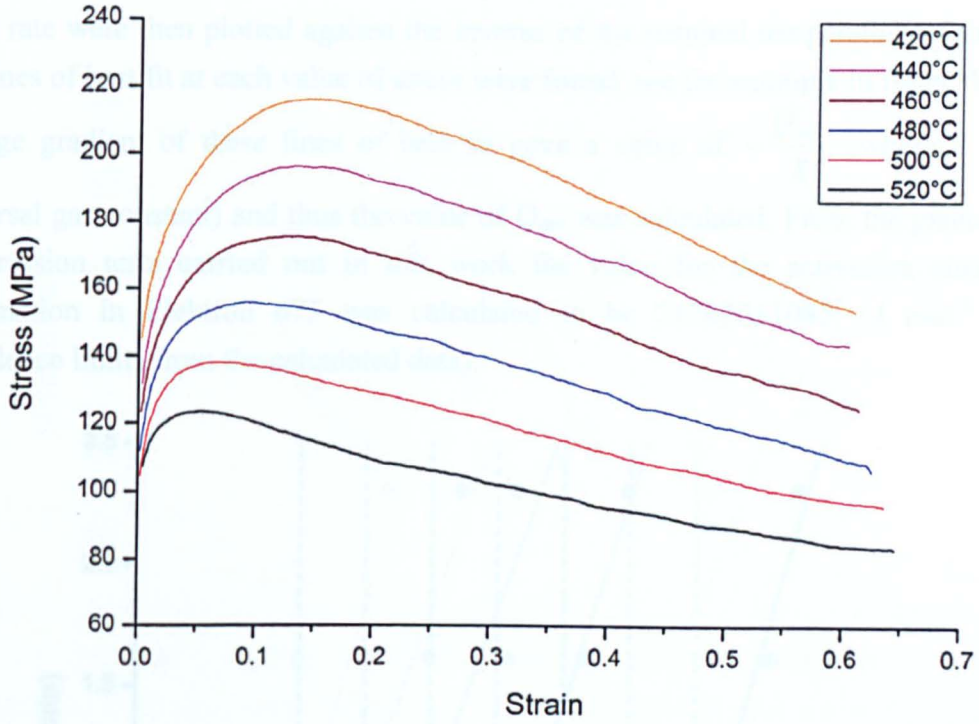

Figure 47 – Uncorrected flow curves for PSC tests carried out at $5s^{-1}$ strain rate and different temperatures

4.3.1 Calculations of Material and Test Constants

The parameters found in this section were required to correct the stress found from plane strain compression testing, but can also be of interest in their own right. Because the methods for calculating these parameters relied on already-corrected stresses, approximate values were first chosen and then an iterative process was used to improve the parameters until each further iteration gave negligible improvement and the correct values had been found.

4.3.1.1 Activation Energy of Deformation (Q_{def})

The activation energy of deformation (Q_{def}) was calculated using the method outlined in Davenport *et al.*[197]. Values of the corrected stress at specific intervals of strain (in this case every 0.02) were obtained for each test in the standard single hit matrix. These were plotted against the natural logarithm of the nominal strain rate and lines of best fit were drawn linking each different temperature tested, see example in figure 48. Lines were drawn onto this plot at specific intervals of stress and the strain rate at the intersections of these lines and the best fit lines for the data was found. These values of

strain rate were then plotted against the inverse of the nominal temperature of the tests and lines of best fit at each value of stress were found, see the example in figure 49. The average gradient of these lines of best fit gave a value of $-\frac{Q_{def}}{R}$ (where R is the universal gas constant) and thus the value of Q_{def} was calculated. From the plane strain compression tests carried out in this work the value for the activation energy of deformation in Elektron 675 was calculated to be 217030±1085 J mol^{-1} (95% confidence limits from the calculated data).

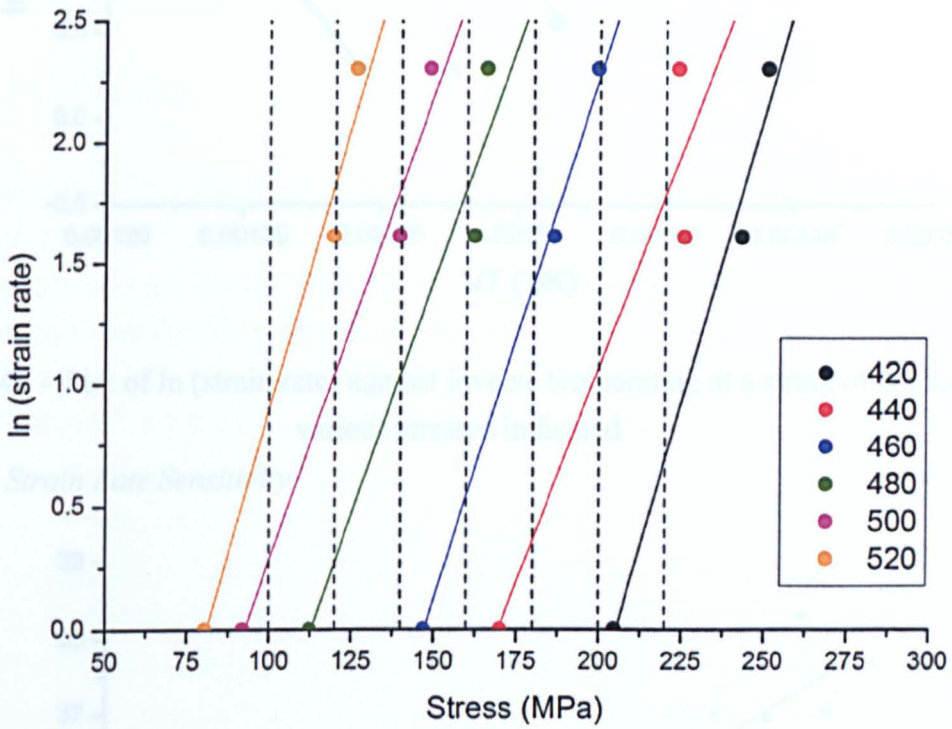

Figure 48 – Plot of ln (strain rate) against stress at a strain of 0.4 for the various temperatures indicated

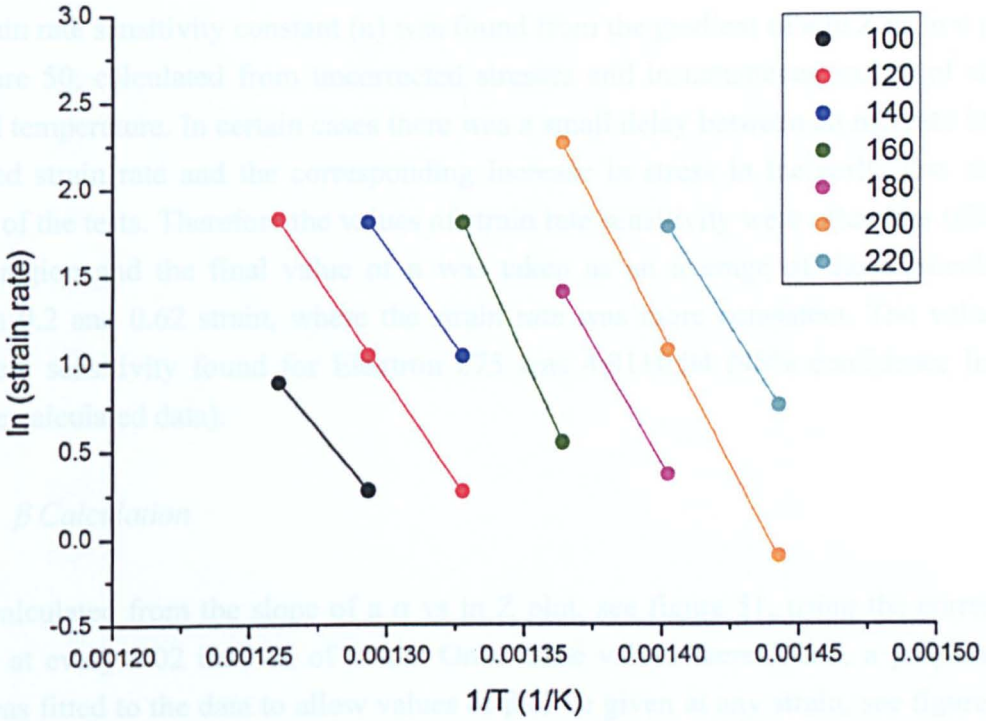

Figure 49 – Plot of ln (strain rate) against inverse temperature at a strain of 0.4 for the various stresses indicated

4.3.1.2 Strain Rate Sensitivity

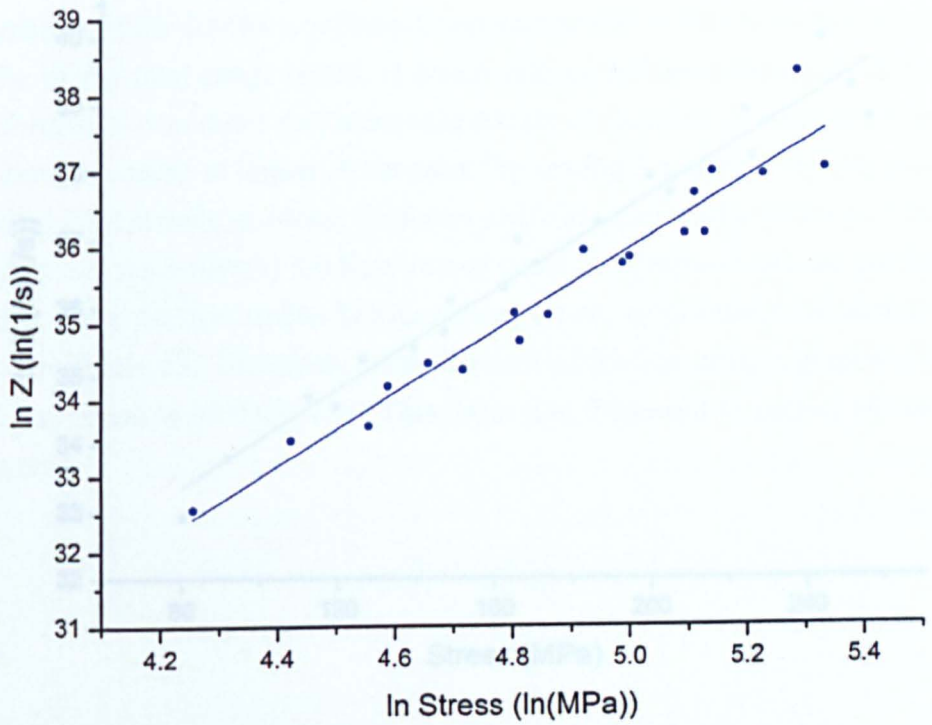

Figure 50 – Plot of ln Z against ln stress at a strain of 0.4

The strain rate sensitivity constant (n) was found from the gradient of a ln Z vs ln σ plot, see figure 50, calculated from uncorrected stresses and instantaneous values of strain rate and temperature. In certain cases there was a small delay between an increase in the measured strain rate and the corresponding increase in stress in the early, less stable regions of the tests. Therefore the values of strain rate sensitivity were often less reliable in this region and the final value of n was taken as an average of those calculated between 0.2 and 0.62 strain, where the strain rate was more consistent. The value of strain rate sensitivity found for Elektron 675 was 4.81±0.04 (95% confidence limits from the calculated data).

4.3.1.3 β Calculation

β was calculated from the slope of a σ vs ln Z plot, see figure 51, using the corrected stresses at every 0.02 interval of strain. Once these values were found, a polynomial curve was fitted to the data to allow values of β to be given at any strain, see figure 52. The equation found for β is given in equation 37:

$$\beta = -3.0968\varepsilon^5 + 7.046\varepsilon^4 - 6.1808\varepsilon^3 + 2.663\varepsilon^2 - 0.5748\varepsilon + 0.0871 \qquad (37)$$

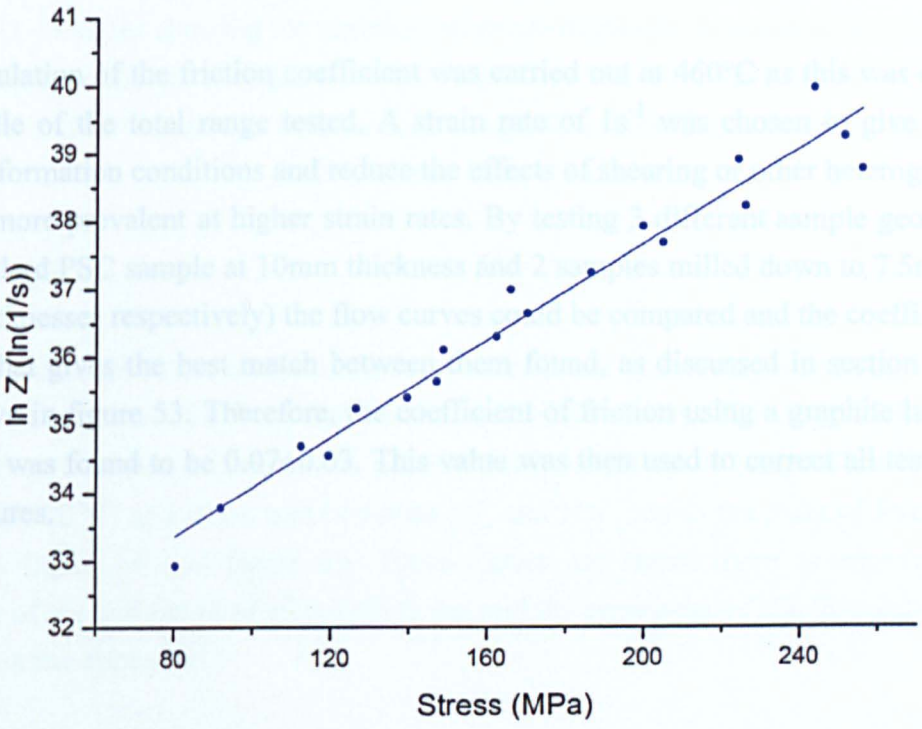

Figure 51 – Plot of ln Z against stress at a strain of 0.4

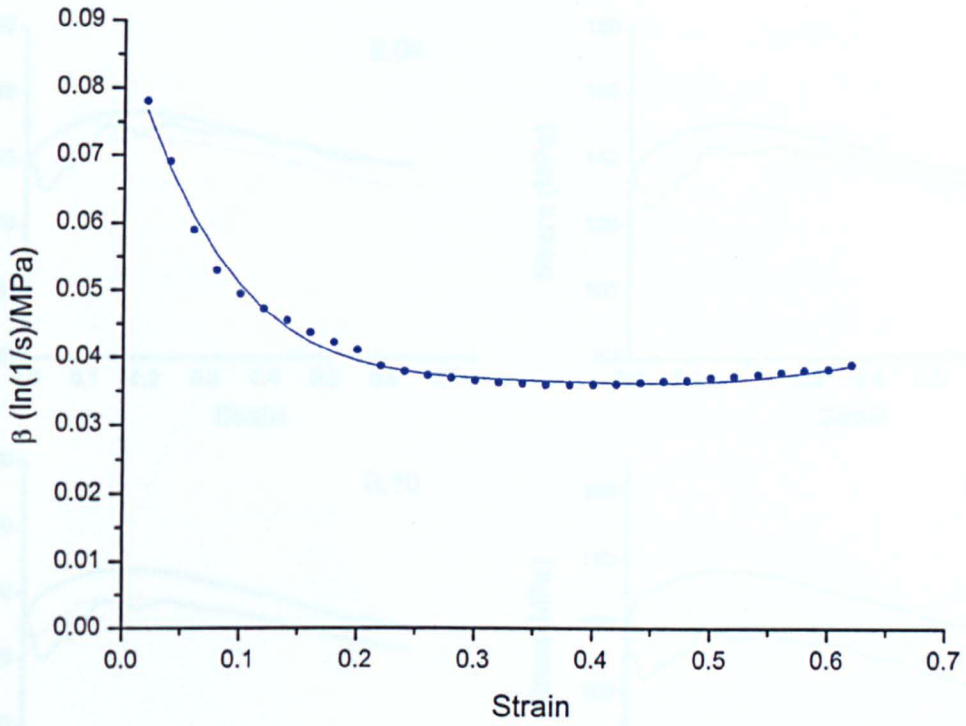

Figure 52 – Plot showing the variation of β with strain

4.3.1.4 Friction Coefficient

The calculation of the friction coefficient was carried out at 460°C as this was close to the middle of the total range tested. A strain rate of $1s^{-1}$ was chosen to give steady, stable deformation conditions and reduce the effects of shearing or other heterogeneities that are more prevalent at higher strain rates. By testing 3 different sample geometries (the standard PSC sample at 10mm thickness and 2 samples milled down to 7.5mm and 5mm thicknesses respectively) the flow curves could be compared and the coefficient of friction that gives the best match between them found, as discussed in section 3.2.3.4 and shown in figure 53. Therefore, the coefficient of friction using a graphite lubricant at 460°C was found to be 0.07±0.03. This value was then used to correct all tests at all temperatures.

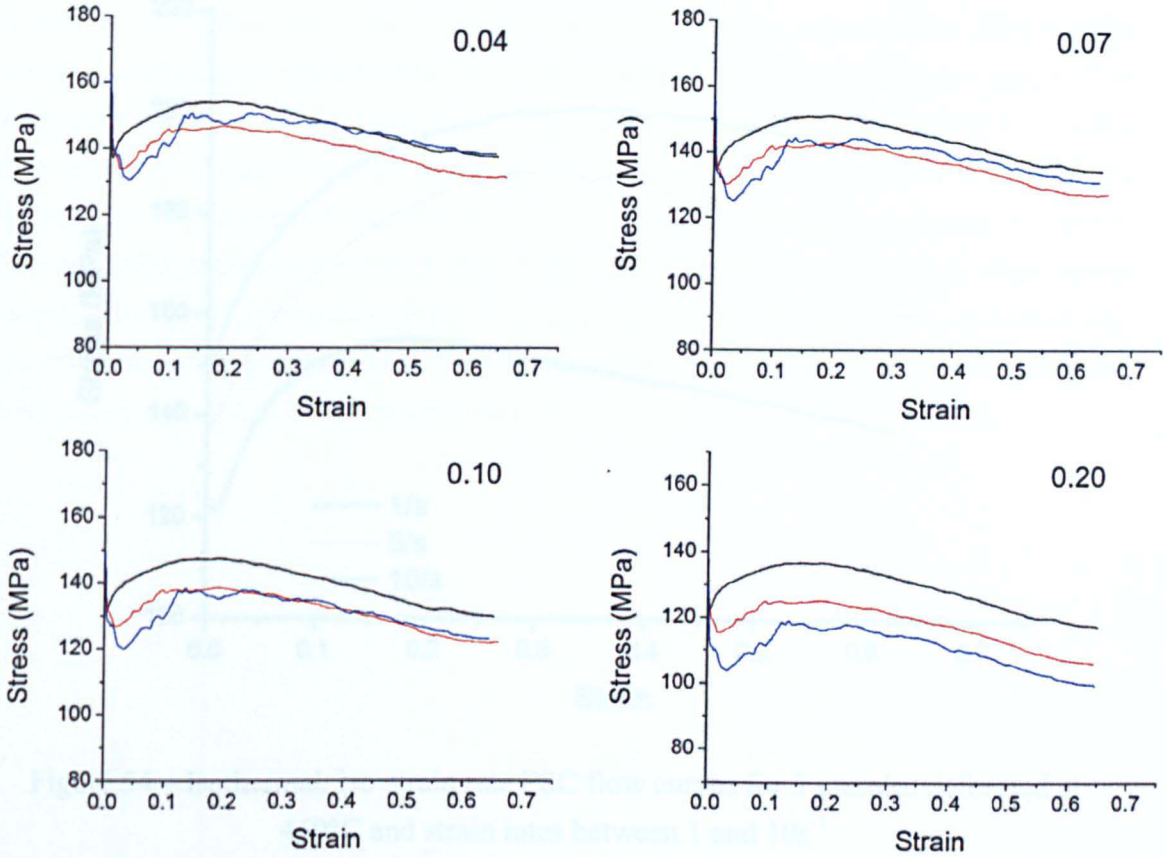

Figure 53 – Graphs showing the variation of stress-strain curves using different values of friction coefficient during the correction process for 3 PSC samples deformed at 460°C and $1s^{-1}$ strain rate with the following initial thicknesses: Black = 10mm, Red = 7.5mm, Blue = 5mm

4.3.2 Single Hit Tests

The standard plane strain compression tests, carried out with a single deformation step to a total deformation of 0.7, all showed similar flow behaviour. The shape of the stress-strain curves followed a comparable pattern at all conditions of temperature (between 380°C and 520°C) and strain rate (between $1s^{-1}$ and $10s^{-1}$) up to the point of fracture, as shown in figure 54 and figure 55. These curves are shown here as representative examples of the full range of tests carried out and the remainder of the flow curves can be found in the appendix.

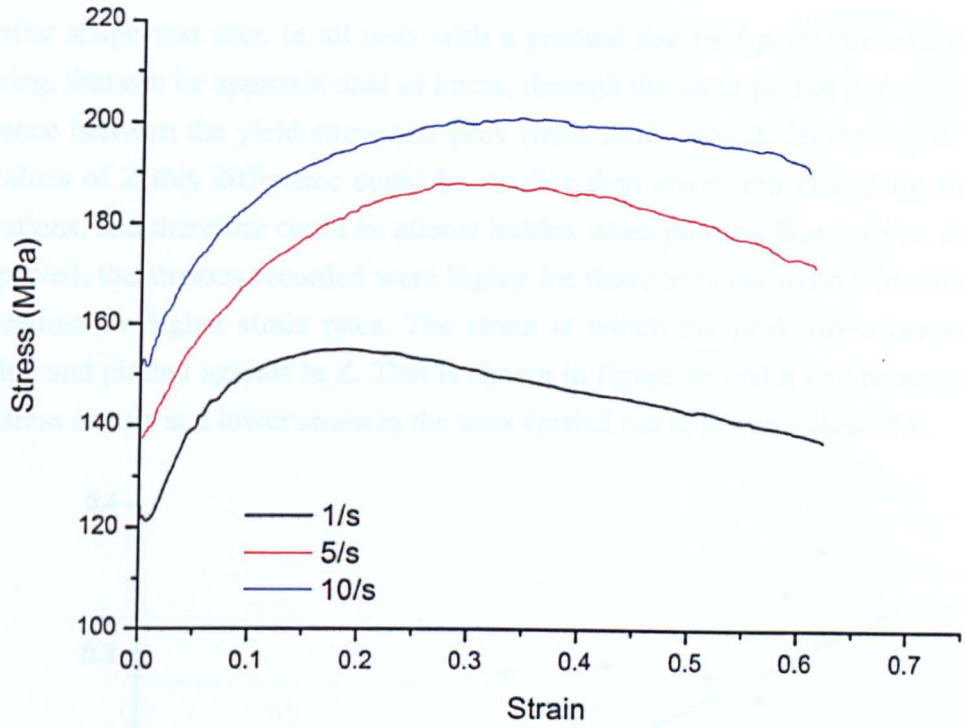

Figure 54 – Isothermal, iso-strain rate PSC flow curves for 3 samples deformed at 460°C and strain rates between 1 and $10s^{-1}$

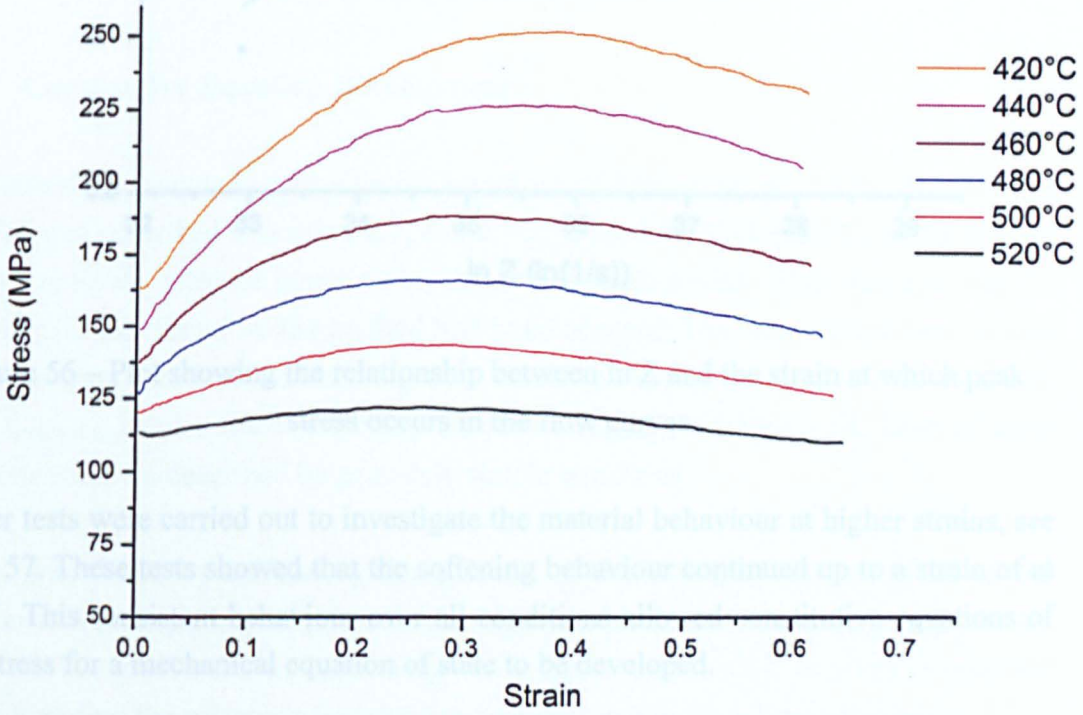

Figure 55 – Isothermal, iso-strain rate PSC flow curves for 6 samples deformed at $5s^{-1}$ strain rate and temperatures between 420°C and 520°C

A similar shape was seen in all tests with a gradual rise to a peak stress followed by softening, that can be approximated as linear, through the latter part of deformation. The difference between the yield stress and peak stress reduced with decreasing Z. At very low values of Z this difference could be smaller than errors introduced by strain rate fluctuations, and therefore could be almost hidden when plotting flow curves. As would be expected, the stresses recorded were higher for those tests carried out at either lower temperatures or higher strain rates. The strain at which the peak stress occurred was recorded and plotted against ln Z. This is shown in figure 56 and it can be seen that the peak stress occurs at a lower strain in the tests carried out at lower values of Z.

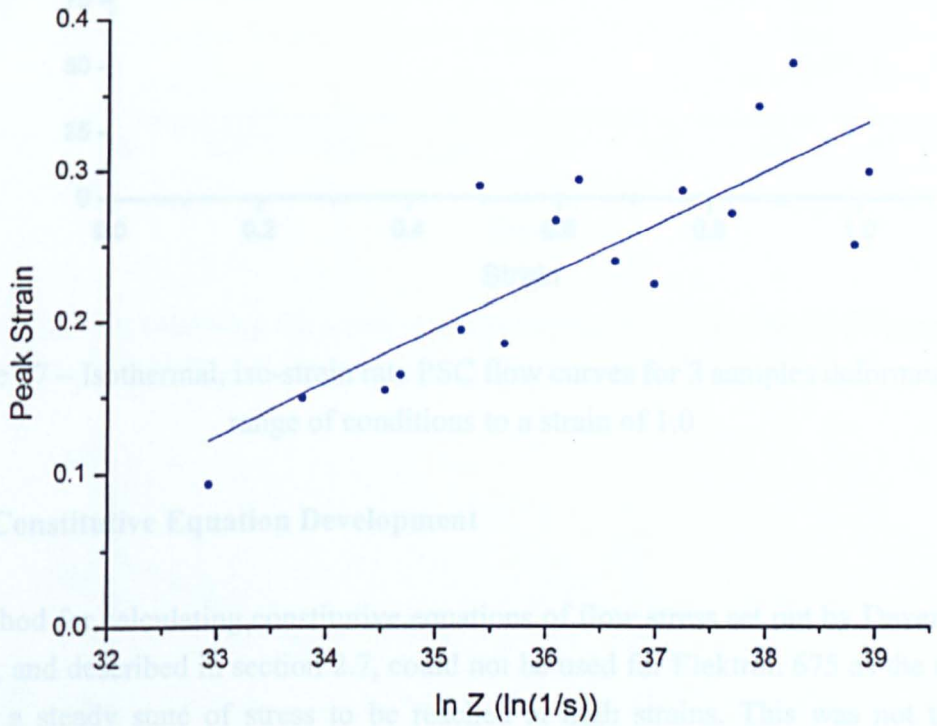

Figure 56 – Plot showing the relationship between ln Z and the strain at which peak stress occurs in the flow curves

Further tests were carried out to investigate the material behaviour at higher strains, see figure 57. These tests showed that the softening behaviour continued up to a strain of at least 1. This consistent behaviour over all conditions allowed constitutive equations of flow stress for a mechanical equation of state to be developed.

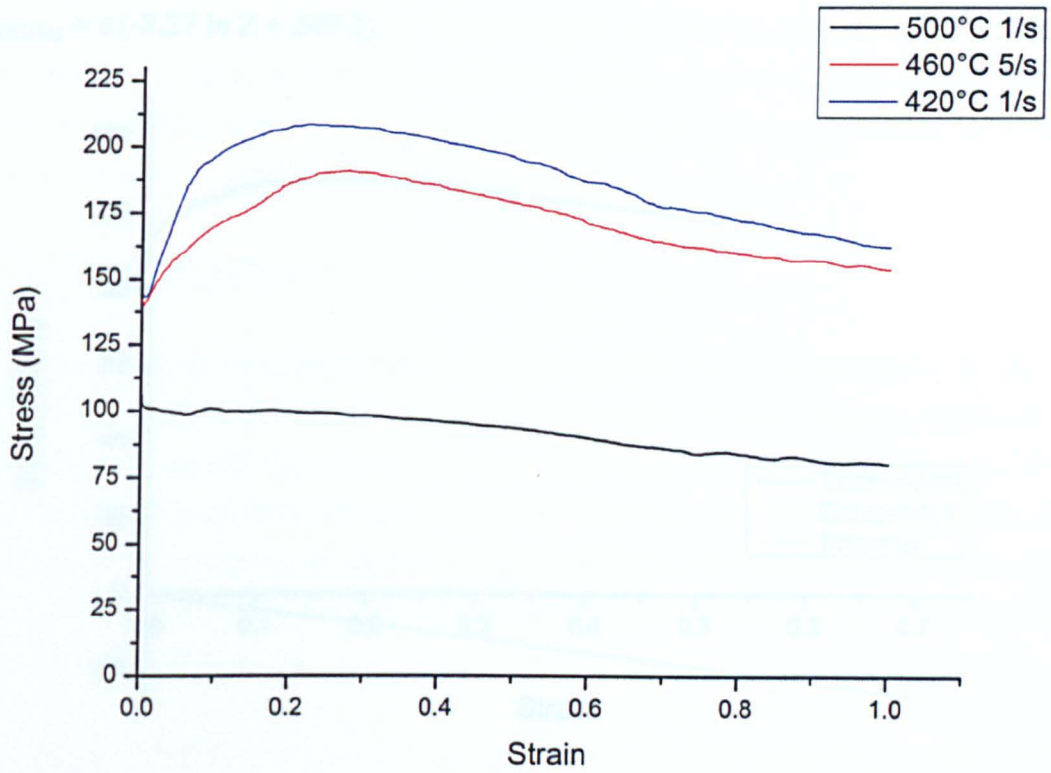

Figure 57 – Isothermal, iso-strain rate PSC flow curves for 3 samples deformed at a range of conditions to a strain of 1.0

4.3.3 Constitutive Equation Development

The method for calculating constitutive equations of flow stress set out by Davenport *et al.*[197], and described in section 2.7, could not be used for Elektron 675 as the method requires a steady state of stress to be reached at high strains. This was not true for Elektron 675 and therefore the method had to be adapted. The flow curves were treated as two separate functions summed together: an extrapolated function that reaches steady state ($f_{steady\text{-}state}$) and a linear softening function ($f_{softening}$), see figure 58. Both of these functions could be described by relatively simple equations.

$f_{softening}$ was found by calculating the gradient of the softening portion of all of the experimental curves and finding a relationship with the Zener-Hollomon parameter, see figure 59. The gradient of this softening was found to vary with Z as given in equation 38 and therefore the softening function is given in equation 39, where ε is strain.

$$\text{gradient} = -8.27 \ln Z + 249.2 \quad (38)$$

$$f_{softening} = \varepsilon (-8.27 \ln Z + 249.2) \quad (39)$$

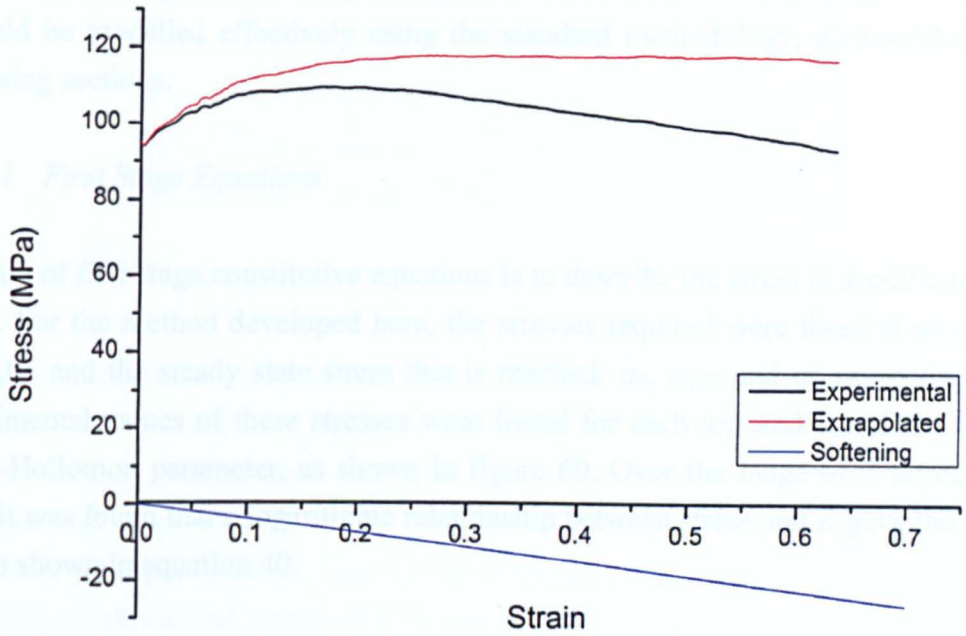

Figure 58 – Plot showing the stress-strain behaviour of a PSC sample deformed at 480°C and $1s^{-1}$, also displaying $f_{softening}$ and the extrapolated curve, $f_{steady\text{-}state}$

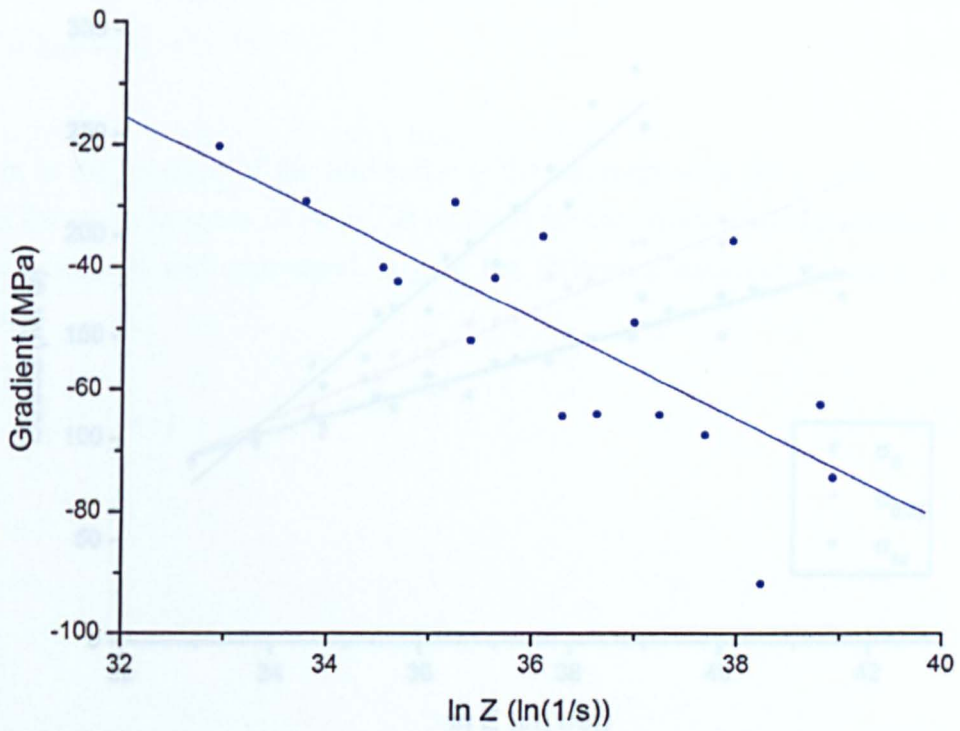

Figure 59 – Plot showing the experimentally determined values of the softening gradient as a function of ln Z

$f_{steady\text{-}state}$ was calculated from the extrapolated curves, themselves calculated by subtracting $f_{softening}$ from the fully corrected data. As this reached a steady state of stress it could be modelled effectively using the standard methodology, as described in the following sections.

4.3.3.1 First Stage Equations

The aim of first stage constitutive equations is to describe the stress at specific points of strain. For the method developed here, the stresses required were those at strains of 0 and 0.05 and the steady state stress that is reached: σ_0, $\sigma_{0.05}$ and σ_{ss} respectively. The experimental values of these stresses were found for each test and correlated with the Zener-Hollomon parameter, as shown in figure 60. Over the range of Z tested in this work it was found that a logarithmic relationship between stress and Z gave the best fit. This is shown in equation 40.

$$\sigma_0, \sigma_{0.05}, \sigma_{ss} = n \ln Z + A \quad (40)$$

where n and A are constants, the values of which are given in table 14.

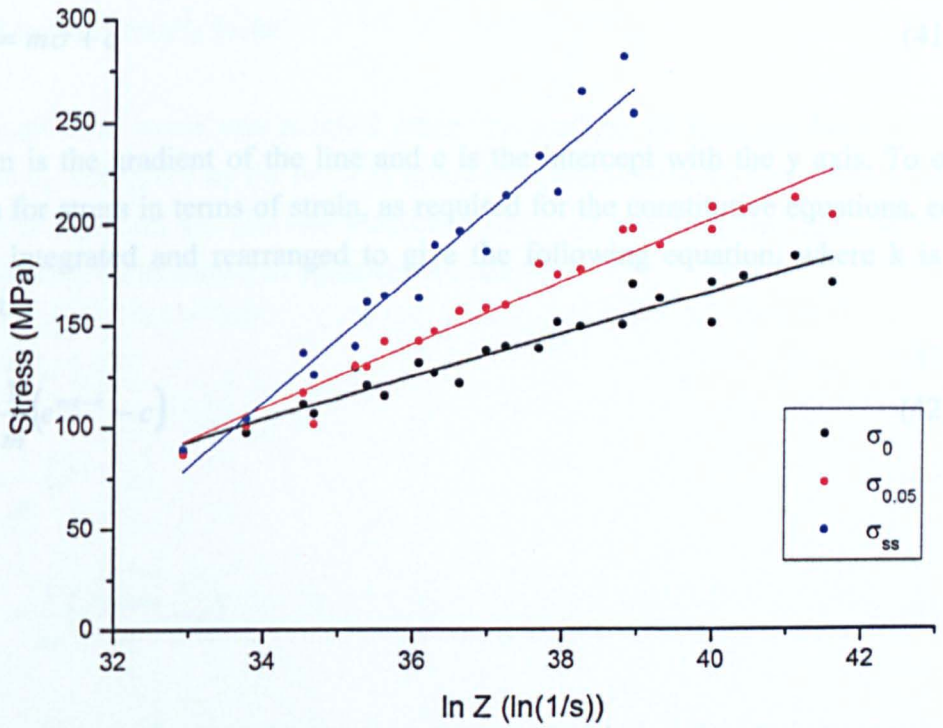

Figure 60 – Plot showing the experimentally determined values of σ_0, $\sigma_{0.05}$ and σ_{ss} as a function of ln Z

Table 14 – Constants for 1st Stage Constitutive Equations

	n (MPa / ln(s^{-1}))	A (MPa)
σ_0	10.51	-253.9
$\sigma_{0.05}$	15.49	-417.5
σ_{ss}	31.20	-949.1

4.3.3.2 Second Stage Equations

Second stage constitutive equations use the points calculated by the first stage equations to define a continuous flow curve. Another adaptation of the Davenport *et al.*[197] method was used to more accurately reflect the initial shape of the stress-strain curves in the region up to the peak stress. To do this, the complex curve of $f_{steady\text{-}state}$ had to be fitted with a simple equation. The Kocks-Mecking plot[214] was developed for work hardening of almost any metal and, as can be seen in figure 61, fits the behaviour of Elektron 675 reasonably well. The standard Kocks-Mecking plot, rather than the modified version, was used in this work for the simplicity of further calculation. Therefore, the stress of $f_{steady\ state}$ (σ) is described by equation 41:

$$\frac{d\sigma}{d\varepsilon} = m\sigma + c \tag{41}$$

where m is the gradient of the line and c is the intercept with the y axis. To obtain a formula for stress in terms of strain, as required for the constitutive equations, equation 41 was integrated and rearranged to give the following equation, where k is a new constant:

$$\sigma = \frac{1}{m}\left(e^{m\varepsilon - k} - c\right) \tag{42}$$

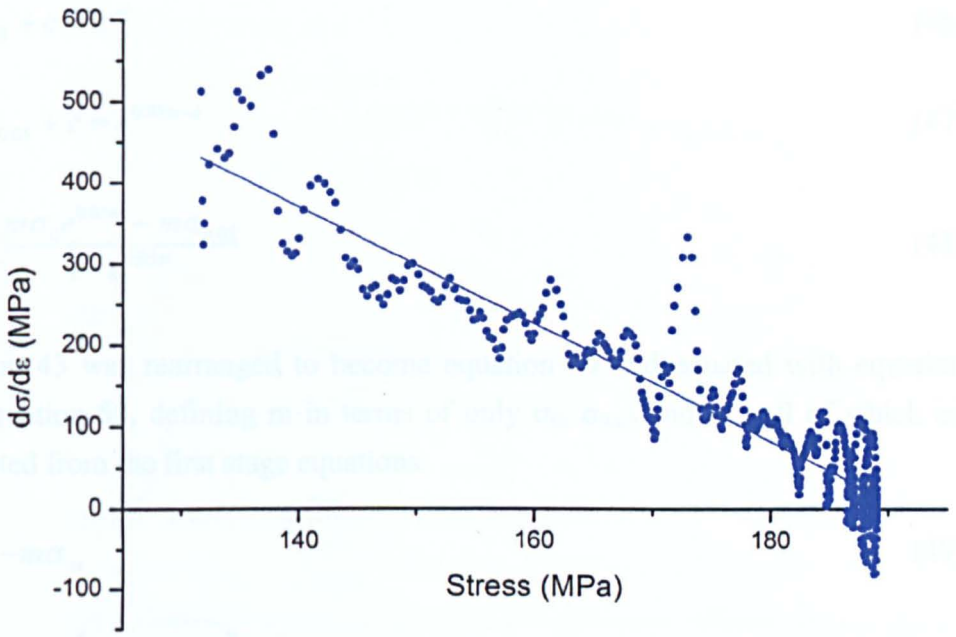

Figure 61 – Kocks-Mecking plot for the deformation behaviour of a sample deformed at 480°C and $5s^{-1}$ strain rate

While the experimental data would allow the values of the unknowns m, k and c to be calculated directly, the first stage constitutive equations were required for those values of Z not experimentally tested.

The steady state stress was reached when the gradient of $f_{steady\text{-}state}$ became zero and therefore σ_{ss} was given by the point at which the Kocks-Mecking plot crosses the x axis, as given in equation 43. The two remaining points of stress, σ_0 and $\sigma_{0.05}$, were defined using equation 42 as shown in equations 44 and 45.

$$0 = m\sigma_{ss} + c \tag{43}$$

$$\sigma_0 = \frac{1}{m}\left(e^{-k} - c\right) \tag{44}$$

$$\sigma_{0.05} = \frac{1}{m}\left(e^{0.05m-k} - c\right) \tag{45}$$

Equations 44 and 45 were rearranged to give equations 46 and 47 and then solved for c, giving equation 48 defining c in terms of only m, σ_0 and $\sigma_{0.05}$.

$$m\sigma_0 + c = e^{-k} \tag{46}$$

$$m\sigma_{0.05} + c = e^{0.05m-k} \tag{47}$$

$$c = \frac{m\sigma_0 e^{0.05m} - m\sigma_{0.05}}{1 - e^{0.05m}} \tag{48}$$

Equation 43 was rearranged to become equation 49 and equated with equation 48 to give equation 50, defining m in terms of only σ_0, $\sigma_{0.05}$ and σ_{ss}, all of which could be calculated from the first stage equations.

$$c = -m\sigma_{ss} \tag{49}$$

$$m = 20\ln\left(\frac{\sigma_{0.05} - \sigma_{ss}}{\sigma_0 - \sigma_{ss}}\right) \tag{50}$$

Therefore, m was defined only in terms of the 1st stage equations and thus could be calculated for any value of Z. Once m was known, c could be calculated from equation 49 and k from a rearrangement of equation 44, given in equation 51. After m, c and k were calculated for a particular value of Z, equation 42 was used to find the function $f_{steady\text{-}state}$.

$$k = -\ln(m\sigma_0 + c) \tag{51}$$

As stated previously, the total flow stress of the system was calculated from the sum of the two functions found here, $f_{softening}$ and $f_{steady\text{-}state}$ as shown in equation 52.

$$\sigma_{total} = f_{steady-state} + f_{softening} \tag{52}$$

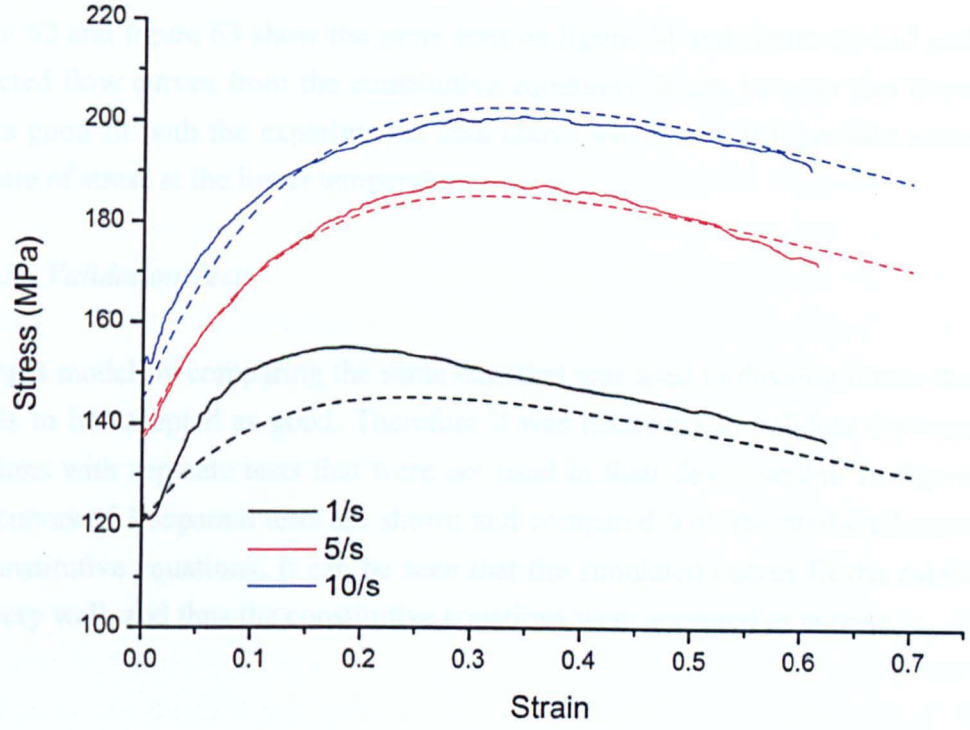

Figure 62 – Graph showing the same PSC flow curves at 460°C as figure 54, with the constitutive equation curves (dotted lines) superimposed

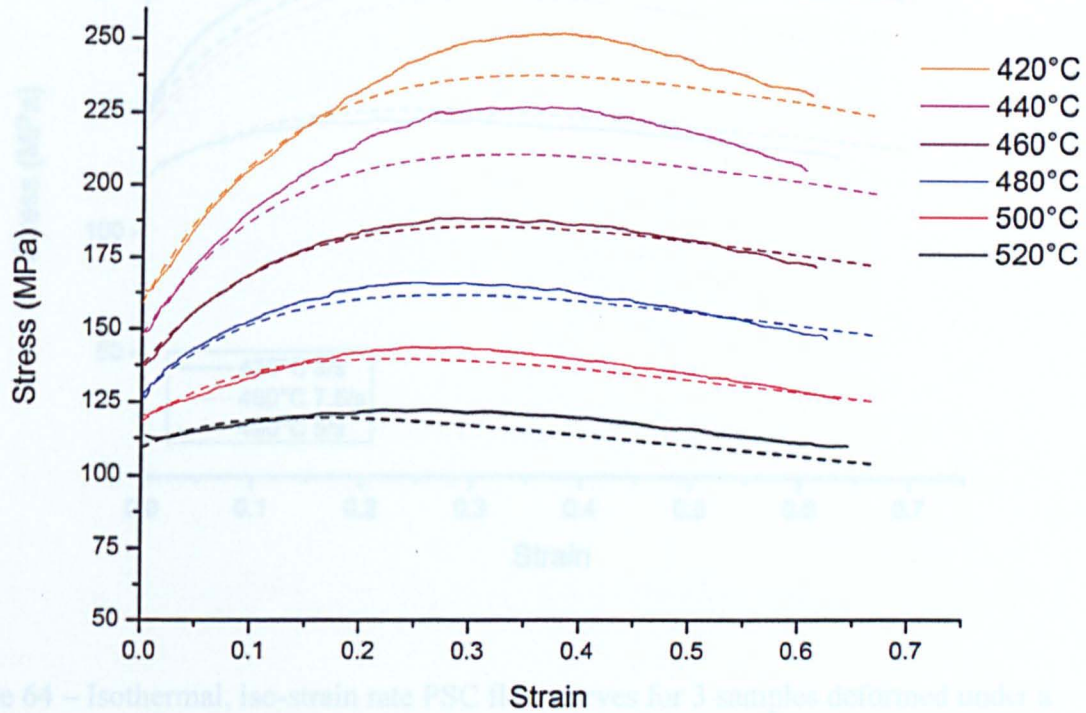

Figure 63 – Plot showing the same PSC curves at $5s^{-1}$ strain rate as figure 55 with the constitutive equation curves (dotted lines) superimposed

Figure 62 and figure 63 show the same tests as figure 54 and figure 55 and include the predicted flow curves from the constitutive equations. It can be seen that these curves have a good fit with the experimental data above 440°C and still provide a reasonable estimate of stress at the lower temperatures.

4.3.3.3 Validation Tests

Testing a model by comparing the same data that was used to develop it can cause poor models to be accepted as good. Therefore it was necessary to validate the constitutive equations with separate tests that were not used in their development. In figure 64 the flow curves of 3 separate tests are shown and compared with the predicted curves from the constitutive equations. It can be seen that the simulated curves fit the experimental data very well, and thus the constitutive equations were accepted as correct.

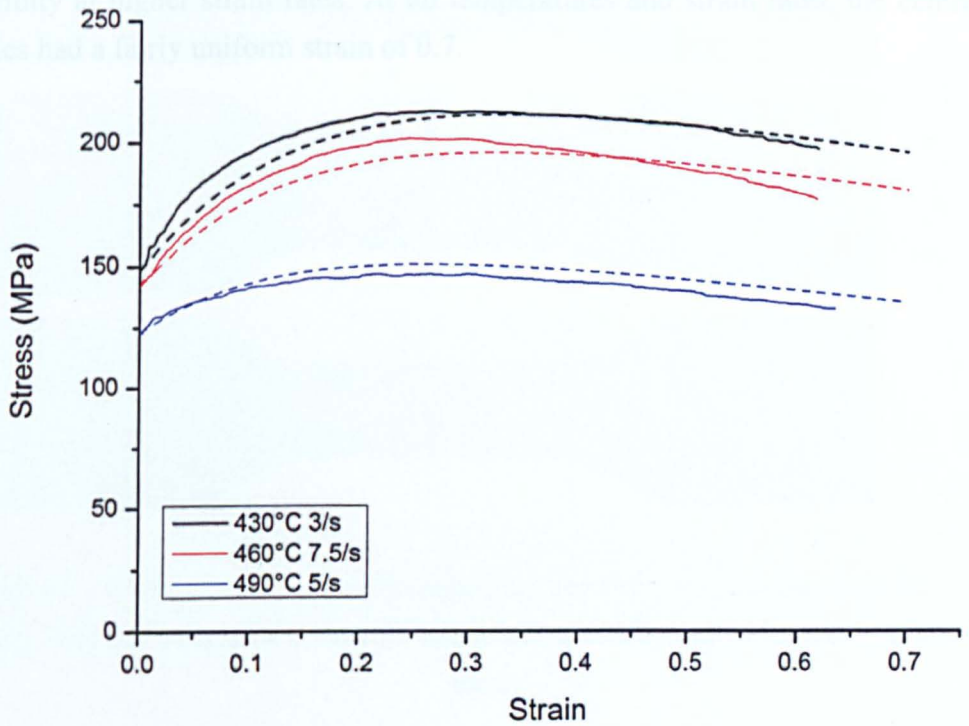

Figure 64 – Isothermal, iso-strain rate PSC flow curves for 3 samples deformed under a range of conditions, with constitutive equation curves (dotted lines) superimposed

4.3.4 Finite Element Modelling of Plane Strain Compression

The constitutive equations were used in a finite element model to calculate the strain and temperature distributions within PSC tests. The changes in strain distribution with increasing total strain are shown in figure 65. It can be seen that the deformation initiated at the corners of the tools and then spread diagonally into the centre of the samples. Within the deformation zone there were large differences in the levels of strain experienced by different parts of the sample. By a total strain of 0.7 the local strain within the centre of the deformation zone had reached approximately 0.7, as intended, but further from the centre line the strain was much more heterogeneous. There were two 'dead zones' on each surface, close to the shoulders, and 2 areas of high strain inside the sample, near the edges of the deformation zone. It can be seen in figure 66, figure 67 and figure 68 that the strain distribution reached at a total strain of 0.7 was relatively unaffected by the processing conditions. The general shape of the heterogeneities was the same at all temperatures with only a slight increase in the strength of the non-uniformity at higher strain rates. At all temperatures and strain rates, the centre of the samples had a fairly uniform strain of 0.7.

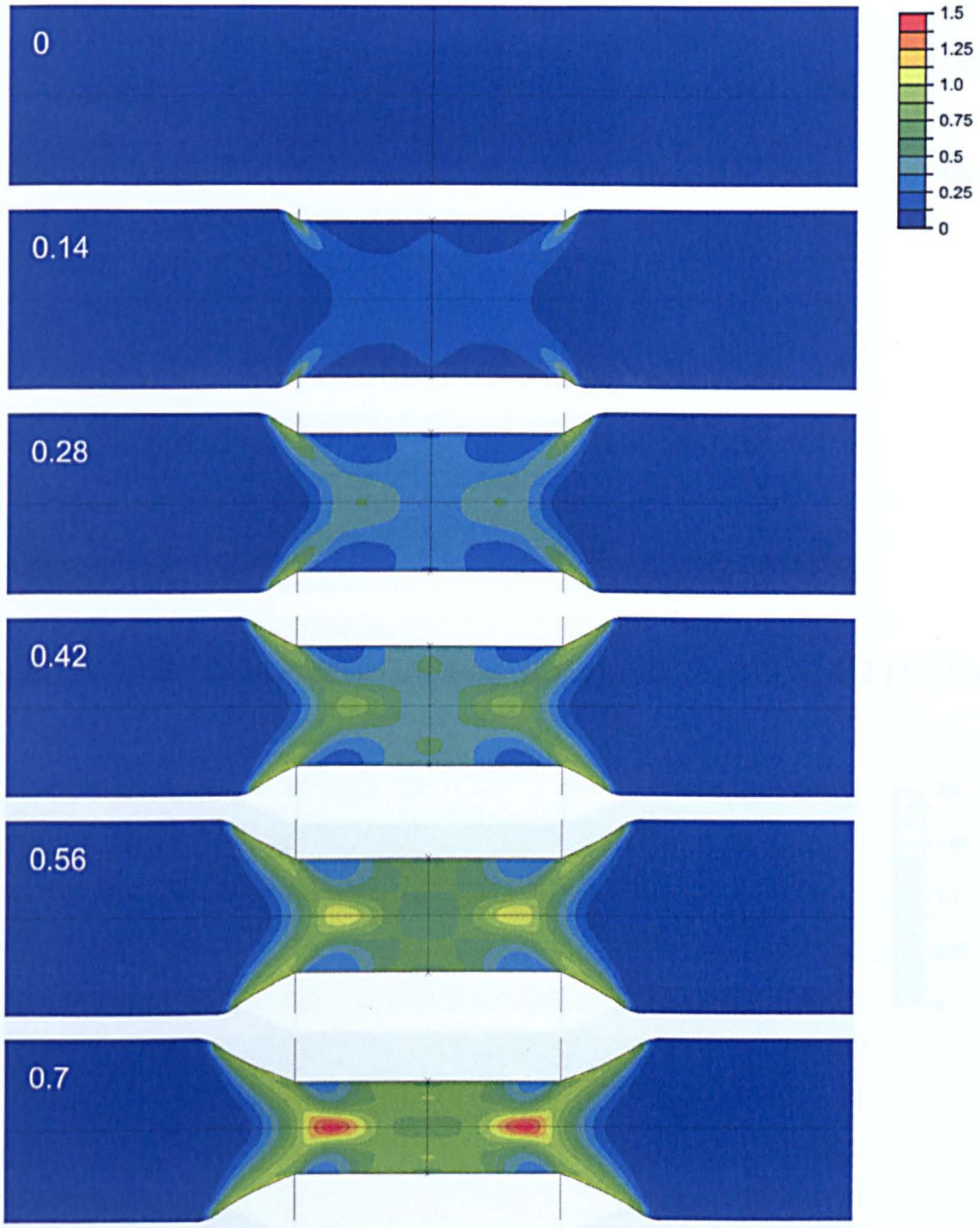

Figure 65 – Finite element modelling showing the strain distribution as a PSC test at 460°C and $5s^{-1}$ progresses. Sample strains are given by the white numbers on each model

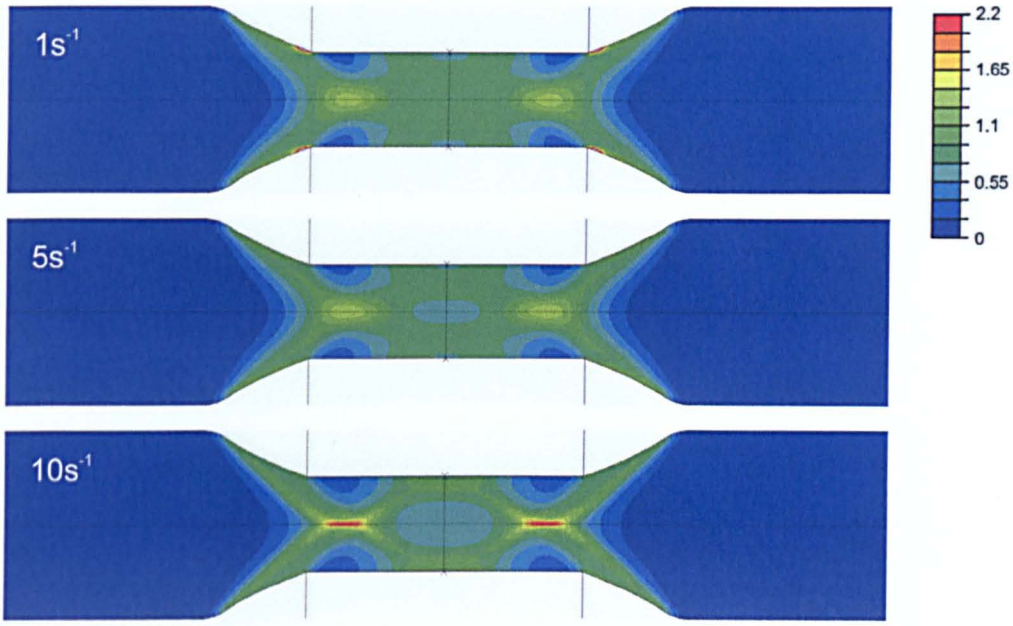

Figure 66 – Finite element modelling showing the strain distribution in 3 PSC tests carried out at 420°C

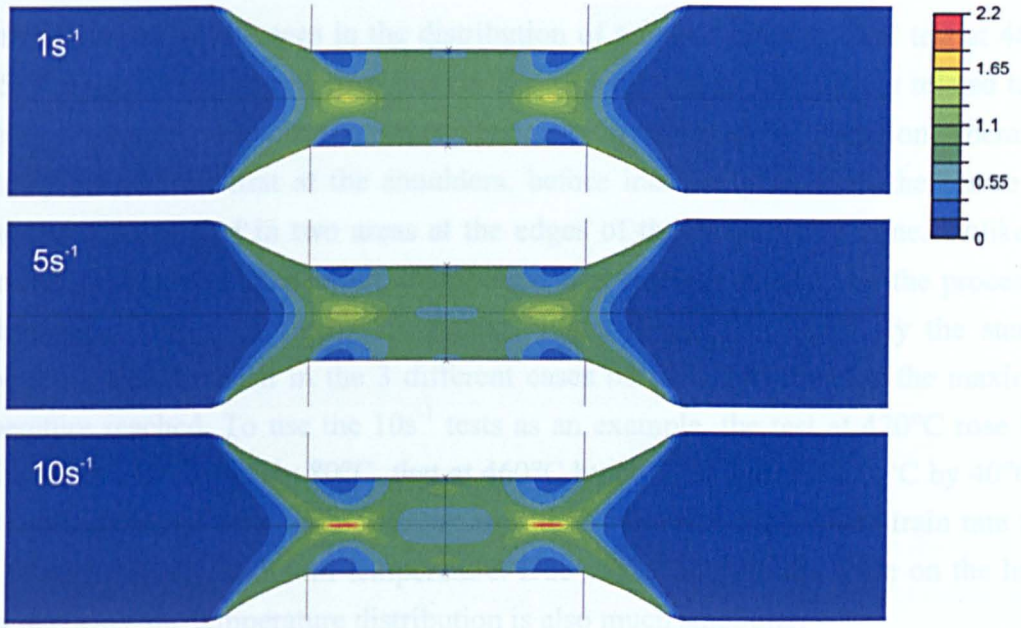

Figure 67 – Finite element modelling showing the strain distribution in 3 PSC tests carried out at 460°C

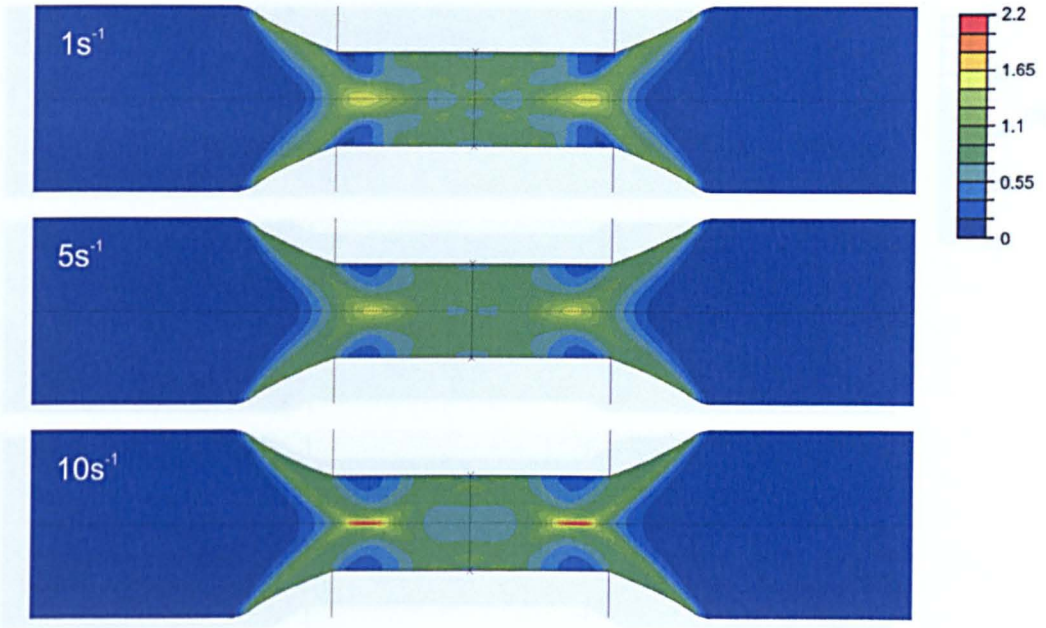

Figure 68 – Finite element modelling showing the strain distribution in 3 PSC tests carried out at 520°C

Figure 69 shows the changes in the distribution of temperature as a PSC test at 460°C and $5s^{-1}$ progresses. It can be seen that the rise in temperature was closely related to the increase in strain, because the heat was generated during plastic deformation. Therefore, the temperature rose first at the shoulders, before increasing more in the centre and becoming concentrated in two areas at the edges of the deformation zone. Unlike the strain distribution, the temperature distribution was strongly affected by the processing conditions, as shown in figure 70, figure 71 and figure 72. Obviously the starting temperature was different in the 3 different cases but this also affected the maximum temperature reached. To use the $10s^{-1}$ tests as an example, the test at 420°C rose by a maximum of approximately 80°C, that at 460°C by 60°C and that at 520°C by 40°C. A similar effect can be seen with differences in the strain rate; the higher strain rate tests give a much higher maximum temperature. Due to the longer time scale on the lower strain rate tests, the temperature distribution is also much smoother.

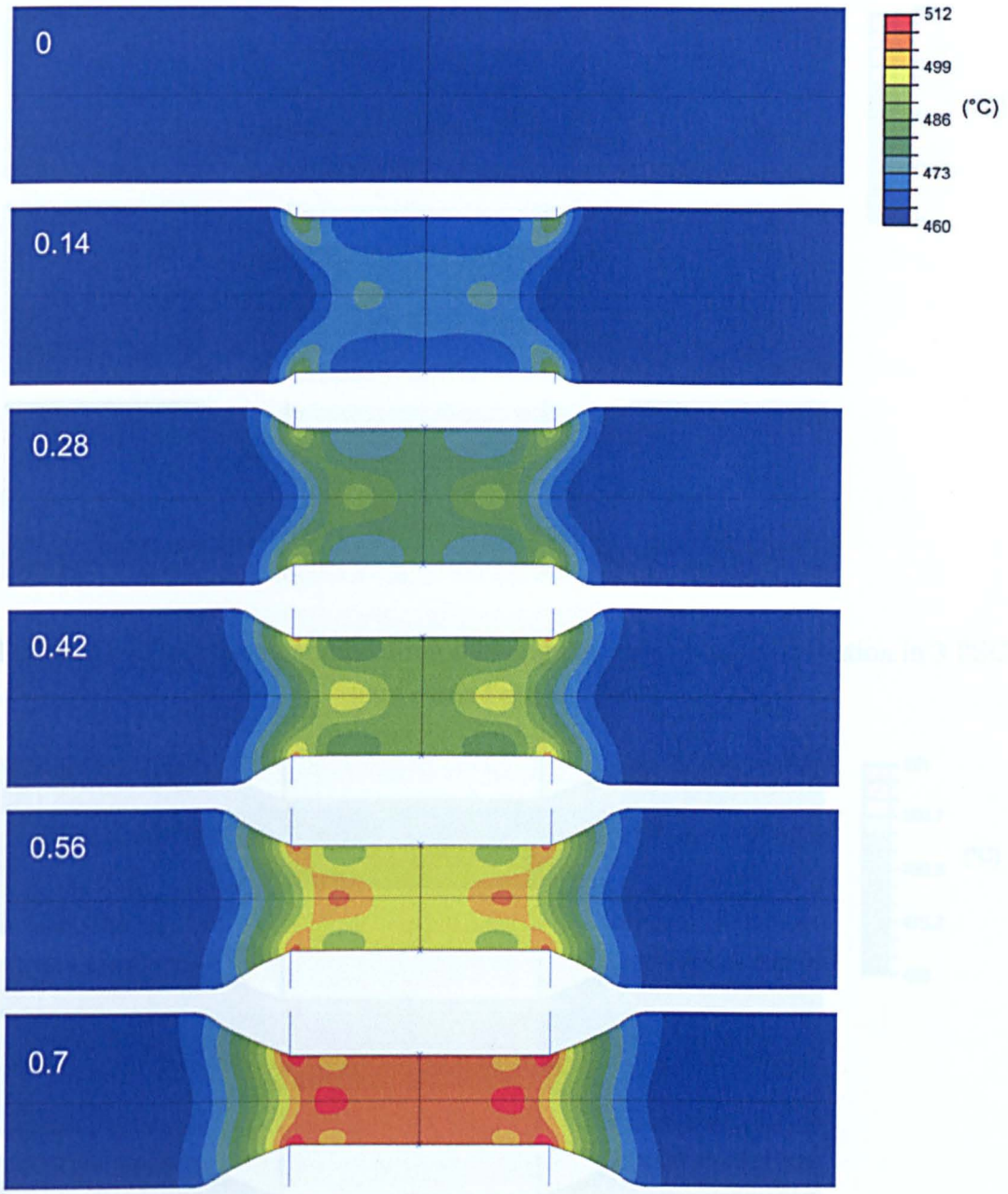

Figure 69 – Finite element modelling showing the temperature distribution as a PSC test at 460°C and $5s^{-1}$ progresses. Sample strains are given by the white numbers on each model

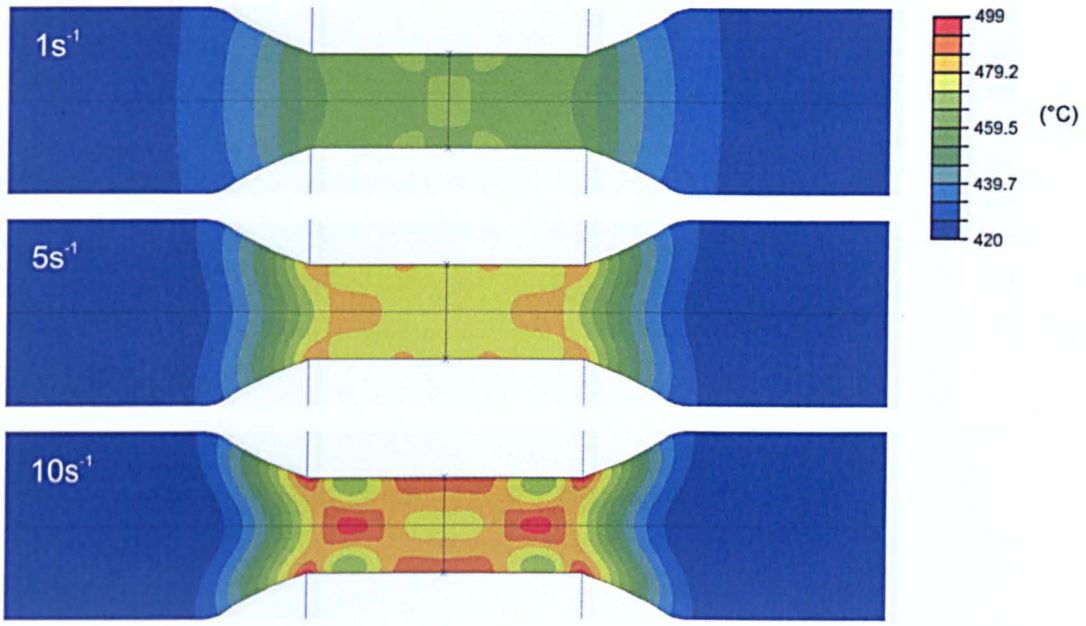

Figure 70 – Finite element modelling showing the temperature distribution in 3 PSC tests carried out at 420°C

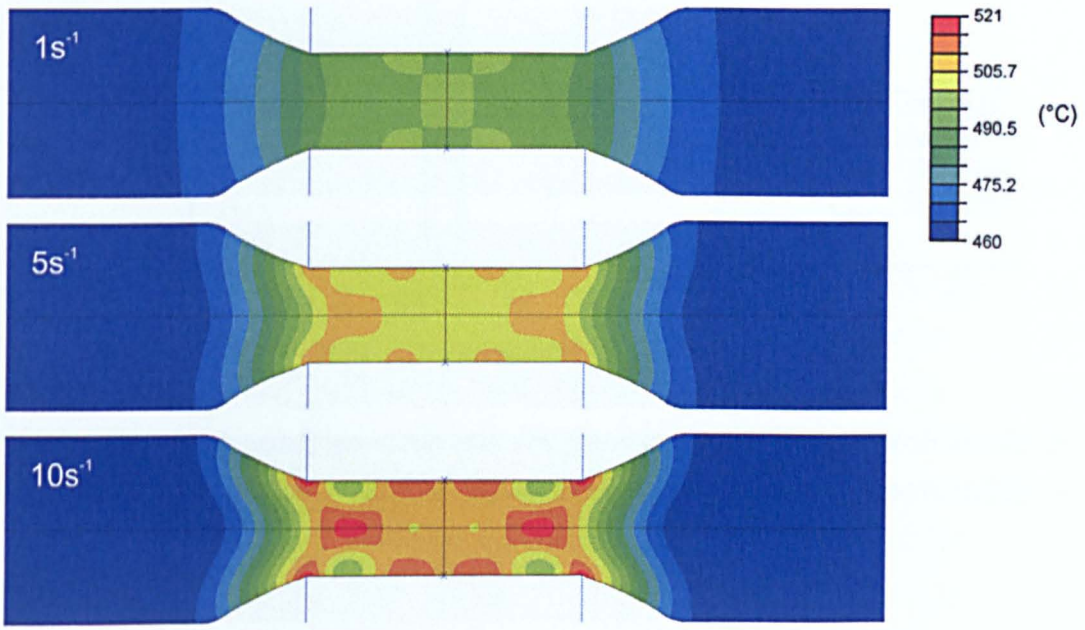

Figure 71 – Finite element modelling showing the temperature distribution in 3 PSC tests carried out at 460°C

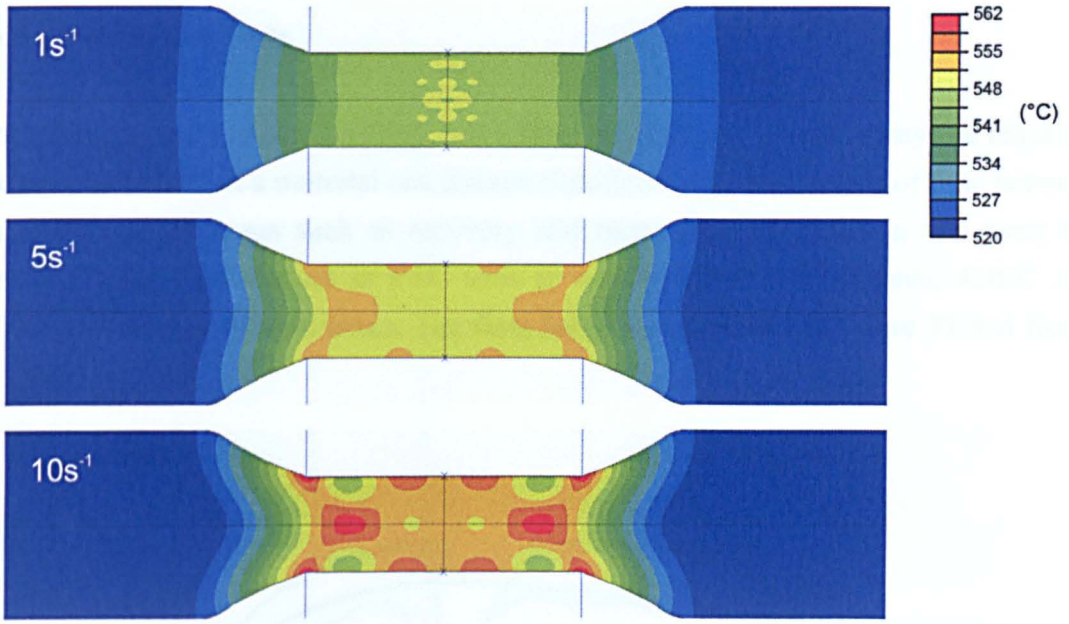

Figure 72 – Finite element modelling showing the temperature distribution in 3 PSC tests carried out at 520°C

4.3.5 Double Hit Tests

When carrying out industrial rolling, more than one pass will almost always be required. The microstructure of a material can change significantly in the periods of time between passes due to processes such as recovery and recrystallisation, and in this work the inter-pass time was studied in PSC tests at two different temperatures, 420°C and 500°C, and a range of hold times. The flow behaviour is shown in figure 73 and figure 74.

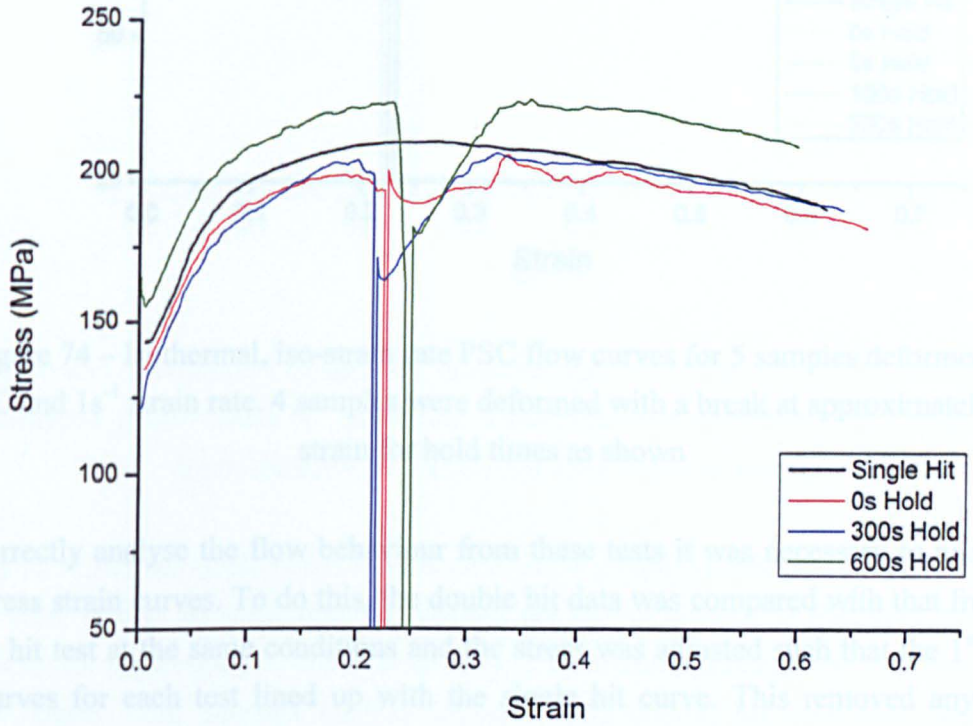

Figure 73 – Isothermal, iso-strain rate PSC flow curves for 4 samples deformed at 420°C and $1s^{-1}$ strain rate. 3 samples were deformed with a break at approximately 0.25 strain for hold times as shown

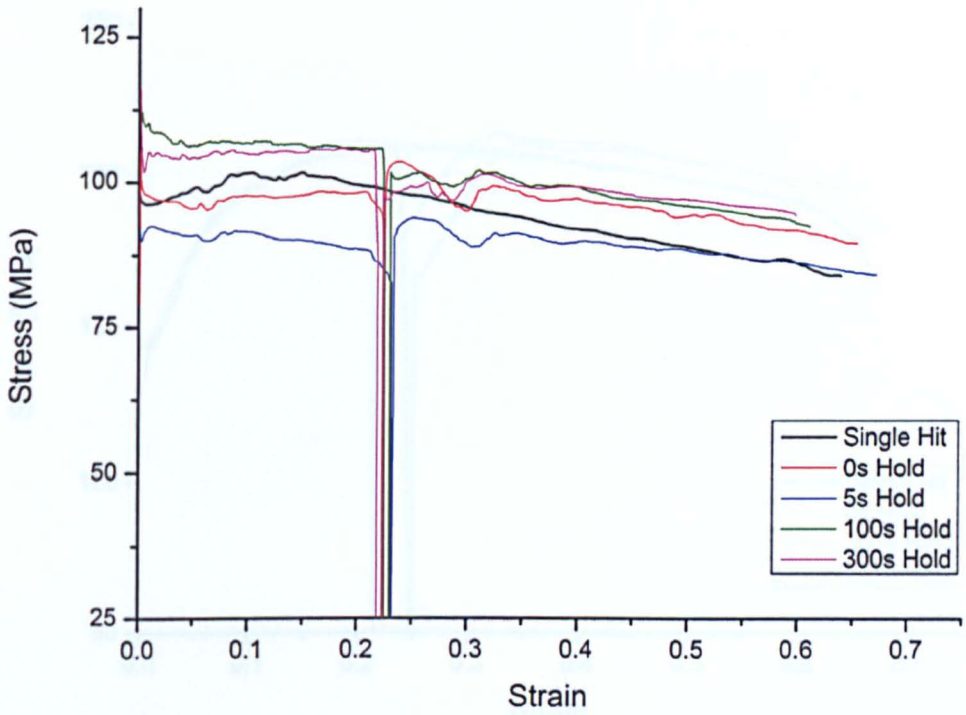

Figure 74 – Isothermal, iso-strain rate PSC flow curves for 5 samples deformed at 500°C and $1s^{-1}$ strain rate. 4 samples were deformed with a break at approximately 0.25 strain for hold times as shown

To correctly analyse the flow behaviour from these tests it was necessary to normalise the stress strain curves. To do this, the double hit data was compared with that from the single hit test at the same conditions and the stress was adjusted such that the 1st hit of the curves for each test lined up with the single hit curve. This removed any small inconsistencies, from differing initial microstructures or small changes in the test, and allowed any changes in the 2nd hit to be compared. The normalised flow curves from these tests are shown in figure 75 and figure 76.

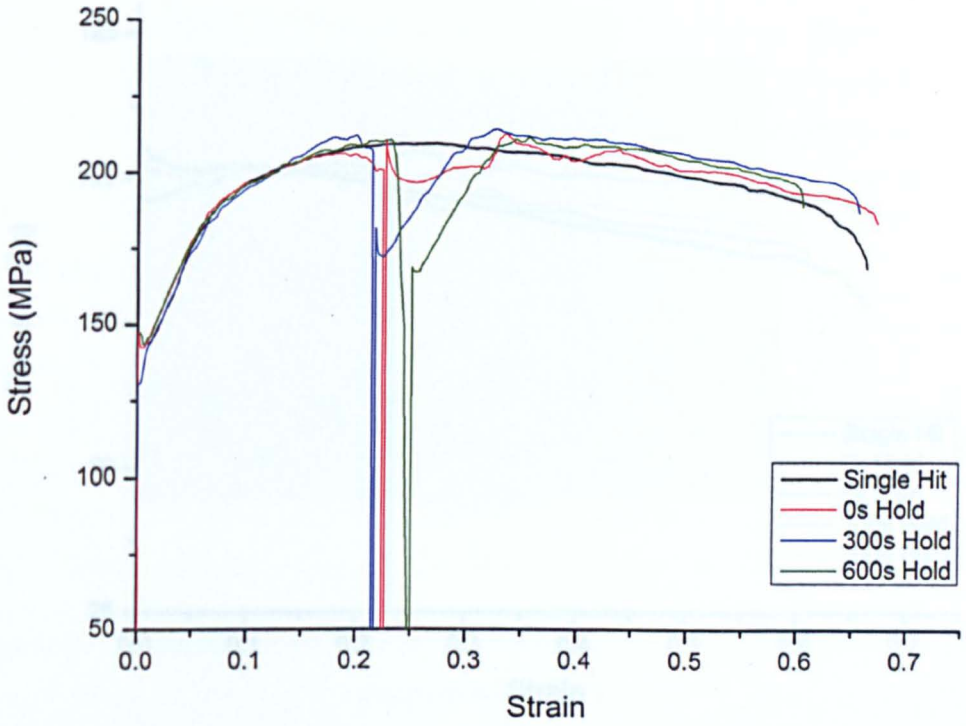

Figure 75 – Normalised isothermal, iso-strain rate PSC flow curves for 4 samples deformed at 420°C and $1s^{-1}$ strain rate. 3 samples were deformed with a break at approximately 0.25 strain for hold times as shown

Figure 75 shows the stress-strain behaviour of the 4 samples deformed at 420°C and $1s^{-1}$ strain rate. It can be seen that the double hit curves generally followed the same behaviour as the single hit curve with only 2 noticeable differences. The stresses at higher strains were perhaps slightly higher in the double hit tests than would be expected from the single hit behaviour, although this is at most a difference of approximately 8MPa, which is felt to be within experimental error. The other interesting point is the start of the second hit in the tests that had 300s and 600s hold times. Here it can be seen that the yield point dropped to a level below that in the 0s hold test and that the return to the stresses of the single hit curve was at a similar gradient to that experienced in the initial parts of all tests. It should, however, be noted that these initial parts of the curves were often strongly affected by changes in strain rate at the point that the tools made contact with the sample, and thus a significant correction was applied in these regions, see section 3.2.5.

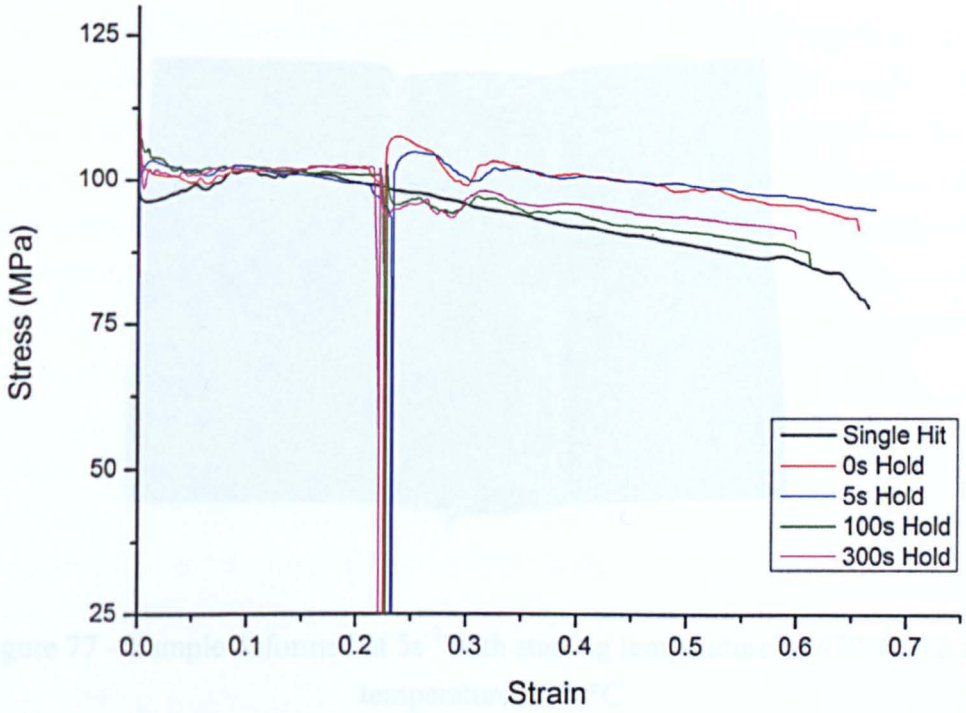

Figure 76 – Normalised isothermal, iso-strain rate PSC flow curves for 5 samples deformed at 500°C and $1s^{-1}$ strain rate. 4 samples were deformed with a break at approximately 0.25 strain for hold times as shown

Figure 76 shows the stress-strain behaviour of the 5 samples deformed at 500°C and $1s^{-1}$ strain rate. It appears that there was a small rise in stress following the hold period with the tests at 0s and 5s; however, this was relatively small when compared to the experimental variation between tests, as seen in figure 74, and therefore was not considered to be significant. It is also possible that the small drop in yield strength for the samples held for 100 and 300s were true material effects but, again, they were smaller than the experimental variation seen so may be errors.

4.3.6 Cold Tools Tests

Tests were carried out to look at the effect of non-isothermal compression using 70°C tools. Both tests showed shear fracture occurring at the shoulders of the samples (see figure 77 and figure 78), similar to that discussed in section 4.2.

Figure 77 – Sample deformed at $5s^{-1}$ with starting temperature of 470°C and tool temperature of 70°C

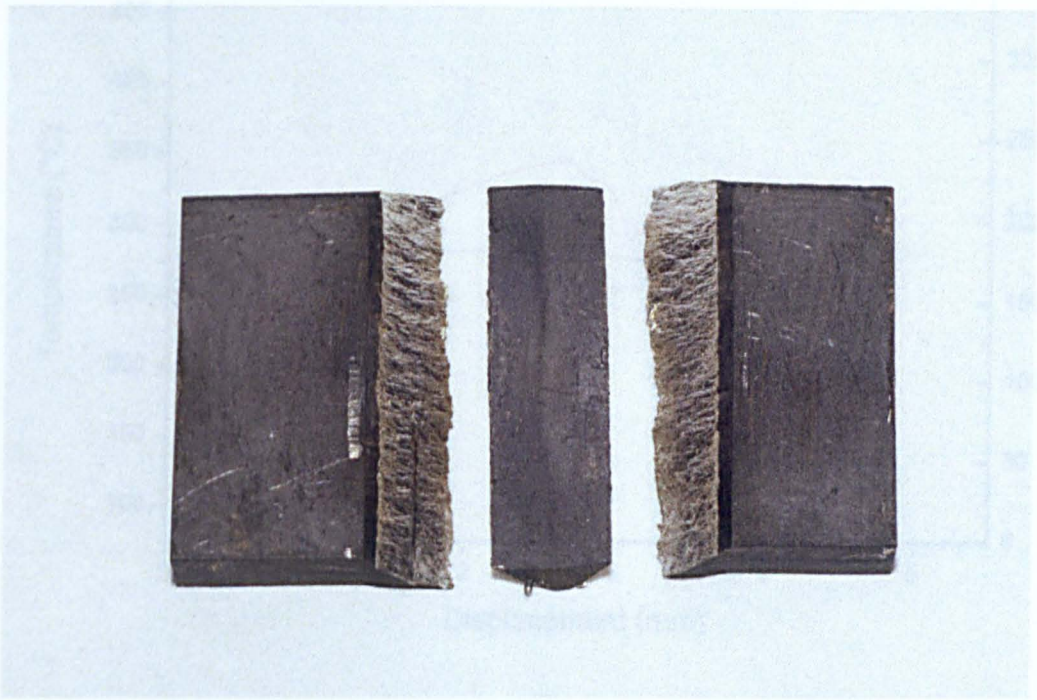

Figure 78 – Sample deformed at $0.5s^{-1}$ with starting temperature of 470°C and tool temperature of 70°C

As can be seen in figure 78, the sample deformed at $0.5s^{-1}$ fractured completely through and the difference in fracture behaviour between the two samples can be understood by looking at the temperature changes during deformation, see figure 79. These graphs

show the load rather than stress due to the fact that the stress calculations require accurate measurements of the final sample shape and this was not possible for these specimens. However, the load plot clearly shows the point of fracture in the sample deformed at $0.5s^{-1}$ and therefore is adequate in this situation. Figure 79 shows that, due to deformation heating, the temperature in the centre of the sample deformed at $5s^{-1}$ never dropped below the starting temperature; therefore, it would not be expected to have undergone fracture in this region. However, it can be clearly seen in figure 77 that fracture occurred at the surface, where the heat loss to the tools was greatest.

From figure 79 it can also be seen that the sample deformed at $0.5s^{-1}$ cooled down relatively quickly and the temperature at which fracture occurred (signified by the dramatic drop in load) was approximately 382°C; the Zener-Hollomon parameter at that point was $1.03x10^{17}\ s^{-1}$.

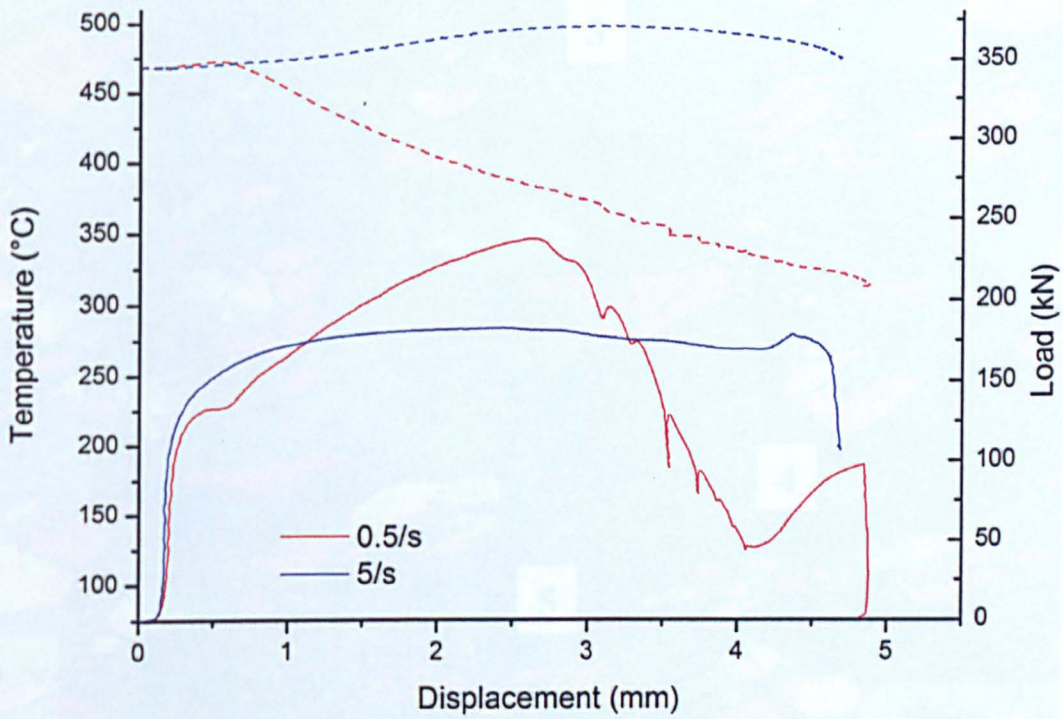

Figure 79 – Graph showing the load (solid lines) and temperature (dotted lines) experienced by 2 samples starting at 470°C and undergoing deformation with 70°C tools

4.4 Microstructure

Figure 80 shows a representative microstructure of Elektron 675 deformed in plane strain compression. It contains most of the features seen in any deformed microstructure studied in this work and will be used to illustrate the major features before they are discussed further, along with any changes due to either strain or processing parameters, in later sections.

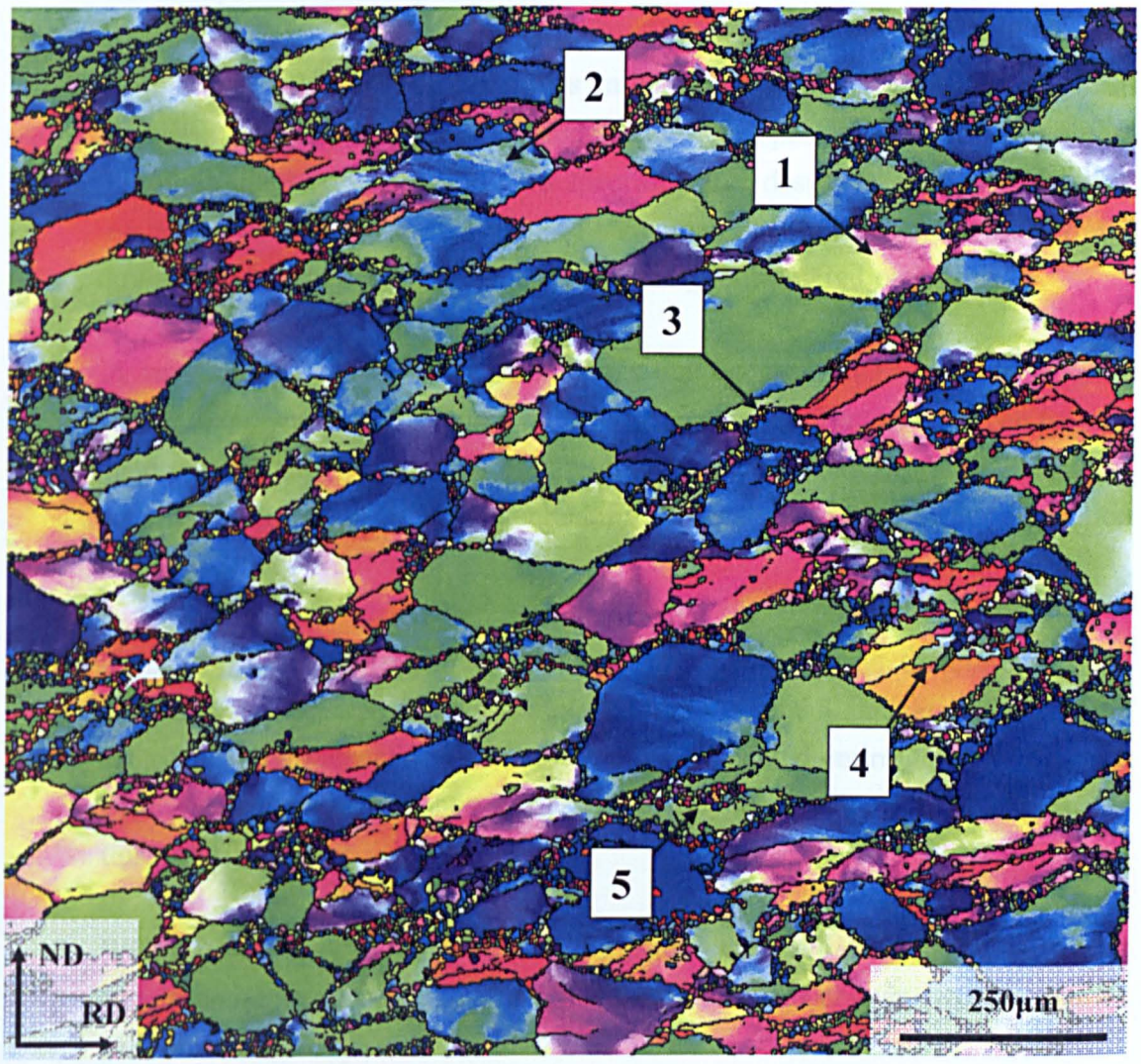

Figure 80 – EBSD map (IPF Colouring) showing a sample deformed in plane strain compression to a total strain of 0.7 at 460°C and $5s^{-1}$

The features indicated in figure 80 are explained below:

1. The strain applied to the material caused relatively large deformation to occur within many grains, and in EBSD this rotation across the grain is shown by the variation in orientation and thus colour. It can also be seen that the grain is no longer equiaxed and has elongated in the rolling direction. These changes were similar for most of the grains in the sample; however, the specific colouring does not always show them up as well as here.

2. Similarly to point 1, this grain shows variation in colour and thus has significant disorientation across it. In this particular case it is possible to see bands across the grain due to repeated slip on a specific plane, described in greater detail in section 4.4.6. Evidence of these slip bands can also be seen from the serrated grain boundary between this grain and the neighbouring red/pink grain.

3. A very influential microstructural change that occurred in Elektron 675 during deformation was the development of dynamic recrystallisation. This can be seen here and in many other areas of the microstructure, having formed a necklace structure around the grain boundaries. Further analysis is carried out in section 4.4.4.

4. Twinning is a more important feature at lower strains and therefore was not especially widespread in this sample, although point 4 indicates a remaining twin boundary. Generally twins would have consumed entire grains by a strain of 0.7, and therefore the boundaries have disappeared. Section 4.4.3 discusses this in further detail.

5. While the majority of dynamic recrystallisation occurred on grain boundaries, a certain amount forms on either twin-matrix boundaries or twin-twin boundaries as shown here.

4.4.1 Variation with Strain

A sequence of tests was carried out at intervals of strain up to 0.7 in order to study the evolution of the microstructure. EBSD maps were carried out on the deformed and quenched microstructures and are presented in figure 81.

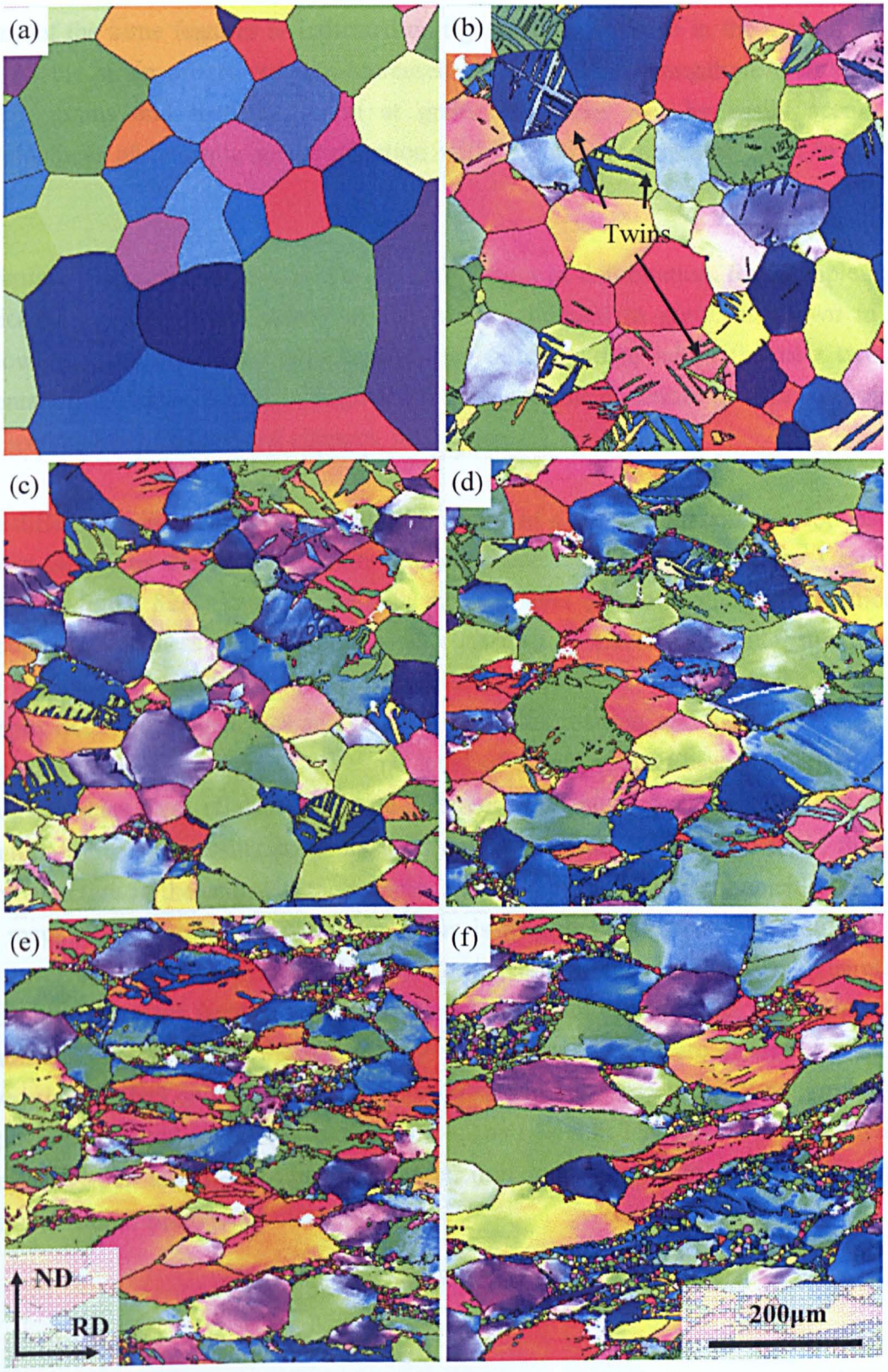

Figure 81 – ESBD maps (IPF colouring) on the transverse plane of 6 samples deformed at 460°C and $5s^{-1}$ strain rate to varying levels of strain: (a) $\varepsilon = 0$, (b) $\varepsilon = 0.1$, (c) $\varepsilon = 0.2$, (d) $\varepsilon = 0.3$, (e) $\varepsilon = 0.5$, (f) $\varepsilon = 0.7$

Many of the same features as indicated on figure 80 can be seen in the maps in figure 81. As the strain progressed, the increased levels of grain elongation, disorientation within grains and recrystallisation at grain boundaries can be easily seen. The development of dynamic recrystallisation will be studied in greater depth in section 4.4.4.

Twinning was particularly visible in the early stages of deformation, for example those indicated in figure 81(b). Many of the twins continued to grow, as shown in the following maps, and eventually caused the entire grain to adopt the new twinned orientation. Evidence for this was given by studies on the quantities of twin boundaries, see section 4.4.3, and textural changes, see section 4.5.1.

The differences in strain through the full thickness of a plane strain compression test are shown clearly by the levels of grain elongation and recrystallisation in the 3 samples shown in figure 82. It can be seen here that the level of strain changed dramatically through the thickness of the samples, and consequently affected the microstructure. It can also be seen that the change in strain was not necessarily symmetrical across each sample, due to heterogeneities and shear bands in deformation, and therefore, the centre of each sample did not have the same level of strain in each case. Generally these inconsistencies were related to minute differences in the tool alignment in the TMC machine or the processing conditions. In order to obtain an EBSD map of the true microstructure in the centre of the sample, and average out the heterogeneities present, the maps would need to be much larger than is feasible at the step sizes required, and the level of shear bands would still create differences between samples. Therefore, although most maps were carried out in the same area of each sample, the deformation conditions experienced in the region may vary. These issues were generally found to have a large effect on the amount of recrystallisation that happened, but not on the size of the recrystallised grains, see sections 4.4.4.2 and 4.4.4.3. The variation in the level of recrystallisation also had a knock-on effect, introducing errors in further analyses of recrystallisation behaviour.

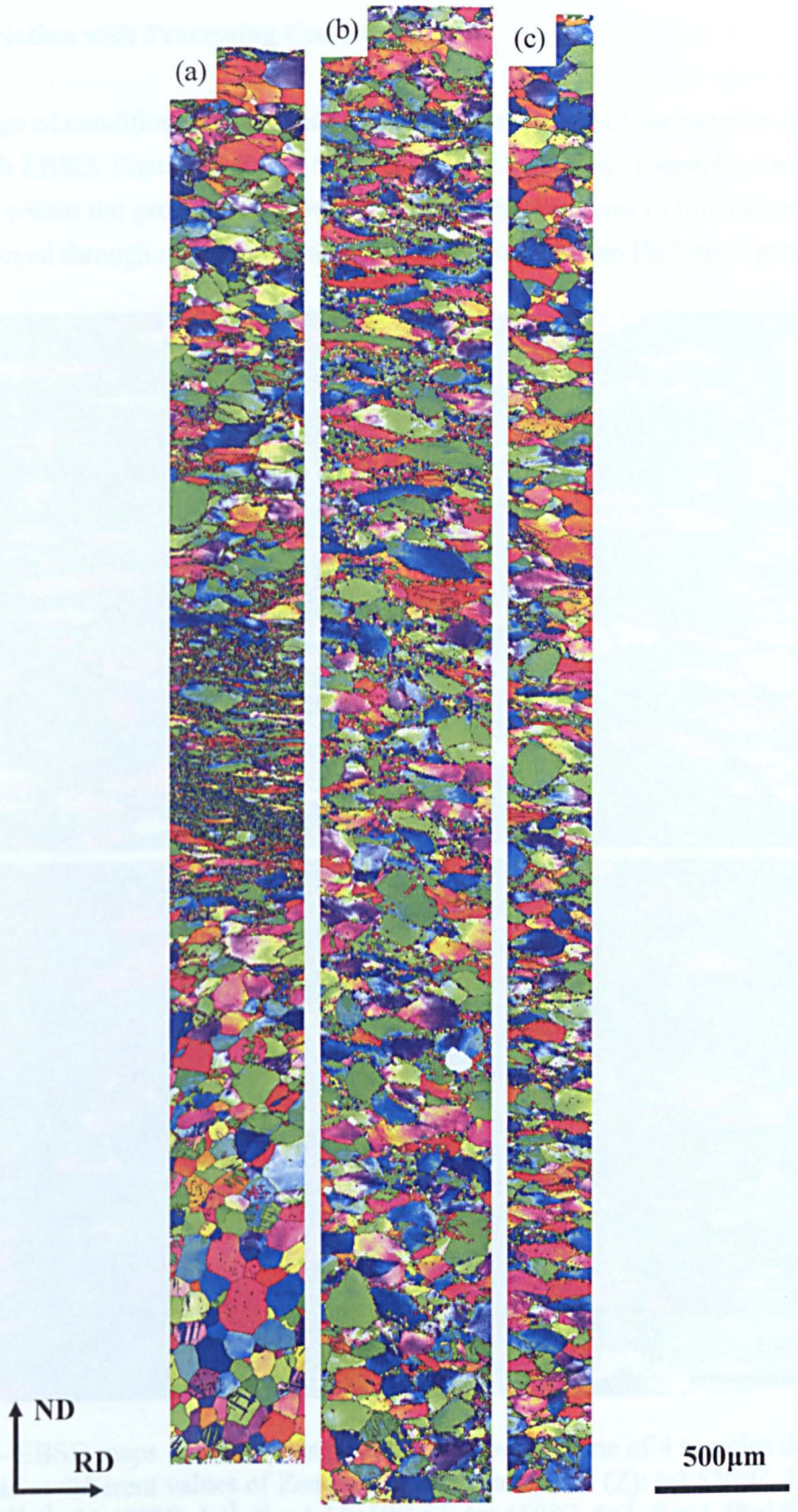

Figure 82 – EBSD maps (IPF colouring) showing the full thickness of 3 samples deformed at: (a) 440°C $10s^{-1}$, (b) 480°C $5s^{-1}$, (c) 480°C $1s^{-1}$

4.4.2 Variation with Processing Conditions

A wide range of conditions were tested in this work and many of the samples have been studied with EBSD. Figure 83 shows a representative selection of samples over the full range of Z within the process window. This shows the variation in microstructure that can be achieved through deformation at differing levels of Zener-Hollomon parameter.

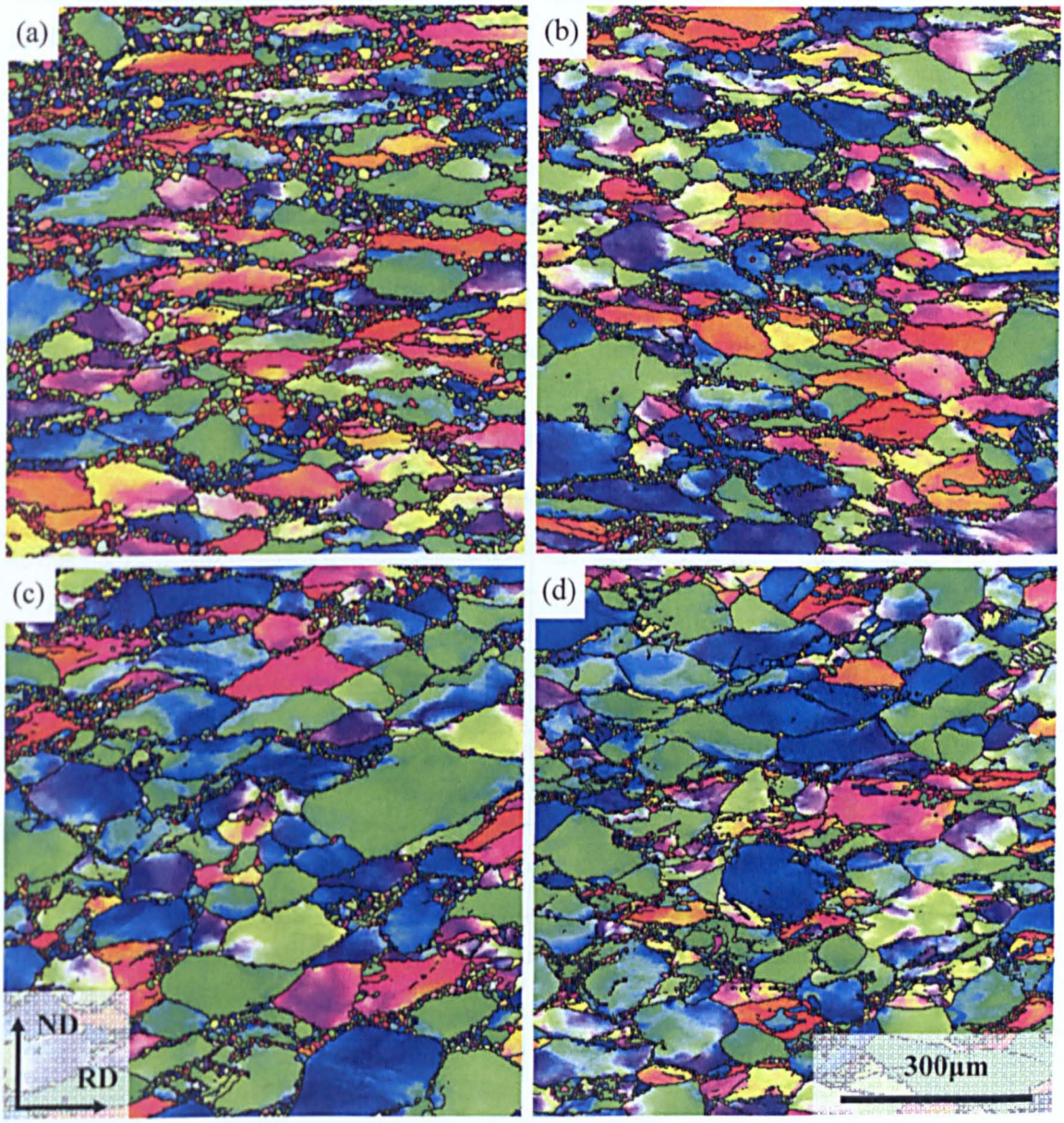

Figure 83 – EBSD maps (IPF colouring) on the transverse plane of 4 samples deformed to 0.7 strain at different values of Zener-Hollomon parameter (Z): (a) 520°C, $1s^{-1}$, Z = $2.00x10^{14}s^{-1}$, (b) 480°C, $1s^{-1}$, Z = $1.15x10^{15}$ s^{-1}, (c) 460°C, $5s^{-1}$, Z = $1.48x10^{16}$ s^{-1}, (d) 420°C, $5s^{-1}$ Z = $1.15x10^{17}$ s^{-1}

There were various differences between the samples shown in figure 83. One major difference was the size and amount of dynamically recrystallised grains present. Both of these factors appear to have decreased with increasing Z and are analysed further in sections 4.4.4.2 and 4.4.4.3. The other noticeable difference between the samples was the apparent decrease in the number of red coloured grains as Z increases. In the IPF colouring system used here, red grains correspond to those that have the c axis aligned with the transverse direction. The texture variations with Z are discussed further in section 4.5.2.

4.4.3 Twin Development

Figure 84 shows the presence of twin boundaries at different levels of strain in samples that were deformed at 460°C and $5s^{-1}$ strain rate, a condition approximately in the middle, and representative, of the full range tested. The different types of twin boundary are represented by different coloured lines using the scheme given in table 15.

Table 15 – Different colours used to represent twin boundaries in figure 84

Twin	Colour
$\{10\bar{1}1\}$	Yellow
$\{10\bar{1}2\}$	Black
$\{10\bar{1}3\}$	Aqua
$\{10\bar{1}1\}-\{10\bar{1}2\}$	Lime Green
$\{10\bar{1}3\}-\{10\bar{1}2\}$	Dark Green
$(10\bar{1}2)-(\bar{1}012)$	Red
$(10\bar{1}2)-(01\bar{1}2)$	Blue
$(10\bar{1}2)-(0\bar{1}12)$	Pink

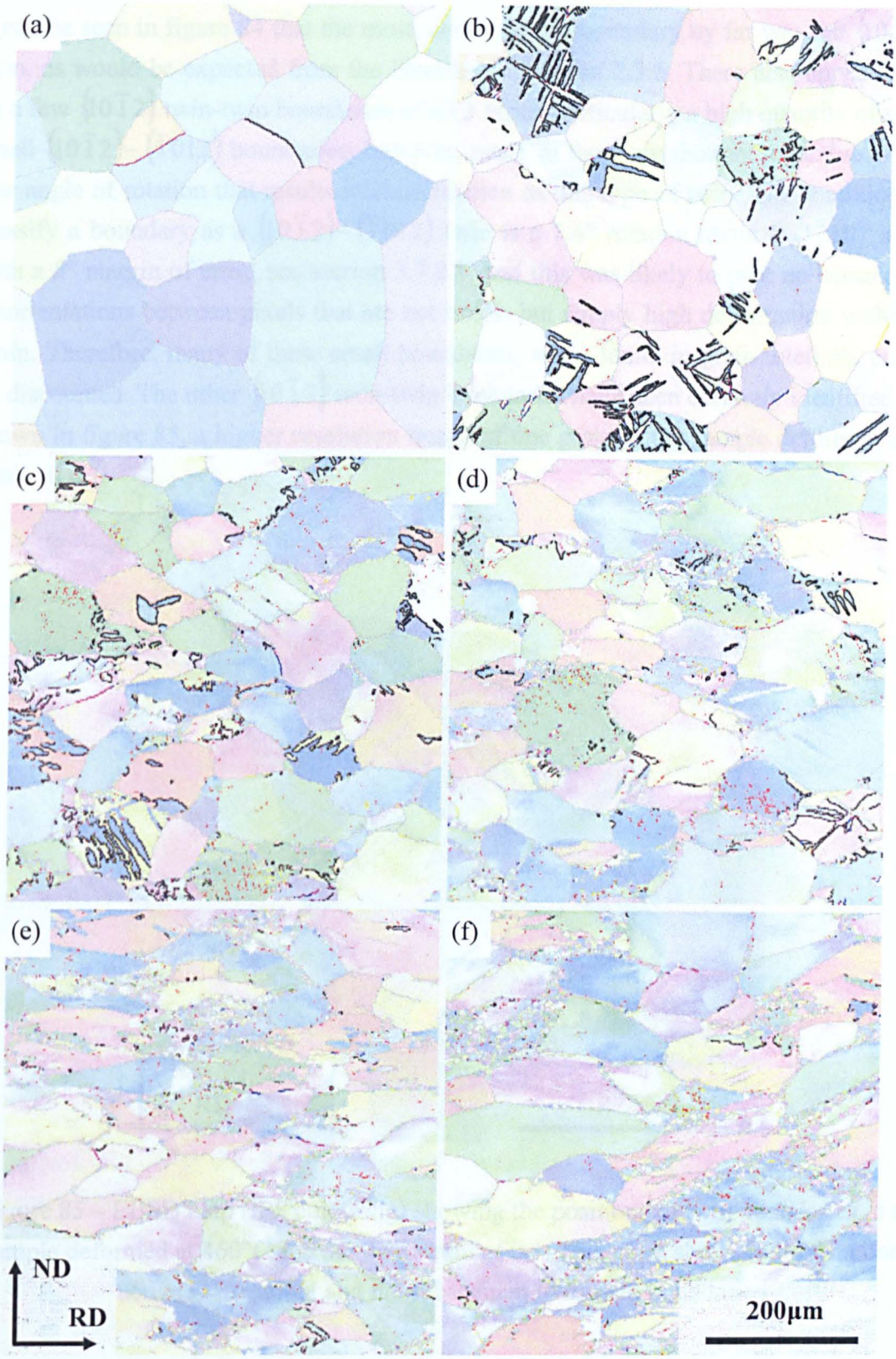

Figure 84 – EBSD maps (IPF colouring) showing the positions of twin boundaries in 6 samples deformed at 460°C and $5s^{-1}$ strain rate to varying levels of strain: (a) $\varepsilon = 0$, (b) $\varepsilon = 0.1$, (c) $\varepsilon = 0.2$, (d) $\varepsilon = 0.3$, (e) $\varepsilon = 0.5$, (f) $\varepsilon = 0.7$

It can be seen in figure 84 that the most common twin boundary by far was the $\{10\bar{1}2\}$ twin, as would be expected from the literature in section 2.3.5. There also appeared to be a few $\{10\bar{1}2\}$ twin-twin boundaries of all 3 types, particularly a high quantity of very small $(10\bar{1}2)$–$(\bar{1}012)$ boundaries; however, many of these are thought to be due to the low angle of rotation that results in classification as this type of twin. The condition to classify a boundary as a $(10\bar{1}2)$–$(\bar{1}012)$ twin is a 7.4° rotation about a $\langle 1\bar{2}10\rangle$ axis, with a 5° margin of error, see section 3.7.2.1, and this was likely to pick up occasional disorientations between pixels that are not twins, but simply high deformation within a grain. Therefore, many of these small boundaries, when found in grain interiors, could be discounted. The other $\{10\bar{1}2\}$ twin-twin boundaries have been correctly identified, as shown in figure 85, a higher resolution image of one grain in the sample deformed to a strain of 0.1.

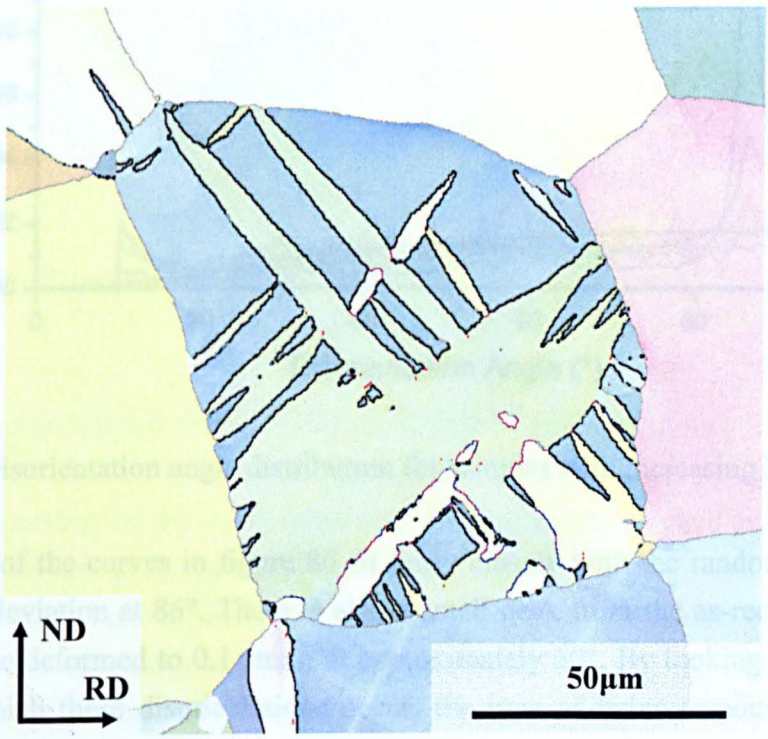

Figure 85 – EBSD map (IPF colouring) showing the positions of twin boundaries in a sample deformed at 460°C and $5s^{-1}$ to a strain of 0.1. This grain shows more than one active twin variant and the subsequent twin-twin boundaries

The most significant result shown in figure 84 is the dramatic reduction in the overall number of twin boundaries present from map (a) at 0.1 strain to map (f) at 0.7 strain. To quantify this reduction, a disorientation plot was made, as shown in figure 86. To calculate this, the software determined the disorientation between every pair of pixels in

the map and counted the frequency at which each angle of disorientation occurs. All disorientations below 10° were ignored so that the many low angle boundaries present did not overshadow the twin boundaries. The expected random distribution of angles[215] is shown by the dotted line and therefore any deviations from this must be caused by an increase in a specific boundary.

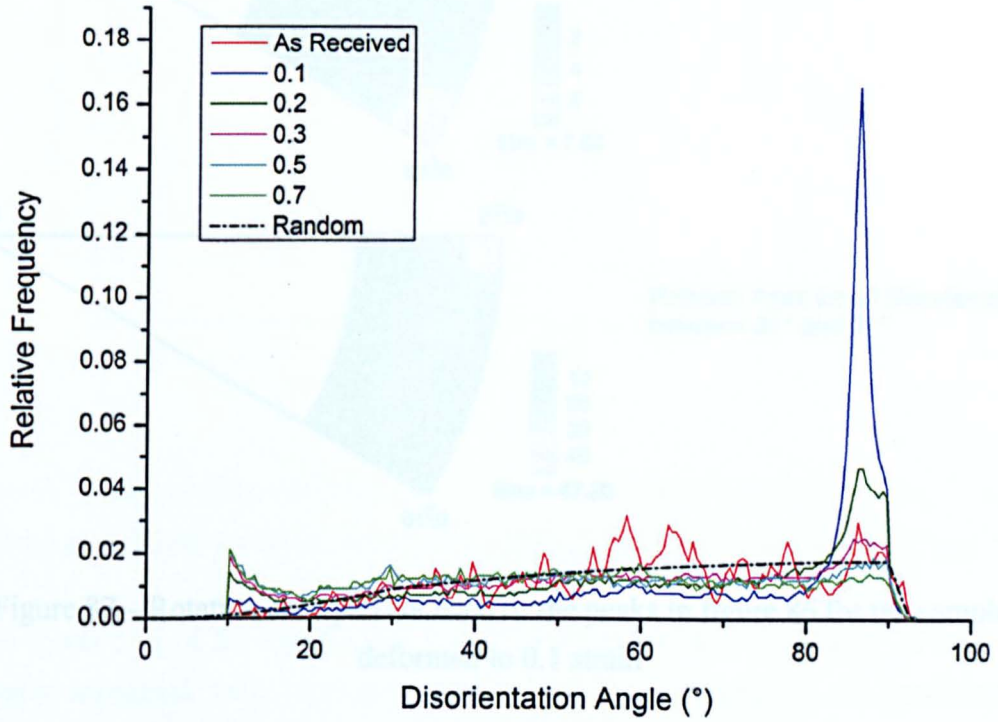

Figure 86 – Disorientation angle distribution for samples with increasing levels of strain

The majority of the curves in figure 86 fit fairly closely with the random distribution, apart from a deviation at 86°. There is also a small peak from the as-received material and the sample deformed to 0.1 strain at approximately 60°. By looking at the rotation axis about which these disorientations occur, the type of twins responsible could be confirmed. Figure 87 shows the rotation axes plots for both peaks in the distribution of the sample deformed to 0.1 strain. A range of 5 degrees either side of the peak was used to include all boundaries of that type and it can be seen that the majority of the boundaries with approximately 60° disorientation had the rotation about the $\langle 10\bar{1}0 \rangle$ axis and those with approximately 86° disorientation had the rotation about the $\langle 11\bar{2}0 \rangle$ axis. This confirmed that the peak at 60° corresponded to both $(10\bar{1}2)-(01\bar{1}2)$ and $(10\bar{1}2)-(0\bar{1}12)$ twin-twin boundaries, and that that at 86° corresponded to $\{10\bar{1}2\}$ twin-matrix boundaries. The as-received sample does not show any peak from the

$\langle 10\bar{1}0 \rangle$ axis and thus the peak in disorientation is not due to the presence of twins but is simply noise in the data.

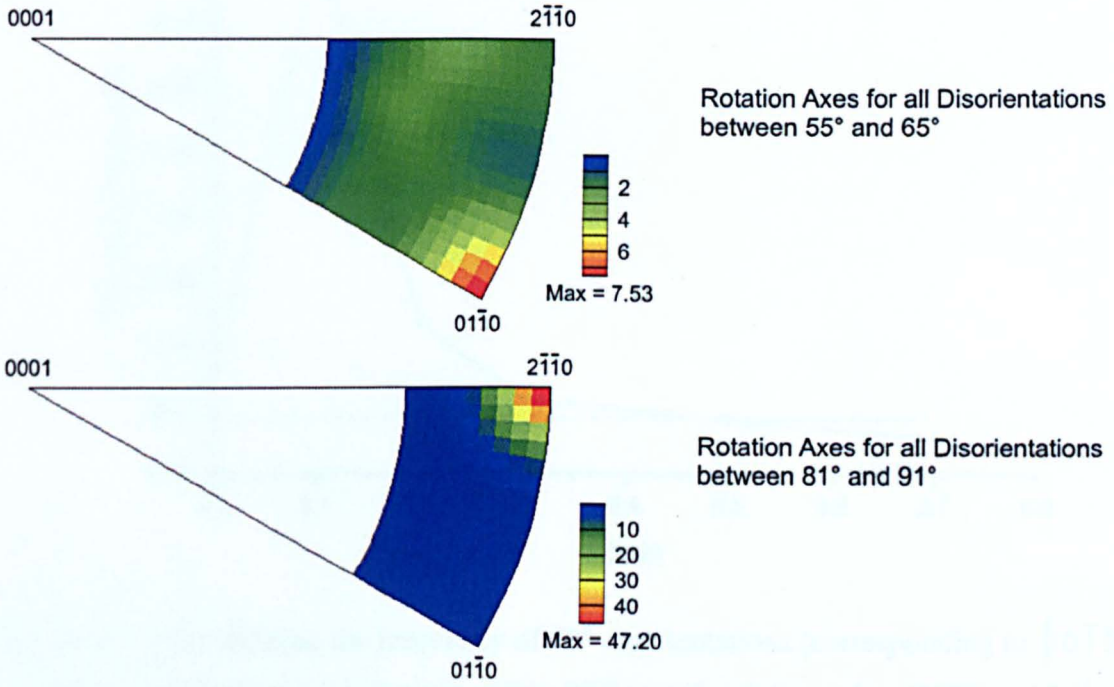

Figure 87 – Rotation axes plot for each of the peaks in figure 86 for the sample deformed to 0.1 strain

The most significant result shown by figure 86 is the frequency of 86° disorientations at different levels of strain. Figure 88 has been plotted to show the change in prevalence of this specific boundary as the strain increased. The dotted line marked at 0.0178 relative frequency shows the predicted random distribution for this particular disorientation angle. Therefore, it can be seen that there was a dramatic increase in $\{10\bar{1}2\}$ twin boundaries in the very early stages of deformation followed by an exponential decay type reduction back to the random frequency by approximately 0.3-0.4 strain. From the shape of the curve in figure 88 it would be expected that the peak in levels of $\{10\bar{1}2\}$ twin boundaries was not actually at 0.1, but at a higher frequency somewhere between 0 and 0.2 strain that has not been directly investigated. Further study would be required to obtain a more exact value for this peak.

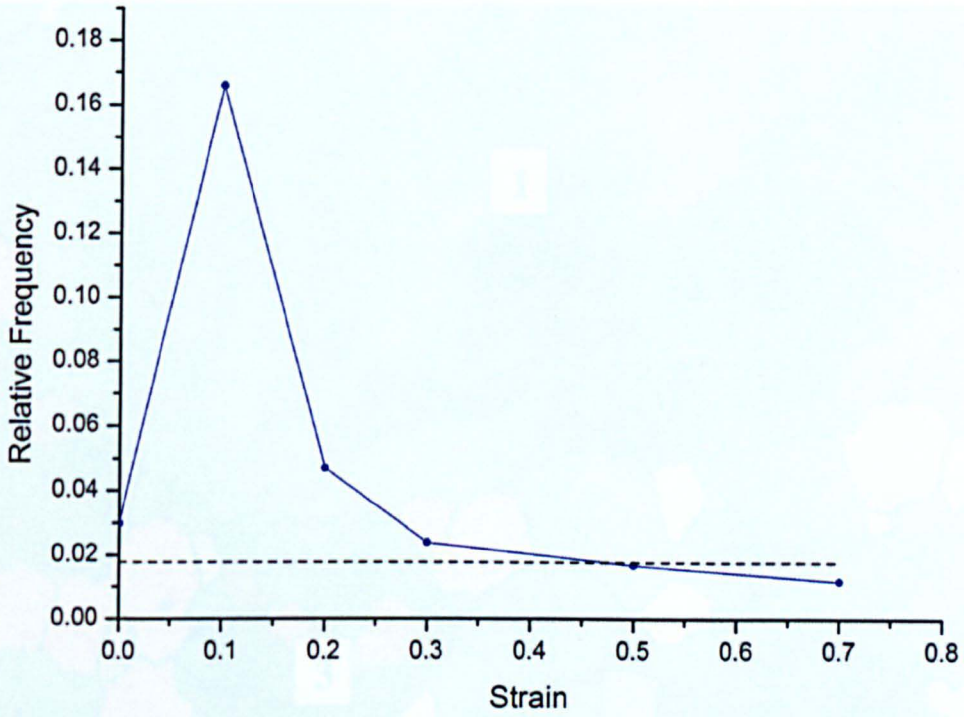

Figure 88 – Plot showing the frequency of 86° disorientations (corresponding to $\{10\bar{1}2\}$ twins) at different levels of strain within PSC samples deformed at 460°C and $5s^{-1}$

At the lower end of the distribution it can be seen that the frequencies of boundaries generally increased with increasing strain. This was an artefact of the calculation process due to the fact that the plot shows a relative frequency. Therefore, a decrease in the number of boundaries at 86° would increase the relative frequency of those at other disorientations.

4.4.4 Dynamic Recovery and Recrystallisation

Dynamic recrystallisation (DRX) occurred readily in almost all samples of Elektron 675 tested in this study and showed primarily the same features in and around the recrystallised grains. Figure 89 is a good example of a DRX microstructure that will be used to demonstrate the typical features present in all samples and introduce the following sections.

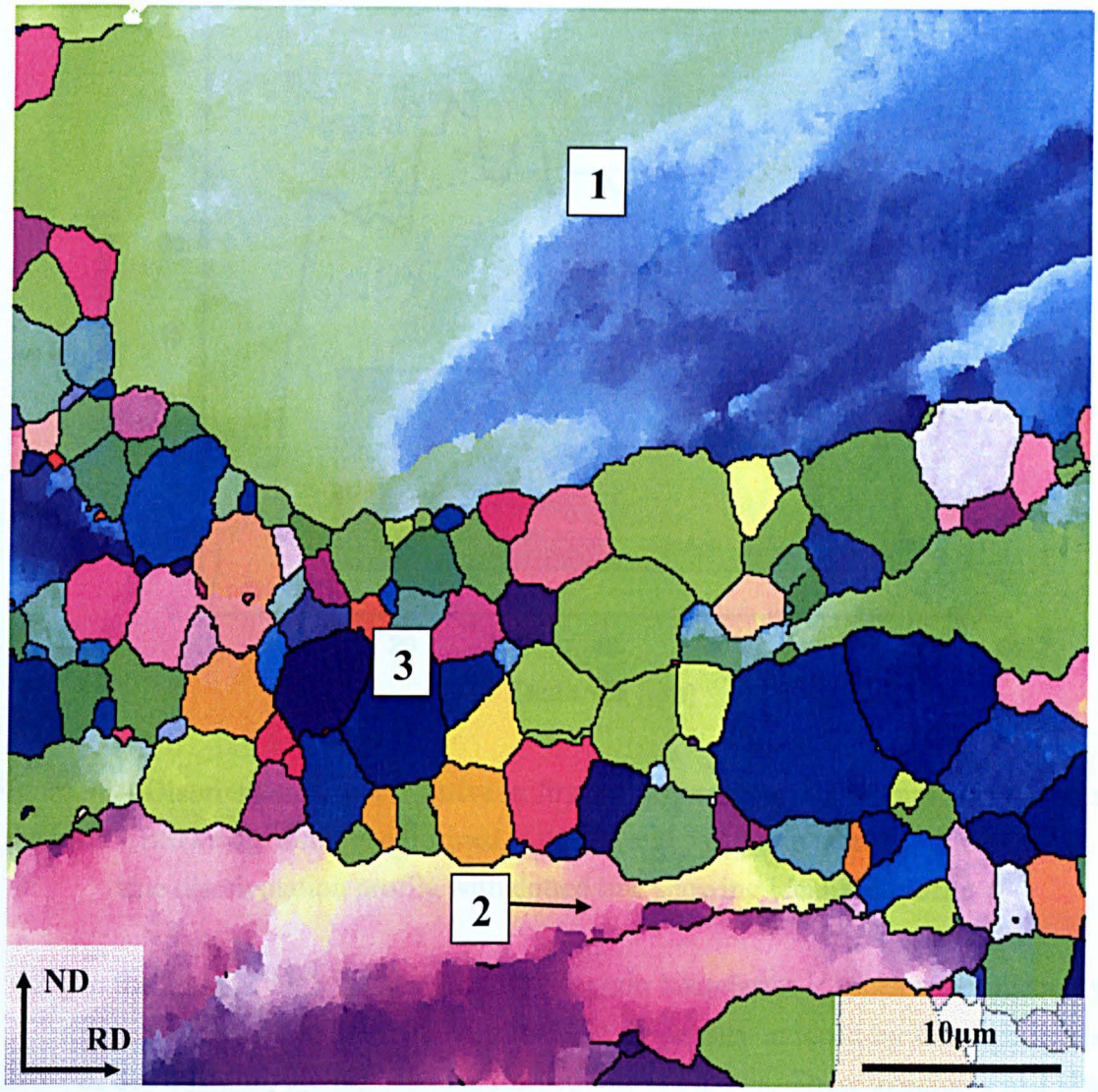

Figure 89 – EBSD map (IPF Colouring) showing a sample deformed in plane strain compression to a total strain of 0.7 at 440°C and $10s^{-1}$

1. The rotations across a grain, that show up as changes in the IPF colouring, were generally more pronounced in the regions close to a grain boundary. This is shown in more detail in figure 90, which displays the disorientation profile across a single grain in a sample deformed at 460°C and $5s^{-1}$. This was a particularly extreme case as the maximum disorientation reaches 28°, indicating a very high level of deformation within the grain. However, the graph shows the features that are present in many other grains, namely very rapid changes in disorientation close to the grain boundaries with a much slower change across the grain interior.

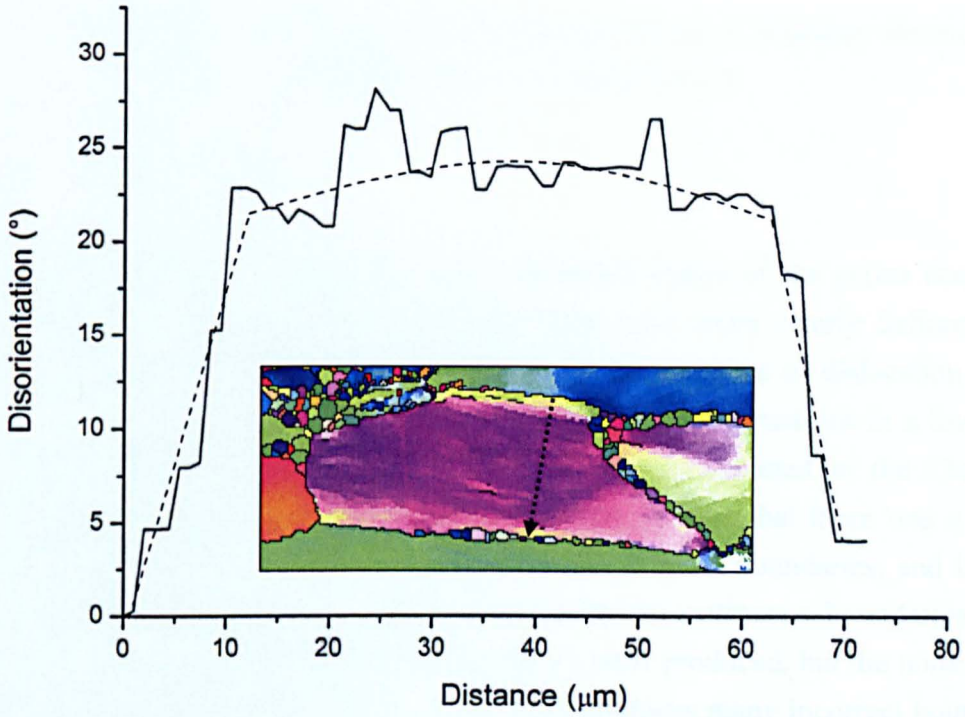

Figure 90 – Disorientation plot (relative to first point) across a single grain, as shown in the inset EBSD map. Sample deformed at 460°C and $5s^{-1}$ strain rate. Solid line shows true disorientation profile with dotted line showing idealised profile

2. In the areas of high rotation around the grain boundaries it appears that recovery was very active. Due to the high dislocation density induced by the high levels of deformation, the dislocations formed into subgrains. These subgrains had low angle boundaries (of the order of 2-10°) and were generally of a similar size to each other. The dependence of this size and other features on processing conditions is detailed in section 4.4.4.1.

3. Following further deformation in the region of high rotations and subgrains, fully recrystallised grains formed with high angle boundaries and low internal dislocation densities. As could be seen in figure 80, this dynamic recrystallisation happened almost exclusively at grain boundaries and is shown very clearly in figure 89. The DRX grains were all of a similar size, a factor that varied with processing conditions but not especially with strain, see section 4.4.4.3. Conversely the volume of recrystallised material that developed is strongly affected by strain, and less so by processing conditions, see section 4.4.4.2. The types of grain and grain boundary that showed a higher proclivity

for dynamic recrystallisation are discussed in terms of boundary disorientation, in section 4.4.4.4, and Schmid factor, in section 4.4.4.5.

4.4.4.1 Subgrain Formation

As discussed above, recovery in the highly deformed region of the grains near to the grain boundaries caused subgrains to form. These were more clearly defined in the samples deformed at lower values of Z, due to the greater ease of dislocation motion and recovery. Figure 91 shows a good example of subgrain structures in a low Z test ($2.00x10^{14}s^{-1}$) with the lower angle subgrain boundaries detected in the Channel 5 EBSD software (2-10°) shown as white lines. It can be seen that there was a greater density of low angle boundaries in the areas nearer to grain boundaries, and in many cases the subgrain structure is visible, albeit with discontinuous boundaries. Maps showing even lower angle boundaries, down to 1°, were produced, but the noise is very high because the inherent error in the EBSD data produces many incorrect boundaries. However, by studying both maps, one with a large amount of noise and the other showing discontinuous boundaries, the true substructure could be postulated. This is displayed in figure 92.

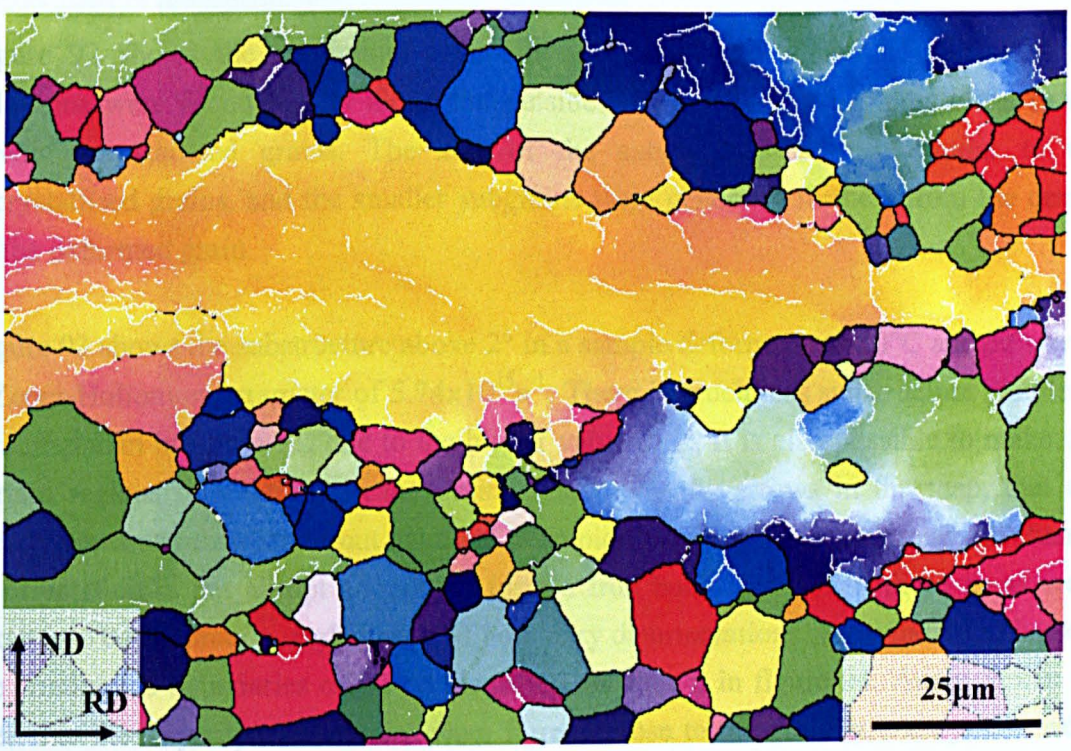

Figure 91 – EBSD map (IPF colouring) of a sample deformed at 520°C and $1s^{-1}$ strain rate with boundaries between 2 and 10° shown in white

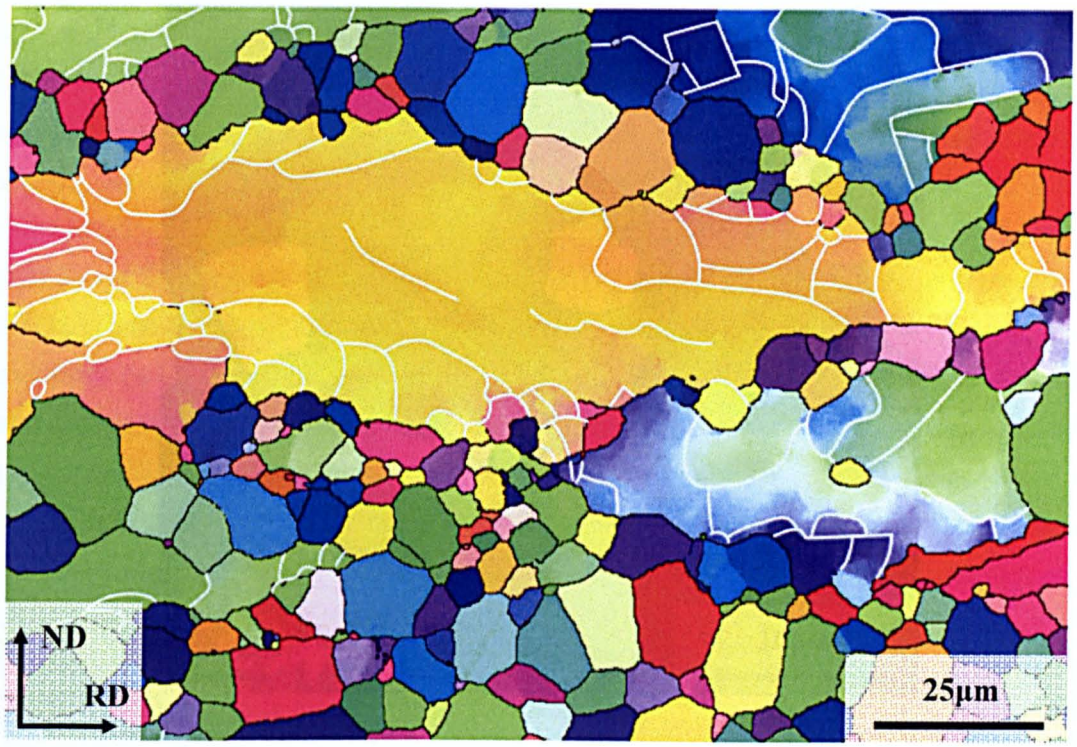

Figure 92 – EBSD map (IPF colouring) of a sample deformed at 520°C and $1s^{-1}$ strain rate with continuous subgrain boundaries superimposed in white

Figure 92 shows the continuous subgrain boundaries and it can be seen that the subgrains were found mostly along the outsides of the deformed grains, close to the newly recrystallised grains. The size of the subgrains was very similar to the recrystallised grains, and the smaller subgrains were generally furthest from the centre of the deformed grain.

Figure 93 shows the substructure above 2° in a sample deformed at 480°C and $5s^{-1}$, with a Zener-Hollomon parameter of $5.74x10^{15}s^{-1}$. There is much less substructure visible in this map than in figure 91, due to the higher value of Z. It is also possible to make out certain regions of rotations in the grains, shown by the arrows in the map, that are clearly areas of substructure but have not been picked out by the software as the change in orientation is not abrupt enough to form a true boundary. When these areas were taken into consideration, and a range of boundary disorientations were studied as before, the continuous boundaries could be identified, as shown in figure 94. Again, it can be seen that the majority of subgrains were formed close to the grain boundary, and were of approximately the same size as the already recrystallised grains.

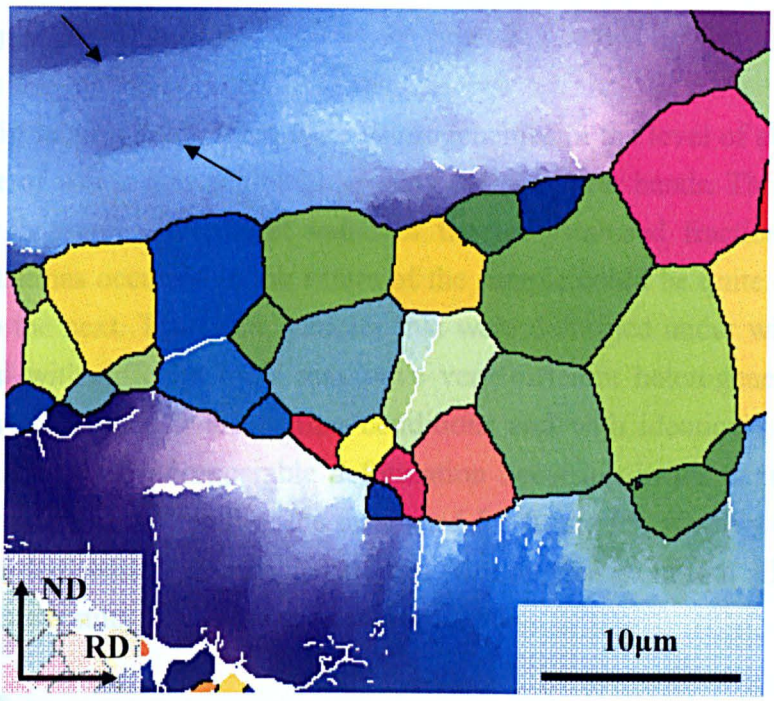

Figure 93 – EBSD map (IPF colouring) of a sample deformed at 480°C and $5s^{-1}$ strain rate with boundaries between 2 and 10° shown in white

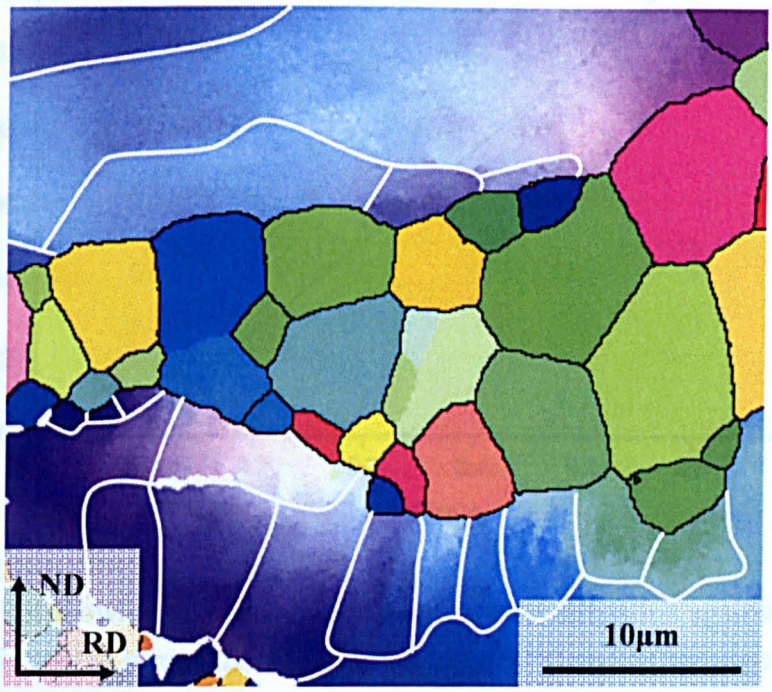

Figure 94 – EBSD map (IPF colouring) of a sample deformed at 480°C and $5s^{-1}$ strain rate with continuous subgrain boundaries superimposed in white

4.4.4.2 Recrystallised Fraction

As explained in section 4.4.1, there were heterogeneities in the level of strain across all samples, some of which also exhibited strongly defined shear bands. This made it hard to accurately measure a consistent value of the recrystallised fraction because the deformation that has occurred in the centre of the sample could be quite different from one sample to the next. Therefore, samples that were deformed under widely different conditions and with different tools may have very different heterogeneities, whereas those that were deformed under similar conditions and with identical tool alignment were more likely to have comparable deformation occurring in the centre, where the analysis was carried out. Therefore the tests used for figure 95, which were all carried out at the same temperature and strain rate and with no change in tool alignment, gave more comparable results than those used for figure 96.

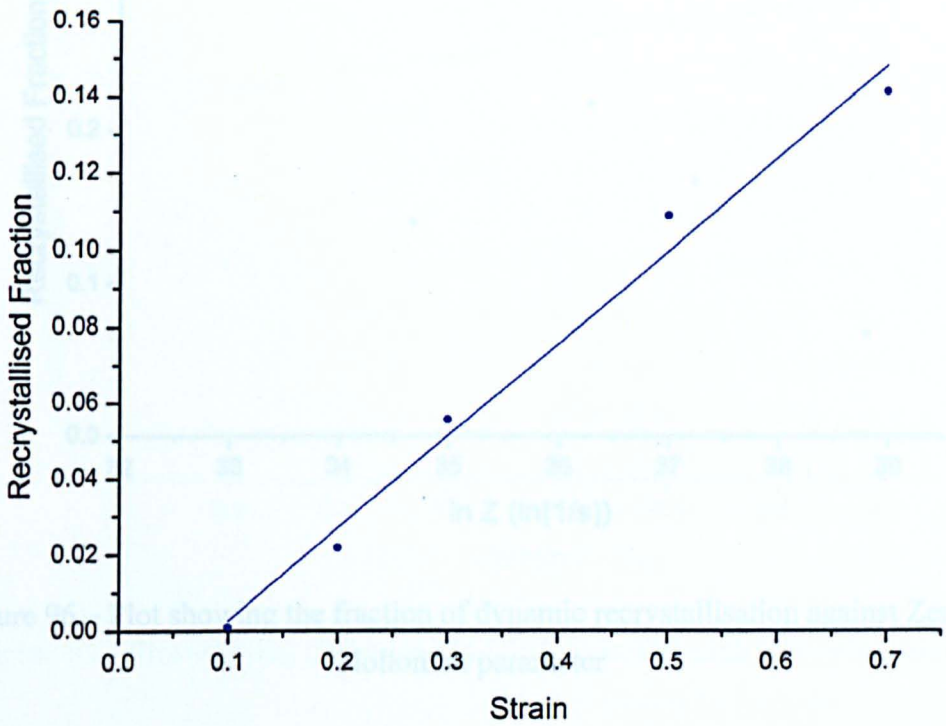

Figure 95 – Plot showing the fraction of dynamic recrystallisation against strain when deformed in plane strain compression at 460°C and $5s^{-1}$ strain rate

EBSD maps were used to measure the fraction of material that underwent dynamic recrystallisation in samples deformed at 460°C and $5s^{-1}$ strain rate to different levels of strain, as shown in figure 95. It is clear from this graph that the process of dynamic recrystallisation started at around 0.1 strain and then continued with an approximately

linear increase in the fraction recrystallised up to the maximum strain tested, 0.7. In this particular case, the maximum fraction of DRX grains was approximately 0.15.

Figure 96 shows the relationship between the Zener-Hollomon parameter and the fraction of recrystallised material at a strain of 0.7 over a range of processing conditions. It can be seen that there is a very large amount of scatter in the data. As explained above, the differences in deformation for these samples was greater due to the larger differences in deformation conditions and tool alignment. Therefore, the heterogeneities of strain are more influential than the Zener-Hollomon parameter.

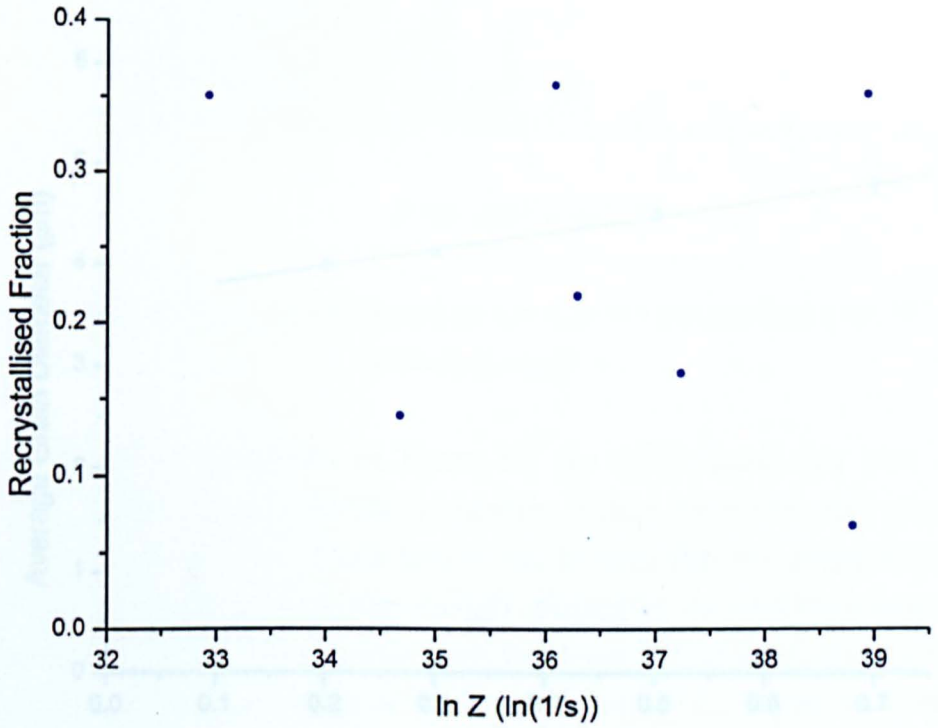

Figure 96 – Plot showing the fraction of dynamic recrystallisation against Zener-Hollomon parameter

4.4.4.3 Recrystallised Grain Size

The new analysis program was used to calculate the average size of the dynamically recrystallised grains from EBSD maps on a range of deformed samples. Figure 97 shows the change in recrystallised grain size as a function of the strain in samples deformed at 460°C and $5s^{-1}$ strain rate. The sample at 0.1 strain was ignored for this graph because there were not enough DRX grains to make a reasonable measure of the average grain size. It can be seen that the dynamically recrystallised grains only

increased in size very slightly as the strain increased. This small growth with increasing strain can also be seen in figure 98, which plots the distribution of DRX grain sizes in the same samples as figure 97. Here it can be seen that, while the distribution is of essentially the same shape at all levels of strain, the lower strain samples were more skewed towards the smaller sizes than the higher strain samples. Therefore, it can be confirmed that there was a small amount of grain growth occurring in the samples as the strain progressed. However, the increase in DRX grain size was much less than would be necessary to account for the large increase in DRX fraction, as displayed in section 4.4.4.2, and therefore much of the increase in DRX fraction must have come from newly formed grains.

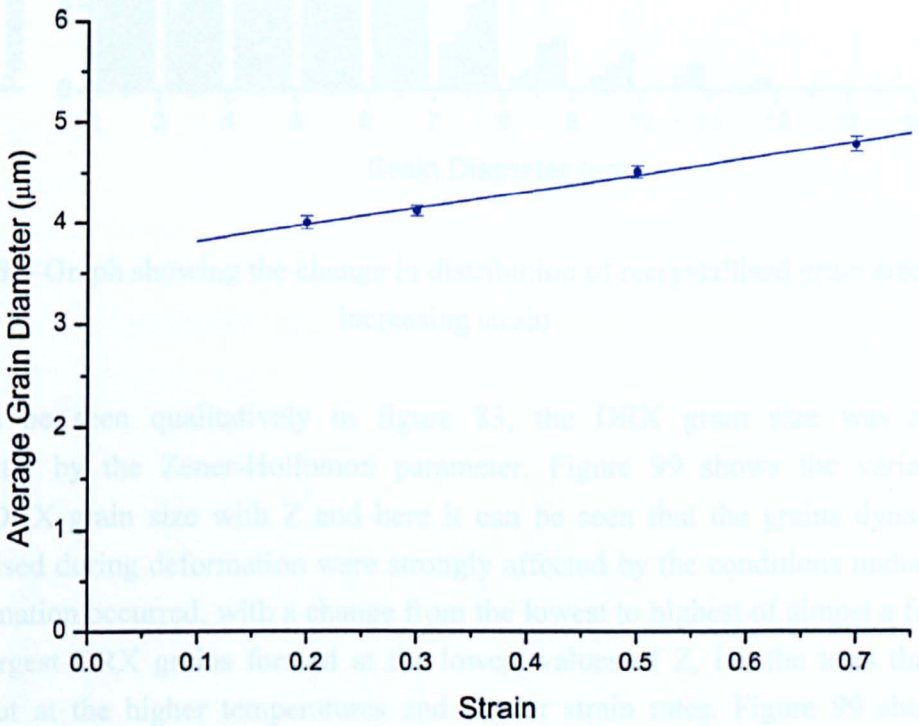

Figure 97 – Plot showing the change in DRX grain size with increasing strain

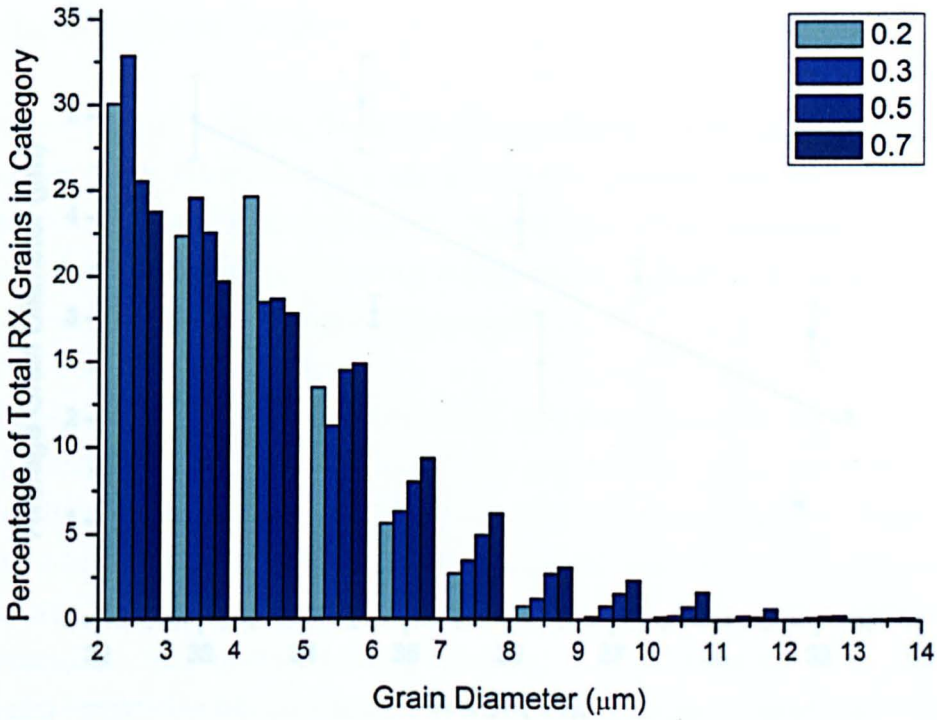

Figure 98 – Graph showing the change in distribution of recrystallised grain sizes with increasing strain

As could be seen qualitatively in figure 83, the DRX grain size was affected significantly by the Zener-Hollomon parameter. Figure 99 shows the variation in average DRX grain size with Z and here it can be seen that the grains dynamically recrystallised during deformation were strongly affected by the conditions under which the deformation occurred, with a change from the lowest to highest of almost a factor of 5. The largest DRX grains formed at the lowest values of Z, i.e. the tests that were carried out at the higher temperatures and slower strain rates. Figure 99 shows the correlation with the Zener-Hollomon parameter, calculated with the starting temperature of the test, whereas figure 100 shows the same data but using the final temperature of the test to calculate Z. It can be seen that the correlation is better when using the final temperature and therefore it can be concluded that the temperature rise during deformation had an effect on the final DRX grain size.

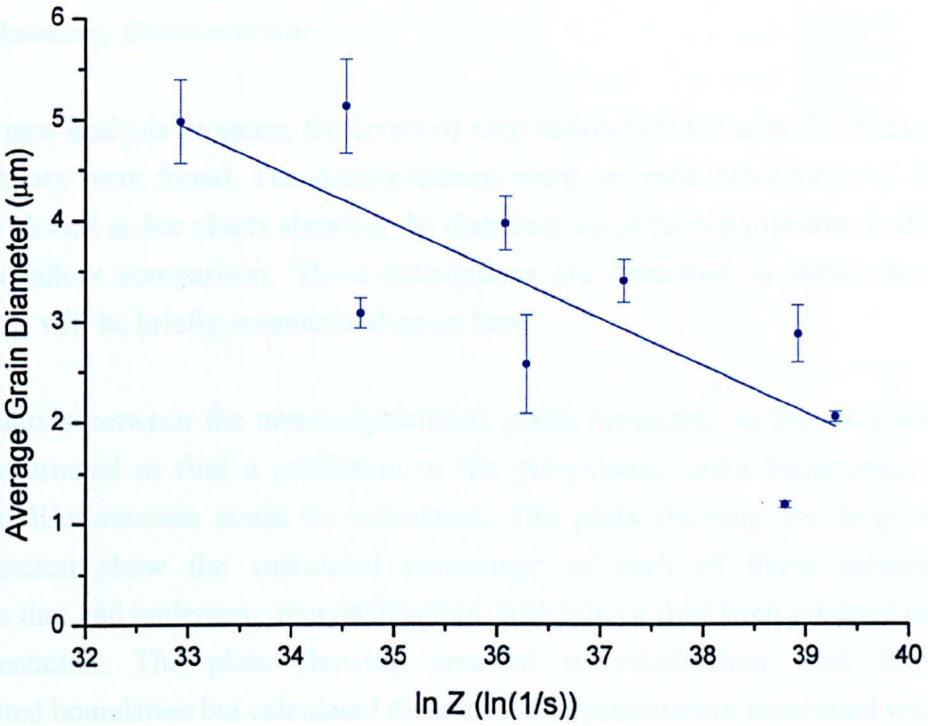

Figure 99 – Plot showing the recrystallised grain size against Zener-Hollomon parameter calculated using initial test temperature

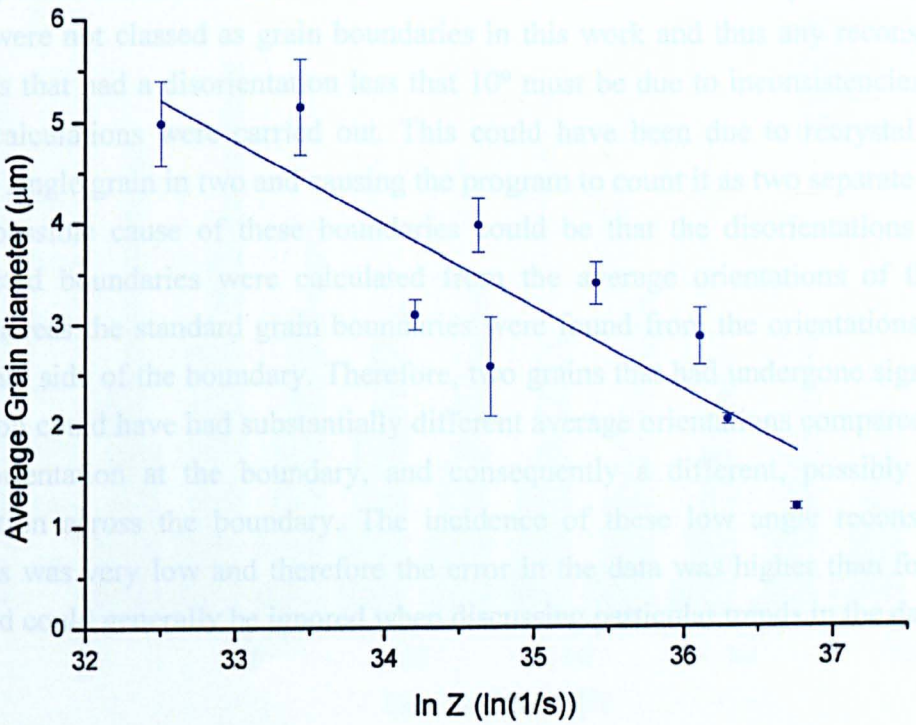

Figure 100 – Plot showing the recrystallised grain size against Zener-Hollomon parameter calculated using final test temperature

4.4.4.4 Boundary Disorientation

Using the new analysis program, the levels of recrystallisation for each disorientation of grain boundary were found. The disorientations were grouped into classes of 10° and have been plotted as bar charts showing the distributions of recrystallisation in different samples to allow comparison. These calculations are described in detail in section 3.7.2.3.2 but will be briefly summarized again here.

The boundaries between the non-recrystallised grains remaining in the microstructure were reconstructed to find a prediction of the pre-existing grain boundaries, across which the disorientation could be calculated. The plots showing the frequency of recrystallisation show the calculated percentage of each of these reconstructed boundaries that had undergone recrystallisation, which have then been grouped in terms of disorientation. The plots showing area of recrystallisation used the same reconstructed boundaries but calculated the area of recrystallisation associated with each boundary and, from that, found the area per length of boundary that had recrystallised.

The boundaries of type 0-10° often show a different result in the following graphs due to the very small number of these boundaries found in the material. Any boundaries less than 10° were not classed as grain boundaries in this work and thus any reconstructed boundaries that had a disorientation less that 10° must be due to inconsistencies in the way the calculations were carried out. This could have been due to recrystallisation splitting a single grain in two and causing the program to count it as two separate grains. Another possible cause of these boundaries could be that the disorientations of the reconstructed boundaries were calculated from the average orientations of the two grains, whereas the standard grain boundaries were found from the orientations of the pixels either side of the boundary. Therefore, two grains that had undergone significant deformation could have had substantially different average orientations compared to the specific orientation at the boundary, and consequently a different, possibly lower, disorientation across the boundary. The incidence of these low angle reconstructed boundaries was very low and therefore the error in the data was higher than for other angles, and could generally be ignored when discussing particular trends in the data.

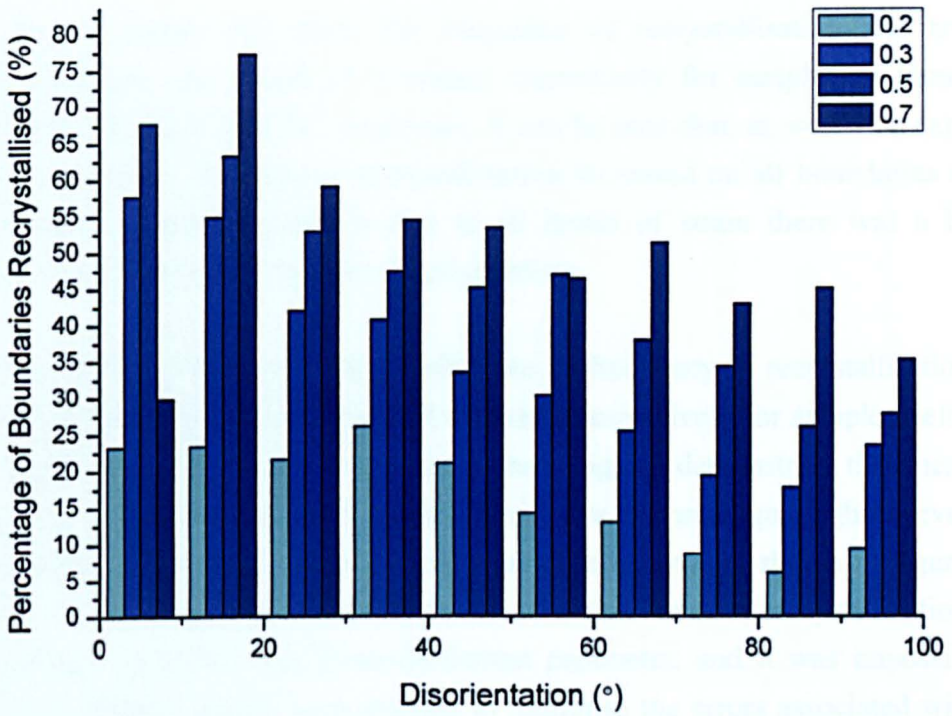

Figure 101 – Plot showing the frequency of recrystallisation on different grain boundaries at increasing levels of strain

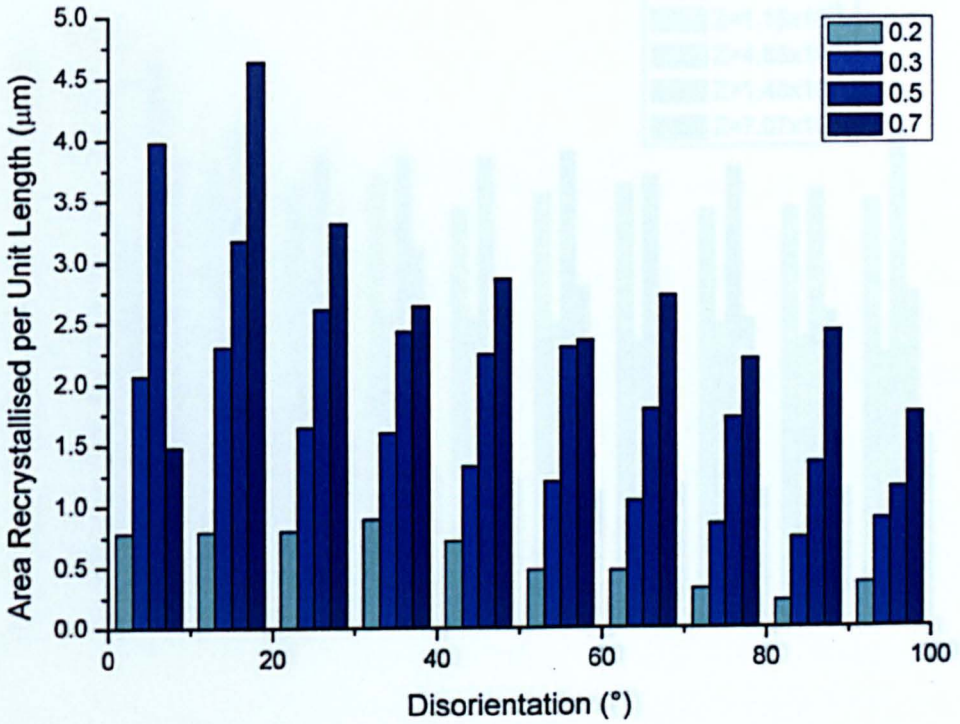

Figure 102 – Plot showing the amount of recrystallised material at different grain boundaries at increasing levels of strain

Figure 101 and figure 102 show the frequency of recrystallisation and area of recrystallisation per unit length of boundary respectively for samples of increasing strain deformed at 460°C and $5s^{-1}$ strain rate. It can be seen that, as would be expected from previous results, the level of recrystallisation increased on all boundaries as the strain increased. Another feature is that at all levels of strain there was a higher frequency of recrystallisation at lower disorientations.

Figure 103 and figure 104 show the distributions of frequency of recrystallisation and area of recrystallisation per unit length of boundary respectively for samples deformed under different processing conditions. Again, these figures demonstrate that there is a tendency for lower disorientation grain boundaries to undergo higher levels of recrystallisation, although the trend is less pronounced than that shown in figure 101 and figure 102. As discussed in section 4.4.4.2, the total level of recrystallisation was more dependent on strain than Zener-Hollomon parameter, and it was impossible to study an area of each sample large enough to minimise the errors associated with the heterogeneities from deformation. Therefore, it can again be seen that the levels of recrystallisation do not strongly correlate with Z.

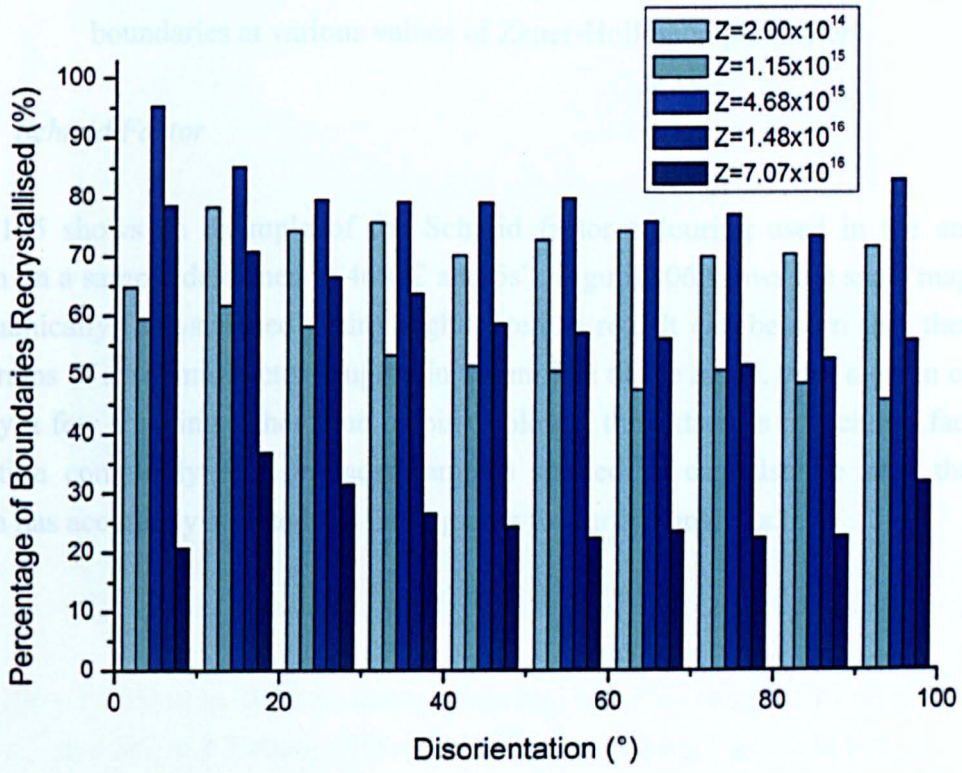

Figure 103 – Plot showing the frequency of recrystallisation on different grain boundaries at various values of Zener-Hollomon parameter

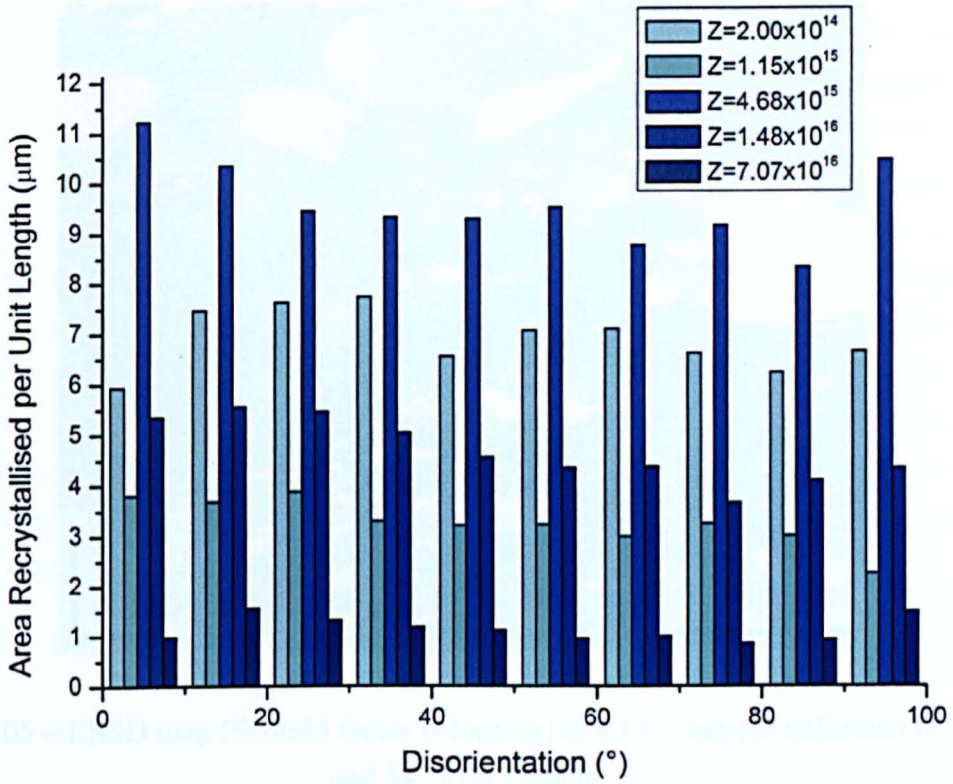

Figure 104 – Plot showing the amount of recrystallised material at different grain boundaries at various values of Zener-Hollomon parameter

4.4.4.5 Schmid Factor

Figure 105 shows an example of the Schmid factor colouring used in the analysis program on a sample deformed at 460°C and $5s^{-1}$. Figure 106 shows the same map with the dynamically recrystallised grains highlighted in red. It can be seen that there are many grains of a Schmid factor roughly in the middle of the range, with a green colour, and only a few showing either blue or pink colours, the extremes of Schmid factor; a distribution commonly seen in most samples studied. It can also be seen that the program has accurately selected the DRX grains for further analysis.

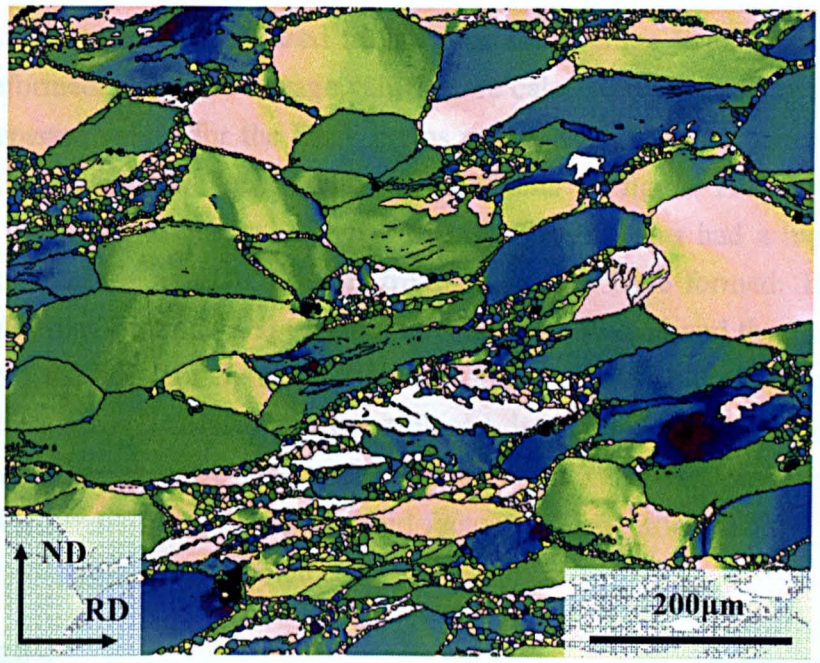

Figure 105 – EBSD map (Schmid factor colouring) of a PSC sample deformed at 460°C and $5s^{-1}$ to 0.7 strain

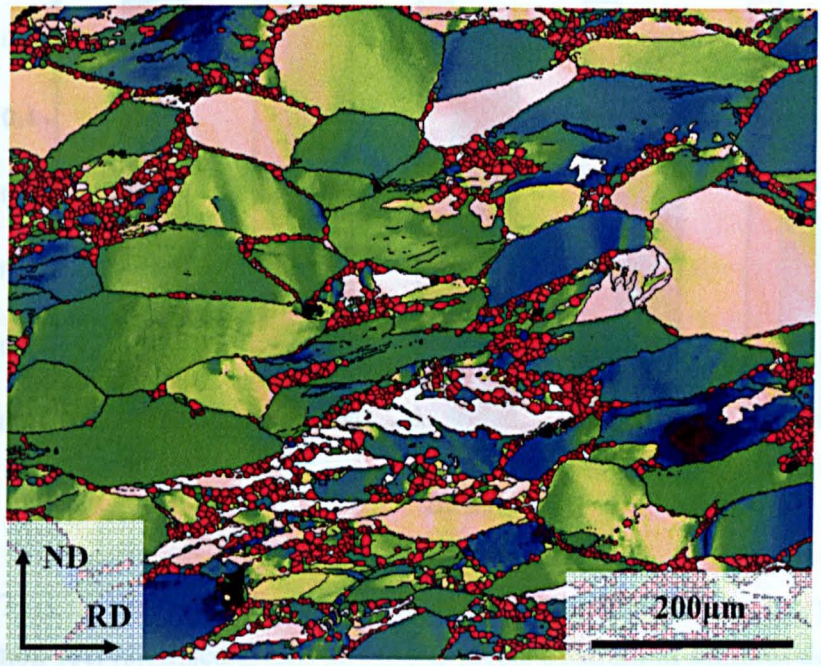

Figure 106 – EBSD map (Schmid factor colouring) of a PSC sample deformed at 460°C and $5s^{-1}$ to 0.7 strain with recrystallised grains highlighted in red

The new analysis program was used to calculate the average Schmid factor across a variety of deformed samples. Average values were calculated for the entire EBSD map as well as separate values for the DRX grains and non-DRX grains. These are shown with respect to strain and Zener-Hollomon parameter in figure 107 and figure 108 respectively. It can be seen that in every case, the DRX grains had a higher average Schmid factor than the non-DRX grains from which they have formed. This was true across the full range of strain and processing conditions studied and therefore it can be concluded that the areas of dynamic recrystallisation would undergo basal slip more easily than those areas that have not recrystallised. It can also be seen from these plots that there was no strong correlation with either strain or Zener-Hollomon parameter. A small downward trend in non-DRX Schmid factor could be inferred from Figure 107, however it is not strong enough to be conclusive.

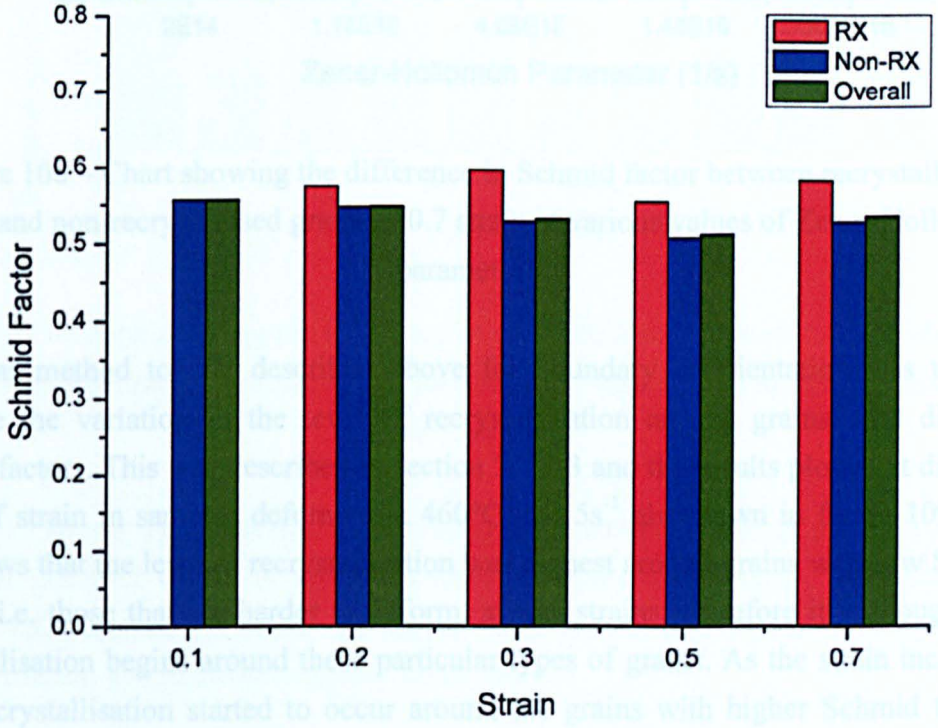

Figure 107 – Chart showing the difference in Schmid factor between recrystallised grains and non-recrystallised grains at various levels of strain in samples deformed at 460°C and $5s^{-1}$

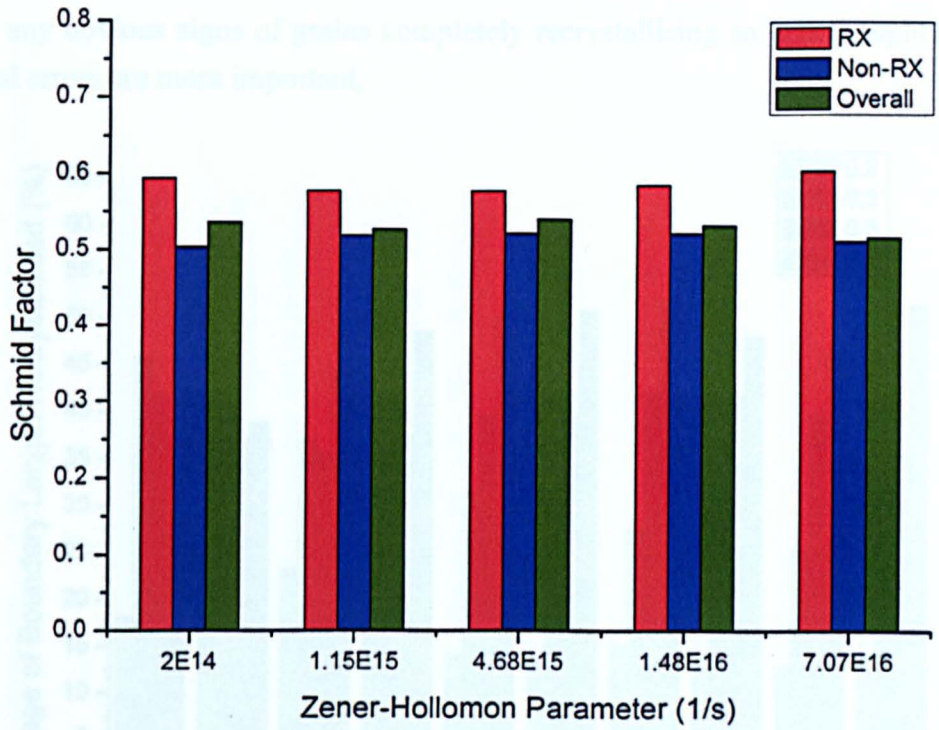

Figure 108 – Chart showing the difference in Schmid factor between recrystallised grains and non-recrystallised grains at 0.7 strain at various values of Zener-Hollomon parameter

A similar method to that described above for boundary disorientation was used to calculate the variation in the level of recrystallisation around grains with different Schmid factors. This was described in section 3.7.2.3 and the results plotted at different levels of strain in samples deformed at 460°C and $5s^{-1}$ are shown in figure 109. This plot shows that the level of recrystallisation was highest around grains with low Schmid factors, i.e. those that are harder to deform, at low strains; therefore it is thought that recrystallisation begins around these particular types of grains. As the strain increased, more recrystallisation started to occur around the grains with higher Schmid factors. The lowest Schmid factor grains appeared to become less recrystallised as strain increased, a fact that is clearly impossible. There are two possible reasons for this: firstly, that this is simply error in the data due to the low number of grains with this Schmid factor; secondly, that the recrystallisation is occurring around some low Schmid factor grains but not others, possibly because of differences in the surrounding grains. If recrystallisation progressed to completion in these grains, they would not be recognised in the later EBSD maps and thus only those that have little or no recrystallised material are measured by the analysis program. The samples used to calculate this data rarely

showed any obvious signs of grains completely recrystallising so it is thought that the statistical errors are more important.

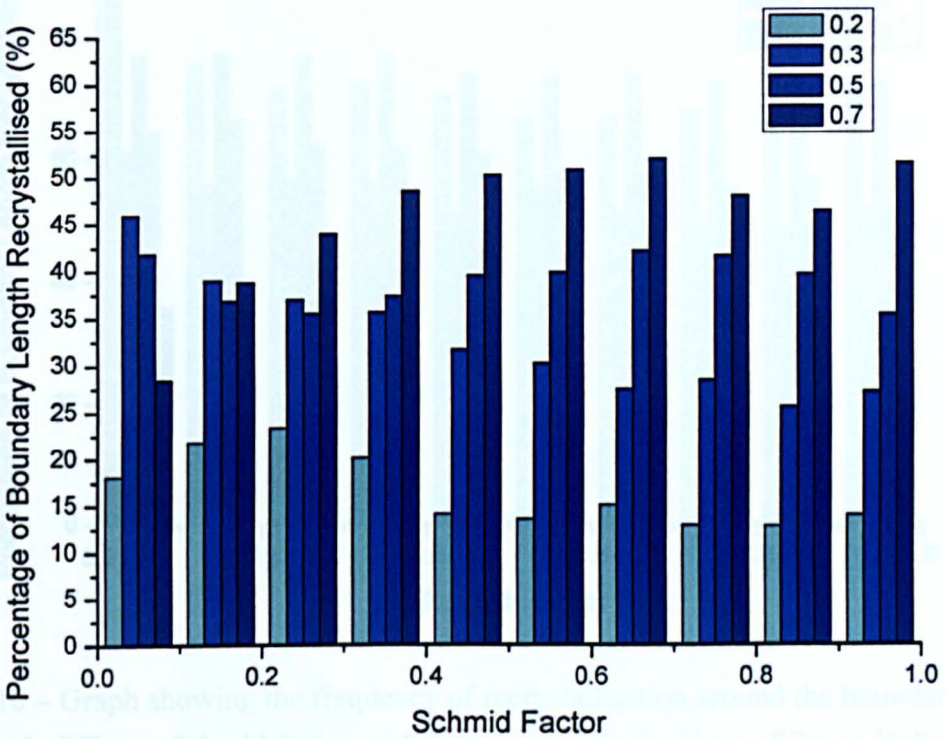

Figure 109 – Graph showing the frequency of recrystallisation around the boundaries of grains with different Schmid factors, at increasing levels of strain in samples deformed at 460°C and $5s^{-1}$

Figure 110 shows the frequency of recrystallisation around grains of different Schmid factors at different values of the Zener-Hollomon parameter. Again, as discussed in section 4.4.4.2, there is little correlation between Z and the level of dynamic recrystallisation due to the heterogeneities in strain.

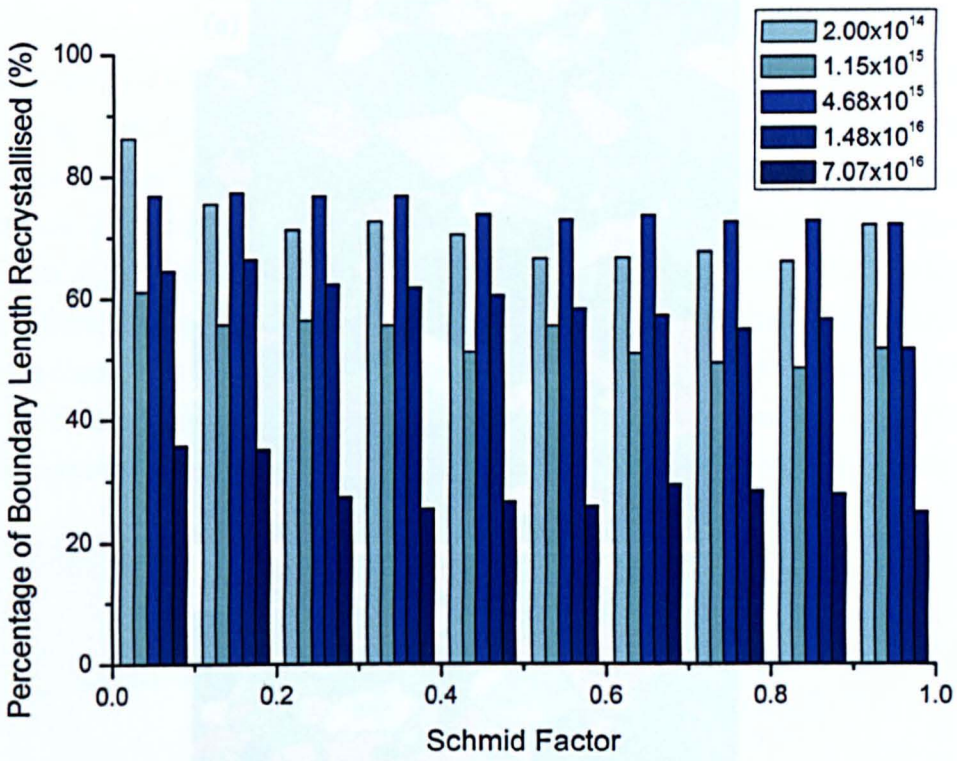

Figure 110 – Graph showing the frequency of recrystallisation around the boundaries of grains with different Schmid factors at 0.7 strain at various values of Zener-Hollomon parameter

4.4.5 Static Recrystallisation (SRX)

Only a small amount of work has been carried out on the static recrystallisation (SRX) behaviour of the material. These samples were tested at 420°C and 500°C as described in section 3.2.3.2 and the full double hit stress-strain curves are shown in section 4.3.5. In this section the interest is in the microstructure evolution during the hold period; therefore, samples that were deformed in the first hit to 0.25 strain and then held at temperature for different lengths of time before a water quench were studied. For each temperature there were 3 samples in the sequence, including one that had no hold period. Figure 111 shows the sequence of tests at 420°C, with hold times of 0, 300 and 600s. Figure 115 shows the samples tested at 500°C, with hold times of 0, 100 and 300s.

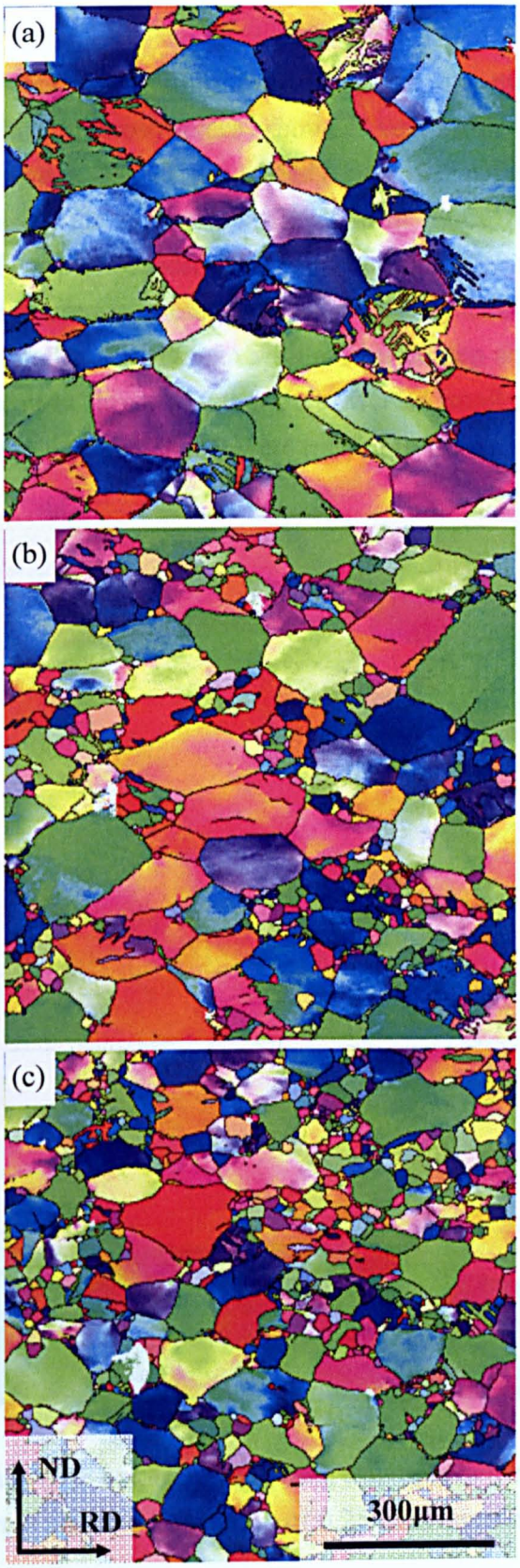

Figure 111 – EBSD maps (IPF colouring) of 3 samples deformed at 420°C and $1s^{-1}$ strain rate to 0.25 total strain then held at 420°C for: (a) 0s, (b) 300s, (c) 600s

Figure 111 shows the static recrystallisation behaviour of the material at 420°C. It can be seen that the initial microstructure showed very little sign of dynamically recrystallised grains. Section 4.4.4.3 has already shown that the DRX grain size was dependent on Z, and using the line of best fit given in figure 100, the expected DRX grain size at these deformation conditions would be approximately 1.7μm. Therefore, with the 1.5μm step size used in these maps, it was likely that the small DRX grains were missed and thus another EBSD map with a smaller step size was carried out, see figure 112. It can be seen in figure 112 that there were a small amount of DRX grains around the grain and twin boundaries that were missed in the previous EBSD map.

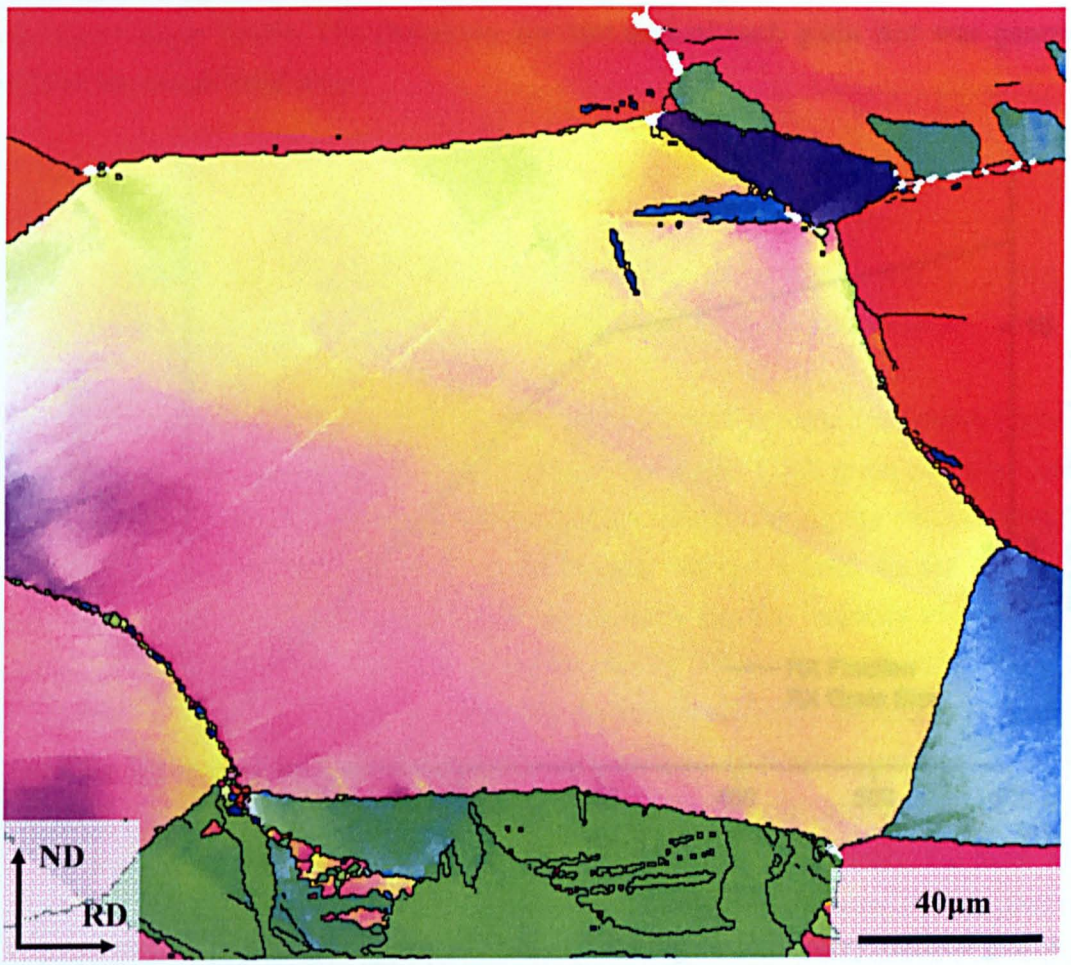

Figure 112 – EBSD map (IPF colouring) showing a sample deformed at 420°C and $1s^{-1}$ strain rate to a total strain of 0.25 then quenched

Figure 113 shows how the fraction and size of recrystallised grains in the samples deformed and held at 420°C increased as the length of time held at temperature

increased. This shows that the growth of the recrystallised material was much faster in the initial stages of the hold period. Figure 114 shows the distribution of recrystallised grain sizes in the three samples at 420°C. The data for 0s hold was taken from the map carried out with a step size of 0.35μm (shown in figure 112) and the data for the samples at 300 and 600s were taken from the maps with 1.5μm step sizes (shown in figure 111). Therefore, there were no grains found below 3μm in the 300 and 600s samples due to the step size; however, it can be inferred from the shape of the curves that there should be a significant number in this region. Figure 114 shows that, following deformation at 420°C, almost all recrystallised grains were in the range of 0 to 2.5μm. The distribution of grain sizes after holding at temperature was very similar in both samples with a skew towards the smaller grains, and a significant tail containing some much larger grains. The frequency per unit area of each grain size was generally higher at the longer hold time.

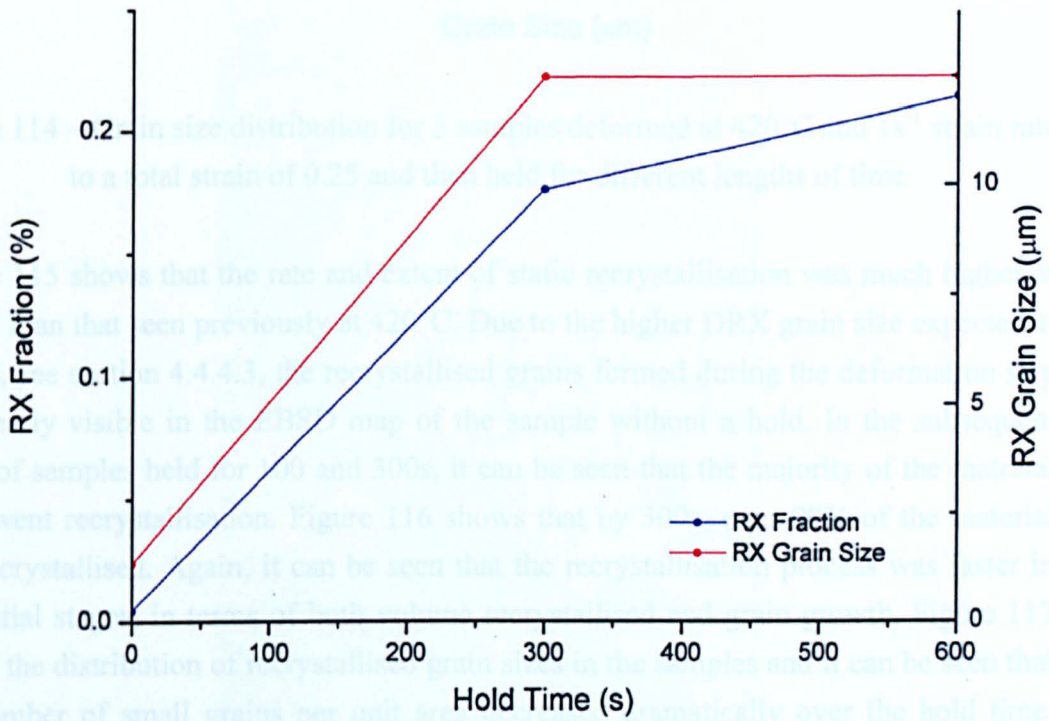

Figure 113 – Graph showing the amount and average size of recrystallised grains against hold time at 420°C

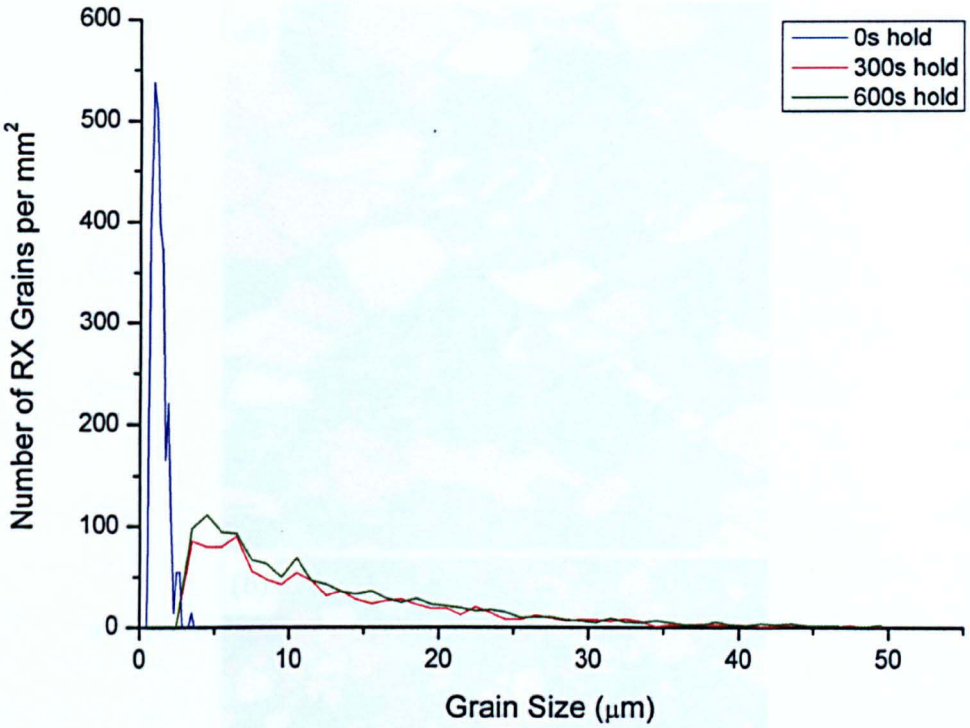

Figure 114 – Grain size distribution for 3 samples deformed at 420°C and $1s^{-1}$ strain rate to a total strain of 0.25 and then held for different lengths of time

Figure 115 shows that the rate and extent of static recrystallisation was much higher at 500°C than that seen previously at 420°C. Due to the higher DRX grain size expected at 500°C, see section 4.4.4.3, the recrystallised grains formed during the deformation step are clearly visible in the EBSD map of the sample without a hold. In the subsequent maps of samples held for 100 and 300s, it can be seen that the majority of the material underwent recrystallisation. Figure 116 shows that by 300s, over 90% of the material had recrystallised. Again, it can be seen that the recrystallisation process was faster in the initial stages, in terms of both volume recrystallised and grain growth. Figure 117 shows the distribution of recrystallised grain sizes in the samples and it can be seen that the number of small grains per unit area decreased dramatically over the hold time, while the number of large grains increased and the maximum size of recrystallised grains found also increased.

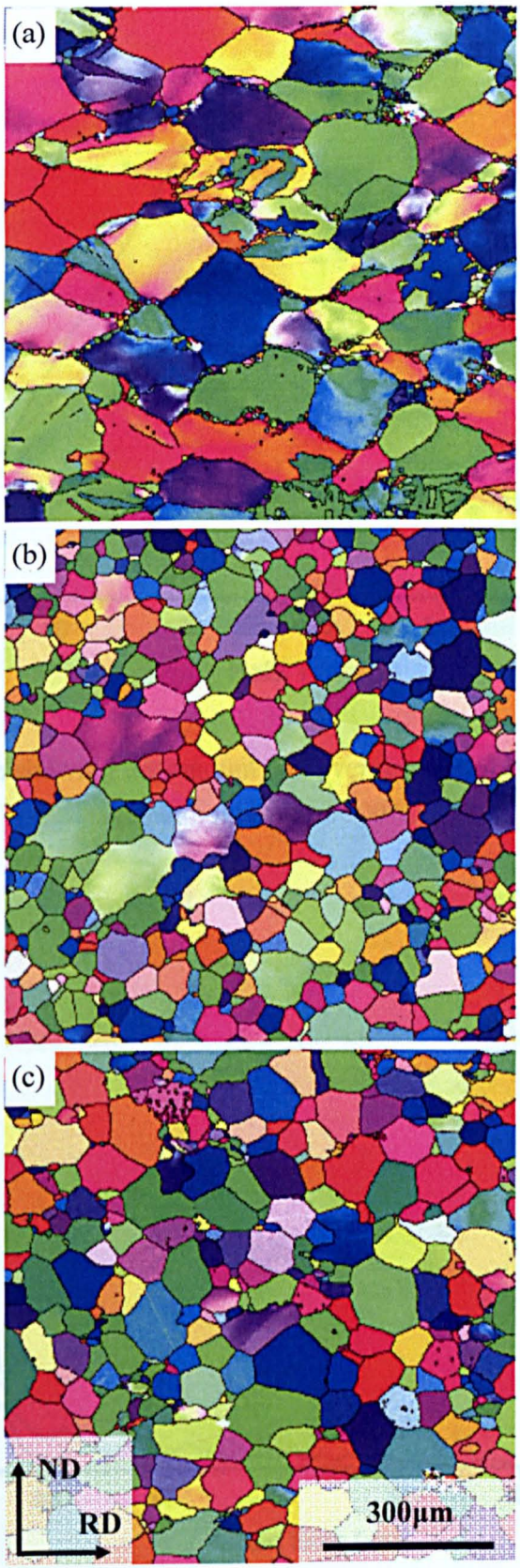

Figure 115 – EBSD maps (IPF colouring) of 3 samples deformed at 500°C and $1s^{-1}$ strain rate to 0.25 total strain then held at 500°C for: (a) 0s, (b) 100s, (c) 300s

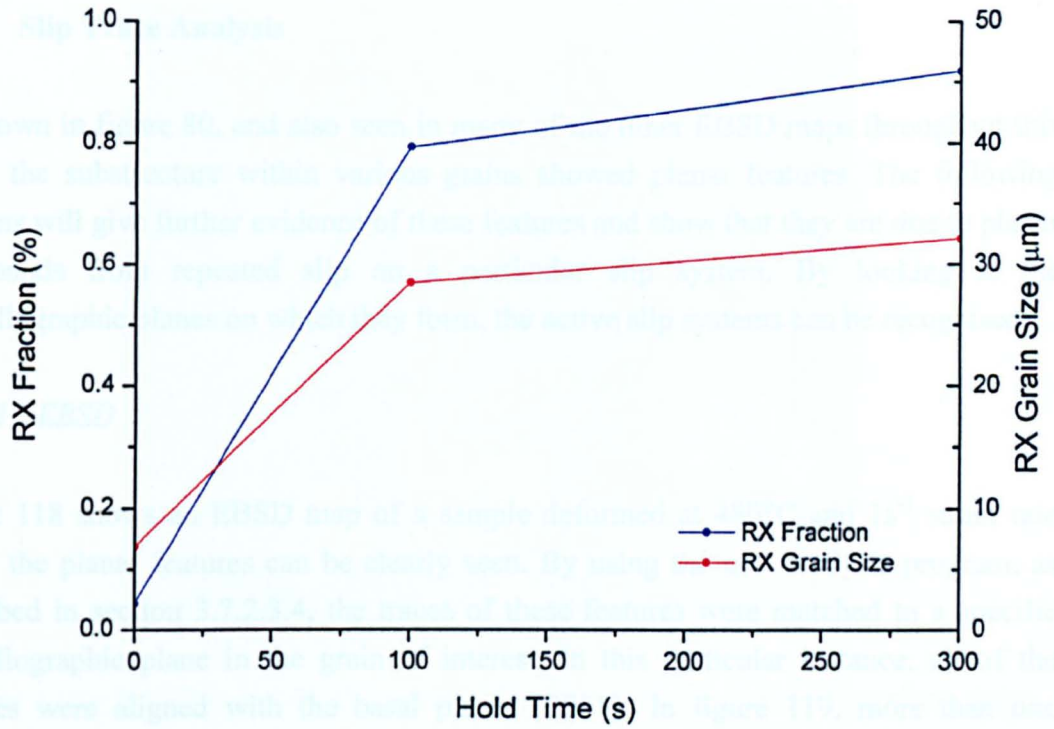

Figure 116 – Graph showing the amount and average size of recrystallised grains against hold time at 500°C

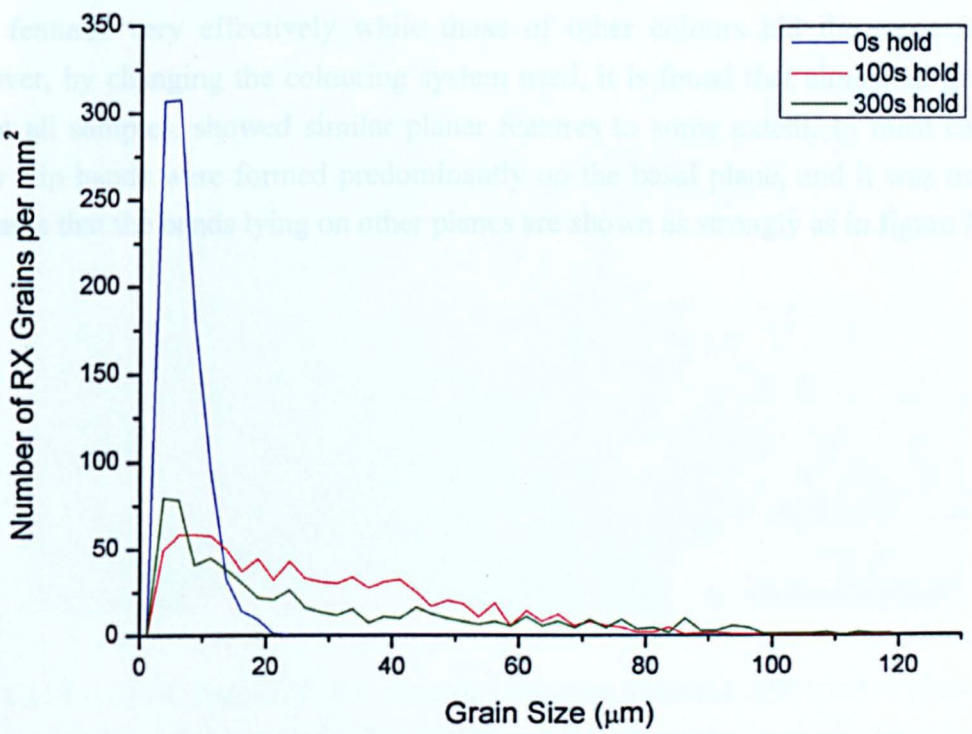

Figure 117 – Grain size distribution for 3 samples deformed at 500°C and $1s^{-1}$ strain rate to a total strain of 0.25 and then held for different lengths of time

4.4.6 Slip Trace Analysis

As shown in figure 80, and also seen in many of the other EBSD maps throughout this work, the substructure within various grains showed planar features. The following sections will give further evidence of these features and show that they are due to planar slip bands from repeated slip on a particular slip system. By looking at the crystallographic planes on which they form, the active slip systems can be recognised.

4.4.6.1 EBSD

Figure 118 shows an EBSD map of a sample deformed at 480°C and $1s^{-1}$ strain rate where the planar features can be clearly seen. By using the new analysis program, as described in section 3.7.2.3.4, the traces of these features were matched to a specific crystallographic plane in the grain of interest. In this particular instance, all of the features were aligned with the basal plane, {0001}. In figure 119, more than one orientation of planar slip band can be seen, and it was found that these three directions lie on the basal and prismatic planes as shown. The two figures shown here display the planar slip bands very clearly due to the colouring system used. It is a small quirk of the IPF colouring system that those grains that happened to be coloured purple showed these features very effectively while those of other colours hid the same features. However, by changing the colouring system used, it is found that almost all grains, in almost all samples, showed similar planar features to some extent. In most cases the planar slip bands were formed predominantly on the basal plane, and it was only in a few cases that the bands lying on other planes are shown as strongly as in figure 119.

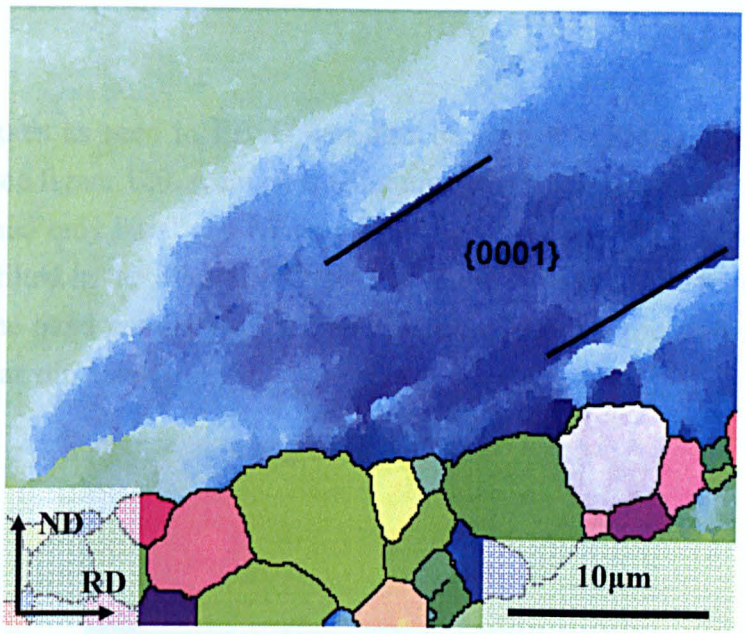

Figure 118 – EBSD map (IPF Colouring) showing a sample deformed in plane strain compression to a total strain of 0.7 at 440°C and $10s^{-1}$ showing planar slip band traces on basal planes

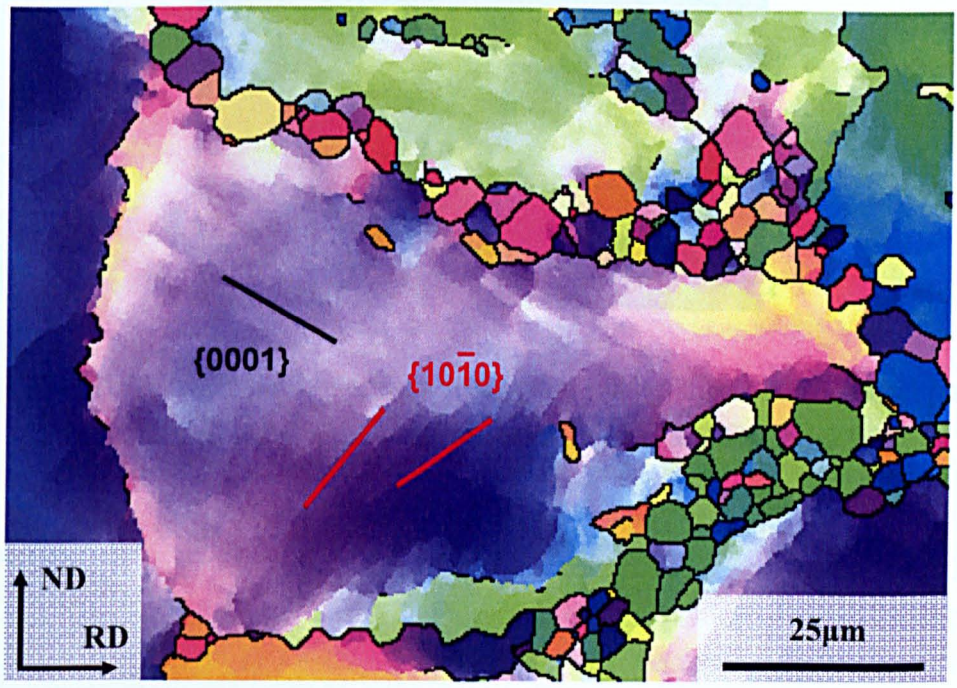

Figure 119 – EBSD map (IPF X Colouring) showing a sample deformed in plane strain compression to a total strain of 0.7 at 480°C and $1s^{-1}$ showing planar slip band traces on basal and prismatic planes. IPF X colouring is used to make the traces more visible

4.4.6.2 TEM

The same features as seen in EBSD can also be seen in TEM, although on a much smaller scale, see figure 120. A much smaller area was studied in TEM than EBSD, and using this method only basal slip bands were observed. Figure 121 shows a planar slip band that was tilted in the microscope to observe the structure. The regular lines along the length of the band are dislocations, and therefore provide proof that these features are indeed planar slip bands.

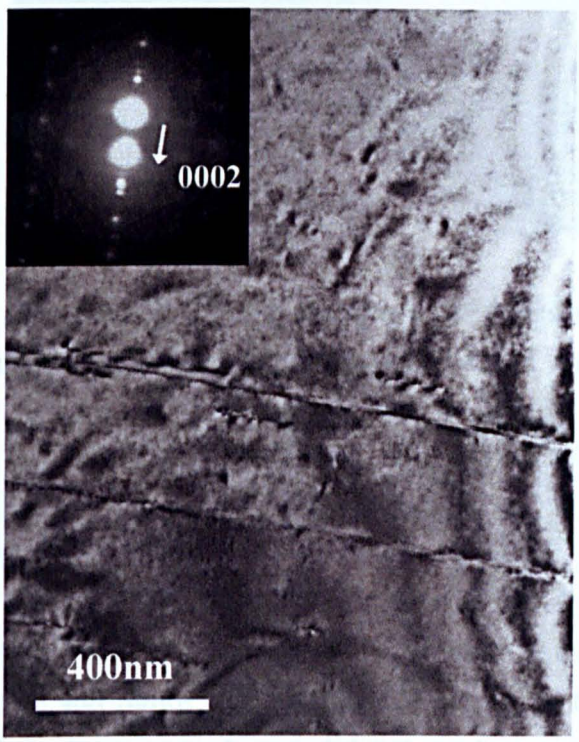

Figure 120 – TEM bright field micrograph showing planar slip bands on basal planes in material deformed in plane strain compression at 480°C and $1s^{-1}$

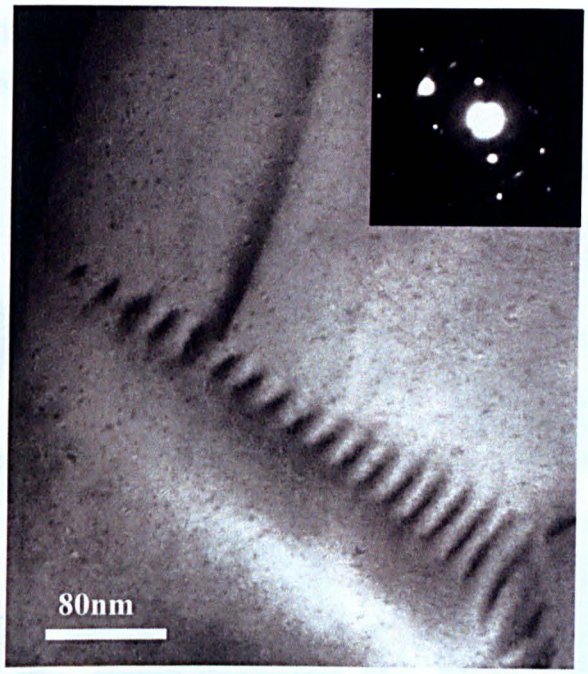

Figure 121 – TEM dark field micrograph showing tilted planar slip band in material deformed in plane strain compression at 480°C and $1s^{-1}$

4.5 Texture

4.5.1 Evolution with Strain

The texture change at various levels of strain in PSC samples deformed at 460°C and $5s^{-1}$ is shown in figure 122 and figure 123. The EBSD maps used to calculate these pole figures were not strictly large enough and did not contain enough grains to give a statistically valid measurement of the texture. This was due to the step size required to study the microstructure and the speed of the analysis equipment. However, it is still possible to see a very clear evolution from a random starting texture to a strong basal texture by a strain of approximately 0.2-0.3. After this point, the texture stayed very similar with most 0002 poles clustered around the normal direction and a weaker stretching of the texture in a band along the transverse direction. The peaks in both the $\langle 10\bar{1}0 \rangle$ and $\langle 11\bar{2}0 \rangle$ pole figures that are aligned with the rolling direction were due to the specific distribution of orientations along the transverse direction shown in the $\langle 0002 \rangle$ pole figure. This causes a weakening of the texture for $\langle 10\bar{1}0 \rangle$ and $\langle 11\bar{2}0 \rangle$ directions in all but the rolling direction. As both pole figures show a peak at similar angles and of similar intensities, it can be concluded that there was no preferred

orientation of the $\langle 10\bar{1}0 \rangle$ or $\langle 11\bar{2}0 \rangle$ directions and therefore the deformation texture is defined entirely by the $\langle 0002 \rangle$ pole figure.

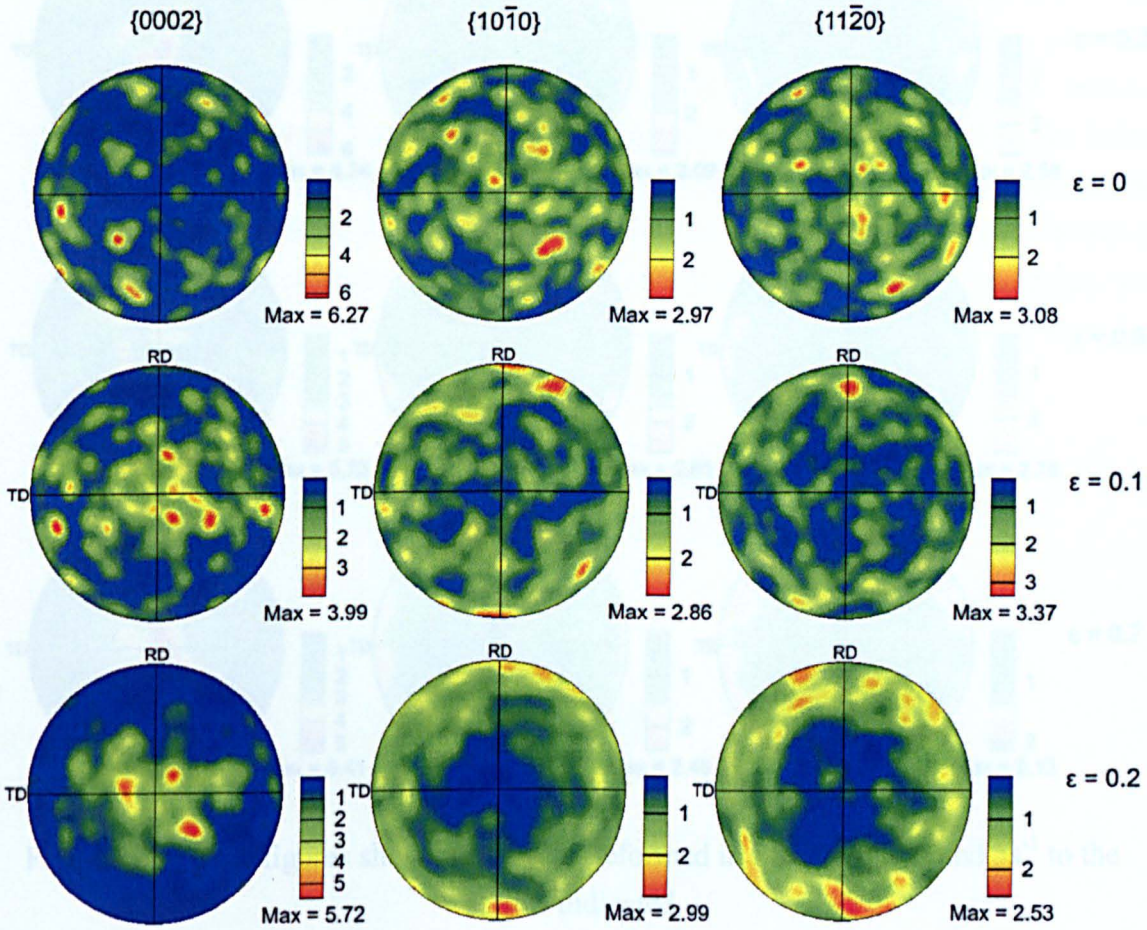

Figure 122 – Pole figures showing as-received material and samples deformed in PSC at 460°C and $5s^{-1}$ to the strains indicated

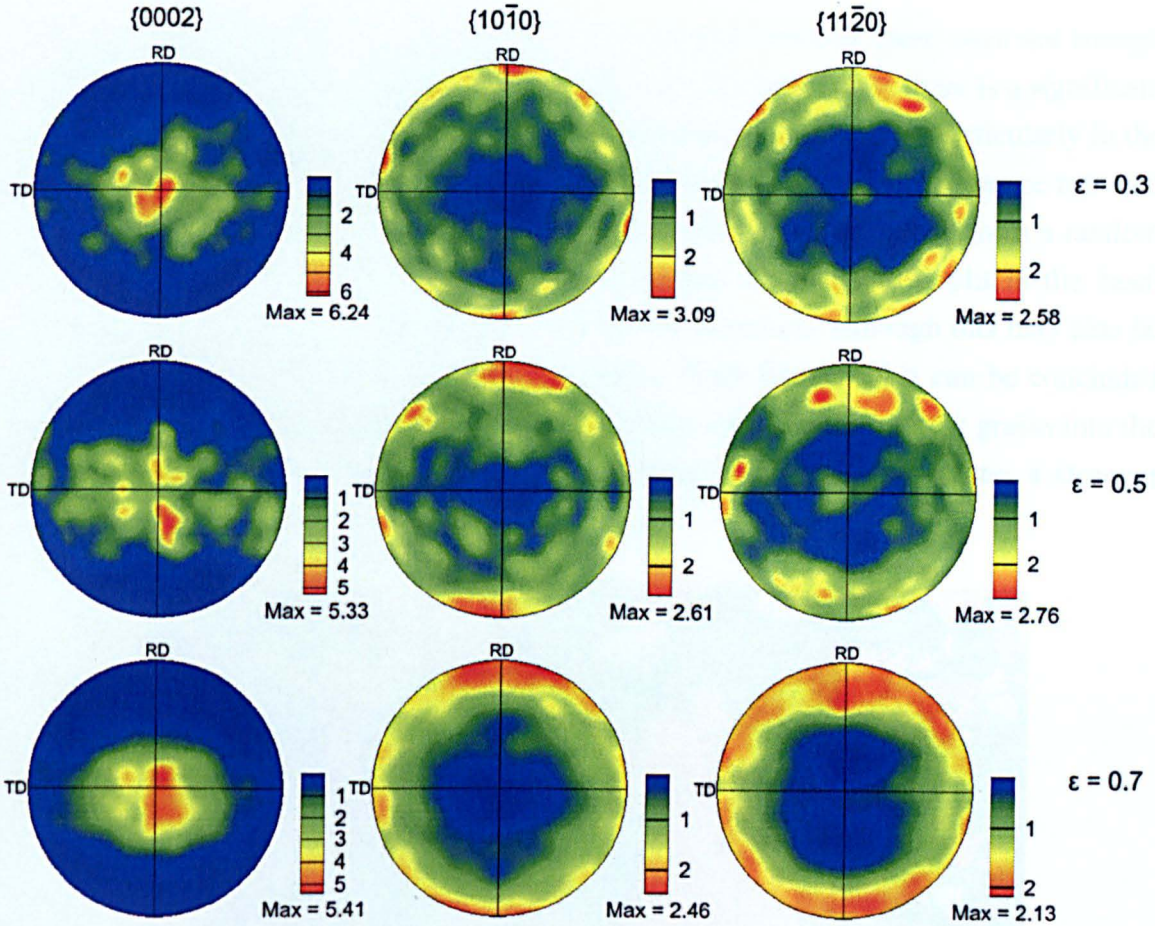

Figure 123 – Pole figures showing samples deformed in PSC at 460°C and $5s^{-1}$ to the strains indicated

The most significant change in texture as strain increased came from twinning. Figure 124 shows a sample in the early stages of deformation (at 0.1 strain) when the density of twin boundaries was at the highest level, see also section 4.4.3. This allowed the twinned and non-twinned material to be easily identified and compared. Figure 125 shows the same map as figure 124 with only the twinned material selected. It can be seen that certain grains have almost completely twinned and could only be definitely identified as twinned material due to the presence of small areas of non-twinned material around the boundaries. Therefore, it is likely that there were a few grains that have undergone complete twinning and were not recognised as twinned material in this selection process.

Figure 126 shows the pole figures for the [0002] direction from the non-twinned and the twinned regions of the map in figure 124. In order to have high enough resolution to correctly identify all twins in the sample, the map could not be carried out over a larger

area than that shown, approximately 1mm x 1mm, and therefore there were not enough grains present to give a correct average pole figure. This means that there is a significant amount of noise in the data, with peaks for each grain, as can be seen particularly in the non-twinned pole figure. However, figure 126 still shows a dramatic difference between texture of the twinned and non-twinned regions, with a distinct change from a random texture to a very strong basal texture. There appears to be a small split in the basal texture of approximately 6-11° along the transverse direction, although this may also be due to the noise in the data from too few grains. From figure 126 it can be concluded that twinning was the dominant mechanism causing a reorientation of the grains into the basal texture. Therefore, a higher level of twinning in the material creates a stronger basal texture.

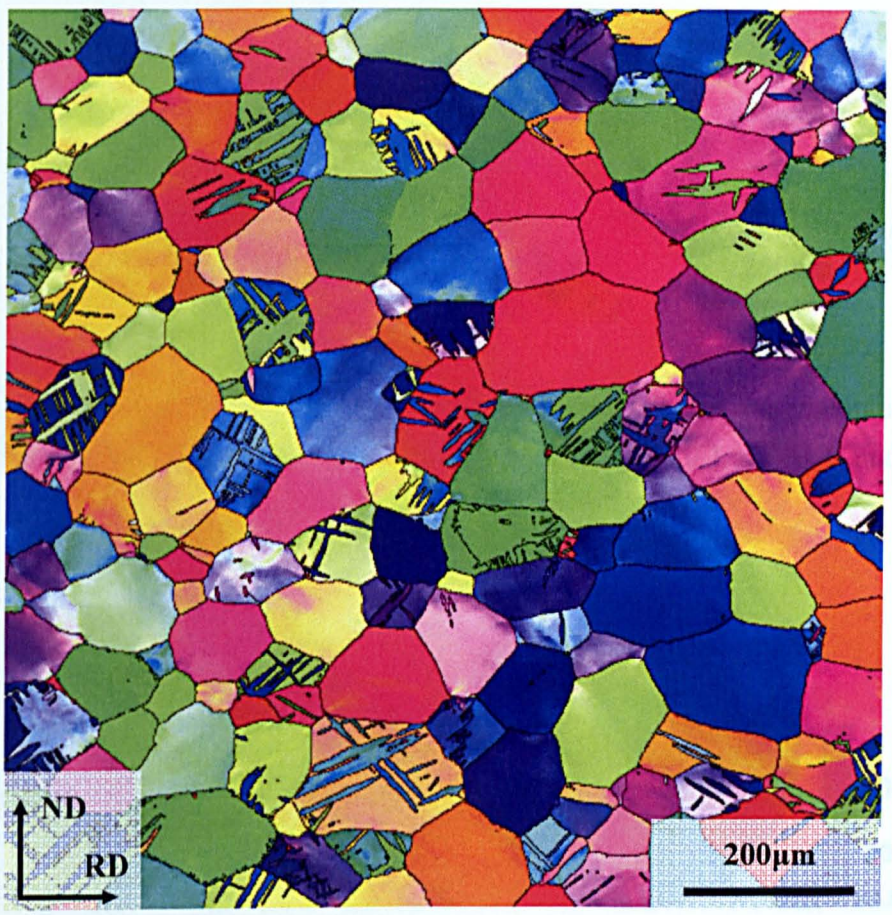

Figure 124 – EBSD map (IPF colouring) showing a sample deformed in plane strain compression to a total strain of 0.1 at 460°C and $5s^{-1}$

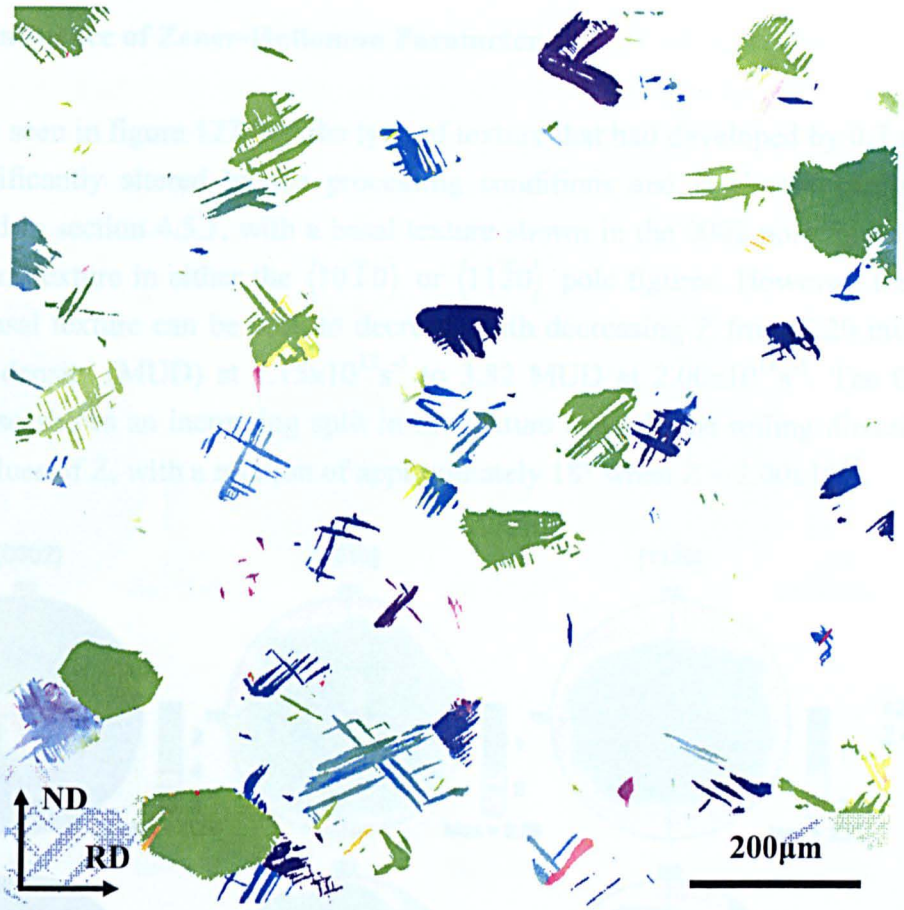

Figure 125 – EBSD map (IPF colouring) showing the twinned material in a sample deformed in plane strain compression to a total strain of 0.1 at 460°C and $5s^{-1}$

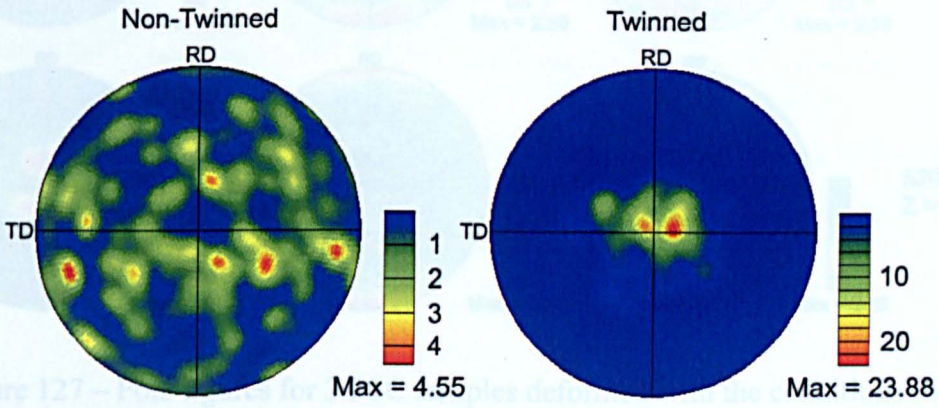

Figure 126 – 0002 pole figures for the non-twinned and twinned regions of a sample deformed at 460°C and $5s^{-1}$ strain rate to 0.1 strain

4.5.2 Influence of Zener-Hollomon Parameter

It can be seen in figure 127 that the type of texture that had developed by 0.7 strain was not significantly altered by the processing conditions and is always similar to that described in section 4.5.1, with a basal texture shown in the 0002 pole figure and little significant texture in either the $\langle 10\bar{1}0 \rangle$ or $\langle 11\bar{2}0 \rangle$ pole figures. However, the strength of the basal texture can be seen to decrease with decreasing Z from 6.29 multiples of uniform density (MUD) at $1.15 \times 10^{17} s^{-1}$ to 3.82 MUD at $2.00 \times 10^{14} s^{-1}$. The 0002 pole figure also shows an increasing split in the texture towards the rolling direction at the lower values of Z, with a rotation of approximately 18° when $Z = 2.00 \times 10^{14}$.

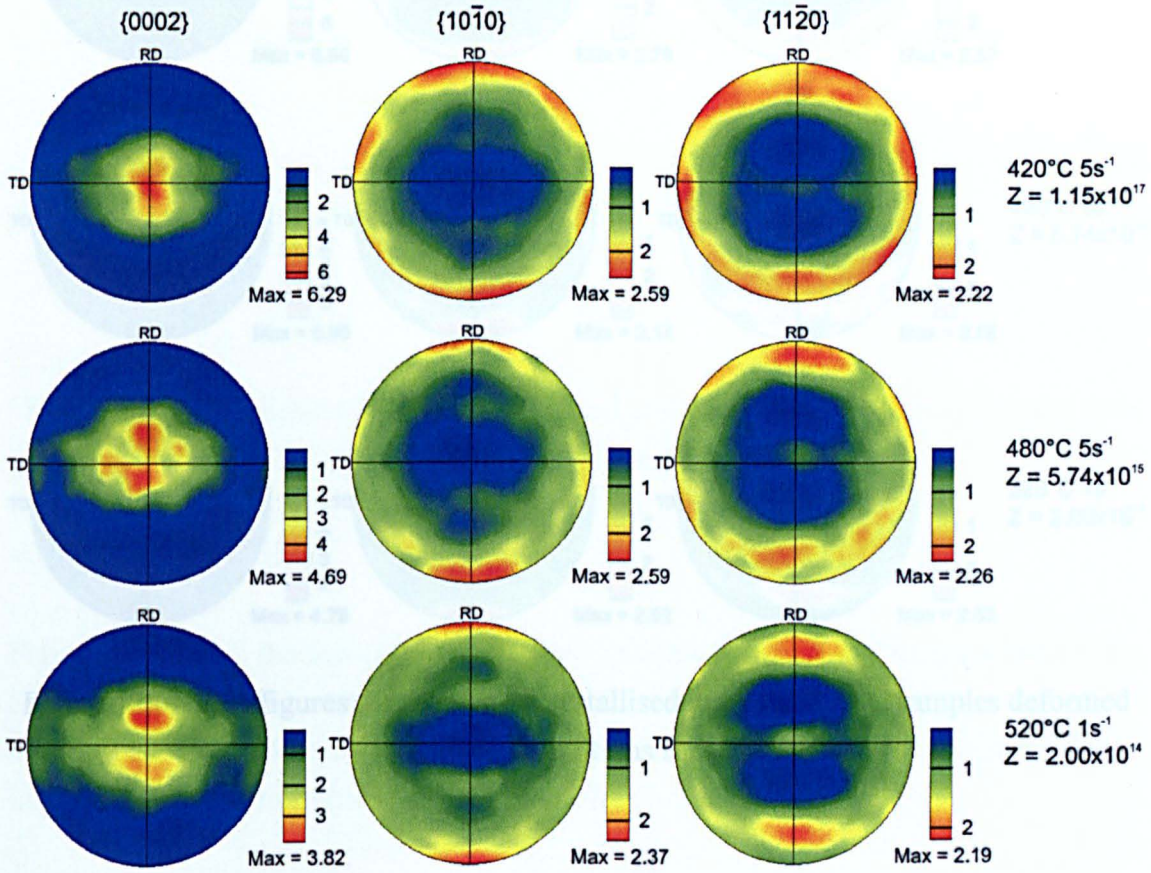

Figure 127 – Pole figures for 3 PSC samples deformed with the conditions shown

Figure 128 and figure 129 show the texture from the non-recrystallised and the recrystallised grains from the same samples as shown in figure 127. It can be seen that the recrystallised grains always showed a very weak basal texture that was approximately the same strength at all values of Z. As the amount of recrystallised material generally increased with decreasing Z, the randomisation of the overall texture

from recrystallisation had a more pronounced effect at the lower values of Z. The non-recrystallised grains showed a very similar texture to that from the entire material, with a weaker texture at lower Z. Therefore, it can be seen that the weakening of the overall texture with decreasing Z came from a change in the texture of both the deformed grains and the recrystallised grains.

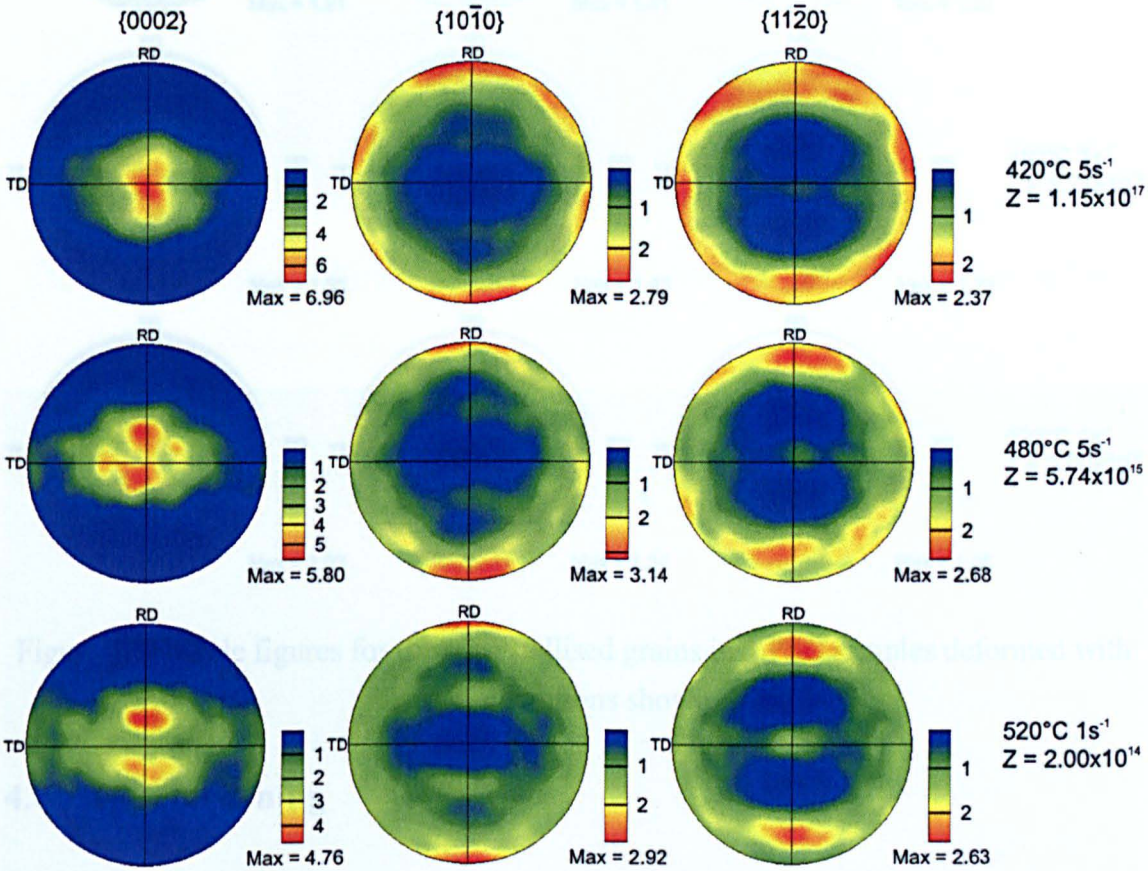

Figure 128 – Pole figures for the non-recrystallised grains in 3 PSC samples deformed with the conditions shown

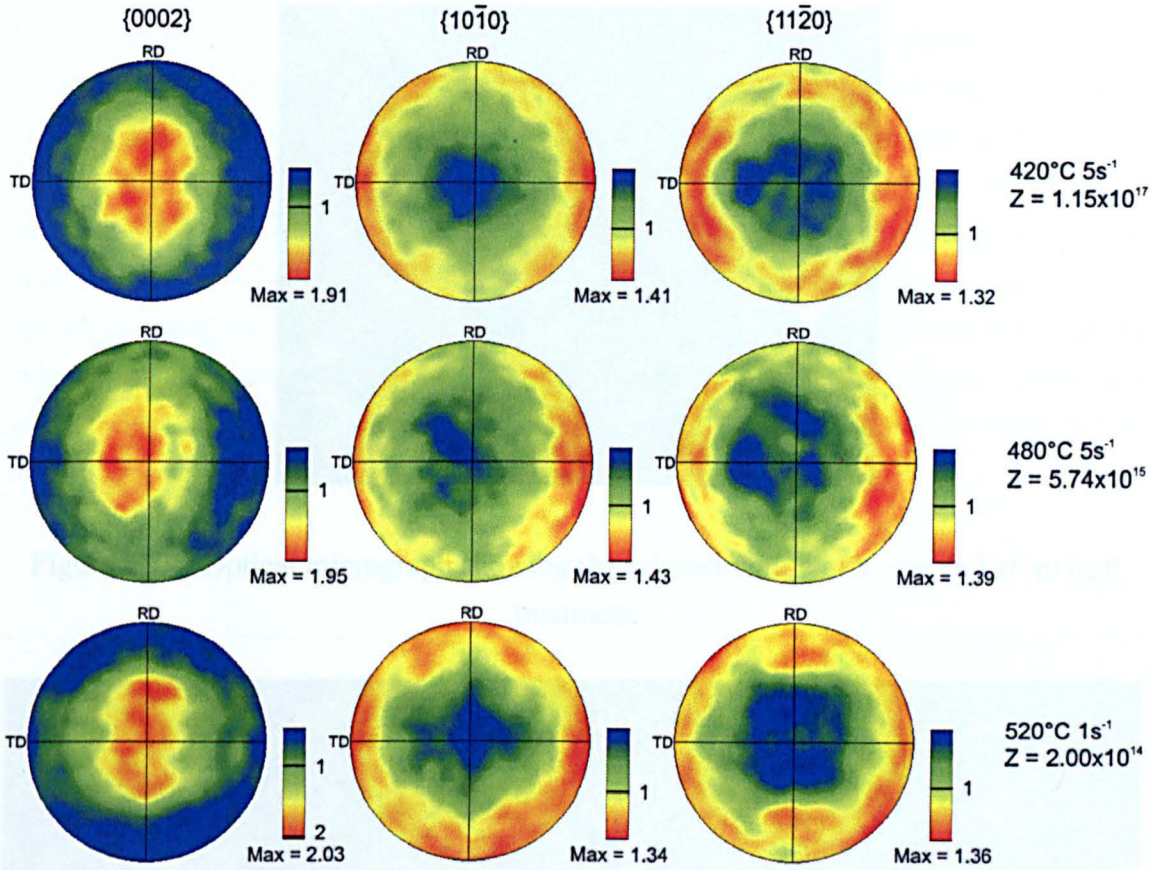

Figure 129 – Pole figures for the recrystallised grains in 3 PSC samples deformed with the conditions shown

4.6 Age Hardening

Figure 130 shows the starting recrystallised microstructure of the samples before any heat treatments were carried out. Figure 131 shows typical microstructures of the samples aged to peak and over aged conditions. During the ageing process there is very little change in microstructure at the scale visible in optical microscopy.

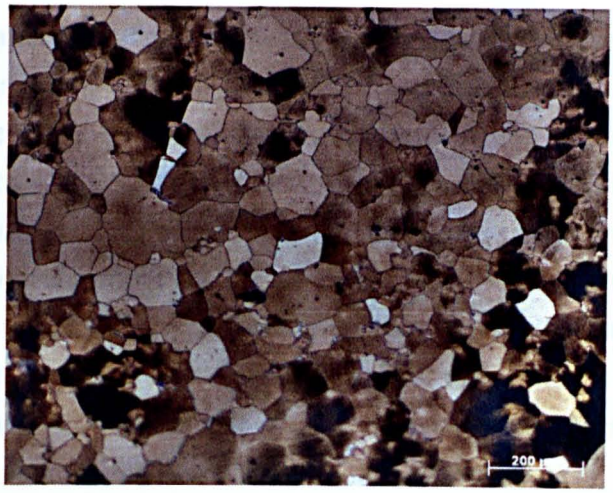

Figure 130 – Optical micrograph showing the microstructure of a sample before heat treatment

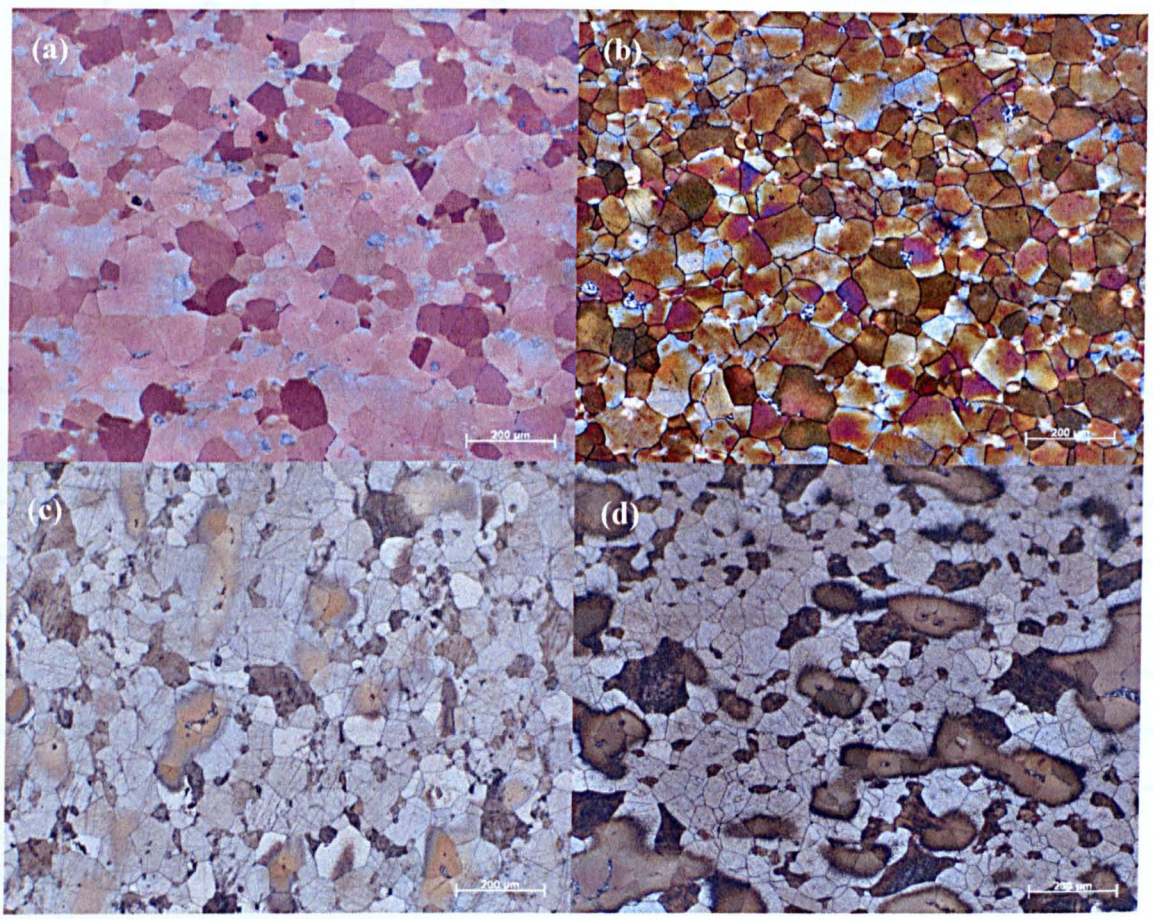

Figure 131 – Optical micrographs of (a) 250°C peak aged (12 hrs), (b) 250°C over-aged (170 hrs), (c) 275°C peak aged (2 hrs), (d) 275°C over-aged (8 hrs)

Grain size measurements using the linear intercept method were taken from optical micrographs of the starting material and it was seen that there was a larger difference than expected between the grain sizes following deformation in the two different casts used. Table 16 shows the difference in grain size between DF9269 and DF9276 following deformation and recrystallisation. Table 17 shows the grain sizes at different positions on a sectioned sample of one of the DF9269 tests. This was carried out to ensure that material could be taken from any position on the PSC test and still have the same microstructure; as the grain sizes are very similar, this is correct. Grain size analysis was also carried out on over-aged samples and it can be seen in table 18 that there was negligible change in grain size during the ageing process.

Table 16 – Grain sizes of the 2 different casts before heat treatment

Cast	Mean grain size (μm)	95% confidence limit (μm)
DF9269	60.05	±3.28
DF9276	51.10	±2.20

Table 17 – Grain sizes at the different positions on a sample from cast DF9269. Positions relate to those in figure 132

Location on Sample	Mean grain size (μm)	95% confidence limit (μm)
A	60.28	±3.02
B	59.81	±2.27
C	59.13	±4.51
D	60.52	±4.23
E	60.99	±2.93

Table 18 – Grain sizes of the over-aged samples at 250°C and 275°C from cast DF 9269

Ageing condition	Mean grain size (μm)	95% confidence limit (μm)
170h at 250°C	59.13	±2.61
8h at 275°C	59.13	±3.45

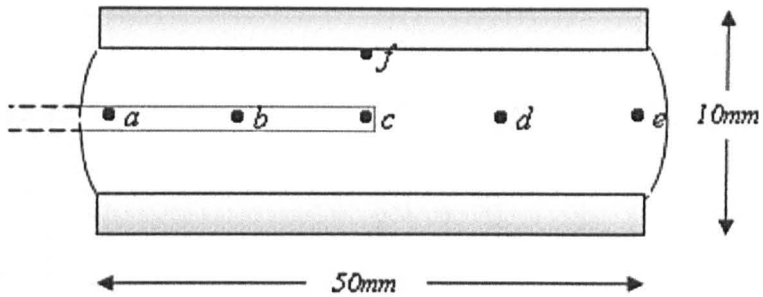

Figure 132 – Positions on the deformed samples used to check grain size consistency

Figure 133 and figure 134 show the ageing curves for Elektron 675 at 250°C and 275°C respectively. The starting hardness cannot be plotted on these curves at the correct value of 0 hrs due to the logarithmic scale used; therefore, they have been plotted at 0.1hr for ease of viewing. Figure 133 shows the age hardening curve for samples aged at 250°C. It can be seen that there is a difference between the samples from each cast, with those from DF9276 generally giving harder results. This is thought to be a direct consequence of the smaller grain size. The peak hardness occurs at 12 hours and reaches approximately 120HV, almost 50% higher than the starting value. It can be seen that there is a gradual rise to the peak hardness, followed by a sharp decline before a plateau is reached in the over-aged condition at around 100-105 HV.

Figure 134 shows the age hardening curve for Elektron 675 aged at 275°C. In this case only one cast was used and therefore, there are no inconsistencies as at 250°C. It can be seen that the hardening effect at 275°C was much faster but also much weaker. The peak hardness is reached after only 2 hours and had a hardness of 93HV, only 15-20% higher than the starting material. The curve shows a similar shape to that at 250°C with a gradual rise to a peak, followed by a steeper decline and a plateau of almost constant hardness in the over-aged condition.

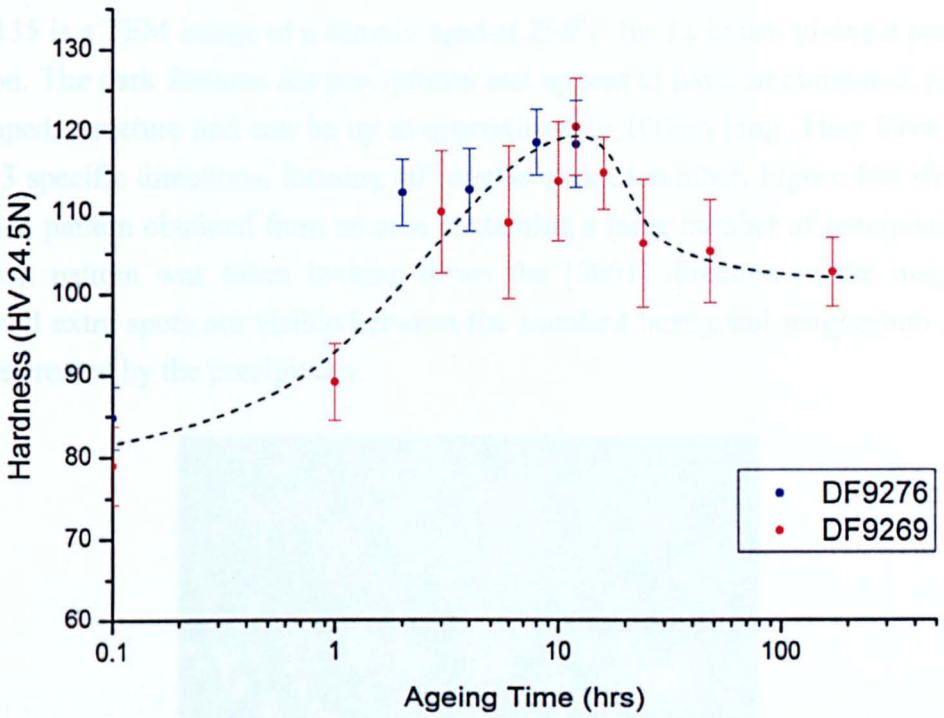

Figure 133 – Ageing curve of Elektron 675 at 250°C following plane strain compression. Dotted line shows the suggested smoothed ageing curve

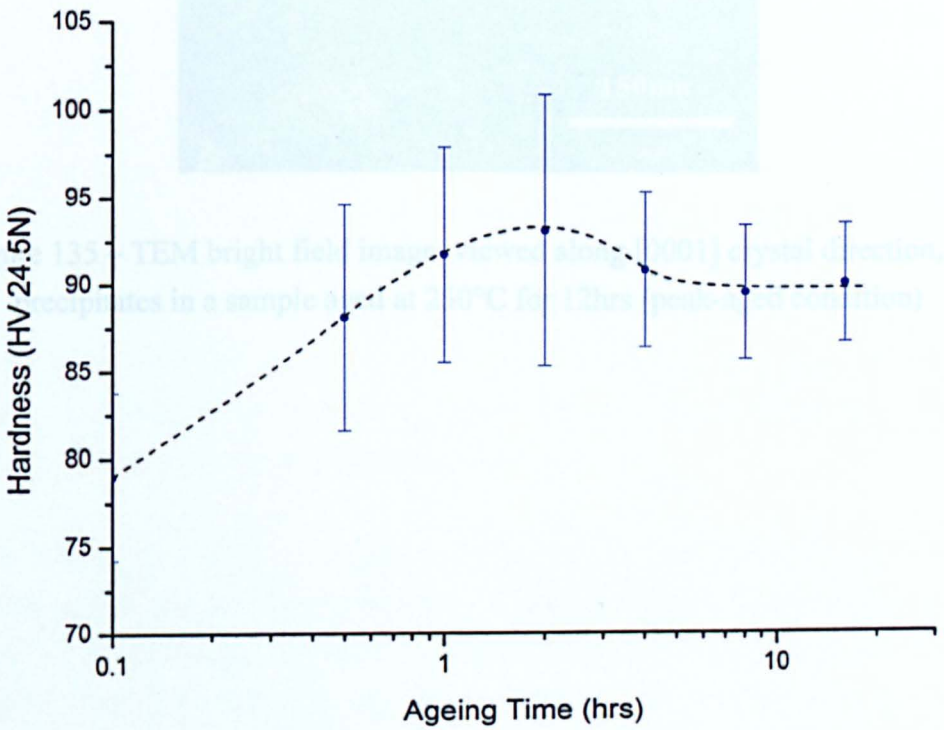

Figure 134 – Ageing curve of Elektron 675 at 275°C following plane strain compression. Dotted line shows the suggested smoothed ageing curve

Figure 135 is a TEM image of a sample aged at 250°C for 12 hours, giving a peak-aged condition. The dark features are precipitates and appear to have an elongated, probably disc shaped, structure and can be up to approximately 100nm long. They have formed only in 3 specific directions, forming 60° angles with each other. Figure 136 shows the diffraction pattern obtained from an area containing a large number of precipitates. The diffraction pattern was taken looking down the [0001] direction in the magnesium matrix and extra spots are visible between the standard hexagonal magnesium pattern; these are created by the precipitates.

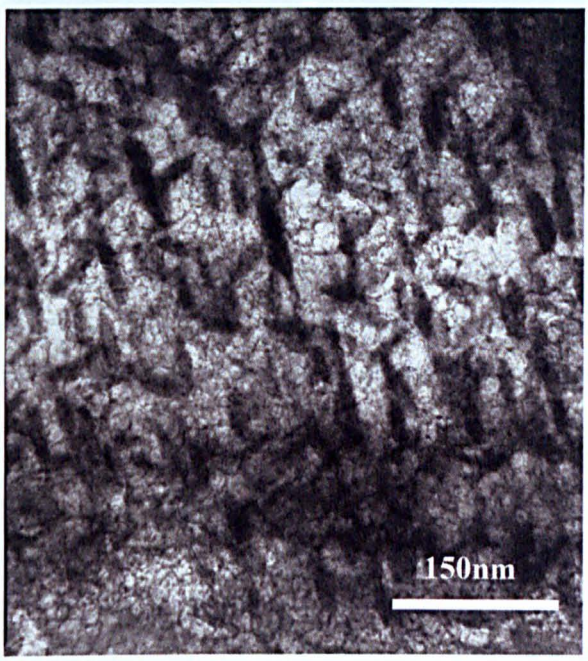

Figure 135 – TEM bright field image, viewed along [0001] crystal direction, of precipitates in a sample aged at 250°C for 12hrs (peak-aged condition)

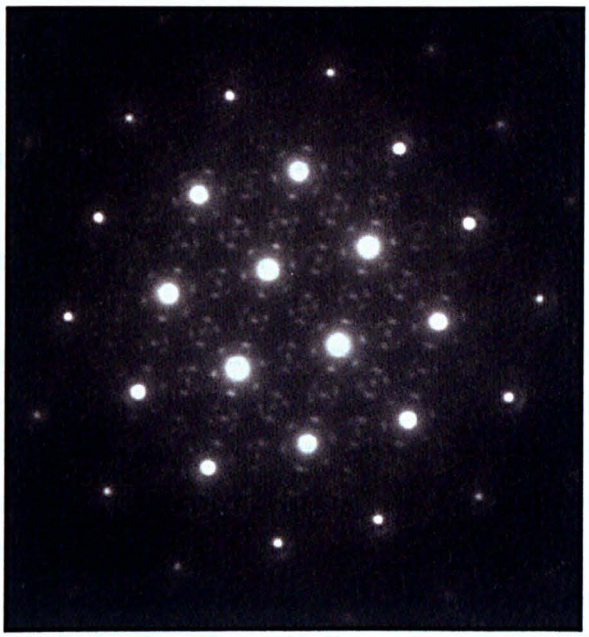

Figure 136 – TEM diffraction pattern along [0001] from a sample aged at 250°C for 12hrs (peak-aged condition). The large spots correspond to the magnesium lattice and the smaller spots correspond to the precipitates

5. Discussion

5.1 Flow Curves and Constitutive Equations

5.1.1 General Stress-Strain Behaviour

Typical stress-strain curves for plane strain compression of Elektron 675 were shown in section 4.3.2. It can be seen that they all show a similar shape with a rise after yielding up to a peak stress, followed by a gradual softening for the remainder of the test. The conditions of temperature and strain rate have a significant effect on the shape of the curves, with much less hardening visible in those at higher temperatures or lower strain rates, i.e. lower values of the Zener-Hollomon parameter. This indicates that flow softening was more prevalent at low Zener-Hollomon parameter. The strain at which the peak stress occurs will be discussed in more detail in section 5.4.1. The softening mechanism is thought to be predominantly dynamic recrystallisation, which will be discussed in more detail in section 5.4.

Due to the nature of the experimental tests carried out, there was a certain amount of variation in flow curves. The first thing to consider is the initial region of the test, where the strain rate fluctuated on contact. As was shown in section 3.2.5, a correction was carried out to remove the effects of strain rate variation. This allowed a much more accurate flow curve to be produced, but there was still a certain level of error inherent. This can be seen in the double hit tests shown in figure 73 and figure 74 because there were repeat tests carried out at exactly the same conditions. From these tests it can be seen that there could be as much as 25MPa difference in the stresses found. This does not appear to be restricted to the very early parts of the flow curves so the strain rate correction is not likely to be responsible. Instead, the differences in flow stress are likely to be due to testing, material or lubrication variations.

The flow behaviour seen in this study is similar to that seen in the literature for other magnesium alloys, for example references [36, 169, 175-177]. These studies all saw a period of work hardening, followed by a peak stress and subsequent softening to a steady state stress. Therefore, the only major difference between the flow curves in the current work and many of those in the literature is that Elektron 675 does not reach a steady state stress up to the strain tested. As discussed in section 2.6, this is not uncommon in magnesium alloys and is normally related to the alloy composition or

processing conditions[126, 176, 178, 179], but steady state would still be expected to be reached at higher strains. Therefore, it is thought that this is also true in the current work and that steady state could be reached if high enough strains could be applied. Unfortunately, the method of plane strain compression starts to become unreliable after a strain of approximately 1 due to problems with lubrication, width to height ratio, and the relative influence of the thermocouple on deformation. Steady state was not reached in any of the tests carried out to a strain of 1, see figure 57, and, therefore, a different method would be needed to attempt observations of steady state behaviour, perhaps torsion or tension testing.

The abnormally long period of softening seen in the current investigations is thought to be due to the nature of the softening mechanism. For a steady state stress to be reached, it would be expected that the microstructure should also reach a steady state. The softening mechanism that is active in Elektron 675 is thought to be dynamic recrystallisation, see section 5.4, and therefore a steady state can only be reached when the entire material has undergone recrystallisation. It was seen in figure 96 that by a strain of 0.7, dynamic recrystallisation had taken up a maximum of ~40% of the microstructure under any conditions. This indicates that the kinetics of dynamic recrystallisation are very slow in Elektron 675; therefore, at the end of the tests, the amount of dynamic recrystallisation is still increasing and causing a continued decrease in the flow stress.

Figure 137 shows a schematic version of the features seen in most Elektron 675 experimental curves. These different regions of behaviour will be used in this chapter to discuss the various features investigated in this work: the work hardening region will be discussed in section 5.3 and the peak strain and flow softening region will be discussed in section 5.4. The limits of ductile behaviour will then be discussed in section 5.5 and the post deformation behaviour of annealing and precipitation will be discussed in section 5.6.

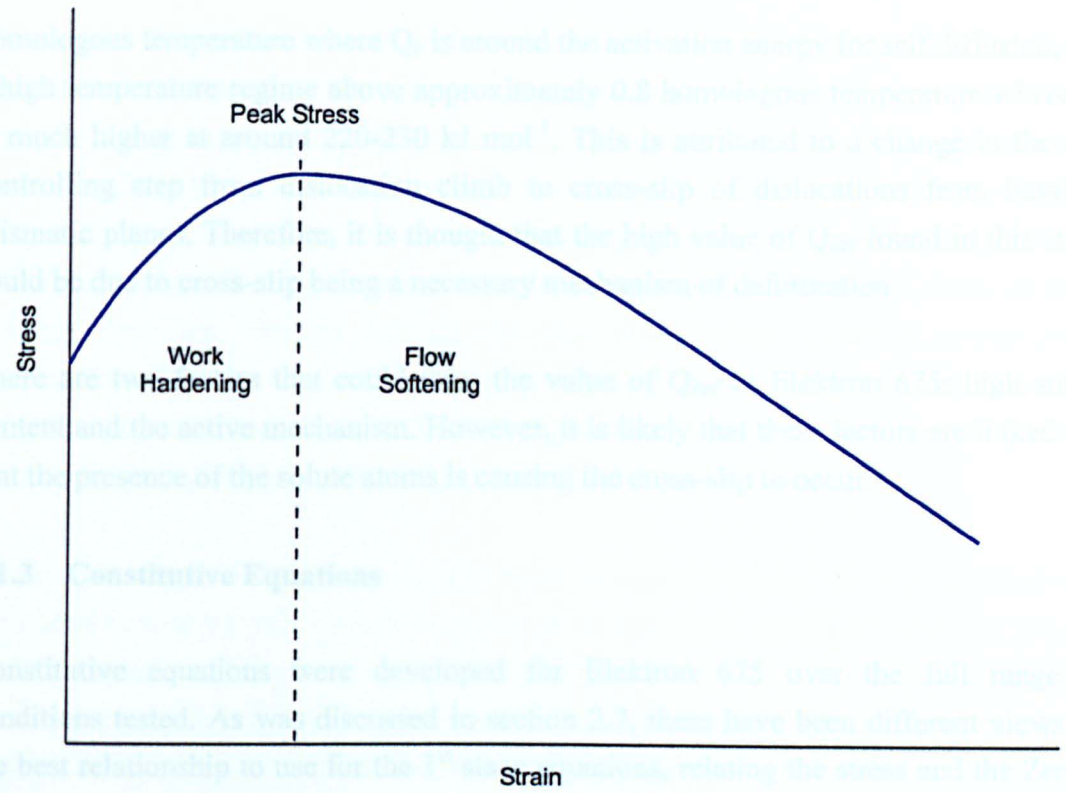

Figure 137 – Schematic diagram of typical flow behaviour in Elektron 675

5.1.2 Activation Energy of Deformation (Q_{def})

The most important constant that has been calculated in the current work is the activation energy of deformation (Q_{def}). This was found to be 217 kJ mol^{-1} for Elektron 675 and is much higher than the standard values reported in the literature for magnesium alloys. Often, values of Q_{def} are clustered around the activation energy for self diffusion, 134 kJ mol^{-1}[2], with values between 112 and 175 kJ mol^{-1} reported for relatively low alloyed magnesium[36, 183-185, 203, 216]. However, it is generally found that as the solute content increases in magnesium alloys the value of Q_{def} also increases[174, 217], a similar finding to that in other materials, such as both ferritic and austenitic stainless steels[198], and ascribed to the greater difficulty of diffusion of the solute atoms. Therefore, due to the atomic size difference of rare earth atoms and magnesium atoms, it can be expected that this will cause a significant increase to the activation energy of deformation.

Other studies[183, 188, 189, 218] have looked at the activation energy for creep (Q_c) in magnesium and its alloys. It has often been found that there are two regimes of Q_c, that are dependent on temperature; a low temperature regime below approximately 0.7

homologous temperature where Q_c is around the activation energy for self diffusion, and a high temperature regime above approximately 0.8 homologous temperature where Q_c is much higher at around 220-230 kJ mol^{-1}. This is attributed to a change in the rate controlling step from dislocation climb to cross-slip of dislocations from basal to prismatic planes. Therefore, it is thought that the high value of Q_{def} found in this study could be due to cross-slip being a necessary mechanism of deformation.

There are two factors that could raise the value of Q_{def} in Elektron 675: high solute content and the active mechanism. However, it is likely that these factors are linked and that the presence of the solute atoms is causing the cross-slip to occur.

5.1.3 Constitutive Equations

Constitutive equations were developed for Elektron 675 over the full range of conditions tested. As was discussed in section 2.7, there have been different views on the best relationship to use for the 1st stage equations, relating the stress and the Zener-Hollomon parameter. The exponential function[174, 201], power law function[96, 109, 174, 183] and sinh function[41, 176, 184, 185] have all been successfully used in magnesium and therefore, it was reasonable to study each to see which gave the closest fit with the experimental data. It was found that the current experimental data, over the range tested, had the least error when fitted with the exponential relationship. It was stated by McQueen and Ryan[198] that the exponential function works best at high stresses in the hot working regime and thus would be expected to provide the best fit in the current work. At lower values of Z than tested, the exponential relationship predicts flow stresses that are negative. This is only a problem when the constitutive equations are introduced into a finite element model that requires predictions of stresses at low Z. In this case, a power law relationship is used as this still provides a reasonable fit with the experimental data, although with larger errors than the exponential relationship, but does not become negative at any value of Z. This does not significantly change the behaviour of the material in the finite element model because the majority of the material modelled experiences conditions within the range tested, where the fit is reasonable.

It was shown in figure 62 and figure 63 that the constitutive equations fit the experimental data well at all conditions tested above 440°C. Below this temperature there is still a reasonable approximation of the flow stresses but the experimental curves appear to become more rounded and thus the constitutive equations do not fit as well.

The stresses in these tests reach higher values than those predicted by the constitutive equations and this could be due to a change in mechanism, although the specific changes are unknown. Following the peak stress, the softening also appears to be greater in these tests. This could be due to a change of softening mechanism at these temperatures, although the microstructural investigations do not show any large changes in dynamic recrystallisation. It could also be caused by the initiation of small amounts of shear cracking. Section 4.2 showed that shear failure occurred at the lower temperatures, but this was only reported if cracking visible to the eye was present. It would be expected that, particularly in the high strain shoulder regions, minute cracking would precede macroscopic cracking and would cause a softening effect.

In the tests above 440°C there is still some variation between the experimental and simulated curves but this does not appear to be any more significant than the general variation due to experimental errors discussed in section 5.1.1, with no deviations more than approximately 15MPa. This error would be expected to be relatively low due to the number of tests used to calculate the constitutive equations.

5.2 Homogeneity of Microstructure in Plane Strain Compression

There are many strain heterogeneities in the plane strain compression test. Some of these come from problems such as tool misalignment or uneven lubricant distribution, but even in a perfect test there is still a non-uniform strain distribution. This was shown in the modelling results in section 4.3.4 and it can be seen that in a sample deformed at 460°C and $5s^{-1}$ the strain present in the deformation zone, at a total strain of 0.7, ranges from 0.25 to 1.5. The low levels of strain are found in dead zones near the shoulders of the sample and the highest strains are found in regions in the middle of the material between the shoulders. The strain in the centre of the samples was found to be very close to the nominal total strain applied to the sample at all conditions of temperature and strain rate.

EBSD maps were carried out along the centre line stretching from one tool to the other. These were presented in figure 82 and show the change in microstructure due to the differences in strains experienced. These maps do not agree entirely with the finite element modelling as they show a noticeably lower strain in the areas close to the tools. Although the models show a small area of lower strain very close to the tools, it is not as large as seen in the EBSD maps. This difference between experimental and simulated results could be due to frictional effects. The friction coefficient was calculated in

section 4.3.1.4 but the coincidence of the curves was not exact so there is a certain margin of error. Therefore, these results suggest that the true friction coefficient is perhaps slightly higher than 0.07. The map in figure 82(a) shows a sample deformed at 440°C and $10s^{-1}$ strain rate. In this map a shear band is very clearly seen, and can be expected to stretch across the majority of the sample. Shear bands dramatically alter the deformation of the material as a large amount of strain is accommodated in the interior. They change the microstructure of the material significantly and are discussed in more detail in section 5.4.3.

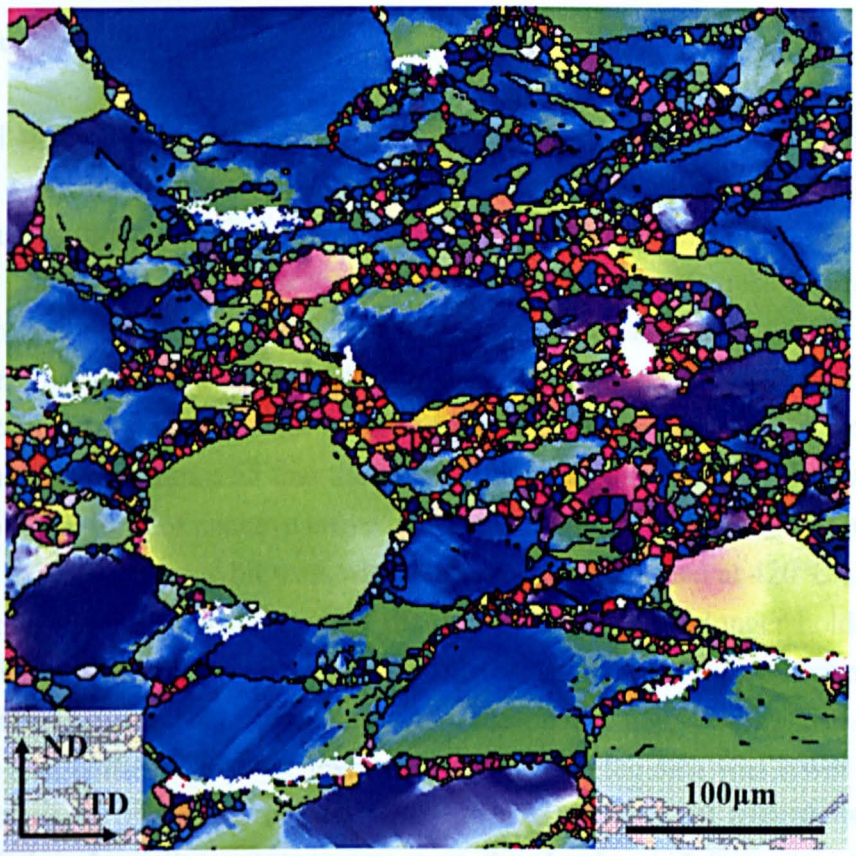

Figure 138 – EBSD map (IPF colouring) showing a sample deformed in plane strain compression to a total strain of 0.7 at 460°C and $5s^{-1}$. Map taken on the rolling plane

Almost all EBSD maps were carried out on the transverse plane of the sample as this contained the two principal stress directions. However, it was necessary to check that the microstructure was not significantly different in other directions. Figure 138 shows an EBSD map carried out on the rolling plane of a sample deformed at 460°C and $5s^{-1}$. It can be seen that, despite the different stress and strain states experienced, the microstructure is very similar to that seen on the transverse plane. Therefore, the

microstructures observed on the transverse plane are believed to be representative of those on all planes.

It has been shown above that in all samples where large shear bands are not present, the strain experienced and microstructure formed on the centre of the transverse plane is fairly representative of the nominal strain applied to the sample.

5.3 Work Hardening Region

5.3.1 The Shape of the Curve

The typical shape for the early region of a metal stress-strain curve is a convex curve of decreasing work hardening rate from the yield point up to a peak stress, before either steady state or softening occurs. It is commonly reported (e.g. references [38, 39, 42, 51, 55, 63, 70, 72, 76, 171, 190]) that the work hardening portion of stress-strain curves for magnesium, and some other metals, can have a concave shape, showing an increasing work hardening rate, in the first stages of deformation. As seen in section 2.6, this has generally been attributed to a high level of twinning during the deformation. It can be seen in figure 54 and figure 55 that the stress-strain behaviour seen in the current work did not show any form of concave curve in normal single hit samples. The only possible exceptions are in the double hit tests where the samples deformed at 420°C showed less definitely convex curves at the start of the second hit after the longer hold times, see figure 75. Unfortunately, the early stages of deformation were those most affected by strain rate fluctuations. Therefore, there was a reasonably high level of data correction carried out and, consequently, the level of confidence in the data was lower than ideal. However, it can be reasonably concluded that the vast majority of tests showed convex curves and therefore slip, not twinning, was the dominant deformation mechanism causing work hardening in the early stages of deformation.

5.3.2 Twinning Systems

The best way to identify which twins were present during the current work was to use the disorientation profile from the EBSD maps, see figure 86. When this was compared against the random orientation distribution, any peaks could be found and correlated to a specific type of boundary. The only peaks that could be resolved above the noise of the data, and therefore could be considered significant, were at approximately 60° and 86°, along with another more general peak at the lowest values. The lower angle peak can be

discounted for twinning as it was due to the low angle subgrain boundaries. By also looking at the axes about which the 60° and 86° boundaries were rotated, see figure 87, it could be concluded that the peaks were caused by $\{10\bar{1}2\}$ twins. This agrees with the qualitative visual analysis from figure 84, where it is clear that the majority of twins are $\{10\bar{1}2\}$ type. Also visible on these maps are a very small amount of other twin boundaries that did not have a high enough concentration to cause a peak in the disorientation distribution. Therefore they can be dismissed because they are either random boundaries that, through chance, had the same disorientation as a twin or, even if they are true twin boundaries, the influence on the deformation behaviour of the material will be negligible.

The twinning behaviour seen in Elektron 675 during hot working is typical of magnesium and many other hcp metals with $\{10\bar{1}2\}$ twins dominating[35, 36, 42, 55, 65, 66, 70, 71]. Other twins have been seen in the literature, the most common of which are $\{10\bar{1}1\}$ twins and $\{10\bar{1}1\}$-$\{10\bar{1}2\}$ double twins[35, 36, 38, 51, 66, 71, 74, 76]. These twins allow compression parallel to the c-axis and can be very important when no slip systems are available to accommodate c-axis compression strains, generally at lower temperatures. As no twins of these types are seen in the current work, and the samples exhibited reasonable ductility, it must be assumed that some other deformation mechanism was operative to provide reduction in the c-axis direction. This is expected at the higher temperatures experienced here, as explained in section 2.3.8.1.

It was shown in figure 88 that the frequency of $\{10\bar{1}2\}$ twin boundaries within the material increased to a maximum around 0.1 strain and then gradually decreased down to a background level by approximately 0.3 to 0.4 strain. As can be seen in figure 84, the frequency of twin boundaries within the material was greatest when the twins were growing into a grain with many surfaces of interaction with the surrounding non-twinned matrix. As the twin progressed, these individual fingers of twinned material grew and joined together, consequently decreasing the amount of twin-matrix boundary present. After further growth, the twinned material can consume the entire grain, leaving no 'matrix' for a twin-matrix boundary to be identified against. Therefore, the twin boundaries will be removed from the material completely and the frequency of 86° boundaries will return to the random distribution. Another possible explanation for the reduction in the number of twin boundaries is that dynamic recrystallisation could have occurred in these areas. This would change the orientation on one, or both, sides of the twin boundary, removing the specific relationship used to identify the twin. However, although dynamic recrystallisation had begun by 0.3 strain, it appears to have formed

mostly on pre-existing grain boundaries and not in the areas where twin boundaries existed at lower strains. A further explanation was put forward by Klimanek and Potzsch[70], who observed a similar decrease in twin boundaries as strain progressed and suggested that the twin lamellae became narrower and eventually could not be resolved by the optical microscopy techniques used. In the current work, much smaller lamellae could be resolved and no areas of fine twinning were ever observed so the Klimanek and Potzsch theory can be discarded. Therefore, it can be concluded that the decrease in twin boundaries can be directly related to an increase in twinned material.

In some cases the twins do not completely consume the grain, leaving small areas around each grain boundary that consist of the original orientation. This can be seen in figure 139, an enlargement of a grain from figure 81, where the grain in the centre has almost fully twinned but has left a small amount of untwinned material at the grain boundaries. The same features were identified by Barnett *et al.*[72] but were not explained. It is thought that, although the stresses in the majority of the grain were ideal for twinning, the compatibility stresses from the neighbouring grains reduced the overall driving force for twinning in these small areas and stopped the boundaries progressing any further.

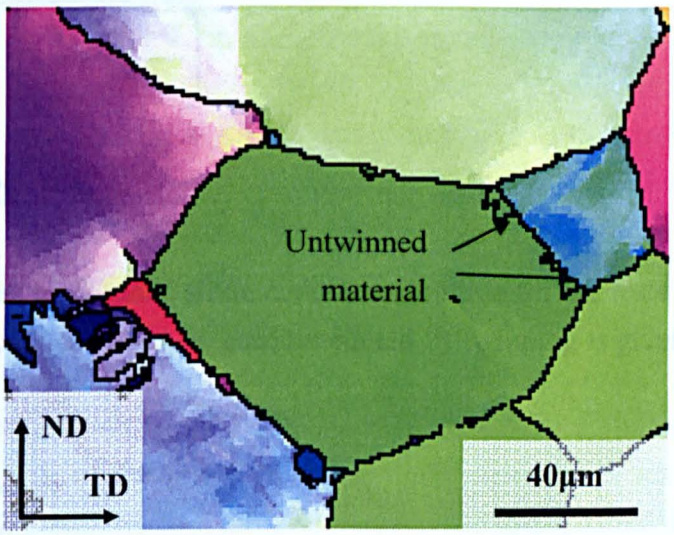

Figure 139 – EBSD map (IPF colouring) of a sample deformed at 460°C and $5s^{-1}$ strain rate to a total strain of 0.1. The grain in the centre has almost fully twinned, leaving a small amount of untwinned material at the grain boundaries

Figure 88 shows that following approximately 0.3 strain, there was very little further twinning occurring in the sample. Therefore twinning was a very active deformation

mechanism in the early stages of compression, approximately up to the peak strain in the flow curves, but all of the grains that were oriented to allow twinning were exhausted relatively quickly.

Although twinning is very active in the early deformation of Elektron 675, the amount of strain that it can accommodate is rather low. Using the formulae in Hall[64] and the lattice parameters calculated in section 4.1.3.1, the twinning shear, s, can be calculated:

$$s = \frac{2}{\tan 2\varphi} \tag{53}$$

where 2φ is the angle between η_1 and η_2. For Elektron 675 the shear of $\{10\bar{1}2\}$ twinning is 0.140. This is slightly higher than the standard values given for pure magnesium of 0.129[48] or 0.130[33] and therefore the alloying additions in Elektron 675 allow slightly more strain to be accommodated by twinning.

Using further equations from Hall, combined in equation 54, the maximum compression, $\left(\frac{l'}{l}\right)_{max}$, can be calculated:

$$\left(\frac{l'}{l}\right)_{max} = \sqrt{1 + s\left(\frac{s - \sqrt{s^2 + 4}}{2}\right)} = 0.932 \tag{54}$$

If it is assumed that ideal plane strain conditions are true for the tests carried out in this work, the total equivalent strain, ε, accommodated by twinning is given by equation 55:

$$\varepsilon = \frac{2}{\sqrt{3}} \ln\left(\frac{l'}{l}\right)_{max} \tag{55}$$

For Elektron 675, the maximum equivalent strain in compression that can be accommodated by twinning is 0.081. However, twinning was seen to be active at strains up to approximately 0.3; therefore, the imposed strain was well above that which could be accommodated by twinning (0.081), so slip, or other mechanisms, must have accounted for nearly three quarters of the strain.

Despite the lack of strain accommodated by twinning, it still has a large influence on the behaviour of the material due to the effect that twinning has on texture reorientation, see section 5.3.4, and work hardening, as already described in section 5.3.1.

5.3.3 Slip Systems

As was discussed in section 5.3.1, the most important mechanism causing work hardening in the early stages of deformation is dislocation slip. The various slip systems will be discussed in this section, although it should be noted that deformation by slip continued through the entirety of the test, including the flow softening region. Work hardening was achieved through the standard process of increasing dislocation density within the sample.

It was seen in section 4.4.6 that slip occurred predominantly on basal planes and also on prismatic planes in certain grains. This agrees well with the most common slip systems observed in the literature, see section 2.3.4.2. It was discussed in section 2.3.4 that 5 independent slip systems are normally required for full plasticity of a polycrystalline material[44, 45] and that the basal and prismatic planes contain only 4 independent systems. The addition of $\{10\bar{1}2\}$ twinning, which was common in the samples, provides another partial independent system but is unidirectional so can only be considered as a further ½ system, bringing the total to 4½[48, 56]. However, most of the samples tested showed good levels of ductility, which would not be expected with only these slip systems, indicating that another system must also be active, most likely <c+a> slip. It was argued by Kocks and Westlake[48] that the strict requirement for 5 independent systems only applies to full plasticity, and that limited plasticity is still achieved with less slip systems. The level of ductility seen by Kocks and Westlake was generally lower than that seen here so it is unlikely that the deformation could have been achieved with no further deformation mechanisms; however, this should not be completely ruled out without further evidence. It is possible that the methods of identification of slip systems used in this work were unable to identify the minor contribution of a further slip system. EBSD analysis relied on the formation of substantial planar slip bands and it would not be expected that such considerable levels of slip would occur on the 5^{th} slip system to be activated. The areas covered by TEM analysis were so small that it is entirely possible that further slip systems were not observed. It is also true that, again, only planar slip bands were studied in TEM and the contribution of another slip system may be so small that slip bands were not formed. Much more in depth studies of

dislocations in TEM would be required to directly conclude about the activity of <c+a> slip.

Despite the fact that <c+a> slip was not directly observed, there were other factors that provided indirect evidence for the activity of this slip system. The subgrains seen in section 4.4.4.1 form with a 3 dimensional structure by the rearrangement of dislocations within the grains. In order for a 3 dimensional structure to form, Galiyev *et al.*[96] stated that <c+a> dislocations must be present to create the required boundaries in all directions. Another indication that <c+a> slip is present is the evolution in texture. This will be discussed in more detail in section 5.4.4, but, essentially, the texture forms with a split in the standard basal texture towards the rolling direction. It will be shown that the most likely cause of this texture change was the presence of <c+a> slip.

5.3.4 Initial Texture Evolution

The basal texture was defined in section 2.5.3 as that in which the c-axes of the crystals are aligned closely with the compression direction in the material. This texture was seen to evolve in plane strain compression of Elektron 675 at relatively low strains. Unfortunately, the area covered in the EBSD analyses at different strains was too small to provide truly accurate pole figures, but it was shown in figure 122 and figure 123 that the basal texture had probably developed by a strain of approximately 0.2 to 0.3. It was shown in figure 126 that the regions of a sample that had undergone $\{10\bar{1}2\}$ twinning show a very strong, almost perfect basal texture and therefore it can be concluded that $\{10\bar{1}2\}$ twinning plays a very significant role in the development of the basal texture. By looking at the pole figure for the non-twinned region in figure 126 it can be seen that the non-twinned regions continued to exhibit a random texture. It can be expected that slip was occurring concurrently with twinning in both the twinned and non-twinned regions. As discussed in section 5.3.3, the most active slip system was probably basal slip and, due to the orientation dependence on the basal plane, this would be expected to be more active in the non-twinned regions. Therefore, basal slip appears to have caused little texture change and the contribution to the total change is minimal in comparison with $\{10\bar{1}2\}$ twinning.

As already stated, the development of basal texture appeared to reach completion by a strain of approximately 0.2 to 0.3. This corresponds well with the reduction in twin boundaries shown in figure 88. It was discussed in section 5.3.2 that the reduction in twin boundaries is directly related to the increase in twinned material and that when the

level of twin boundaries returns to the random distribution, twinning is complete. This again demonstrates that $\{10\bar{1}2\}$ twinning is primarily responsible in Elektron 675 for the production of a strong basal texture.

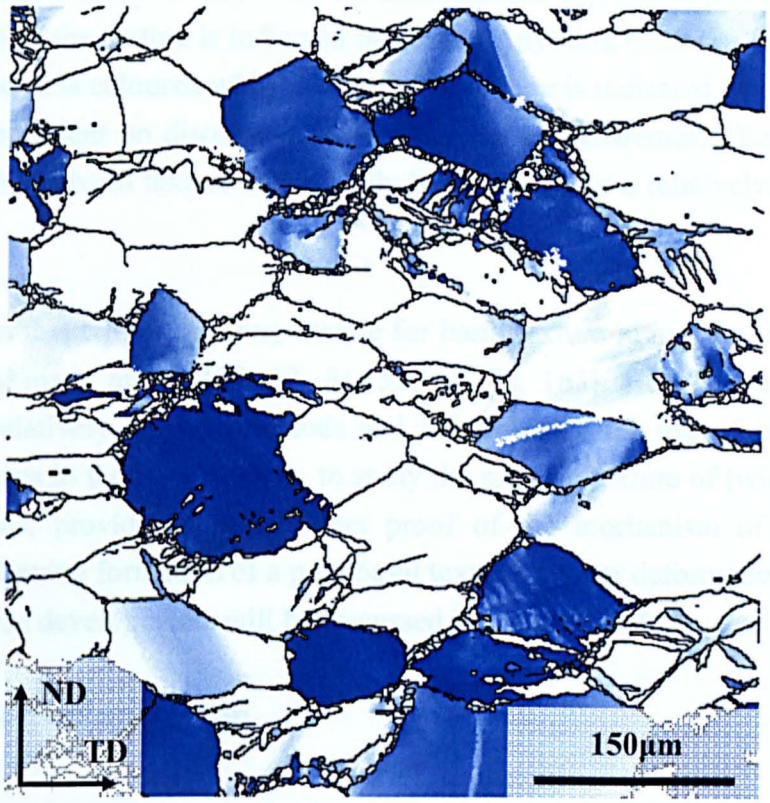

Figure 140 – EBSD map (texture colouring) showing a PSC sample deformed at 460°C and $5s^{-1}$ to a total strain of 0.3. Blue indicates basal texture, fading to white at 30° disorientation and greater

The textures seen from all grains, see figure 122 and figure 123, are not as sharp as that produced directly from twinning, seen in figure 126. However, it is not expected that every grain will be in an orientation suitable for twinning; indeed Calnan and Clews[37] stated that only those grains with their c-axis more than 68° from the compression direction will undergo $\{10\bar{1}2\}$ twinning. If it is assumed that all grains above this critical angle undergo twinning, and no grains less than the critical angle do, then the 0002 pole figure would see a complete depletion around the edge and a strengthening in the centre, i.e. a basal texture, but there would still be a significant distribution out to 68°. The grains oriented such that twinning would cause extension in the transverse direction are also less likely to operate due to the constraint imposed in that direction[57]. This leads to the weaker band of 0002 poles in the transverse direction. The local stress and strain distributions will be much more complex within the material

than this simplification, although it does give an indication as to how a more dispersed basal texture formed. Pole figures themselves can also distort the appearance of texture because the eye is drawn to the strong peak and the remainder of the pole figure can appear inconsequential. This issue is well demonstrated by a texture map, as shown in figure 140, where the texture is indicated by colour. Anything more than 30° disoriented from perfect basal is coloured white and the basal texture is indicated by deep blue, with a gradation dependent on disorientation between the two extremes. This demonstrates that a fairly strong basal texture can actually be produced by a relatively small number of grains.

The conclusion that twinning is responsible for basal texture in magnesium has already been stated by many authors[37, 42, 51, 52, 57, 70, 163]. However, many of these studies used relatively indirect methods and it is felt that the use of high resolution EBSD techniques in the current work, to study the specific texture of twinned and non-twinned regions, provides a more direct proof of the mechanism of basal texture formation. Following formation of a pure basal texture, further deformation changed the texture and these developments will be discussed in section 5.4.4.

5.4 Flow Softening Region

As was discussed in section 2.6.3, the mechanism causing flow softening actually begins before the peak stress and causes the decrease in work hardening rate, the peak stress and subsequent true softening behaviour. It is often stated in the literature that flow softening in magnesium is caused by dynamic recrystallisation[51, 181, 182, 193] and this is also thought to be the dominant softening mechanism in Elektron 675. Dynamic recrystallisation is discussed further in section 5.4.2. The evidence for this being the main softening mechanism is the clear observations in microscopy, for example figure 83 and figure 89, and the time and temperature dependent nature of the peak stress, explained in the following section. However, shear band formation has also been thought to cause some softening and will be discussed in section 5.4.3.

5.4.1 Peak Strain

The peak stress is reached when the work hardening and softening effects are equal. Softening does not often start at the very beginning of deformation, normally requiring time for nucleation or a critical stored energy to be reached. It is stated in the literature that the initiation of softening can be measured from an inflection point on a $d\sigma/d\varepsilon - \sigma$

plot that will exist shortly before the peak stress[96]. However, in the current tests there is too much noise in this region to accurately determine this point; therefore the strain at which the peak stress occurs (the peak strain) has been used as an indicator of the start of softening but it should be remembered that the softening will actually have begun slightly earlier. Figure 56 shows that the peak stress was reached sooner in tests carried out at lower values of Z. Therefore, it can be deduced that the softening mechanism is time and temperature dependent, which fits well with dynamic recrystallisation, as proposed in the literature[51, 181, 182, 193].

5.4.2 Dynamic Recovery and Recrystallisation

The major features of dynamic recovery and recrystallisation in Elektron 675 were seen in section 4.4.4. It was shown that strong disorientations developed across large grains and that substructure formed as a consequence. It was also seen that dynamic recrystallisation occurred in a necklace structure around grain boundaries and the volume fraction increased linearly with strain. However, completion of recrystallisation was not reached by a strain of 0.7 in any samples tested. The average size of the recrystallised grains was similar to that of the subgrains, and was strongly affected by temperature and strain rate but not the strain. The texture of the recrystallised grains was found to be notably different from the parent grains.

5.4.2.1 Mechanisms of Dynamic Recrystallisation

The various mechanisms by which dynamic recrystallisation can occur were discussed in section 2.4.3 and will be briefly summarized here. The two major mechanisms are discontinuous dynamic recrystallisation (DDRX) and continuous dynamic recrystallisation (CDRX). DDRX progresses by grain boundary bulging and migration, whereas CDRX occurs by the rearrangement of dislocations into subgrains, followed by the absorption of further dislocations to produce high angle grain boundaries. DDRX is known to be a standard DRX mechanism across a wide range of materials and the process is generally identical in all situations. CDRX, on the other hand, is less well known and there are various mechanisms by which it can occur. The relevant mechanisms for magnesium are those of conventional CDRX, twin CDRX and continuous dynamic rotation recrystallisation (CDRRX). Conventional CDRX occurs in polycrystals that deform fairly homogeneously and in which multiple slip systems can be activated across large areas of the grains. Thus, polygonization of the grains can occur through dynamic recovery of dislocations and these will convert to grain

boundaries with absorption of further dislocations. Twin CDRX operates in the same manner, but in areas in and around twins where the formation of the twins increases the stress and activates more slip systems. The dislocation rearrangement in these areas creates subgrains involving the twin boundaries. The later absorption of dislocations takes place not only in the low angle boundaries, but also in the twin boundaries, changing them to random grain boundaries. CDRRX also operates in a very similar manner but requires the production of a large number of geometrically necessary dislocations to form the low angle boundaries. These are produced by large rotations of the crystal lattice in the regions surrounding grain boundaries. Following this, the same processes of subgrain formation and dislocation absorption occur.

Initially, the processes of dynamic recovery should be considered. The formation of cell and subgrain boundaries was studied using EBSD in section 4.4.4.1 and the substructure was identified in figure 92 and figure 94. The substructure seen at higher temperatures showed more clearly defined boundaries, although the cells/subgrains formed were of a larger size. This is typical of dynamic recovery[85, 112, 219], as the climb and cross-slip processes required are more easily activated at higher temperature. Thus, the recovery can progress faster and more annihilation and rearrangement can occur to give a lower energy, and more ordered, structure. Generally the wider, less ordered, boundaries, as seen in figure 93, are referred to as cell walls and the more ordered boundaries as subgrain boundaries, as seen in figure 91. It is commonly found that higher values of the Zener-Hollomon parameter give smaller subgrains. He *et al.*[119] suggested that this is due to the slower transformation from low angle to high angle boundaries; if the dislocations are not being absorbed as quickly in the previously formed low angle boundaries, the density will be higher and there will exist a driving force for the formation of new low angle boundaries.

The EBSD analyses in the current work do not show any bulging of grain boundaries. This is a necessary precursor to DDRX and has been seen in many studies in which magnesium underwent DDRX[128, 137, 140, 146]. Therefore, it is unlikely that DDRX was active to any significant levels in any of the tests carried out. It was also seen in the current work that the majority of dynamic recrystallisation occurred around the grain boundaries. This is typical of all DRX mechanisms apart from twin CDRX, as that predominantly occurs at twins and twin intersections. Figure 81 shows that at low strains dynamic recrystallisation is already operational and, despite the large number of twin boundaries present, the new grains are formed mostly at grain boundaries, with no great tendency to form in or around twins. If twin CDRX had been highly active, it

would have been possible for twins to have fully recrystallised before the test was stopped and the EBSD map taken. This would have meant that the twin boundaries would have disappeared but it would still be expected that the underlying shape of the twin, protruding into the grain, would be visible. As this is not the case in any EBSD maps carried out here, it is thought that twin CDRX within twins is of minimal importance. There is, however, a small tendency for DRX grains to form more at the grain boundaries near twins than in grains that do not contain twin boundaries. This is not strictly twin CDRX and both conventional CDRX or CDRRX would be assisted by the increased compatibility stresses at the twin boundaries.

The defining feature of CDRRX is the rotation of the crystal structure in the grain boundary regions. It is assumed that the recrystallised grains retain a similar texture to the rotated part of the parent grain from which they formed. Therefore, the recrystallised grains should give a reasonable indication of the level of rotation occurring. It was shown in figure 128 and figure 129 that DRX in Elektron 675 caused a significant weakening effect from the basal deformation texture. This implies that the DRX grains are formed from regions in the parent grains that have undergone substantial rotation. It is stated in the literature that texture is not affected by recrystallisation in hcp metals[118, 138, 152-154] with all mechanisms other than CDRRX[51, 88]. This rotation is also visible in a disorientation plot across an entire deformed grain, for example figure 90. Therefore, this all provides further evidence for the conclusion that CDRRX is the dominant dynamic recrystallisation mechanism in Elektron 675.

There have been a reasonable number of studies carried out in the literature looking at the dynamic recrystallisation behaviour in magnesium. It was shown in section 2.4.3 that all the possible mechanisms of DRX have been seen previously in magnesium and its alloys. It was noted that, in general, those studies carried out at higher temperatures showed DDRX[36, 136, 137], while those carried out at lower temperatures underwent CDRX[88, 120, 138, 139]. This does not agree well with the results from the present work as CDRX has been observed during hot working. However, many of the other studies were carried out at lower strain rates, often in the creep range. Therefore, if the Zener-Hollomon parameter (Z) is used instead of purely temperature, the current work becomes more comparable, as the higher strain rate used equates to a lower temperature. Another factor that changes the value of Z is the activation energy of deformation (Q_{def}), calculated to be 217 kJ mol^{-1} in section 4.3.1.1 and discussed in section 5.1.2. As stated previously, the value found in this work is higher than that given in much of the literature, thought to be due to the high level of rare earth additions, and therefore, the

values of Z calculated at any temperature and strain rate are higher than they would be for other alloys. A comparison between Z calculated for Elektron 675 and that for AZ31, using the commonly quoted value of Q_{def} of 134 kJ mol^{-1}, is given in table 19. The range of Z values tested in the current work was roughly between 10^{14} and $10^{18}s^{-1}$. Table 20 shows that the conditions required to obtain the same values of Z in AZ31 occur at a much lower temperature, particularly when low strain rates are used, such as those in the literature. Even with a relatively high strain rate of $10s^{-1}$, the Zener-Hollomon range tested in Elektron 675 is exceeded at around 250°C. Therefore, the Zener-Hollomon range tested in the current work corresponds to the 'high Z' range previously described, and the observations of CDRX fit well with the literature.

Table 19 – A comparison between Zener-Hollomon parameters for Elektron 675 and AZ31 at the range of conditions tested here

		Elektron 675	AZ31
		Q_{def} = 217 kJ mol^{-1}	Q_{def} = 134 kJ mol^{-1}
Temperature (°C)	Strain Rate (s^{-1})	Z (s^{-1})	Z (s^{-1})
380	5	$1.16x10^{18}$	$2.64x10^{11}$
520	1	$2.00x10^{14}$	$6.75x10^{8}$

Table 20 – A selection of conditions that give similar values of Z in AZ31 to those experienced in Elektron 675

		AZ31
		Q_{def} = 134 kJ mol^{-1}
Temperature (°C)	Strain Rate (s^{-1})	Z (s^{-1})
50	10^{-5}	$4.69x10^{16}$
150	10^{-2}	$3.55x10^{14}$
150	10	$3.55x10^{17}$
250	10	$2.43x10^{14}$

It is thought that CDRRX is active because of the general difficulty of slip in Elektron 675. The high level of alloying gives a very strong solution hardening effect and restricts dislocation motion on all slip systems. By increasing the required stresses for slip in the grain interiors, even higher stresses would build up at grain boundaries,

allowing more non-basal slip and shearing of the grain boundary region. Therefore, dynamic recrystallisation could logically progress by the mechanism of CDRRX.

5.4.2.2 Recrystallised Fraction

The fraction of dynamically recrystallised material showed a wide variation with both strain and deformation conditions, see section 4.4.4.2. It was already discussed in section 4.4.4.2 that the large heterogeneities of strain within the samples, for example due to differences in temperature or tool alignment, cause significant differences in the volume fraction of recrystallised grains between different areas. All EBSD maps used to measure the recrystallised fraction were carried out in the centre of the deformation zone, but unfortunately, the level of strain that this region experienced was not exactly the same from one sample to the next. Therefore, although all measurements of recrystallised fraction as a function of Z were carried out at a nominal strain of 0.7, there is an unknown variation inherent in the results. Further complicating the recrystallised fraction measurements were the formation of large shear bands. Again, these formed due to factors such as tool misalignment and could be on a macroscopic scale, for example in figure 82. In samples that formed shear bands, the strain was strongly localized in these areas and reached levels much higher than 0.7. Often these regions showed much higher than expected recrystallised fractions, for example the test at 440°C and $10s^{-1}$ strain rate, shown in figure 82. In the shear band in this sample, many grains had completely recrystallised and, therefore, the measurement of recrystallised fraction is entirely dependent on how much of the shear band is included. To obtain this very high level of recrystallisation it is thought that another DRX mechanism could be operating. Geometric dynamic recrystallisation occurs when grains become so elongated by strain that opposite grain boundaries become very close. During deformation, grain boundaries often become serrated, due to the production of subgrains, and eventually these serrations will contact those on the opposite grain boundary, splitting the grain into many smaller grains. With only a small amount of rearrangement of the grain boundaries, an equiaxed structure of small grains is formed, and thus the process is considered to be recrystallisation. In the current work, there is only indirect evidence that this mechanism is active: there are many severely elongated grains, showing some serration, and the final microstructure matches that in the literature[112]. Lower strain tests would need to be carried out on samples that exhibit this effect to fully conclude that the mechanism is operating. However, it is felt that the addition of this recrystallisation mechanism within the shear bands could explain the unexpectedly high level of recrystallisation observed. If the measurement at 440°C and

$10s^{-1}$ is removed from figure 96, and it is re-plotted in figure 141, a steady decrease in the volume fraction at higher values of Z becomes apparent, as expected from the literature[126, 220]. However, there is still a large amount of scatter in this data, due to the heterogeneities already mentioned, so the assumption that lower values of Z give more recrystallisation must not be taken as definite.

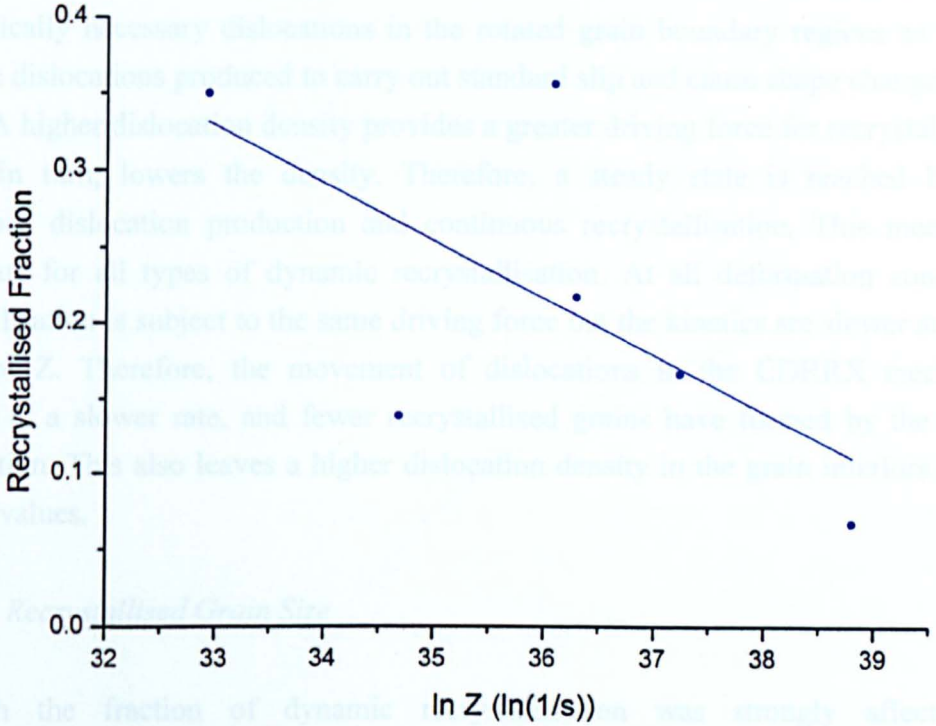

Figure 141 – Plot showing the fraction of dynamic recrystallisation against Zener-Hollomon parameter, with the point at 440°C and $10s^{-1}$ strain rate removed

The measurements of recrystallised fraction on samples of differing strain were much more reliable than those deformed under different conditions. This is because the tests were all carried out at around the same time and thus the tool alignment, even if slightly misaligned, was the same for all tests. Problems with shear bands were less common at the value of Z used for these tests, and the lower strains for many of the tests lessened the strength of the heterogeneities.

The change in recrystallised fraction with increasing strain was shown in figure 95. The volume of dynamically recrystallised grains started increasing at a strain of approximately 0.1 and then increased almost linearly through the remainder of the deformation. It could be argued that there is a sigmoidal type shape, where the gradient of the curve increases to a maximum in the middle of deformation and then starts to

reduce again in the latter stages. However, the trend is not strong enough to conclude that this shape is correct, only that increasing the strain significantly increases the level of recrystallisation, a feature commonly reported[112].

The increase in recrystallised grains with increasing strain is due to the continuous production of dislocations during deformation. In CDRRX these dislocations come from geometrically necessary dislocations in the rotated grain boundary regions as well as from the dislocations produced to carry out standard slip and cause shape changes in the grains. A higher dislocation density provides a greater driving force for recrystallisation which, in turn, lowers the density. Therefore, a steady state is reached between continuous dislocation production and continuous recrystallisation. This mechanism holds true for all types of dynamic recrystallisation. At all deformation conditions, recrystallisation is subject to the same driving force but the kinetics are slower at higher values of Z. Therefore, the movement of dislocations in the CDRRX mechanism happens at a slower rate, and fewer recrystallised grains have formed by the end of deformation. This also leaves a higher dislocation density in the grain interiors than at lower Z values.

5.4.2.3 Recrystallised Grain Size

Although the fraction of dynamic recrystallisation was strongly affected by heterogeneities in the strain across samples, this had much less of an effect on the size of the recrystallised grains. This is because the size of the recrystallised grains was hardly affected by the strain that they were subjected to. During CDRRX, the grain size is dictated by the subgrain size that forms from the recovery of dislocations. Once these subgrains have formed, the mobility of the boundaries is relatively low, and thus recrystallisation progresses by the movement of dislocations into the boundaries rather than the movement of the boundaries themselves, as in DDRX. Therefore, the grain size that forms at the beginning of recrystallisation is constant through further deformation with little grain coarsening or refinement. This is shown in figure 97, which gives the recrystallised grain sizes at increasing strain in samples deformed at 460°C and $5s^{-1}$ strain rate. Although recrystallisation had begun at a strain of 0.1, there were so few grains that a true average grain size could not be calculated. Therefore, the graph does not start until a strain of 0.2 when there are enough grains to make it statistically valid. A small increase in grain size can be seen as the strain increased and there are a couple of possible reasons for this. One explanation is that the grains were undergoing a standard grain coarsening process, driven by the reduction in stored energy from the

reduction in grain boundary area[112]. This is generally more prevalent if the material is held at temperature following recrystallisation, but could play a small part during deformation itself. Another possible explanation is the change in grain sizes formed due to the temperature. It is known that the temperature of the material rose during deformation, as shown in figure 142, and as will be shown below, the temperature has a strong effect on the recrystallised grain size. Therefore, the rise in temperature during the test would cause the recrystallised grains forming later to be of a slightly larger size. The distribution of grain sizes was also studied, see figure 98, and this shows that the percentage of small grains decreased while the percentage of larger grains increased. This would be true of both proposed mechanisms so does not distinguish between them.

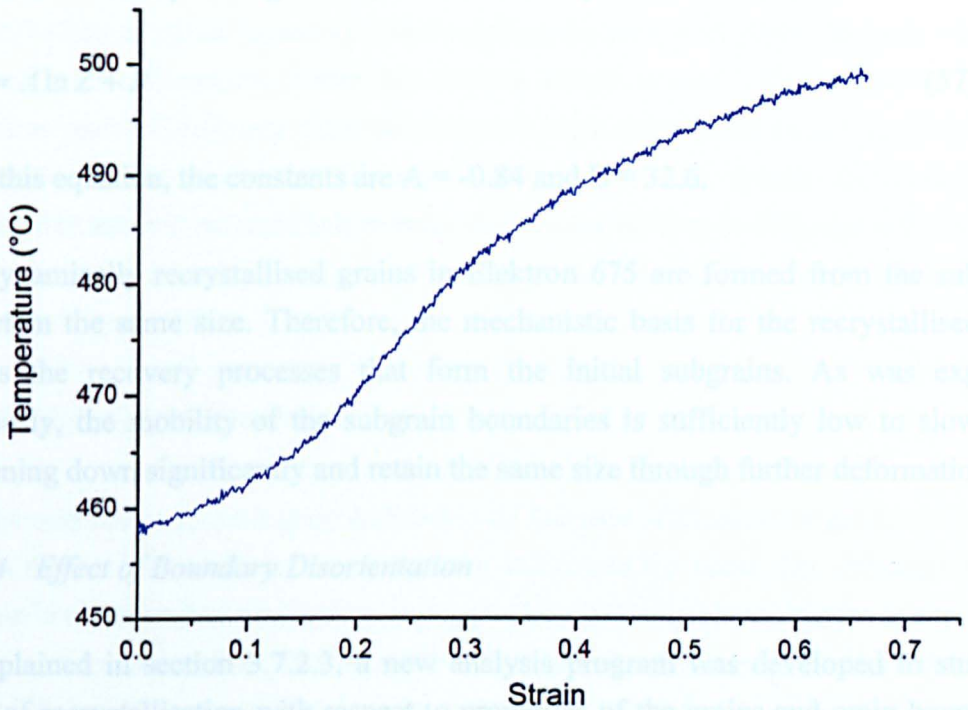

Figure 142 – Graph showing the temperature rise during a PSC carried out at 460°C and $5s^{-1}$ strain rate

Figure 100 shows the variation of the dynamically recrystallised grain size with the Zener-Hollomon parameter. The best correlation was found when the final temperature of the test was used to calculate Z, which would suggest that the temperature change during deformation has an effect on the final grain size. Therefore, while grain coarsening is expected to be present during dynamic recrystallisation, the deformation heating probably has more influence on the recrystallised grain size. The correlation of recrystallised grain size with the Zener-Hollomon parameter follows the general

relationship reported in the literature, discussed in section 2.4.3.4, of larger grains at higher values of Z[51, 96, 127, 137, 142]. The linear correlation with ln(Z) seen in figure 100 gives the best fit with the data but does not correspond to the equation reported in the literature, as given below:

$$Z = kd^{-N} \tag{56}$$

where k and N are constants.

The fit with this equation is reasonably good, and gives constants of $k = 2.15 \times 10^{16}$ and $N = 2.51$, but the equation given below more closely fits the trend in the current work:

$$d = A \ln Z + B \tag{57}$$

From this equation, the constants are $A = -0.84$ and $B = 32.6$.

The dynamically recrystallised grains in Elektron 675 are formed from the subgrains and retain the same size. Therefore, the mechanistic basis for the recrystallised grain size is the recovery processes that form the initial subgrains. As was explained previously, the mobility of the subgrain boundaries is sufficiently low to slow grain coarsening down significantly and retain the same size through further deformation.

5.4.2.4 Effect of Boundary Disorientation

As explained in section 3.7.2.3, a new analysis program was developed to study the levels of recrystallisation with respect to properties of the grains and grain boundaries. The results of the boundary disorientation analyses are presented in section 4.4.4.4 and show that there is a weak trend towards higher recrystallisation at lower disorientations. This trend is more apparent in the tests carried out at different strains, rather than those at different values of Z, a fact that highlights the problems inherent in this analysis. The EBSD maps used for the tests at different strains had 1μm step sizes, whereas those used for Zener-Hollomon variation had 2μm step sizes. The reasons for this were discussed in the results chapter and were essentially due to the different requirements of the maps and the scale of the microstructure. However, this issue has meant that the analysis program has recognised more grains as being recrystallised in the larger step size map because there are fewer pixels in each grain to give the critical disorientation. As the analysis is always checked by eye, there is some correction carried out but it is

impossible to correct every grain selected. Therefore, there were a higher number of true recrystallised grains in the 1μm step size map that were not identified correctly, and a higher number of small non-recrystallised grains that were misidentified in the 2μm step size map. Consequently, the measurements of the level of recrystallisation at each grain boundary are higher in the 2μm step size map. This effect appears to be stronger at the higher disoriented boundaries and thus the trend is weaker in the larger step size maps. The same heterogeneities as before also affect these results and thus the variation with Z showed the same large scatter. The test at 440°C and $10s^{-1}$ was removed from these charts because the recrystallisation mechanism appears to be different and not comparable.

The influence of grain boundary disorientation on recrystallisation has not been well reported in the literature. There has been a small amount of work looking at the migration rates of different disorientations of high angle grain boundaries[112, 221]. This has an effect on the formation of recrystallised grains in discontinuous recrystallisation, but not continuous recrystallisation, as seen in Elektron 675. The trend seen in the current work is not conclusive and, therefore, this is an area in which further study would be useful.

5.4.2.5 Effect of Schmid Factor

The Schmid factor gives a good indication of the ease with which a grain can undergo slip. In the current work this has only been calculated for basal slip, although it is felt that this is a reasonable assumption in magnesium as slip on basal planes is expected to be much more active than that on other non-basal slip systems. A higher value of the Schmid factor indicates that the grain is better oriented for basal slip in plane strain compression, and conversely a low value shows that the grain is hard to deform. The effect of the parent grain Schmid factor on the levels of dynamic recrystallisation were shown in section 4.4.4.5. It could be seen that there was a significant change in the levels of recrystallisation around different Schmid factor grains at different strains. Figure 109 showed that, at low strains, there was more recrystallisation around lower Schmid factor grains, i.e. those that were harder to deform. It is thought that it is not actually the low Schmid factor grains that are undergoing recrystallisation, rather that they transfer higher stresses onto the surrounding grains, which consequently underwent more strain and thus more recrystallisation. Therefore, at low strains, the majority of grains that had reached strains suitable for recrystallisation in the mantle region neighboured low Schmid factor grains. At higher strains many more grains could reach

the critical strain required for recrystallisation and thus the Schmid factor effect becomes less. Again, there is no real correlation with the Zener-Hollomon parameter due to the heterogeneities of strain distribution.

There are no reports of the effect of Schmid factor on dynamic recrystallisation previously reported in the literature. Although this study has given some findings and possible explanations, further study is required in this area to obtain a fuller understanding of the process.

5.4.3 Shear Bands

In a few of the samples deformed at the higher values of Z, large shear bands were seen diagonally through the entire thickness of the samples. It is thought that this is due to misaligned tools creating a macroscopic shear through the sample, amplified by the deformation behaviour of the alloy under these conditions. The difficulty of initiating slip at these temperatures and strain rates means that strain localises in the bands. This causes a large amount of dynamic recrystallisation, possibly through geometric dynamic recrystallisation as described in section 5.4.2.2, creating areas of weaker texture that is more suitably oriented for slip. Therefore, the bands provide a softening effect as they can undergo deformation more easily than the rest of the sample. Although this mechanism can provide a softening effect in the material, the large scale shear bands are only seen in a minority of samples tested.

Ion *et al.*[51] described the formation of a smaller scale shear zone that is similar to a shear band, see section 2.3.7. There is little obvious evidence that these shear zones formed during deformation of Elektron 675, see the microstructures shown in section 4.4, although it could be considered that areas of dynamic recrystallisation on the scale of one or two grains are of this nature. This type of shear zone also causes softening in the material through strain localisation and repeated deformation and recrystallisation of the previous recrystallised grains. Ion *et al.* did not observe any grain boundary sliding (GBS) but, from other literature[35, 79-82], it would be expected at the grain sizes observed in these regions. The original grains in the material are far too large to undergo GBS but once much smaller grains have been formed by dynamic recrystallisation, in bands oriented at the correct angle to the stress axis, GBS in these regions could become a useful deformation mechanism to allow non-recrystallised grains to move past each other. This is an extension of softening through dynamic recrystallisation but provides a new mechanism of strain accommodation between original grains badly oriented for

slip. Further investigations would be needed to confirm if GBS is occurring in these shear zones.

5.4.4 Texture Evolution

By the end of the work hardening region, a true basal texture had developed, see figure 122 and figure 123. In section 5.3.4 the initial development of a pure basal texture was discussed. It can be seen in figure 127 that the 0002 pole figure often has a split in the basal texture towards the rolling direction. This is commonly reported in the literature and has a deviation of approximately 10-20° from the normal direction[52, 118, 222], which fits well with the 18° measured in the current work. The split in texture does not specifically form in the flow softening region but generally forms after the grains have reoriented to a pure basal texture because it requires further deformation mechanisms to be activated. Early works concluded that the split in texture was produced by the activation of $\{10\bar{1}1\}$ twinning that was then retwinned by $\{10\bar{1}2\}$ twins[74, 87]. However, more recent studies have come to the conclusion that the split is due to the activation of <c+a> slip[52, 78, 118, 138, 165, 222, 223]. Various studies[52, 222, 223] used a texture simulation method to predict the textures produced with different active deformation mechanisms and compared the results to experimentally produced textures. They all came to the conclusion that <c+a> slip is more important than twinning to produce the split in the basal texture. It was shown in section 4.4.3 that there were negligible amounts of either $\{10\bar{1}1\}$ twins or $\{10\bar{1}1\}$-$\{10\bar{1}2\}$ double twins found in the current study so it can be concluded that the split seen in the texture must come from <c+a> slip. The split in texture was also more pronounced at lower values of Z, which agrees with a slip mechanism, as non-basal slip systems are expected to be more active at higher temperatures and lower strain rates. Although <c+a> slip has also not been observed in the current work, this is expected to be much harder to see because the small amounts present are unlikely to produce the distinct slip traces used to identify other active slip systems.

The softening mechanisms are thought to be more active when the Zener-Hollomon parameter is low. It is also seen in figure 127 that the samples deformed at lower Z showed a weaker final texture. Dynamic recrystallisation, shear band formation and grain boundary sliding have all been reported to weaken the texture in magnesium and other hcp materials[88, 89, 137, 224, 225]. As was discussed in previous sections, the dominant softening mechanism in Elektron 675 is thought to be continuous dynamic rotation recrystallisation, which causes a significant change in texture; therefore, this is

thought to be a significant mechanism responsible for the weakening of the basal texture.

It was seen in figure 128 that the non-recrystallised grains also showed a weaker texture at lower values of Z. This would indicate that DRX is not solely responsible for the weakening of texture at higher temperatures or slower strain rates and there are various possible reasons for this observation. It is possible that the selection of recrystallised grains in the EBSD map was not entirely accurate and some have been included in the non-recrystallised pole figures. Another reason is related to the activity of twinning at the different deformation conditions; twinning is thought to be the major mechanism causing a strong basal texture but is less prevalent at the lower values of Z. Therefore, there are likely to be many more grains that were not reoriented by twinning in these samples, causing a weaker overall texture at the end of deformation. The weaker texture shown in tests at lower Z is thought to be due to both an increased level of dynamic recrystallisation and a decreased level of twinning.

5.5 Failure

5.5.1 Process Window

It was shown in section 4.2 that both an upper and lower limit of ductility was found for Elektron 675 in plane strain compression. The upper limit occurred when the combination of starting temperature and deformation heating raised the temperature of the material to a point at which it underwent incipient melting. This was thought to have occurred above approximately 545°C. Further investigations, with greater safety controls, would be needed to understand more about this behaviour. The lower limit was found to rely directly on the Zener-Hollomon parameter, with all those tests carried out above $9.5x10^{16} \pm 1.5x10^{16} s^{-1}$ showing shear fracture.

As discussed in section 2.6.4, there have been very few studies carried out to look at the process window of magnesium alloys. Even when studies have been carried out, the limits of ductility are very strongly influenced by the processing history of the material, the alloy composition, and the type of deformation used; therefore, comparisons are only of little use. Prasad and Rao[169] state that AZ31 has a wide workability range from 350-550°C and $0.0003\text{-}0.3 s^{-1}$. This fits reasonably well with the process window calculated in the current work, although a lower temperature can be used in AZ31. It is expected that the high levels of rare earths in Elektron 675 increase the strength of the

material, compared to AZ31, such that sufficient slip cannot occur at these low temperatures. Slooff *et al.* [178] produced processing maps for different AZ series alloys and calculated a 'safe region' where there is good ductility with dynamic recrystallisation occurring. The maps showed a similar shape for each alloy with the safe region in approximately the same area for each. The boundaries of the safe region are given below:

AZ41	300 to 450°C	1 to $35s^{-1}$
AZ61	275 to 400°C	1 to $35s^{-1}$
AZ80	less than 300 to 375°C	0.5 to $20s^{-1}$

It should be noted that the safe regions from Slooff *et al.* occur at a lower temperature as the alloy content is increased. This drop in upper temperature limit is thought to be due to the presence of a β phase in the higher Al alloys that melts at higher temperatures. Therefore, the change with alloy content is not applicable to Elektron 675.

Both the upper and lower limits of ductility described here for Elektron 675 are for plane strain compression tests; however, the objective of this work was to use PSC as a simulation of rolling. It is likely that the window of possible operating conditions in rolling would be wider than found here, as rolling exhibits fewer stress concentrations than are imposed during plane strain compression testing. For example, the incipient melting that occurred during PSC testing happened around the thermocouple. The initial drilled hole and the different properties of the thermocouple compared to the bulk material both created a non-uniform stress state in this region that was likely to reach strains above those for the bulk. The same issue also applies to the shoulders of the samples where the shear fracture occurred. Standard rolling does not feature any of these stress concentrations and thus the process window is likely to be wider. However, it is thought that the slightly narrower process window calculated here provides a useful margin for error when scaling up to industrial rolling.

In industrial rolling, it is very rare to have the rolls at the same temperature as the material. This means that there is a cooling inherent in the rolling process and this was studied in the current work through cold tools PSC tests. The results of these tests were presented in section 4.3.6 and it was shown that tests carried out at 470°C and both $0.5s^{-1}$ and $5s^{-1}$ strain rates with tools at 70°C showed some level of fracture. The test carried out at $0.5s^{-1}$ fractured completely while the test carried out at $5s^{-1}$ only showed fracture on the surface. The difference between these two tests was due to the change in

temperature during deformation from the conduction of heat away from the sample and the level of deformation heating. Therefore, the slower test reached a much lower temperature across the entirety of the sample while that at $5s^{-1}$ was only cooled at the surface. The centre of the sample strained at $0.5s^{-1}$ was at approximately 382°C when fracture occurred, which equates to a Zener-Hollomon parameter of $1.03x10^{17}$ s^{-1}. It was stated in section 4.2 that fracture would occur in a sample if Z was above $9.5x10^{16}$ s^{-1}; therefore, fracture in the cold tool test was initiated approximately when this limit was reached.

The process window and cold tools tests show that the industrial rolling schedule for Elektron 675 must be tightly controlled to ensure the material does not reach temperatures or strain rates outside the calculated limits. It has also been shown that using cold rolls could cause problems, but this issue could be reduced by the use of higher strain rates.

5.6 Post-Deformation Transformations

5.6.1 Annealing Behaviour

The annealing behaviour of Elektron 675 was studied through the use of double hit PSC tests and the results were presented in section 4.3.5. It was shown in figure 75 and figure 76 that the change in flow stress following a hold period was almost completely unchanged from that in the single hit test. There are some small variations visible but there is no real correlation with hold time and the differences are thought to be within experimental error. This is unusual behaviour and it would normally be expected that a material held at high temperature for times such as these would undergo a significant change in microstructure, which would consequently affect the flow behaviour. Therefore, the microstructure following the hold periods was investigated, and the results were presented in section 4.4.5.

At both temperatures investigated, significant changes to the microstructure occurred due to static recrystallisation. At 420°C, static recrystallisation happened relatively slowly, only reaching 21% recrystallised material after 600s of holding. At 500°C, recrystallisation was much faster, with almost complete recrystallisation of the material by 300s of holding. In both cases, the statically recrystallised grain size increases during annealing and becomes much larger than the recrystallised grains found from dynamic recrystallisation; therefore, there must be a significant level of grain growth occurring

during static recrystallisation. This means that the mechanism of static recrystallisation cannot be continuous recrystallisation through subgrain formation, as is thought to be active in dynamic recrystallisation. A useful way to determine the mechanism of dynamic recrystallisation was to look at the difference in texture of the recrystallised grains. The 0002 pole figure for the sample held at 500°C for 300s, which underwent almost complete static recrystallisation, is shown in figure 143.

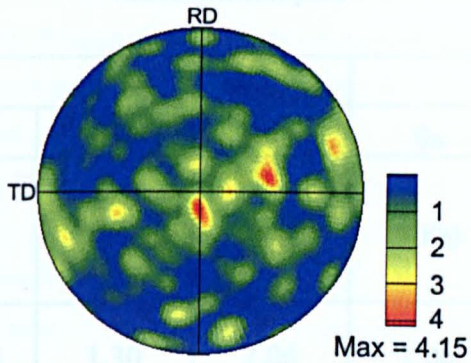

Figure 143 – 0002 pole figure for a PSC sample deformed at 500°C and $1s^{-1}$ to a strain of 0.25 then held for 300s at 500°C

Although the EBSD map did not contain a sufficiently large number of grains to provide an accurate pole figure, it can still be seen that there is a weak basal texture present, with many grains deviating a long way from the ideal texture. The texture of the material at a strain of 0.25 is expected to be a fairly strong basal texture, see figure 122 and figure 123, and therefore, this indicates that the static recrystallisation mechanism causes a texture randomisation effect. As discussed in section 2.4.3.5, standard discontinuous recrystallisation, from grain boundary bulging and migration, retains a very similar texture to that of the parent grains, so can also be discounted as the dominant mechanism in this case. Senn and Agnew[226] stated that the randomisation of texture in magnesium-rare earth alloys was through the nucleation of recrystallisation at shear bands, where the texture had already been weakened; however, no significant shear bands were seen in most of the current samples that still exhibited texture randomisation. It was shown in figure 113 and figure 116 that the recrystallised grains grow during annealing and in figure 114 and figure 117 that the number of small grains present decreased during annealing. This suggests that the pre-existing small dynamically recrystallised grains did not persist through further recrystallisation and thus were either consumed by the new grains, or grew to become the new grains. It was shown in figure 129 that the dynamically recrystallised grains have a much weaker texture than the parent grains and thus, if they were to form the nuclei of the statically

recrystallised grains, the weak texture would be retained. For this theory to hold true, the number of recrystallised grains could not increase during static recrystallisation. Table 21 shows the number of recrystallised grains per square mm for the EBSD maps carried out on the annealed samples.

Table 21 – Table showing the number of recrystallised grains per square mm in different samples

	420°C			500°C		
	0s	300s	600s	0s	100s	300s
Total RX grains in EBSD map	205	1255	2342	1000	1239	699
Area of EBSD map (mm^2)	0.0726	1.30	2.06	1.06	1.47	1.10
Number of RX grains per mm^2	2822	962	1140	947	841	636

The much higher value for the sample deformed at 420°C and not annealed is probably due to the values being taken from the map carried out at a smaller step size. The reasons for producing this map were discussed in section 4.4.5. Table 21 shows that, in general, the frequency of recrystallised grains decreases as the annealing time increases, as would be expected from a mechanism of grain growth and no further nucleation. The only anomalous point to this trend is that at 420°C and 600s, where the frequency of RX grains is higher than at 300s. It can be seen in figure 111 that there are certain features at both 300s and 600s that have the same shape as twins, either extending into or across parent grains, but contain recrystallised grains. This would suggest that twinning recrystallisation is active during annealing, and would not be expected at 500°C as twinning is much less prevalent at the higher temperature. This is a possible explanation of the new nucleation mechanism in the longer annealing times, although a more in depth study would be needed to discount the possibility that this is simply a statistical error. Therefore, it is thought that the dominant annealing process causing microstructural change is the growth of the pre-existing dynamically recrystallised grains. Although this is technically a grain growth mechanism, rather than true recrystallisation, it is often referred to as metadynamic recrystallisation as the pre-existing grains are considered to be nuclei[112]. As was discussed in section 2.4.4, most mechanisms of static recrystallisation and grain growth have previously been observed

in magnesium alloys, although the current work provides more direct evidence of metadynamic recrystallisation[156-161].

A change in microstructure of the scale experienced during annealing of these samples would normally be accompanied by a change in the flow stress of the material. However, in Elektron 675 this was not found to be the case as the flow stress following a hold period was almost completely unchanged. This would suggest that there are balancing softening and hardening mechanisms occurring together. Recrystallisation of the material removes defects and thus makes it easier for slip to occur, hence causing a softening effect. Another softening effect would be expected from the texture randomisation, as any weakening of the basal texture puts more grains in a suitable orientation for basal slip. Recrystallisation reduces the grain size from the initial material and it would normally be expected, due to the Hall-Petch relationship, that this would cause hardening. However, it has been reported that a reduction in grain size can inhibit twinning and promote dynamic recrystallisation, and thus cause a softening effect in magnesium[107, 140]. If, prior to the hold period, the strain has been accommodated to some extent in shear zones, recrystallisation may remove the zones and cause hardening while they are re-established in the second deformation step. Therefore, there are various possible mechanisms that can cause the material to either soften or harden and the only explanation for the steady flow behaviour is a balance between them. It is unusual to observe a balance such as this over a wide range of conditions and thus this is an area in which further study would be very useful.

5.6.2 Precipitation

The precipitation hardening behaviour of Elektron 675 was discussed in section 4.6 and it was found that, following deformation and recrystallisation, the material could be heat treated to give a substantial age hardening response. When aged at 250°C the hardness increased by 50% at the peak ageing time of 12 hours. It is stated in the literature that the peak hardness is due to the formation of a large number of β' precipitates[21, 22]. These have a lens-shaped morphology, often around 150nm in diameter and 10nm in width, and form on prismatic planes in the magnesium matrix[19, 21, 22, 26]. It can be clearly seen in figure 135 that similarly shaped and oriented precipitates are visible in the peak-aged sample of Elektron 675. A more accurate way to distinguish between different precipitate structures is to use a diffraction pattern, as shown in figure 136. This diffraction pattern is taken looking down the [0001] direction in the magnesium matrix and shows the hexagonal Mg pattern with other smaller spots distributed in

between. This pattern is identical to that reported in other studies and has been attributed to the presence of β' precipitates[21, 26, 28]. Gao *et al.*[21] showed how the full diffraction pattern is made up of the magnesium matrix along with three different orientations of β' precipitates, corresponding to the three different prismatic planes on which they can lie, as shown in figure 144. Therefore, it can be concluded that the precipitates in the peak aged sample of Elektron 675 are β' phase. When over-aging the material, the hardness drops, again a feature commonly seen in magnesium-rare earth systems and attributed to a change in the precipitates from a β' phase to both the β_1 phase and the equilibrium β phase. These both form as coarser, more widely dispersed precipitates and β is fully incoherent with the matrix; therefore, they provide less of a hardening effect[13, 21, 22, 24, 227]. The precipitation in the over-aged samples has not been fully investigated in the current work but β_1 and β' are thought to be responsible for the drop in hardness in Elektron 675.

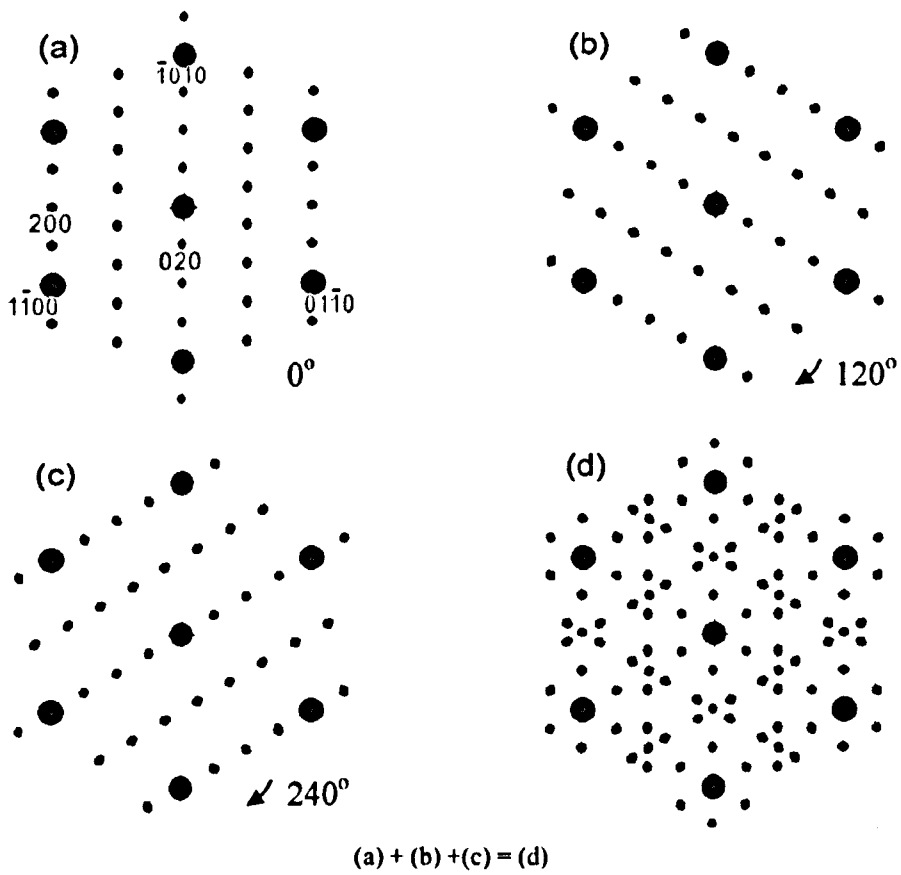

Figure 144 – Schematic patterns for the superimposed β' phase and matrix. (a-c) show the diffraction patterns for each individual orientation of β' phase along with the matrix. (d) shows the superimposition of all three, giving the full diffraction patterns[21]

At 275°C, peak-age was reached in two hours but gave a much smaller rise in hardness, of only 15-20%. This difference with temperature is typical for many alloy systems, including magnesium-rare earth alloys[7, 227, 228]. The higher temperature increases the rate of diffusion of solute atoms, speeding up the formation of precipitates but also increasing the coarsening rate[26, 227]. Therefore, the peak stress is reached sooner but is lower due to the reduced hardening effect of the coarse precipitates. The solubility of rare earths is also higher at a hotter temperature and thus the volume fraction of precipitates is smaller, giving a lower hardening effect[26].

It was considered that the hardness of the material may not be entirely due to precipitates because other factors in the microstructure can also affect the properties. Optical micrographs were carried out on the original and heat treated samples and it can be seen in section 4.6 that there are no significant changes to the microstructure. The grain size between the two different casts significantly affected the hardness of the samples due to the Hall-Petch effect; the samples with the smaller grain size showed higher hardnesses as expected. Grain size analysis was also carried out to check for any grain coarsening during the heat treatments. It was found that the grain sizes were the same before and after heat treatment, and therefore, it can be concluded that the changes in hardness of the material with ageing time are entirely due to precipitation.

6. Conclusions

Elektron 675 has been tested in plane stain compression at temperatures between 380°C and 520°C and strain rates between 1 and $10s^{-1}$ along with certain other tests. The flow data and the deformed microstructures have been investigated and the following conclusions have been drawn:

6.1 Stress-Strain Behaviour

- Elektron 675 exhibits similar flow behaviour over the full range of single hit tests, showing a rise to a peak stress, followed by continuous, approximately linear flow softening, which continues to strains of at least 1

- The strain at which peak stress occurs increases with increasing values of the Zener-Hollomon parameter

- Constitutive equations of flow stress have been developed that fit the experimental tests above 440°C to a good degree of accuracy

- The friction coefficient between the PSC tools and the magnesium sample was found to be 0.07±0.03

- The activation energy of deformation (Q_{def}) has been found to be 217±1 kJ mol^{-1}, much higher than many of the values reported for other magnesium alloys

- The process window for Elektron 675 in plane strain compression was found. Incipient melting occurred in tests above approximately 545°C and shear fracture occurred in tests where the Zener-Hollomon parameter was above $9.5x10^{16}$

- There is very little change in the flow stress after annealing for different lengths of time during double hit PSC tests

- Using cold tools during a PSC test causes the sample to cool dramatically and fracture to occur

6.2 Deformation Modes

- Only $\{10\bar{1}2\}$ twinning is observed at any significant level during deformation
- In grains that undergo twinning, the twins are active at low strains and generally grow to consume the entire grain reasonably quickly
- Slip is seen to occur on basal and prismatic slip systems and there is indirect evidence that <c+a> pyramidal slip is also active
- Slip is more active in tests at lower values of the Zener-Hollomon parameter, and consequently twinning is less active
- Large shear bands, on the scale of the sample, can form during tests at high Z

6.3 Dynamic Recrystallisation

- The dominant mechanism of dynamic recrystallisation in Elektron 675 is continuous dynamic rotation recrystallisation
- Dynamic recrystallisation occurs gradually through the majority of the deformation and forms a necklace structure surrounding the grain boundaries
- Dynamic recrystallisation occurs relatively slowly when compared to other magnesium alloys, such as AZ31, and does not reach completion under any conditions tested
- Dynamic recrystallisation requires a short incubation period until a strain of approximately 0.1
- The fraction of dynamically recrystallised grains increases approximately linearly with strain
- There is a only a weak correlation measured between the Zener-Hollomon parameter and the fraction of recrystallisation, with a larger volume of recrystallised grains found in samples deformed at lower Z

- The dynamically recrystallised grains undergo minimal grain growth during deformation but the grain size is strongly affected by the deformation conditions, with smaller grains formed at higher values of Z

- Recrystallised grains have higher Schmid factors, indicating that they are easier to deform than the parent grains

- There is a weak correlation between the disorientation of a grain boundary and its propensity to undergo dynamic recrystallisation, with lower disorientation boundaries having a higher frequency of recrystallisation

- Grains neighbouring those of lower Schmid factor experience higher stresses during the early stages of deformation, and thus undergo higher levels of dynamic recrystallisation. Later in the deformation, other grains reach similar levels of recrystallisation and lessen the effect

- Dynamic recrystallisation is thought to be responsible for the softening effect seen in the flow curves

6.4 Texture

- Deformation causes a fairly strong basal texture to develop in Elektron 675

- $\{10\bar{1}2\}$ twinning causes a very fast reorientation to a basal texture in grains that are suitably oriented

- Recrystallised grains formed with a much more random texture than the remaining areas of the parent grains

- Tests carried out at lower Z showed weaker texture, due to both more dynamic recrystallisation causing a greater randomisation effect and the lower level of twinning causing less reorientation of grains

- The activity of <c+a> slip caused a split in the basal texture towards the rolling direction

6.5 Other Conclusions

- The lattice parameters of Elektron 675 were found to be slightly different to those of pure magnesium, giving a lower c/a ratio of 1.615

- Finite element models of PSC tests have been produced that show the temperature and strain distributions through the cross-section of the samples

- Following deformation, static recrystallisation occurs during holding at temperatures of 420°C and above; at 500°C, recrystallisation approaches completion after only 300s

- Static recrystallisation occurs through a metadynamic process where the pre-existing dynamically recrystallised grains act as nuclei

- Elektron 675 showed a significant hardening response following deformation and recrystallisation, with improvements of up to 50% possible

- The peak hardening response was achieved by distribution of fine β' precipitates

7. Further Work

There have been various conclusions drawn from the current investigations that could have been made stronger or taken further through the use of more experiments or analysis. Due to time and equipment constraints these have not been carried out, but suggestions are given below for improvements and further work.

A reasonable number of single hit tests were carried out to a strain of 0.7 that covered the full range of temperatures possible. However, the lower strain rate was limited to only $1s^{-1}$ by the control of the thermomechanical compression machine. At strain rates lower than $1s^{-1}$, the hydraulic systems used to control the movement of the tools and the application of the load introduced high levels of noise and the tests were unreliable. It is unlikely that industrial processes would use strain rates lower than $1s^{-1}$, and therefore, the range of tests carried out in the current work is acceptable on that basis but falls down when developing constitutive equations for finite element modelling. It should be possible to adapt the thermomechanical compression machine to allow lower strain rates through the use of different servo-valves and improved PID control.

Total strains of 0.7 were used as this gave a reduction of approximately 50%, usually enough to study all behaviour in a material and reach steady state stresses. However, it has been shown that steady state is not reached by a strain of 0.7 in any test carried out in the current work and not even by a strain of 1 in the three tests deformed to that strain. It would be interesting to find out whether steady state is reached at higher strains in Elektron 675 and therefore, different testing methods would have to be used. If it was still carried out in plane strain compression then thicker samples could be used to allow for a greater deformation, or the thermocouple could be moved out of the deformation zone to stop that causing a hindrance at high strains. Both of these methods would affect the accuracy of the testing and therefore, it may be better to use an entirely different technique, such as torsion testing, which can produce higher strains. It is often reported in the literature, see section 2.6, that steady state is reached sooner at lower values of the Zener-Hollomon parameter; therefore, it would be sensible to focus on tests at those conditions when first attempting to find this behaviour in Elektron 675.

In order to improve on the PSC testing technique it would have been useful to have investigated the friction coefficient in more detail. The simple method of deforming tests of different heights was used in the current work, but the finite element modelling

showed that there may be a small error in the value of friction coefficient found. Another method that could be used to confirm or recalculate the value found is the 'ring test'[229]. This uses a ring shaped sample with a dimensions in the ratio of outer diameter : inner diameter : thickness of 6:3:1. The friction coefficient is calculated from the percentage change of the inner diameter following a known reduction in thickness.

Although the lower limit of the process window could be investigated in a reasonable amount of detail, further investigation into the upper limit would require better safety procedures in order to study melting of the material. Performing tests under an inert atmosphere may be required to find the true upper limit.

The constitutive equations were used for the modelling of PSC tests but can be used similarly for modelling other processes. Work has already started, with Dr Krzysztof Muszka, to model the stress, strain and temperature distributions in the rolling process used by Magnesium Elektron; preliminary results are presented below. This used temperatures similar to those experienced in industry, with the material at 449°C and the roll at 123°C, and used a plane of symmetry to model only the top half of the system. It is expected that this work will continue and full models will be produced for use by Magnesium Elektron.

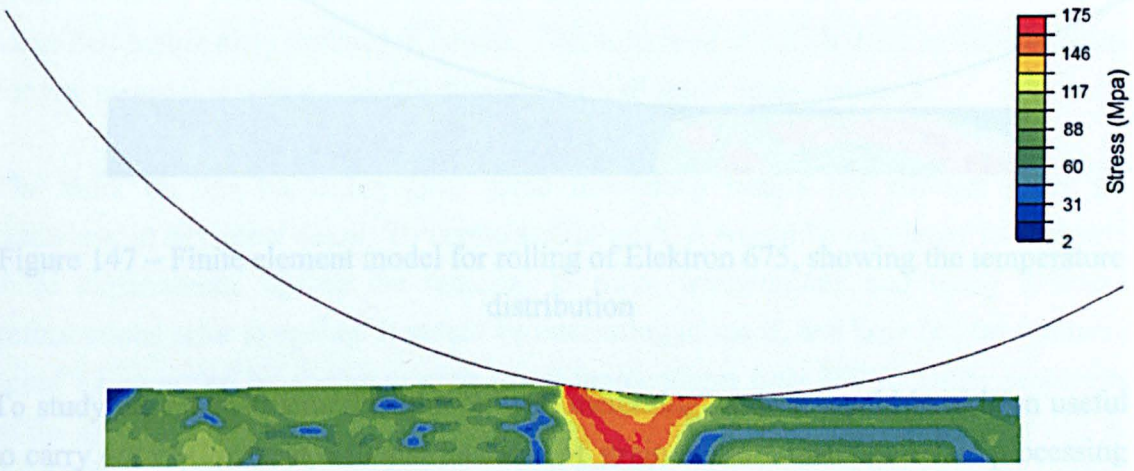

Figure 145 – Finite element model for rolling of Elektron 675, showing the stress distribution

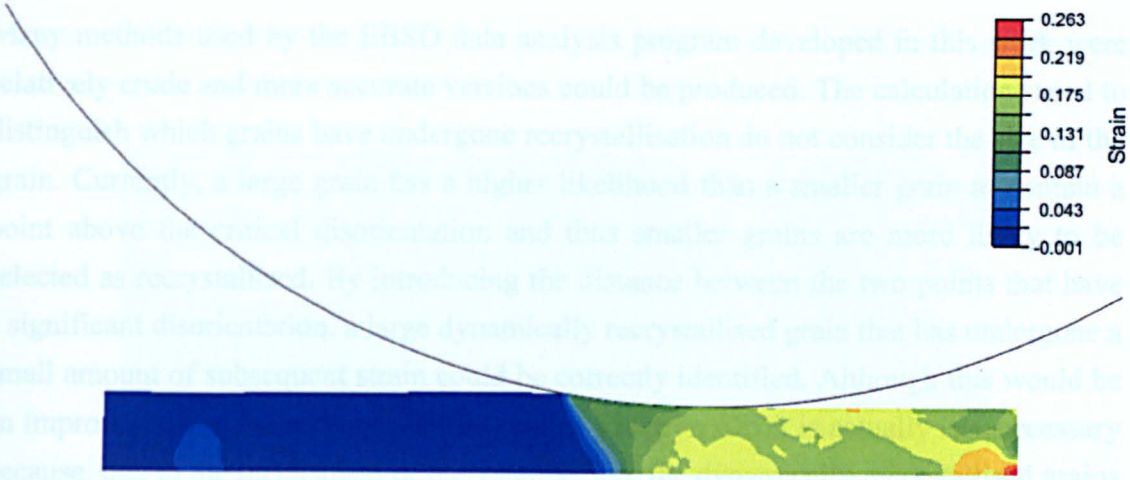

Figure 146 – Finite element model for rolling of Elektron 675, showing the strain distribution

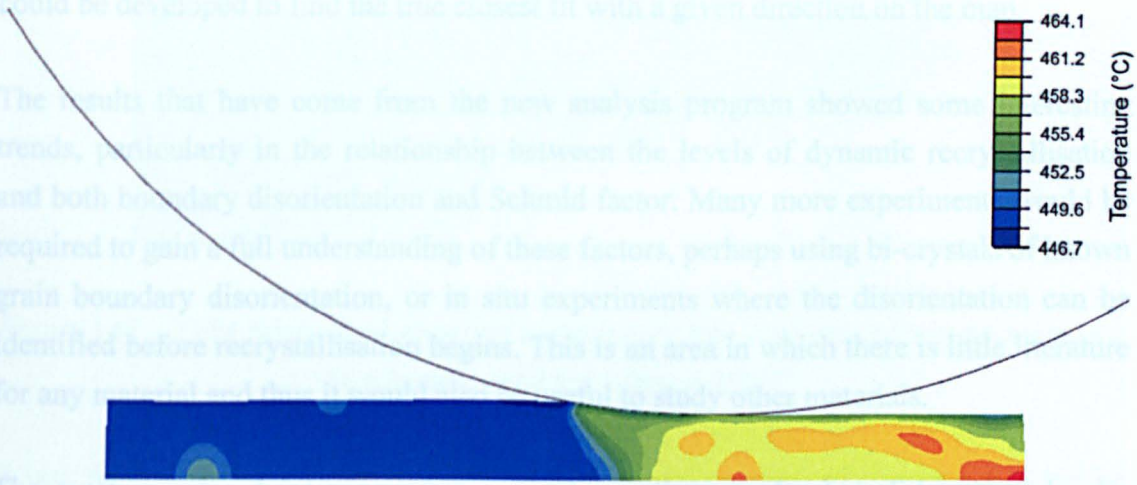

Figure 147 – Finite element model for rolling of Elektron 675, showing the temperature distribution

To study the microstructural evolution with increasing strain it would have been useful to carry out PSC tests at different intervals of strain at more than one set of processing conditions. Although the tests at 460°C and $5s^{-1}$ gave a representative idea of the processes occurring in the middle of the full range, these are likely to be significantly different at other conditions. Full texture analysis would also be useful on these maps, including those at 460°C and $5s^{-1}$, and this would provide a fuller understanding of the active mechanisms of deformation.

Many methods used by the EBSD data analysis program developed in this work were relatively crude and more accurate versions could be produced. The calculations used to distinguish which grains have undergone recrystallisation do not consider the size of the grain. Currently, a large grain has a higher likelihood than a smaller grain to contain a point above the critical disorientation and thus smaller grains are more likely to be selected as recrystallised. By introducing the distance between the two points that have a significant disorientation, a large dynamically recrystallised grain that has undergone a small amount of subsequent strain could be correctly identified. Although this would be an improvement to the software, in the case of Elektron 675 it is actually less necessary because, due to the mechanism of recrystallisation, the dynamically recrystallised grains are mostly formed in a rather narrow range of small grain sizes. Another improvement to the software could come in the slip trace analysis as currently the trace within the microstructure is matched to the calculated plane traces by eye. Instead, the software could be developed to find the true closest fit with a given direction on the map.

The results that have come from the new analysis program showed some interesting trends, particularly in the relationship between the levels of dynamic recrystallisation and both boundary disorientation and Schmid factor. Many more experiments would be required to gain a full understanding of these factors, perhaps using bi-crystals of known grain boundary disorientation, or in situ experiments where the disorientation can be identified before recrystallisation begins. This is an area in which there is little literature for any material and thus it would also be useful to study other materials.

The work on age hardening gave some interesting results but did not study the behaviour in any great detail. To continue this work, it would be necessary to carry out more experiments, ageing the material at more temperatures and using different deformations prior to ageing. It would be interesting to see if, and how far, the hardness could be improved by ageing at even lower temperatures than 250°C. Other properties of the aged material, such as ductility or strength, could also be studied and would be of great interest to industry; Magnesium Elektron themselves are likely to have either studied this previously or in the near future.

To understand the precipitation sequence better, it would be necessary to carry out a much more extensive TEM study on the precipitates formed, particularly those in the peak-aged condition at 275°C to find out why the hardness is much lower. While carrying out TEM on the sample aged at 250°C to the peak-aged condition, it was noted that precipitate free zones were formed around grain boundaries, see figure 148. This

was not studied further in the current work but would be expected to have an effect on final properties, and thus more work in this area would be useful.

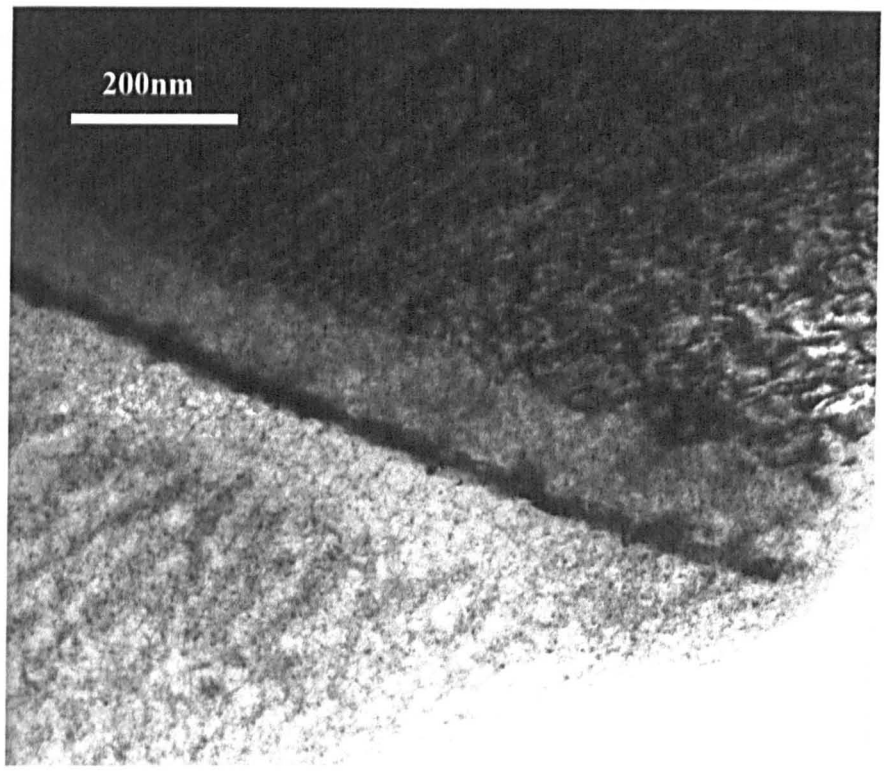

Figure 148 – TEM bright field image of a precipitate free zone around a grain boundary in a sample aged for 12hrs at 250°C

It was found that <c+a> slip is active during the deformation of Elektron 675 but no direct evidence was seen. Therefore, an in depth study of individual dislocations in TEM would be useful to prove that <c+a> dislocations are present in the material.

The areas of recrystallisation around grain boundaries are expected to undergo higher levels of deformation than the large unrecrystallised grains, although the method of strain accommodation is unknown. It has been suggested that they either deform through slip and repeated recrystallisation or by a grain boundary sliding mechanism. Experiments could be carried out to investigate this further, by either using an in situ technique, and deforming in the microscope, or by marking a grid on the recrystallised grains before further deformation.

The behaviour during annealing was not analysed in any great detail in the current work and therefore, there is wide scope for further study in this area. It is currently unknown

why there is a balance between the hardening and softening mechanisms to produce little change in the flow curves. More tests could be carried out using different parameters. The strain at which annealing takes place should be varied to see how this affects the behaviour and different temperatures and strain rates of deformation should be studied. It should be easiest to recognise the active mechanisms in the very early stages of recrystallisation and therefore, samples with short hold times should be studied in high resolution microscopy to observe the nucleation of any recrystallised grains.

The conclusions drawn in this work apply specifically to Elektron 675 and it is unknown how widely they can be applied to other alloys. Therefore, a further extension to this work would be to study other similar, rare earth containing alloys to find similarities in behaviour.

8. Bibliography

[1] Emley EF, *Principles of magnesium technology*, 1966, Pergamon, Oxford.

[2] Raynor GV, *The Physical Metallurgy of Magnesium and its Alloys*, [International Series of Monographs on Metal Physics and Physical Metallurgy. vol. 5.], 1959, Pergamon Press, London.

[3] Friedrich HE and Mordike BL, *Magnesium technology: metallurgy, design data, automotive applications*, 2006, Springer, Berlin.

[4] Polmear IJ, *Light alloys: from traditional alloys to nanocrystals*, 4th ed, 2006, Elsevier Butterworth-Heinemann, Amsterdam ; London.

[5] U.S. Geological Survey., *Mineral Commodity Summaries 2010: U.S. Geological Survey*, 2010, United States Government Printing Office, Washington.

[6] Neite G, Kubota K, Higashi K, and Hehmann F, *Magnesium-Based Alloys*, in *Materials science and technology : a comprehensive treatment Vol. 8, Structure and properties of Non-Ferrous Alloys*, Cahn RW, Haasen P, and Kramer EJ, Editors. 1996, VCH: Weinheim; Cambridge. p. 113.

[7] Rokhlin LL, *Magnesium alloys containing rare earth metals: structure and properties*, Advances in metallic alloys; v. 3, 2003, Taylor & Francis, London.

[8] Mordike BL, *Creep-resistant magnesium alloys,* Mater. Sci. Eng. A, 2002, **324**(1-2), 103-112.

[9] Henning W and Mordike BL, in *Strength of Metals and Alloys*, McQueen HJ, Editor. 1985, Pergamon: Montreal. p. 803.

[10] Mordike BL, *Development of highly creep resistant magnesium alloys,* J. Mater. Process. Technol., 2001, **117**(3), 391-394.

[11] Leontis TE, *The properties of sand cast magnesium-rare earth alloys,* J. Metals, 1949, **1**(12), 968-983.

[12] Leontis TE, *Effect of rare-earth metals on the properties of extruded magnesium,* J. Metals, 1951, **3**(11), 987-993.

[13] Cizek J, Prochazka I, Smola B, Stulikova I, and Ocenasek V, *Influence of deformation on precipitation process in Mg-15 wt.%Gd alloy,* J. Alloys Compd., 2007, **430**(1-2), 92-96.

[14] Nie JF, Gao X, and Zhu SM, *Enhanced age hardening response and creep resistance of Mg-Gd alloys containing Zn,* Scripta Mater., 2005, **53**(9), 1049-1053.

[15] He SM, Peng LM, Zeng XQ, Ding WJ, and Zhu YP, *Comparison of the microstructure and mechanical properties of a ZK60 alloy with and without 1.3 wt.% gadolinium addition,* Mater. Sci. Eng. A, 2006, **433**(1-2), 175-181.

[16] Suzuki M, Sato H, Maruyama K, and Oikawa H, *Creep behavior and deformation microstructures of Mg-Y alloys at 550 K,* Mater. Sci. Eng. A, 1998, **252**(2), 248-255.

[17] Wang JG, Hsiung LM, Nieh TG, and Mabuchi M, *Creep of a heat treated Mg-4Y-3RE alloy,* Mater. Sci. Eng. A, 2001, **315**(1-2), 81-88.

[18] Peng QM, Wu YM, Fang DQ, Meng J, and Wang LM, *Microstructures and properties of Mg-7Gd alloy containing Y,* J. Alloys Compd., 2007, **430**(1-2), 252-256.

[19] Vostry P, Smola B, Stulikova I, von Buch F, and Mordike BL, *Microstructure evolution in isochronally heat treated Mg-Gd alloys,* Phys. Status Solidi A, 1999, **175**(2), 491-500.

[20] Peng QM, Wang JL, Wu YM, and Wang LM, *Microstructures and tensile properties of Mg-8Gd-0.6Zr-xNd-yY (x+y=3, mass%) alloys,* Mater. Sci. Eng. A, 2006, **433**(1-2), 133-138.

[21] Gao X, He SM, Zeng XQ, Peng LM, Ding WJ, and Nie JF, *Microstructure evolution in a Mg-15Gd-0.5Zr (wt.%) alloy during isothermal aging at 250 degrees C,* Mater. Sci. Eng. A, 2006, **431**(1-2), 322-327.

[22] He SM, Zeng XQ, Peng LM, Gao X, Nie JF, and Ding WJ, *Precipitation in a Mg-10Gd-3Y-0.4Zr (wt.%) alloy during isothermal ageing at 250 degrees C,* J. Alloys Compd., 2006, **421**(1-2), 309-313.

[23] Smola B, Stulikova I, von Buch F, and Mordike BL, *Structural aspects of high performance Mg alloys design,* Mater. Sci. Eng. A, 2002, **324**(1-2), 113-117.

[24] Nie JF and Muddle BC, *Characterisation of strengthening precipitate phases in a Mg-Y-Nd alloy,* Acta Mater., 2000, **48**(8), 1691-1703.

[25] Apps PJ, Karimzadeh H, King JF, and Lorimer GW, *Precipitation reactions in magnesium-rare earth alloys containing Yttrium, Gadolinium or Dysprosium,* Scripta Mater., 2003, **48**(8), 1023-1028.

[26] He SM, Zeng XQ, Peng LM, Gao X, Nie JF, and Ding WJ, *Microstructure and strengthening mechanism of high strength Mg-10Gd-2Y-0.5Zr alloy,* J. Alloys Compd., 2007, **427**(1-2), 316-323.

[27] Apps PJ, Karimzadeh H, King JF, and Lorimer GW, *Phase compositions in magnesium-rare earth alloys containing yttrium, gadolinium or dysprosium,* Scripta Mater., 2003, **48**(5), 475-481.

[28] Antion C, Donnadieu P, Perrard F, Deschamps A, Tassin C, and Pisch A, *Hardening precipitation in a Mg-4Y-3RE alloy,* Acta Mater., 2003, **51**(18), 5335-5348.

[29] Li ZC, Zhang H, Liu L, and Xu YB, *Growth and morphology of beta phase in an Mg-Y-Nd alloy,* Mater. Lett., 2004, **58**(24), 3021-3024.

[30] Nie JF, Xiao XL, Luo CP, and Muddle BC, *Characterisation of precipitate phases in magnesium alloys using electron microdiffraction,* Micron, 2001, **32**(8), 857-863.

[31] Socjusz-Podosek M and Litynska L, *Effect of yttrium on structure and mechanical properties of Mg alloys,* Mater. Chem. Phys., 2003, **80**(2), 472-475.

[32] Zhang MX and Kelly PM, *Morphology and crystallography of Mg24Y5 precipitate in Mg-Y alloy,* Scripta Mater., 2003, **48**(4), 379-384.

[33] Kelly A, Groves GW, and Kidd P, *Crystallography and crystal defects*, Rev. ed, 2000, Wiley, Chichester.

[34] Hull D and Bacon DJ, *Introduction to dislocations*, 4th ed, 2001, Butterworth Heinemann, Oxford.

[35] Koike J, *Enhanced deformation mechanisms by anisotropic plasticity in polycrystalline Mg alloys at room temperature,* Metall. Mater. Trans. A, 2005, **36A**(7), 1689-1696.

[36] Barnett MR, *Influence of deformation conditions and texture on the high temperature flow stress of magnesium AZ31,* J. Light Met., 2001, **1**(3), 167-177.

[37] Calnan EA and Clews CJB, *The Development of Deformation Textures in Metals - .3. Hexagonal Structures,* Philos. Mag., 1951, **42**(331), 919-931.

[38] Koike J, Kobayashi T, Mukai T, Watanabe H, Suzuki M, Maruyama K, and Higashi K, *The activity of non-basal slip systems and dynamic recovery at room temperature in fine-grained AZ31B magnesium alloys,* Acta Mater., 2003, **51**(7), 2055-2065.

[39] Kelley EW and Hosford WF, *Plane-Strain Compression of Magnesium and Magnesium Alloy Crystals,* Trans. Metall. Soc. AIME, 1968, **242**(1), 5.

[40] Akhtar A and Teghtsoonian E, *Solid Solution Strengthening of Magnesium Single Crystals .I. Alloying Behaviour in Basal Slip,* Acta Metall., 1969, **17**(11), 1339.

[41] Barnett MR, *A Taylor model based description of the proof stress of magnesium AZ31 during hot working,* Metall. Mater. Trans. A, 2003, **34A**(9), 1799-1806.

[42] Gehrmann R, Frommert MM, and Gottstein G, *Texture effects on plastic deformation of magnesium,* Mater. Sci. Eng. A, 2005, **395**(1-2), 338-349.

[43] Akhtar A and Teghtsoonian E, *Solid Solution Strengthening of Magnesium Single Crystals .2. Effect of Solute on Ease of Prismatic Slip,* Acta Metall., 1969, **17**(11), 1351.

[44] Von Mises R, *Mechanics of the ductile form changes of crystals,* Z. Angew. Math. Mech., 1928, **8**, 161-185.

[45] Taylor GI, *Plastic strain in metals,* J. Inst. Metals, 1938, **62**, 307-324.

[46] Groves GW and Kelly A, *Independent Slip Systems in Crystals,* Philos. Mag., 1963, **8**(89), 877.

[47] Hutchinson JW, *Creep and Plasticity of Hexagonal Polycrystals as Related to Single-Crystal Slip,* Metall. Trans. A, 1977, **8**(9), 1465-1469.

[48] Kocks UF and Westlake DG, *Importance of Twinning for Ductility of Cph Polycrystals,* Trans. Metall. Soc. AIME, 1967, **239**(7), 1107.

[49] Obara T, Yoshinga H, and Morozumi S, *[112bar2](11bar23) Slip System in Magnesium,* Acta Metall., 1973, **21**(7), 845-853.

[50] Stohr JF and Poirier JP, *Electron-Microscope Study of Pyramidal Slip [1122] [1123] in Magnesium,* Philos. Mag., 1972, **25**(6), 1313.

[51] Ion SE, Humphreys FJ, and White SH, *Dynamic Recrystallization and the Development of Microstructure During the High-Temperature Deformation of Magnesium,* Acta Metall., 1982, **30**(10), 1909-1919.

[52] Agnew SR, Yoo MH, and Tome CN, *Application of texture simulation to understanding mechanical behavior of Mg and solid solution alloys containing Li or Y,* Acta Mater., 2001, **49**(20), 4277-4289.

[53] Philippe MJ, Serghat M, Vanhoutte P, and Esling C, *Modeling of Texture Evolution for Materials of Hexagonal Symmetry .2. Application to Zirconium and Titanium Alpha-Alloys or near-Alpha-Alloys,* Acta Metall. Mater., 1995, **43**(4), 1619-1630.

[54] Philippe MJ, Wagner F, Mellab FE, Esling C, and Wegria J, *Modeling of Texture Evolution for Materials of Hexagonal Symmetry .1. Application to Zinc-Alloys,* Acta Metall. Mater., 1994, **42**(1), 239-250.

[55] Staroselsky A and Anand L, *A constitutive model for hcp materials deforming by slip and twinning: application to magnesium alloy AZ31B,* Int. J. Plast., 2003, **19**(10), 1843-1864.

[56] Brown DW, Agnew SR, Bourke MAM, Holden TM, Vogel SC, and Tome CN, *Internal strain and texture evolution during deformation twinning in magnesium,* Mater. Sci. Eng. A, 2005, **399**(1-2), 1-12.

[57] Al-Samman T and Gottstein G, *Room temperature formability of a magnesium AZ31 alloy: Examining the role of texture on the deformation mechanisms,* Mater. Sci. Eng. A, 2008, **488**(1-2), 406-414.

[58] Yoo MH, *Slip, Twinning, and Fracture in Hexagonal Close-Packed Metals,* Metall. Trans. A, 1981, **12**(3), 409-418.

[59] Price PB, *Pyramidal Glide and the Formation and Climb of Dislocation Loops in Nearly Perfect Zinc Crystals,* Philos. Mag., 1960, **5**(57), 873.

[60] Reed-Hill RE and Robertson WD, *Deformation of Magnesium Single Crystals by Nonbasal Slip,* Trans. Metall. Soc. AIME, 1957, **209**, 496-502.

[61] Munroe N, Tan XL, and Gu HC, *Orientation dependence of slip and twinning in HCP metals,* Scripta Mater., 1997, **36**(12), 1383-1386.

[62] Hirth JP and Lothe J, *Theory of dislocations*, 2nd ed, 1992, Krieger Pub. Co., Malabar, FL.

[63] Kelley EW and Hosford WF, *Deformation Characteristics of Textured Magnesium,* Trans. Metall. Soc. AIME, 1968, **242**(4), 654.

[64] Hall EO, *Twinning and Diffusionless Transformations in Metals*, 1954, Butterworths Scientific Publications: London,

[65] Cahn RW, *Twinned Crystals,* Adv. Phys., 1954, **3**(12), 363-445.

[66] Christian JW and Mahajan S, *Deformation Twinning,* Prog. Mater. Sci., 1995, **39**(1-2), 1-157.

[67] Mahajan S and Williams DF, *Deformation twinning in metals and alloys(literature review),* International Metallurgical Reviews, 1973, **18**, 43-61.

[68] Bingert JF, Mason TA, Kaschner GC, Maudlin PJ, and Gray GT, *Deformation twinning in polycrystalline Zr: Insights from electron backscattered diffraction characterization,* Metall. Mater. Trans. A, 2002, **33**(3), 955-963.

[69] Fundenberger JJ, Philippe MJ, and Esling C, *Mechanical Twinning at High-Temperatures in Some Hexagonal Alloys,* Scripta Metall. Mater., 1990, **24**(7), 1215-1220.

[70] Klimanek P and Potzsch A, *Microstructure evolution under compressive plastic deformation of magnesium at different temperatures and strain rates,* Mater. Sci. Eng. A, 2002, **324**(1-2), 145-150.

[71] Barnett MR, Nave MD, and Bettles CJ, *Deformation microstructures and textures of some cold rolled Mg alloys,* Mater. Sci. Eng. A, 2004, **386**(1-2), 205-211.

[72] Barnett MR, Keshavarz Z, Beer AG, and Atwell D, *Influence of grain size on the compressive deformation of wrought Mg-3Al-1Zn,* Acta Mater., 2004, **52**(17), 5093-5103.

[73] Gharghouri MA, Weatherly GC, Embury JD, and Root J, *Study of the mechanical properties of Mg-7.7at.% Al by in-situ neutron diffraction,* Philos. Mag. A, 1999, **79**(7), 1671-1695.

[74] Wonsiewicz BC and Backofen WA, *Plasticity of Magnesium Crystals,* Trans. Metall. Soc. AIME, 1967, **239**(9), 1422.

[75] Reedhill RE and Robertson WD, *Additional Modes of Deformation Twinning in Magnesium,* Acta Metall., 1957, **5**(12), 717-727.

[76] Nave MD and Barnett MR, *Microstructures and textures of pure magnesium deformed in plane-strain compression,* Scripta Mater., 2004, **51**(9), 881-885.

[77] Reed-Hill RE and Robertson WD, *Additional Modes of Deformation Twinning in Magnesium,* Acta Metall., 1957, **5**(12), 717-727.

[78] Tome CN, Lebensohn RA, and Kocks UF, *A Model for Texture Development Dominated by Deformation Twinning - Application to Zirconium Alloys,* Acta Metall. Mater., 1991, **39**(11), 2667-2680.

[79] Koike J, Ohyama R, Kobayashi T, Suzuki M, and Maruyama K, *Grain-boundary sliding in AZ31 magnesium alloys at room temperature to 523 K,* Mater. Trans., 2003, **44**(4), 445-451.

[80] Tan JC and Tan MJ, *Dynamic continuous recrystallization characteristics in two stage deformation of Mg-3A1-lZn alloy sheet,* Mater. Sci. Eng. A, 2003, **339**(1-2), 124-132.

[81] Hwang S, Nishimura C, and McCormick PG, *Deformation mechanism of nanocrystalline magnesium in compression,* Scripta Mater., 2001, **44**(8-9), 1507-1511.

[82] Mabuchi M, Ameyama K, Iwasaki H, and Higashi K, *Low temperature superplasticity of AZ91 magnesium alloy with non-equilibrium grain boundaries,* Acta Mater., 1999, **47**(7), 2047-2057.

[83] Kumar NVR, Blandin JJ, Desrayaud C, Montheillet F, and Suery M, *Grain refinement in AZ91 magnesium alloy during thermomechanical processing,* Mater. Sci. Eng. A, 2003, **359**(1-2), 150-157.

[84] Hauser FE, Starr CD, Tietz L, and Dorn JE, *Deformation mechanisms in polycrystalline aggregates of magnesium,* Trans. Am. Soc. Met., 1955, 102.

[85] Sevillano JG, Vanhoutte P, and Aernoudt E, *Large Strain Work-Hardening and Textures,* Prog. Mater. Sci., 1980, **25**(2-4), 71-412.

[86] Deve HE and Asaro RJ, *The Development of Plastic Failure Modes in Crystalline Materials - Shear Bands in Fcc Polycrystals,* Metall. Trans. A, 1989, **20**(4), 579-593.

[87] Couling SL, Pashak JF, and Sturkey L, *Unique deformation and aging characteristics of certain magnesium-base alloys,* Trans. Am. Soc. Met., 1959, 94.

[88] del Valle JA, Perez-Prado MT, and Ruano OA, *Texture evolution during large-strain hot rolling of the Mg AZ61 alloy,* Mater. Sci. Eng. A, 2003, **355**(1-2), 68-78.

[89] Stanford N and Barnett MR, *The origin of "rare earth" texture development in extruded Mg-based alloys and its effect on tensile ductility,* Mater. Sci. Eng. A, 2008, **496**(1-2), 399-408.

[90] Li M, *Constitutive Modelling of Slip, Twinning, and Untwinning in AZ31B Magnesium,* 2006, PhD Thesis, Department of Materials Science and Engineering, The Ohio State University, Columbus, U.S.A.

[91] Zener C and Hollomon JH, *Effect of strain rate upon plastic flow of steel,* J. Appl. Phys., 1944, **15**(1), 22-32.

[92] Flynn PW, Mote J, and Dorn JE, *On the thermally activated mechanism of prismatic slip in magnesium single crystals,* Trans. Metall. Soc. AIME, 1961, **221**, 1148-1154.

[93] Reed-Hill RE and Robertson WD, *The Crystallographic Characteristics of Fracture in Magnesium Single Crystals,* Acta Metall., 1957, **5**(12), 728-737.

[94] Ando S and Tonda H, *Non-basal slip in magnesium-lithium alloy single crystals,* Mater. Trans. JIM, 2000, **41**(9), 1188-1191.

[95] Yoshinaga BH and Horiuchi R, *Deformation mechanisms in magnesium single crystals compressed in the direction parallel to hexagonal axis,* Trans JIM, 1963, **4**, 1-8.

[96] Galiyev A, Kaibyshev R, and Gottstein G, *Correlation of plastic deformation and dynamic recrystallization in magnesium alloy Zk60,* Acta Mater., 2001, **49**(7), 1199-1207.

[97] Saxl I and Haslingerová I, *Double prismatic slip in textured Mg-2% Be alloy,* Czechoslovak Journal of Physics, 1974, **24**(12), 1351-1361.

[98] Jiang L, Jonas JJ, Mishra RK, Luo AA, Sachdev AK, and Godet S, *Twinning and texture development in two Mg alloys subjected to loading along three different strain paths,* Acta Mater., 2007, **55**(11), 3899-3910.

[99] Meyers MA, Vohringer O, and Lubarda VA, *The onset of twinning in metals: A constitutive description,* Acta Mater., 2001, **49**(19), 4025-4039.

[100] Nilles JL and Owen WS, *In: Mechanical Behavior of Materials.* 1972, The Society of Metals, Japan.

[101] Lohe D and Vohringer O, *On the Influence of Mechanical Twinning on Deformation Behaviour of Ferritic Iron Base Alloys,* Z. Metallkd., 1986, **77**(9), 557-563.

[102] Narita N and Takamura J, *Dislocations in Solids.* 1992: Elsevier.

[103] Song SG and Gray GT, *Influence of Temperature and Strain-Rate on Slip and Twinning Behavior of Zr,* Metall. Mater. Trans. A, 1995, **26**(10), 2665-2675.

[104] Harding J, *Yield and Fracture Behaviour of High-Purity Iron Single Crystals at High Rates of Strain,* Proc. R. Soc. London, Ser. A, 1967, **299**(1459), 464.

[105] Harding J, *Yield and Fracture of High-Purity Iron Single Crystals under Repeated Tensile Impact Loading,* Mem. Etud. Sci. Rev. Met., 1968, **65**(JUN), 245.

[106] Thornton PR and Mitchell TE, *Deformation Twinning in Alloys at Low Temperatures,* Philos. Mag., 1962, **7**(75), 361.

[107] Lahaie D, Embury JD, Chadwick MM, and Gray GT, *A Note on the Deformation of Fine-Grained Magnesium Alloys,* Scripta Metall. Mater., 1992, **27**(2), 139-142.

[108] Kaibyshev R, Galiev A, and Sitdikov O, *On the possibility of producing a nanocrystalline structure in magnesium and magnesium alloys,* Nanostructured Materials, 1995, **6**(5-8), 621-624.

[109] Agnew SR and Duygulu O, *Plastic anisotropy and the role of non-basal slip in magnesium alloy AZ31B,* Int. J. Plast., 2005, **21**(6), 1161-1193.

[110] Stanford N, Sabirov I, Sha G, La Fontaine A, Ringer SP, and Barnett MR, *Effect of Al and Gd Solutes on the Strain Rate Sensitivity of Magnesium Alloys,* Metall. Mater. Trans. A, 2010, **41A**(3), 734-743.

[111] Agnew SR, Horton JA, and Yoo MH, *Transmission electron microscopy investigation of < c+a > dislocations in Mg and alpha-solid solution Mg-Li alloys,* Metall. Mater. Trans. A, 2002, **33**(3), 851-858.

[112] Humphreys FJ and Hatherly M, *Recrystallization and related annealing phenomena,* 2nd ed, 2004, Elsevier Science Ltd, Amsterdam; London.

[113] Hardwick D and Tegart WJM, *Structural Changes During the Deformation of Copper, Aluminium and Nickel at High Temperatures and High Strain Rates,* J. Inst. Metals, 1961, **90**(1), 17-21.

[114] Sastry DH, Prasad YVR, and Vasu KI, *On Stacking Fault Energies of Some Close-Packed Hexagonal Metals,* Scripta Metall., 1969, **3**(12), 927.

[115] Murr LE, *Interfacial phenomena in metals and alloys,* 1975, Addison-Wesley, Reading, Mass.; London.

[116] Somekawa H, Hirai K, Watanabe H, Takigawa Y, and Higashi K, *Dislocation creep behavior in Mg-Al-Zn alloys,* Mater. Sci. Eng. A, 2005, **407**(1-2), 53-61.

[117] Gottstein G and Kocks UF, *Dynamic Recrystallization and Dynamic Recovery in (111) Single-Crystals of Nickel and Copper,* Acta Metall., 1983, **31**(1), 175-188.

[118] Perez-Prado MT, del Valle JA, Contreras JM, and Ruano OA, *Microstructural evolution during large strain hot rolling of an AM60 Mg alloy,* Scripta Mater., 2004, **50**(5), 661-665.

[119] He YB, Pan QL, Qin YJ, Liu XY, Li WB, Chiu YL, and Chen JJJ, *Microstructure and mechanical properties of ZK60 alloy processed by two-step equal channel angular pressing,* J. Alloys Compd., 2010, **492**(1-2), 605-610.

[120] Jin L, Dong J, Wang R, and Peng LM, *Effects of hot rolling processing on microstructures and mechanical properties of Mg-3%Al-1%Zn alloy sheet,* Mater. Sci. Eng. A, 2010, **527**(7-8), 1970-1974.

[121] Gottstein G, Chang L, and Yung HF, *Dynamic Recrystallization and Microstructural Evolution in Ni3al,* Mater. Sci. Tech., 1991, **7**(2), 158-166.

[122] Valiev RZ, Ivanisenko YV, Rauch EF, and Baudelet B, *Structure and deformation behaviour of armco iron subjected to severe plastic deformation,* Acta Mater., 1996, **44**(12), 4705-4712.

[123] Mote JD and Dorn JE, *Deformation and Fracture of Magnesium Bicrystals,* Trans. Metall. Soc. AIME, 1960, **218**(3), 491-497.

[124] Chen B, Lin DL, Zeng XQ, and Lu C, *Effects of yttrium and zinc addition on the microstructure and mechanical properties of Mg-Y-Zn alloys,* J. Mater. Sci., 2010, **45**(9), 2510-2517.

[125] Spigarelli S, El Mehtedi M, Cabibbo M, Evangelista E, Kaneko J, Jager A, and Gartnerova V, *Analysis of high-temperature deformation and microstructure of an AZ31 magnesium alloy,* Mater. Sci. Eng. A, 2007, **462**(1-2), 197-201.

[126] Liu LF and Ding HL, *Study of the plastic flow behaviors of AZ91 magnesium alloy during thermomechanical processes,* J. Alloys Compd., 2009, **484**(1-2), 949-956.

[127] Hakamada M, Watazu A, Saito N, and Iwasaki H, *Effects of homogenization annealing on dynamic recrystallization in Mg-Al-Ca-RE (rare earth) alloy,* Mater. Trans., 2008, **49**(5), 1032-1037.

[128] Myshlyaev MM, McQueen HJ, Mwembela A, and Konopleva E, *Twinning, dynamic recovery and recrystallization in hot worked Mg-Al-Zn alloy,* Mater. Sci. Eng. A, 2002, **337**(1-2), 121-133.

[129] Xu SW, Kamado S, Matsumoto N, Honma T, and Kojima Y, *Recrystallization mechanism of as-cast AZ91 magnesium alloy during hot compressive deformation,* Mater. Sci. Eng. A, 2009, **527**(1-2), 52-60.

[130] Belyakov A, Miura H, and Sakai T, *Dynamic recrystallization under warm deformation of polycrystalline copper,* Isij International, 1998, **38**(6), 595-601.

[131] Belyakov A, Miura H, and Sakai T, *Dynamic recrystallization under warm deformation of a 304 type austenitic stainless steel,* Mater. Sci. Eng. A, 1998, **255**(1-2), 139-147.

[132] White S, *The effects of strain on the microstructures, fabrics, and deformation mechanisms in quartzites,* Philos. Trans. R. Soc. London, Ser. A, 1976, **283**(1312), 69-86.

[133] McQueen HJ and Bergerson S, *Dynamic recrystallization of copper during hot torsion,* Metal Science, 1972, **6**(1), 25-29.

[134] Belyakov A, Gao W, Miura H, and Sakai T, *Strain-induced grain evolution in polycrystalline copper during warm deformation,* Metall. Mater. Trans. A, 1998, **29**(12), 2957-2965.

[135] Iwahashi Y, Horita Z, Nemoto M, and Langdon TG, *An investigation of microstructural evolution during equal-channel angular pressing,* Acta Mater., 1997, **45**(11), 4733-4741.

[136] Sivakesavam O, Rao IS, and Prasad Y, *Processing Map for Hot-Working of as Cast Magnesium,* Mater. Sci. Tech., 1993, **9**(9), 805-810.

[137] Al-Samman T and Gottstein G, *Dynamic recrystallization during high temperature deformation of magnesium,* Mater. Sci. Eng. A, 2008, **490**(1-2), 411-420.

[138] Yi SB, Zaefferer S, and Brokmeier HG, *Mechanical behaviour and microstructural evolution of magnesium alloy AZ31 in tension at different temperatures,* Mater. Sci. Eng. A, 2006, **424**(1-2), 275-281.

[139] Jin L, Lin DL, Mao DL, Zeng XQ, and Chen B, *Microstructure evolution of AZ31 Mg alloy during equal channel angular extrusion,* Mater. Sci. Eng. A, 2006, **423**(1-2), 247-252.

[140] Barnett MR, Beer AG, Atwell D, and Oudin A, *Influence of grain size on hot working stresses and microstructures in Mg-3Al-1Zn,* Scripta Mater., 2004, **51**(1), 19-24.

[141] Gourdet S and Montheillet F, *A model of continuous dynamic recrystallization,* Acta Mater., 2003, **51**(9), 2685-2699.

[142] Sitdikov O and Kaibyshev R, *Dynamic recrystallization in pure magnesium,* Mater. Trans., 2001, **42**(9), 1928-1937.

[143] Trepmann CA and Stockhert B, *Microfabric of folded quartz veins in metagreywackes: dislocation creep and subgrain rotation at high stress,* J. Metamorph. Geol., 2009, **27**(8), 555-570.

[144] Humphreys FJ, *Dynamic Recrystallisation - The Influence of Crystal Structure,* in *Deformation of Polycrystals: Mechanisms and Microstructures,* Hansen N, et al., Editors. 1981, RISO National Laboratory: Roskilde. p. 305-310.

[145] Yang XY, Miura HM, and Sakai T, *Dynamic evolution of new grains in magnesium alloy AZ31 during hot deformation,* Mater. Trans., 2003, **44**(1), 197-203.

[146] Watanabe H, Tsutsui H, Mukai T, Ishikawa K, Okanda Y, Kohzu M, and Higashi K, *Grain size control of commercial wrought Mg-Al-Zn alloys utilizing dynamic recrystallization,* Mater. Trans., 2001, **42**(7), 1200-1205.

[147] Shahzad M and Wagner L, *The role of Zr-rich cores in strength differential effect in an extruded Mg-Zn-Zr alloy,* J. Alloys Compd., 2009, **486**(1-2), 103-108.

[148] Homma T, Mendis CL, Hono K, and Kamado S, *Effect of Zr addition on the mechanical properties of as-extruded Mg-Zn-Ca-Zr alloys,* Mater. Sci. Eng. A, 2010, **527**(9), 2356-2362.

[149] Mabuchi M, Kubota K, and Higashi K, *New Recycling Process by Extrusion for Machined Chips of Az91 Magnesium and Mechanical-Properties of Extruded Bars,* Mater. Trans. JIM, 1995, **36**(10), 1249-1254.

[150] Mabuchi M, Chino Y, Iwasaki H, Aizawa T, and Higashi K, *The grain size and texture dependence of tensile properties in extruded Mg-9Al-1Zn,* Mater. Trans., 2001, **42**(7), 1182-1189.

[151] Barnett MR, *Quenched and annealed microstructures of hot worked magnesium AZ31,* Mater. Trans., 2003, **44**(4), 571-577.

[152] Helis L, Okayasu K, and Fukutomi H, *Microstructure evolution and texture development during high-temperature uniaxial compression of magnesium alloy AZ31,* Mater. Sci. Eng. A, 2006, **430**(1-2), 98-103.

[153] Li HL, Hsu E, Szpunar J, Utsunomiya H, and Sakai T, *Deformation mechanism and texture and microstructure evolution during high-speed rolling of AZ31B Mg sheets,* J. Mater. Sci., 2008, **43**(22), 7148-7156.

[154] Beausir B, Biswas S, Kim DI, Toth LS, and Suwas S, *Analysis of microstructure and texture evolution in pure magnesium during symmetric and asymmetric rolling,* Acta Mater., 2009, **57**(17), 5061-5077.

[155] Perez-Prado MT, del Valle JA, and Ruano OA, *Effect of sheet thickness on the microstructural evolution of an Mg AZ61 alloy during large strain hot rolling,* Scripta Mater., 2004, **50**(5), 667-671.

[156] Beer AG and Barnett MR, *Microstructure evolution in hot worked and annealed magnesium alloy AZ31,* Mater. Sci. Eng. A, 2008, **485**(1-2), 318-324.

[157] Bohlen J, Yi SB, Swiostek J, Letzig D, Brokmeier HG, and Kainer KU, *Microstructure and texture development during hydrostatic extrusion of magnesium alloy AZ31,* Scripta Mater., 2005, **53**(2), 259-264.

[158] Perez-Prado MT and Ruano OA, *Texture evolution during annealing of magnesium AZ31 alloy,* Scripta Mater., 2002, **46**(2), 149-155.

[159] Kim HK and Kim WJ, *Microstructural instability and strength of an AZ31 Mg alloy after severe plastic deformation,* Mater. Sci. Eng. A, 2004, **385**(1-2), 300-308.

[160] Higgins GT, *Secondary Recrystallisation in Magnox Al 80,* J. Nucl. Mater., 1963, **8**(2), 153-159.

[161] Wang SR, Kang SB, and Cho J, *Effect of hot compression and annealing on microstructure evolution of ZK60 magnesium alloys,* J. Mater. Sci., 2009, **44**(20), 5475-5484.

[162] Randle V and Engler O, *Introduction to texture analysis: macrotexture, microtexture and orientation mapping,* 2000, Gordon & Breach, Amsterdam, The Netherlands.

[163] Yang P, Yu Y, Chen L, and Mao W, *Experimental determination and theoretical prediction of twin orientations in magnesium alloy AZ31,* Scripta Mater., 2004, **50**(8), 1163-1168.

[164] Bohlen J, Nurnberg MR, Senn JW, Letzig D, and Agnew SR, *The texture and anisotropy of magnesium-zinc-rare earth alloy sheets,* Acta Mater., 2007, **55**(6), 2101-2112.

[165] Tenckhoff E, *Development of Deformation Texture in Zirconium During Rolling in Sequential Passes,* Metall. Trans. A, 1978, **9**(10), 1401-1412.

[166] Kocks UF, Tome CN, and Wenk H-R, *Texture and anisotropy: preferred orientations in polycrystals and their effect on materials properties*, 1998, Cambridge University Press, New York; Cambridge.

[167] Zinov'ev AV, Ionov AM, Kaputkina LM, Mironov PV, Kaputkin EY, Sigalov YM, and Solomonik YL, *A study of the process of hot deformation of magnesium alloy AZ31*, Met. Sci. Heat Treat., 2006, **48**(11-12), 494-498.

[168] Lukac P and Trojanova Z, *Hardening and softening in selected magnesium alloys*, Mater. Sci. Eng. A, 2007, **462**(1-2), 23-28.

[169] Prasad Y and Rao KP, *Processing maps for hot deformation of rolled AZ31 magnesium alloy plate: Anisotropy of hot workability*, Mater. Sci. Eng. A, 2008, **487**(1-2), 316-327.

[170] Zhang XP and Wang JT, *The flow stress during hot compression deformation of a Mg-Gd-Y-Zr magnesium alloy: Experiments and numerical simulations*, in *Magnesium Technology 2008*, Pekguleryuz MO, et al., Editors. 2008, Minerals, Metals & Materials Soc: Warrendale. p. 183-187.

[171] Jiang L, Jonas JJ, Luo AA, Sachdev AK, and Godet S, *Influence of {10-12} extension twinning on the flow behavior of AZ31 Mg alloy*, Mater. Sci. Eng. A, 2007, **445**, 302-309.

[172] Caceres CH and Blake AH, *On the strain hardening behaviour of magnesium at room temperature*, Mater. Sci. Eng. A, 2007, **462**(1-2), 193-196.

[173] Mathis K, Trojanova Z, and Lukac P, *Hardening and softening in deformed magnesium alloys*, Mater. Sci. Eng. A, 2002, **324**(1-2), 141-144.

[174] Guo Q, Yan HG, Chen ZH, and Zhang H, *Elevated temperature compression behaviour of Mg-Al-Zn alloys*, Mater. Sci. Tech., 2006, **22**(6), 725-729.

[175] Shamsi M, Sanjari M, and Hanzaki AZ, *Study of fractional softening of AZ31 magnesium alloy under multistage hot deformation*, Mater. Sci. Tech., 2009, **25**(8), 1039-1045.

[176] Zhou HT, Li QB, Zhao ZK, Liu ZC, Wen SF, and Wang QD, *Hot workability characteristics of magnesium alloy AZ80-A study using processing map*, Mater. Sci. Eng. A, 2010, **527**(7-8), 2022-2026.

[177] Srinivasan N, Prasad Y, and Rao PR, *Hot deformation behaviour of Mg-3Al alloy - A study using processing map*, Mater. Sci. Eng. A, 2008, **476**(1-2), 146-156.

[178] Slooff FA, Dzwonczyk JS, Zhou J, Duszczyk J, and Katgerman L, *Hot workability analysis of extruded AZ magnesium alloys with processing maps*, Mater. Sci. Eng. A, 2010, **527**(3), 735-744.

[179] Galiyev A, Sitdikov O, and Kaibyshev R, *Deformation behavior and controlling mechanisms for plastic flow of magnesium and magnesium alloy*, Mater. Trans., 2003, **44**(4), 426-435.

[180] Yang Z, Li JP, Zhang JX, Guo YC, Wang BW, Xia F, and Liang MX, *Effect of homogenization on the hot-deformation ability and dynamic recrystallization of Mg-9Gd-3Y-0.5Zr alloy*, Mater. Sci. Eng. A, 2009, **515**(1-2), 102-107.

[181] Zhou HT, Liu CM, and Chen MA, *Constitutive model development and hot extrusion simulation for AZ61 magnesium alloy*, Mater. Sci. Tech., 2006, **22**(5), 597-603.

[182] Yang YQ, Li BC, and Zhang ZM, *Flow stress of wrought magnesium alloys during hot compression deformation at medium and high temperatures*, Mater. Sci. Eng. A, 2009, **499**(1-2), 238-241.

[183] Frost HJ and Ashby MF, *Deformation-mechanism maps: the plasticity and creep of metals and ceramics.* 1982, Pergamon: Oxford. p. 166.

[184] Slooff FA, Duszczyk J, and Katgerman L, *Constitutive analysis of wrought magnesium alloy Mg-AL4-Znl,* Scripta Mater., 2007, **57**(8), 759-762.

[185] Mwembela A, Konopleva EB, and McQueen HJ, *Microstructural development in Mg alloy AZ31 during hot working,* Scripta Mater., 1997, **37**(11), 1789-1795.

[186] Li DJ, Wang QD, Blandin JJ, Suery M, Dong J, and Zeng XQ, *High temperature compressive deformation behavior of an extruded Mg-8Gd-3Y-0.5Zr (wt.%) alloy,* Mater. Sci. Eng. A, 2009, **526**(1-2), 150-155.

[187] Anyanwu IA, Kamado S, and Kojima Y, *Creep properties of Mg-Gd-Y-Zr alloys,* Mater. Trans., 2001, **42**(7), 1212-1218.

[188] Vagarali SS and Langdon TG, *Deformation Mechanisms in Hcp Metals at Elevated-Temperatures .1. Creep-Behavior of Magnesium,* Acta Metall., 1981, **29**(12), 1969-1982.

[189] Vagarali SS and Langdon TG, *Deformation Mechanisms in Hcp Metals at Elevated-Temperatures .2. Creep-Behavior of a Mg-0.8-Percent Al Solid-Solution Alloy,* Acta Metall., 1982, **30**(6), 1157-1170.

[190] Karaman I, Sehitoglu H, Beaudoin AJ, Chumlyakov YI, Maier HJ, and Tome CN, *Modeling the deformation behavior of Hadfield steel single and polycrystals due to twinning and slip,* Acta Mater., 2000, **48**(9), 2031-2047.

[191] Wang CY, Wang XJ, Chang H, Wu K, and Zheng MY, *Processing maps for hot working of ZK60 magnesium alloy,* Mater. Sci. Eng. A, 2007, **464**(1-2), 52-58.

[192] Zhao X, Zhang K, Li XG, Li YJ, He QB, and Sun JF, *Deformation behavior and dynamic recrystallization of Mg-Y-Nd-Gd-Zr alloy,* J. Rare Earths, 2008, **26**(6), 846-850.

[193] Yu K, Li WX, Zhao J, Ma ZQ, and Wang RC, *Plastic deformation behaviors of a Mg-Ce-Zn-Zr alloy,* Scripta Mater., 2003, **48**(9), 1319-1323.

[194] Beladi H and Barnett MR, *Influence of aging pre-treatment on the compressive deformation of WE54 alloy,* Mater. Sci. Eng. A, 2007, **452**, 306-312.

[195] Lapovok RY, Barnett MR, and Davies CHJ, *Construction of extrusion limit diagram for AZ31 magnesium alloy by FE simulation,* J. Mater. Process. Technol., 2004, **146**(3), 408-414.

[196] Anbuselvan S and Ramanathan S, *Hot deformation and processing maps of extruded ZE41A magnesium alloy,* Mater. Des., 2010, **31**(5), 2319-2323.

[197] Davenport SB, Silk NJ, Sparks CN, and Sellars CM, *Development of constitutive equations for modelling of hot rolling,* Mater. Sci. Tech., 2000, **16**(5), 539-546.

[198] McQueen HJ and Ryan ND, *Constitutive analysis in hot working,* Mater. Sci. Eng. A, 2002, **322**(1-2), 43-63.

[199] Sellars CM and Tegart WJM, *Relationship between Strength and Structure in Deformation at Elevated Temperatures,* Mem. Etud. Sci. Rev. Met., 1966, **63**(9), 731.

[200] Garofalo F, *An Empirical Relation Defining Stress Dependence of Minimum Creep Rate in Metals,* Trans. Metall. Soc. AIME, 1963, **227**(2), 351.

[201] Takuda H, Fujimoto H, and Hatta N, *Modelling on flow stress of Mg-Al-Zn alloys at elevated temperatures,* J. Mater. Process. Technol., 1998, **80-1**, 513-516.

[202] Li L, Zhou J, and Duszczyk J, *Determination of a constitutive relationship for AZ31B magnesium alloy and validation through comparison between simulated and real extrusion,* J. Mater. Process. Technol., 2006, **172**(3), 372-380.

[203] Bhattacharya R, Wynne BP, Rainforth WM, and Davies B, *Flow stress modelling of magnesium AZ31 alloy based on high strain plane strain compression data.* in *Magnesium Technology 2008.* 2008. New Orleans: The Minerals, Metals & Materials Soc.

[204] Watts AB and Ford H, *On the basic yield stress curve for a metal,* Proc. Instn. Mech. Eng., 1955, **169**, 1141-1156.

[205] Hinton JS, *Laboratory Simulation of Microstructural Evolution in AISI 430 Ferritic Stainless Steel during the Steckel Mill Process*, 2006, PhD Thesis, Department of Engineering Materials, University of Sheffield, Sheffield, UK.

[206] Loveday MS, Mahon GJ, Roebuck B, Lacey AJ, Palmiere EJ, Sellars CM, and van der Winden MR, *Measurement of flow stress in hot plane strain compression tests,* Mater. High Temp., 2006, **23**(2), 85-118.

[207] Alexander JM, *The Effect of Coulomb Friction in the Plane-Strain Compression of a Plastic-Rigid Material,* J. Mech. Phys. Solids, 1955, **3**(4), 233-245.

[208] Silk NJ and van der Winden MR, *Interpretation of hot plane strain compression testing of aluminium specimens,* Mater. Sci. Tech., 1999, **15**(3), 295-300.

[209] Tukey JW, *Exploratory Data Analysis*, Addison-Wesley Series in Behavioral Science: Quantitative Methods, 1977, Addison-Wesley, Reading, Mass.

[210] Winder A, *The Ageing Response of Magnesium Alloy Elektron 675*, 2010, MEng Thesis, Department of Engineering Materials, University of Sheffield, Sheffield.

[211] Schwartz AJ, Kumar M, and Adams BL, *Electron backscatter diffraction in materials science*, 2000, Kluwer Academic, New York; London.

[212] Davies PS, *An Investigation of Microstructure and Texture Evolution in the Near-α Titanium Alloy Timetal® 834*, 2009, PhD Thesis, Department of Engineering Materials, University of Sheffield, Sheffield, UK.

[213] Cullity BD, *Elements of X-ray diffraction*, 2nd ed, Addison-Wesley series in metallurgy and materials, 1978, Addison-Wesley, Reading, Mass.; London.

[214] Estrin Y and Mecking H, *A Unified Phenomenological Description of Work-Hardening and Creep Based on One-Parameter Models,* Acta Metall., 1984, **32**(1), 57-70.

[215] Grimmer H, *Distribution of Disorientation Angles If All Relative Orientations of Neighboring Grains Are Equally Probable,* Scripta Metall., 1979, **13**(2), 161-164.

[216] Guo Q, Yan HG, Zhang H, Chen ZH, and Wang ZF, *Behaviour of AZ(31) magnesium alloy during compression at elevated temperatures,* Mater. Sci. Tech., 2005, **21**(11), 1349-1354.

[217] Zhou HT, Zeng XQ, Liu LL, Dong J, Wang QD, Ding WJ, and Zhu YP, *Microstructural evolution of AZ61 magnesium alloy during hot deformation,* Mater. Sci. Tech., 2004, **20**(11), 1397-1402.

[218] Crossland IG and Jones RB, *Dislocation Creep in Mg,* Met. Sci. J., 1972, **6**, 162.

[219] Hasegawa T and Kocks UF, *Thermal Recovery Processes in Deformed Aluminum,* Acta Metall., 1979, **27**(11), 1705-1716.

[220] Zhang Y, Zeng XQ, Lu C, and Ding WJ, *Deformation behavior and dynamic recrystallization of a Mg-Zn-Y-Zr alloy,* Mater. Sci. Eng. A, 2006, **428**(1-2), 91-97.

[221] Zhang YB, Godfrey A, Liu Q, Liu W, and Jensen DJ, *Analysis of the growth of individual grains during recrystallization in pure nickel,* Acta Mater., 2009, **57**(9), 2631-2639.

[222] Styczynski A, Hartig C, Bohlen J, and Letzig D, *Cold rolling textures in AZ31 wrought magnesium alloy,* Scripta Mater., 2004, **50**(7), 943-947.

[223] Li HL, Hsu E, Szpunar J, Verma R, and Carter JT, *Determination of active slip/twinning modes in AZ31 Mg alloy near room temperature,* J. Mater. Eng. Perform., 2007, **16**(3), 321-326.

[224] Edington JW, Melton KN, and Cutler CP, *Superplasticity,* Prog. Mater. Sci., 1976, **21**(2), 63-170.

[225] Liu Y and Wu X, *An electron-backscattered diffraction study of the texture evolution in a coarse-grained AZ31 magnesium alloy deformed in tension at elevated temperatures,* Metall. Mater. Trans. A, 2006, **37A**(1), 7-17.

[226] Senn JW and Agnew SR, *Texture randomization of magnesium alloys containing rare earth elements*, in *Magnesium Technology 2008*, Pekguleryuz MO, et al., Editors. 2008, Minerals, Metals & Materials Soc: Warrendale. p. 153-158.

[227] Hou XL, Peng QM, Cao ZY, Xu SW, Kamado S, Wang LD, Wu YM, and Wang LM, *Structure and mechanical properties of extruded Mg-Gd based alloy sheet,* Mater. Sci. Eng. A, 2009, **520**(1-2), 162-167.

[228] Yang Z, Li JP, Guo YC, Liu T, Xia F, Zeng ZW, and Liang MX, *Precipitation process and effect on mechanical properties of Mg-9Gd-3Y-0.6Zn-0.5Zr alloy,* Mater. Sci. Eng. A, 2007, **454**, 274-280.

[229] Dieter GE and Bacon D, *Mechanical metallurgy*, SI metric ed, 1988, McGraw-Hill,

Appendix – Flow Curves

The full flow curves, including those that fractured during deformation are shown below.

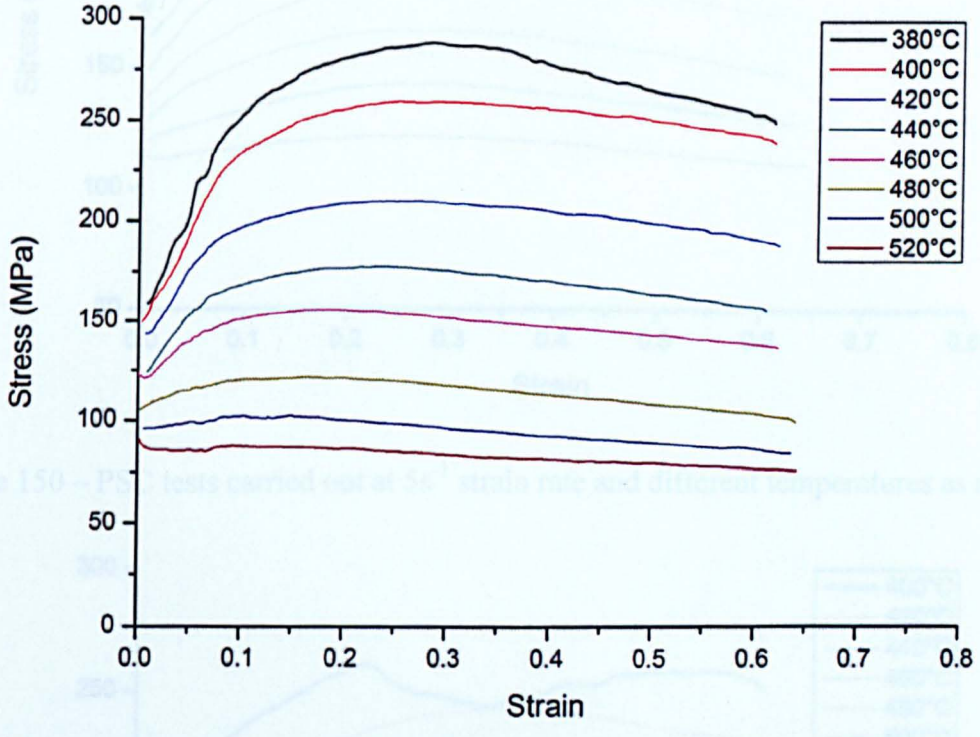

Figure 149 – PSC tests carried out at $1s^{-1}$ strain rate and different temperatures as shown

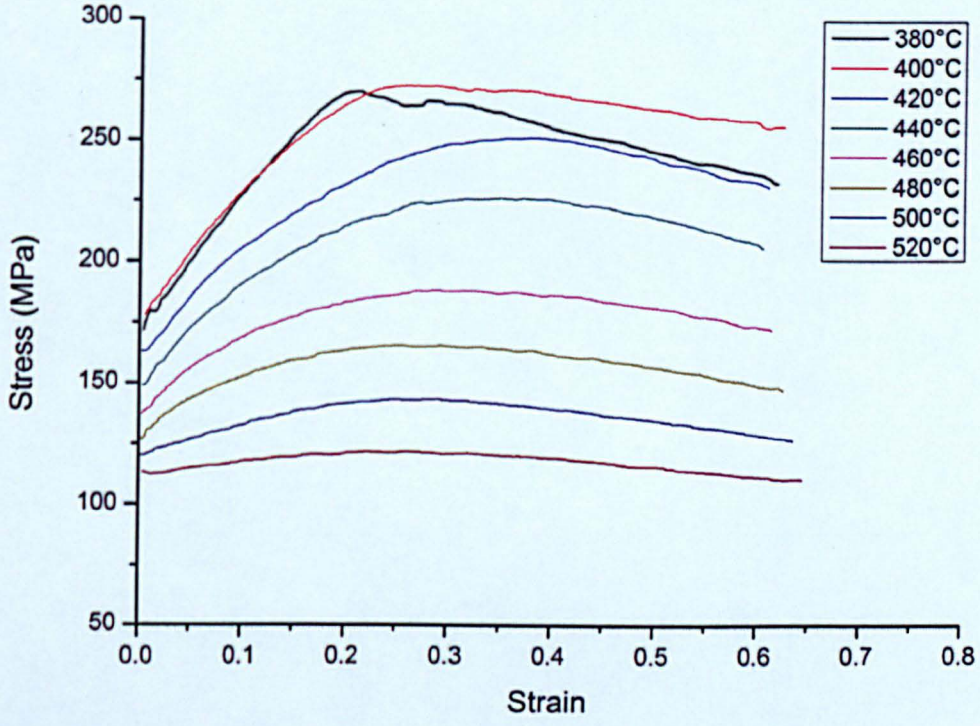

Figure 150 – PSC tests carried out at $5s^{-1}$ strain rate and different temperatures as shown

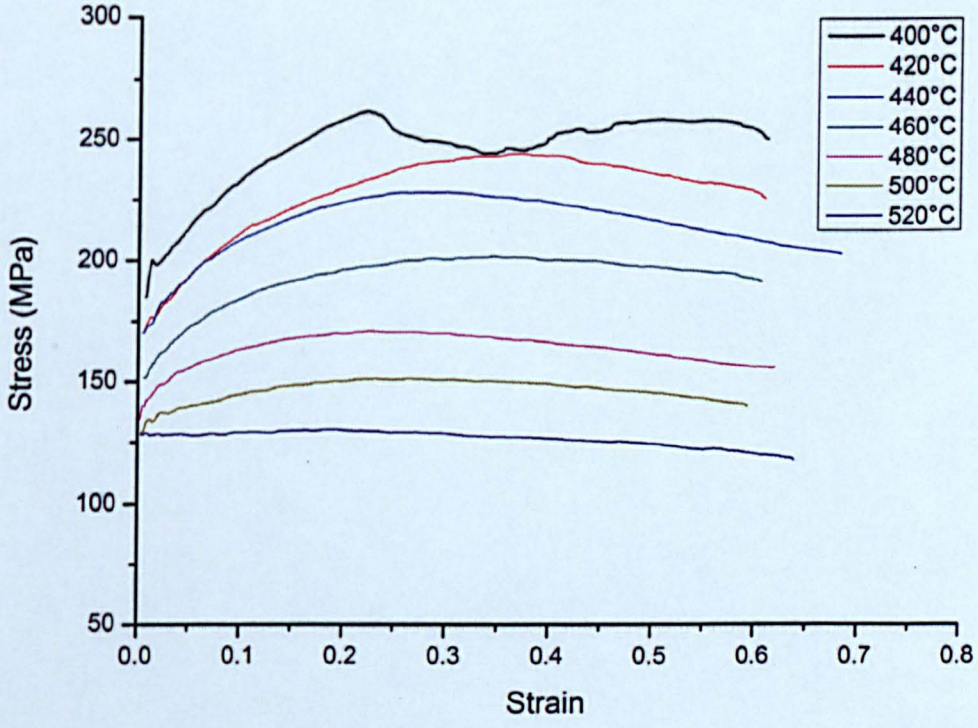

Figure 151 – PSC tests carried out at $10s^{-1}$ strain rate and different temperatures as shown